CHARGE TRANSPORT AND DIRECTED ASSEMBLY OF NANO-CONFINED PORPHYRIN MOLECULES ON SURFACES: TOWARDS MOLECULAR AND ORGANIC ELECTRONICS

A Dissertation

by

ALISON ANDREA PAWLICKI

Submitted to the Office of Graduate and Professional Studies of
Texas A&M University
in partial fulfillment of the requirements for the degree of

DOCTOR OF PHILOSOPHY

Chair of Committee,	James D. Batteas
Committee Members,	Jorge M. Seminario
	Sreeram Vaddiraju
	Robert R. Lucchese
Head of Department,	Ibrahim Karaman

December 2016

Major Subject: Materials Science and Engineering

ABSTRACT

Presently, the aim of molecular/organic electronics is to incorporate organic materials into conventional silicon-based devices and complimentary metal-oxide semiconductor (CMOS) technology to expand the functionality of electronic devices, exploit bottom-up fabrication techniques, and to achieve nanoscopic dimensions. However, the success of molecular/organic electronics depends upon tailoring the function of devices by intentionally modifying the properties of the molecular components starting at the single molecule level and continuing to fabricate meaningful molecular structures.

Here, porphyrins were used as a platform to study the structure/electronic property relationship because they are candidates for molecule-containing devices and have vast chemical tunability. The structure of these porphyrins consists of a macrocycle attached to an alkanethiol tether that bonds to Au surfaces and were assembled within a dodecanethiol (C12) self-assembled monolayer (SAM). The physical morphology of the mixed SAM was examined and manipulated by Atomic Force Microscopy (AFM). The molecular-level morphology and the electronic properties were examined by Scanning Tunneling Microscopy (STM).

The porphyrin chemical structure was systematically perturbed and allowed to randomly self-assemble within a C12 SAM. Contrary to original expectations of molecular/organic electronics, chemical structure perturbations did not lead to variations in the electronic properties for single porphyrin molecules with consistent indications of

tunneling dominated by the alkanethiol tether. To recover the ability to tune the electronic properties, assemblies large enough to stabilize charge were formed with indications of Coulomb Blockade. However, increasing variations in the relative conductance were observed for increasing assembly size. To interrogate this, the electronic properties were examined as a function of assembly duration and a stark difference in the current-voltage (I-V) characteristics attributed to subtle changes in nearest neighbor interactions.

To utilize the electronic properties of porphyrins found here in a pre-defined manner, a facile two-step method was developed to direct porphyrin assembly. First, the surface tether, pentanedithiol (C5DT), was controllably attached to the Au(111) surface in pre-defined geometries. Second, porphyrins were selectively attached to the C5DT by "click" chemistry. Employing this method, porphyrins built-up into a pi-stacked hierarchy on the C5DT domains and displayed the desired I-V characteristics.

DEDICATION

I dedicate this dissertation to my future husband, Dr. Bruno Turcksin, who has selflessly encouraged my education and did not allow me to falter in my times of unsteadiness.

ACKNOWLEDGEMENTS

The work presented herein has been achieved with the assistance of many supporters. I dedicate this dissertation to my future husband, Dr. Bruno Turcksin, who has selflessly encouraged my education and did not allow me to falter in my times of unsteadiness. I would like to thank my family, in particular, my parents and grandparents, who prepared me to pursue my dream of contributing to science and engineering by earning a Ph.D. I will proudly continue the line of engineers in my family following my grandfather, Mr. Charles Weibust, and my father, Mr. Jeffrey Pawlicki. I am sincerely grateful for my research advisor, Dr. James D. Batteas, for his scientific and professional guidance, as well as empowering me with the capabilities to conduct this research. Furthermore, I would like to give a warm thanks to my committee members, Dr. Robert R. Lucchese, Dr. Jorge M. Seminario, and Dr. Sreeram Vaddiraju, for their time and continued support.

I would like to recognize the collaborators who contributed to this work. I truly appreciate Dr. Charles Michael Drain and Dr. Matthew Jurow, who synthesized the porphyrin molecules that were integral to this research. Thank you to Dr. Ayelet Vilan, who contributed her expertise on the analysis of I-V characteristics and for being a role model to me as a successful woman in science with a full family life. Thank you to Ms. Erin Avery, for allowing me to guide her during the Research Experience for Undergraduates (REU) Program at Texas A&M University and aiding in the execution of part of my scientific ideas.

I am grateful for the guidance given to me by past mentors and peers. During my graduate career I am grateful for the support, in the form of initial laboratory training and insightful scientific conversations, provided early-on in my graduate career by Dr. Bradley Ewers. I would also like to recognize the members of the Batteas Research Group, for their continued support and willingness to share ideas and skills. During my undergraduate career, I am appreciative of Dr. Christopher Wiebe, who granted me my first experience in materials research at Florida State University as a student employee at the National High Magnetic Field Laboratory. A special thanks to Dr. Laura Green, who mentored me while I was working in her laboratory at the University of Illinois as an REU student, and continued mentoring long distance in the many years to come. Thank you to Dr. Matri Wathrasuwithana for guiding me through my Undergraduate Honors Thesis and for making it possible for me to carry out research with the specialized magnets at the National High Magnetic Field Laboratory. I appreciate Dr. David Mandrus and Dr. Athena Safa-Sefat for the experience that I gained working in government research at Oak Ridge National Laboratory. I am deeply grateful for my friendship with Mr. Christopher Segal and our years of collaboration. These people have collectively raised me up to achieve my dream and I will continue to repay their services by helping others as they have helped me.

Finally, I would like to acknowledge the financial support for this work. Thanks to the National Science Foundation (NSF) for bestowing upon me the Graduate Research Fellowship (GRF), as well as, additional support through grants, CHE-1213082 to JDB and CHE-1213962 to CMD.

CONTRIBUTORS AND FUNDING SOURCES

Contributors

The work presented herein was supported by a dissertation committee composed of Dr. James D. Batteas (chair), jointly appointed in the Department of Materials Science and Engineering and the Department of Chemistry, Dr. Jorge M. Seminario (member), jointly appointed in the Department of Materials Science and Engineering and the Department of Chemical Engineering, Dr. Sreeram Vaddiraju (member), jointly appointed in the Department of Materials Science and Engineering and the Department of Chemical Engineering, as well as Dr. Robert R. Lucchese (outside department member), of the Department of Chemistry.

All the porphyrin derivatives studied were provided and synthesized by Dr. Charles Michael Drain and Dr. Matthew Jurow. The optimized geometry and corresponding electronic structure calculations with –F and –H substituent on the phenyl linker of the porphryin-thiols, as presented in Chapter II, were carried out by Dr. Bradley Ewers. Ms. Megan Link was guided by myself and collected a part of the apparent height measurements with STM imaging of one of the porphyrin derivatives discussed in Chapter II. Chapter III was a collaborative effort between Dr. Ayelet Vilan and myself, in which Dr. Ayelet Vilan assisted in the statistical analysis of the I-V data. A portion of the nanografting experiments in Chapter IV were carried out by Ms. Erin Avery under my direction as part of Ms. Erin Avery's Research Experience for Undergraduates (REU) Program at Texas A&M University. Dr. Bradley Ewers and I created the pattern

relocation schemes shown in Appendix C. Mr. Cody Chalker fabricated the Focused Ion Beam (FIB) pattern of Figure 49(C) in Appendix C. With the supervision of Dr. Bradley Ewers and myself, Mr. Alexis Blanco helped to test the method for Scanning Tunneling Spectroscopy (STS) measurements detailed in Appendix D. All other work conducted for this dissertation was completed by myself independently.

Funding Sources

Graduate study was supported by a research fellowship from the National Science Foundation under the Graduate Research Fellowship Program (NSF GRFP). Additional financial support was provided by grants, CHE-1213082 to JDB and CHE-1213962 to CMD.

NOMENCLATURE

16MUA	16-Mercaptohexadecanoic Acid
AFM	Atomic Force Microcopy
BJ	Break Junction
C	Capacitance
C12	Dodecanethiol
C5DT	1, 5 Pentanedithiol
CMOS	Complementary Metal Oxide Semiconductor
CRLS	Contact Radius to Line Step
CS	Current Sensing
D1	One Day
D3	Three Days
D5	Five Days
DFT	Density Functional Theory
DLTJ	Double Layer Tunnel Junction
DNA	Deoxyribonucleic Acid
DRAM	Dynamic Random Access Memory
DSC	Dye Sensitized Solar Cell
e	Charge of an Electron
E_C	Charging Energy
FIB	Focused Ion Beam

F-Phenyl	5,10,15-Tri(4-Phenyl)-20-(4-(1',5'-Dithiopentyl)-2,3,5,6-Tetraflourophenyl) Porphyrin
F-Pyridyl	5,10,15-Tri(4-Pyridyl)-20-(4-(1',5'-Dithiopentyl)-2,3,5,6-Tetraflourophenyl) Porphyrin
FTIR	Fourier Transform Infrared Spectroscopy
FWHM	Full Width at Half the Maximum
G	Conductance
G_0	Conductance Quantum
G_{Eq}	Equilibrium Conductance
h	Plank's Constant
h_{C12}	Dodecanethiol Physical Height with Respect to the Substrate
HOMO	Highest Occupied Molecular Orbital
h_p	Porphyrin Physical Height with Respect to the Substrate
H-Pyridyl	5,10,15-Tri(4-Pyridyl)-20-(4-(1',5'-Dithiopentyl)-2,3,5,6-Tetrahydrophenyl) Porphyrin
I	Current
IETS	Inelastic Tunneling Spectroscopy
IQR	Interquartile Range
I-V	Current-Voltage
k_B	Boltzmann's Constant
LB	Langmuir-Blodgett
LUMO	Lowest Unoccupied Molecular Orbital
NDR	Negative Differential Resistance
NEGF	Nonequilibrium Green's Function

NEXAFS	Near-Edge X-ray Absorption Fine Structure
nTP	Nanotransfer Printing
OFET	Organic Field Effect Transistor
OPE	Oligo Phenylene Ethynylene
P_{sp}	Current and Voltage Set-Point Ratio
r	Radius of Porphyrin Island
R_T	Barrier Tunnel Resistance
SAM	Self Assembled Monolayer
SEM	Scanning Electron Microscopy
SPIP	Scanning Probe Image Processor
SPM	Scanning Probe Microscopy
STD	Sampling Standard Deviation
STS	Scanning Tunneling Microscopy
T	Temperature
$T(E)$	Transmission Function
TEM	Transmission Electron Microscopy
TPP	Tetra Phenyl Porphyrin
TPPF5	5,10,15-Tris(4'-Pyridyl)-20-2,3,4,5,6-Pentaflourophenyl) Porphyrin
UHV	Ultra High Vacuum
UV-vis	Ultraviolet–visible
V	Voltage
V_N	Negative Onset Bias

V_{noise}	Current Count Below the Noise Level
V_P	Positive Onset Bias
$V_{P(N)}$	Highest(Lowest) Bias Where the Conductance Exceeds Ten Times the Equilibrium Conductance
V_{tunn}	Difference Between the Positive and Negative Onset Bias
XPS	X-ray Photoelectron Spectroscopy
Zn F-Phenyl	5,10,15-Tri(4-Phenyl)-20-(4-[(5-Mercaptopentyl)Thio)]-2,3,5,6-Tetrafluorophenyl)Porphyrinato) Zinc(II)
Zn F-Pyridyl	(5,10,15-Tri(4-Pyridyl)-20-(4-[(5-Mercaptopentyl)Thio)]-2,3,5,6-Tetrafluorophenyl)Porphyrinato) Zinc(II)
Zn H-Pyridyl	5,10,15-Tri(4-Pyridyl)-20-(4-(1',5'-Dithiopentyl)-2,3,5,6-Tetrahydrophenyl)Porphyrinato) Zinc(II)
ZnTPPF4-SC5SH	5,10,15-Tri(4-Phenyl)-20-(4-(1',5'-Dithiopentyl)-2,3,5,6-Tetrafluorophenyl)Porphyrinato) Zinc(II)
ZnTPyP	Zinc Tetra Pyridyl Porphyrin
α	Porphyrin Tilt Angle Along the Long Axis with Respect to the Surface Normal
β_P	Porphyrin Tunneling Efficiency or Decay Constant
β_{C12}	Dodecanethiol Tunneling Efficiency or Decay Constant
β_{vac}	Vacuum Tunneling Efficiency or Decay Constant
δ_{AFM}	Physical Height Difference Between Porphyrin and Dodecanethiol as Extracted from Atomic Force Microscopy
$\Delta\delta_{AFM, C12}$	Physical Height of Dodecanethiol Extracted from Atomic Force Microscopy
$\Delta\delta_{AFM, P}$	Physical Height of Porphyrin Features Extracted from Atomic Force Microscopy and Measured with Respect to Dodecanethiol

$\Delta\delta_{STM,\,C12}$	Apparent Height of Dodecanethiol Extracted from Scanning Tunneling Microscopy
$\Delta\delta_{STM,\,P}$	Apparent Height of Porphyrin Features Extracted from Scanning Tunneling Microscopy and Measured with Respect to Dodecanethiol
Δh_{C12}	Change in Dodecanethiol Height Measured Between Scanning Tunneling Microscopy and Atomic Force Microscopy
Δh_P	Change in Porphyrin Height Measured Between Scanning Tunneling Microscopy and Atomic Force Microscopy
δ_{STM}	Apparent Height Difference Between Porphyrin and Dodecanethiol as Extracted from Scanning Tunneling Microscopy
δ_V	Bias Interval
ε	Permittivity of the Dielectric Medium

TABLE OF CONTENTS

Page

Page

Page

LIST OF FIGURES

Page

Page

Page

Page

Page

Page

Page

Page

Page

LIST OF TABLES

Page

Page

CHAPTER I

INTRODUCTION AND LITERATURE REVIEW

1.1 Overview: Molecular/Organic Electronics

In molecular/organic electronics molecules and organic materials are used as fundamental, electro-active units to modulate charge transport. To achieve this, there has been an appreciable amount of fundamental research on the electronic properties of molecules and the assembly of molecules on electrode surfaces. The idea of using molecules and organic materials for this purpose has been around since the 1950s,[1-3] but the techniques for advancement were lacking. Molecular/organic electronics rapidly developed with the seminal work of Aviram and Ratner constructing a molecular rectifier[1] and shortly thereafter, with the invention of the Scanning Tunneling Microscope (STM)[4] and the Atomic Force Microscope (AFM)[5] which allowed for visualization and manipulation of these molecules and organic materials. Currently STM, AFM, and other since developed scanning probe techniques are heavily relied upon in molecular/organic electronics to form nanoscopic junctions, examine local I-V characteristics, investigate charge transport mechanisms, and to pattern molecules/organics on surfaces to study the impact of structural design on their collective charge transport ability.

Molecular/organic materials are considered as alternatives[6] for traditional silicon-based and complementary metal oxide semiconductors (CMOS) with several advantages. Molecules and organic materials have vast combinatorial freedom in which

they can be synthesized as individual molecules or collectively assembled on surfaces, enabling vast possibilities of electronic properties and functions, including functions that cannot be achieved with silicon-based/CMOS technology such as flexibility and perhaps functions yet unknown.[7] Consequently, combining molecules/organics with silicon-based/CMOS technology will expand the device function and enhance performance. Furthermore, the inherent nanometer scale of molecules and organic materials are the same scales of electronic devices that are desired presently and have the potential to increase the density of devices per chip. In fact, molecules and organic materials can be fabricated into device architectures from the bottom-up wherein molecular components are consecutively added one unit at a time, often through facile self-assembly and exploiting intermolecular interactions. Bottom-up techniques can easily produce nanoscopic architectures with minimal material waste, limits complex fabrication steps, as well as permits vast tunable capacity in the electronic properties and function by the choice of individual ligands, side groups, substituents, among others. This is contrary to the top-down fabrication technique used in CMOS technology wherein devices emerge by etching away material from the bulk. Top-down techniques involve many complex lithographic steps that can achieve nanoscopic architectures but usually through arduous processing development. Additionally, molecules and organic materials often use solution-based processing that are more cost effective than their lithographic counter-parts and can be scaled for industrial applications.

In particular, porphyrin molecules are arguably among the most important materials for molecular/organic electronic applications because of their rich redox

chemistry and synthetic modulatiry.[8-9] The molecular structure of porphyrins is easily modified during synthesis for different surface attachments, intermolecular interactions benefiting from robust coordination chemistry, and for tuning the electronic properties; all of which can be used to design for diverse electronic functions and therefore application. (Further discussion of porphyrins is presented in Section 1.2).

At present, the aim of molecular/organic electronic is to incorporate molecules/organics into current silicon-based and CMOS technology, but has been challenging in application.[6] In the future, the aim is to fabricate devices composed solely of molecules/organics, but has only been achieved in some laboratory settings.[6] To expand the use of these alterative electronic materials and the advancement of molecular/organic electronics largely depends upon tailoring device functions by designing the properties of the molecular components. Design starts at synthesis, considering the charge transport through a single molecule, and continues to considering the intermolecular interactions which dictates assembly organization and can untimely affect the charge transport of the assembly. Therefore, in this work three questions have been researched to gain a more comprehensive understanding of the relationship between molecular structure, assembly organization, and the emergent electronic properties. *1) How do systematic perturbations in the molecular structure of porphyrins affect the resulting electronic properties? 2) How does molecular assembly affect the cooperative electronic properties of porphyrins on surfaces? 3) How can the assembly of porphyrins be pre-designed and directed into specific architectures to produce a distinctive, targeted electronic property?* By addressing these questions, the

advancement of molecular/organic electronics benefits by enabling devices to be engineered with pre-designed functions at the molecular level.

Following, research conducted in areas related to the above questions is presented. First, much consideration is given to research on the electronic properties of porphyrins on surfaces highlighting single molecules, molecular assemblies, and porphyrins incorporated into devices. Second, discussion is expanded to consider other molecular/organic materials by specifically considering the effect of small chemical perturbations on the electronic properties as well as the electronic properties of single molecules as compared to molecular assemblies. Third and finally, methods to control the electronic properties of molecular/organic materials are considered by way of controlling the assembly organization with emphasis on self-assembly and nanografting.

1.2 Porphyrins for Use in Electronics

Porphyrins (Figure 1) are planer, macrocycle organic compounds based on porphin, four pyrrole rings connected by methane bridges, with some or all of the peripheral positions substituted with a variety of sides chains.[10] Porphyrins are one of the most important functional pigments in nature owning to their remarkable properties; extraordinary stability and robustness, aromaticity and extensive conjugation with 18 delocalized pi electrons, ample metal coordination chemistry with nearly all metal ions in the period table, and versatile as well as modular synthetic tailorability.[9, 11-12]

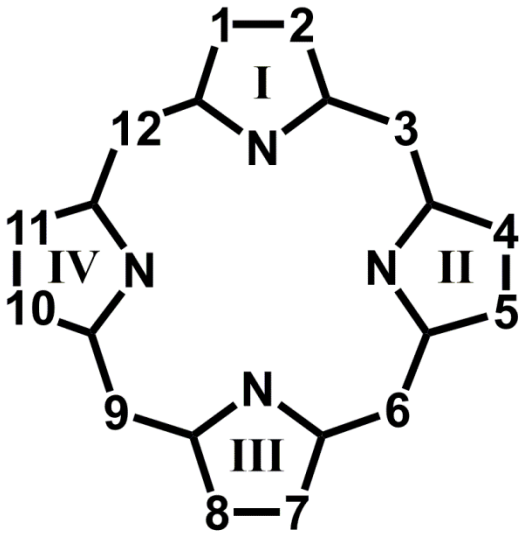

Figure 1. Basic porphyrin molecule structure. The Arabic numerals 3, 6, 9, and 12 denote the *meso* positions and 1, 2, 4, 5, 7, 8, 10, and 11 denote the β positions.

Commonly, nature takes advantage of porphyrins as heme for electron transport in cells and as chlorophyll in the crucial process for converting light to energy[13] Inspired by their uses in nature, porphyrins also have applications in a wide scope of disciplines such as photovoltaics,[14] dye sensitized solar cells,[15] nonlinear optical materials,[16] and nanotechnology.[17-18] Additionally, porphyrins are important materials as electro-active components in molecular/organic electronics because of their advantageous properties allowing them to be highly conducting, small charge injection barriers, and the ability to be chemically tailored for electronic fine-tuning as well as for surfaced assembly fine-tuning.[9] Especially because of their electronic and surface assembly tunability, porphyrins have become a platform to study the chemical structure-function relationship to gain valuable and necessary knowledge for the rational design of molecular/organic electronics.[19-20]

1.2.1 Electronic Properties of Single Porphyrin Molecules

Examining single porphyrin molecules enables the examination of intrinsic electronics properties that are free from properties that may emerge from assembly or bulk effects. Even though assembly and bulk effects can lead to interesting electronic properties (Section 1.2.1), rationally designing assemblies with predictable electronic properties necessitates understanding of the individual units. Commonly, break junction (BJ)[21-22] techniques are used to study the electronic properties of single molecular wires wherein a molecule spans two electrodes and the distance between the two electrodes is modulated by a push rod (in the mechanical controlled-BJ set-up)[21] or a piezoelectric transducer (in the STM-BJ set-up)[23] near the moment of junction formation and breaking. Other methods[24] include isolating electro-active molecules within an inter matrix for examination by STM/AFM,[20] electromigration techniques,[25] and Au nanoparticle dumbbells with lithographically fabricated electrodes.[26] Single molecules measurements are necessary but challenging because they can suffer from low junction yields and uncertain contact configurations. To compliment experimental work and further understand experimental results, computation methods are also employed such as density function theory (DFT)[27-28] often in combination with nonequilibrium Green's Function (NEGF)[29] in which molecular properties within atomic-scale junctions are predicted, such as ground state energy, by using functionals to describe the spatially dependant electron density. DFT-NEGF methods can provide descriptions of contact configurations and electron-phonon coupling but since it is a mean field approach, it has

limitations in describing strongly correlated electron effects and the positions of energy levels.[3]

With these experimental and computational methods, electronic investigations of single porphyrin molecules has provided insight into electron decay coefficients,[19-20, 30] transport mechanisms,[19, 31] transport pathways,[32-33] as well how to fine-tune these through studying the role of chemical perturbations, such as differing substituents[32-36] and chelated metal ions,[37] as well as the role of the electrical contacts.[38] Tunneling decay coefficients for porphyrins typically range from 0.034 $Å^{-1}$ to 1.2 $Å^{-1}$. On the low end and with efficient transport through a *meso-meso*, ethylene bridged Zn-porphyrin wire between two electrodes.[39] On the high end with inefficient transport through a free base (no chelated metal ion), tetra phenyl porphyrin attached to an Au(111) surface by an alkanethiol tether, where the alkanethiol tether dominates the transport.[20] In a single Zn-porphyrin wire, that is a porphyrin macrocycles connected by butadiyne bridges for conjugation and with pyridine terminal groups for contact with Au electrodes were found to transport via phase coherent tunneling.[31] In another porphyrin wire system, it was found that contrary to the conventional assumption, the transport pathway is not always the shortest, but can follow more than one path with the alternative suspected to be the through the most stable part of the molecules.[33] To modulate charge within a junction the, electron-donating side chains have been found to extend the pi conjugation of the porphyrin macrocycle thereby lowering the HOMO and LUMO energy levels.[34] Additionally electron-donation and –withdrawing groups were found to alter the redox activity of the porphyrin macrocycle[35] and furthermore, the position of the attachment to

the porphyrin can affect the level of influence; in particular the influence of the electron-withdrawing groups at the β rather than the *meso* position was found to be more significant.[34] Moreover, the position of the attachment of thiols to the porphyrin macrocycle for immobilization on electrode surfaces was also found to be significant.[36] Another way to modulate transport of porphyrins in a junction is to incorporate different metal ions at the center of the macrocycle. Different metal centers can tune the HOMO-LUMO gap and enhance the conductance two-fold thought to be originating from subtle differences in electroneativity.[37] Besides the chemistry of the porphyrin molecule within the junction, the electrical contacts also need to be considered. The electrodes can affect the measured electronic properties and sometimes completely dominate, hence overcoming any transport modulation by the porphyrin.[19, 38] Modularity of the porphyrin, coming from the vast possibility of substitution and metallation, has resulted in thousands of porphyrins synthesized in the laboratory. The knowledge of the electronic properties of these many porphyrin compounds is growing but are seemly sporadic. Few systematic studies of how small chemical perturbations in porphyrins affect the electronic properties are appearing[34, 37] but more is necessary to fully elucidate the chemical structure/ electronic function relationship. Understanding this relationship is even more essential when considering building structures and organized assemblies of porphyrins where bulk and assembly effects are significant.

1.2.2 Assembly of Porphyrins on Surfaces and the Emergent Electronic Properties

To integrate porphyrin molecules as building blocks into electronic devices with advanced functions, the development of methods to and the understanding of the

assembly of functional porphyrin architectures supported on surfaces are required. Fabricating architectures in which the porphyrins molecules are organized into well-defined geometries with respect to the supporting substrate and their neighbors has been an area of research. This is achieved almost exclusively though self-assembly and solution processing with carful control of intermolecular interactions and porphyrin-surface interactions. Further discussion on self-assembly as a method to pattern molecules on surfaces is given in Section 1.5.1. Careful control of these interactions involves perturbing the chemical structure of the individual porphyrin molecules during synthesis and perturbing the chemistry of the supporting surface. By doing this, it was found that porphyrins assemble into an abundance of molecular aggregates/islands, close-packed arrays, wires, and pours networks on surfaces and importantly different porphyrin organizations can lead to different emergent electronic properties.[19] Assembly structures are examined by use of microscopy techniques such as AFM, TEM (Transmission Electron Microscopy), and most predominantly STM for the visualization of porphyrin assemblies, sometimes with molecular level resolution, and at low temperatures in ultra high vacuum to reveal the finer details like the interior of individual molecular units.[40] The detailed chemical nature and bonding properties of porphyrin assemblies are examined by use of space-averaging techniques such as X-ray photoelectron spectroscopy (XPS), Fourier Transform Infrared Spectroscopy (FTIR), and Near-Edge X-ray Absorption Fine Structure (NEXAFS). Often times, DFT-based calculations compliment experimental data, and in combination a fuller understanding of porphyrin assemblies on surfaces is gained.

- The organization of porphyrins is affected by the interactions with the supporting surface. Common supporting surfaces include noble metals,[19,41-43] silicon-based materials[42, 44-48] and most recently graphene-based materials.[49-50] The choice of supporting surface material largely depends on the application and type of electronic information being sought. For example noble metal supports such as Au and Ag are used because of their facile preparation and SAM modification for fundamental electronic studies whereas Si and SiO_2 are used for studies of porphyrins in possible device configurations for direct incorporation into pre-existing silicon-based technology.[51] On many support surfaces porphyrins assemble with the macrocycle plane "face down" on the surface mainly via physisorption.[10, 52-53] As a consequence, the molecular orbitals of the porphyrins mix with the electronic states of conducting surfaces and influences the electronic properties of the porphyrins.[10] Strategies to separate the electronic states, thereby recovering the ability of the porphyrins to modulate electron charge alone, include depositing an ultrathin oxide spacer layer on the surface before porphyrin assembly[54] or attaching spacer side-groups to the porphyrins during synthesis.[20] In the case of oxide spacer layers, the porphyrins also tend to assemble "face down" where pi-stacking parallel to the surface is possible. However, in the case of additional side-groups, the porphyrins can assemble in a more edge-on organization on the surface where pi-stacking perpendicular to the surface is possible.[19, 44, 48] Side-group substituents affect the interactions between the support surface and the porphyrin and serve as attachment tethers binding porphyrins to support surfaces forming strong chemical bonds for example forming covalent bonds between thiol groups and Au surfaces[20] as

well as between diazonium and reduced graphene oxide surfaces.[55] By such bonds, the orientation of the porphyrins with respect to the surface can be somewhat-controlled in that the porphyrins can orient standing-up instead of simple physisorption face-down on the surface. But the conformation of the porphyrins in the standing-up orientation may be dynamic with macrocycle twisting and bending. Additionally, the organization of the assembled porphyrin layer depends strongly on the atomic structure of the underlying support surface. It was found that a mixed self-assembled monolayer of Cu-octaethylporphyrin and Co-phthalocyanine organized into a $\sqrt{3} \times \sqrt{22}$ phase on Au(111), well-ordered alternate packing phase on Au(100)-(hex), and disordered phase on Au(100)-(1 x 1) [52, 56] These results uncovered the possibility of templating the organization of porphyrins on surfaces by controlling the structure of the underlying support at the atomic level. Thought not strictly at the atomic level, surfaces have been modified to template porphyrin assemblies by using norbornene-based homopolymer driving J-aggregation[57] and p-(hexadecyloxycarbonyl)phenylacetylene atop graphite driving "face-down" pi-stacking.[58]

The organization of porphyrins on surface is also affected by intermolecular interactions. Since individual porphyrin molecules are modular and easy to chemically modify, intermolecular interactions can be perpetually tuned for self-assembly of a multitude of architectures on surfaces. By this, porphyrins have been assembled into arrays, molecular islands, two- and three-dimensional networks, nanorings, heterostructures, and one-dimensional block copolymers among others.[10] Porphyrins are

chemically modified by the choice of chelated metal ion within the macrocycle and by substituent side groups at either the *meso* or β positions.

Metal ions within the porphyrin macrocycle mainly drives aggregation and self-assembly of porphyrins on surfaces via metal-side group substituent coordination. This has been done by using pyridyl[59-61] and carbonitrile[60] side groups and can offer conformational flexibility, adapting to the support surface or other environmental situations.[62] With coordination, networks,[59, 63] one dimensional chains,[62, 64] and supramolecular arrangements[60, 64] were produced. Typically, within these assemblies the individual porphyrins molecules do not arrange to pi-stack, but instead arrange edge-face or edge-edge with neighboring porphyrins. Porphyrin assemblies driven by interactions with metal ions can encompass a wide variety of metal ions, but often Zn,[19, 65] Fe,[66] Co,[66] Mg[65], and Cu[67] ions are incorporated. To tune porphyrin assemblies via metal ions, the metal ion is chosen for specific coordination number. For example high coordination numbers of the lanthanides allows coordination with many tetrapyrrole ligands providing multiple structural degrees of freedom; Ce- and Ce_2-tetraphenyl porphyrins were assembled into three-dimensional, double-decker stacks.[68] Sometimes, the choice of metal ion is not for assembly purposes but for the benefit of electronic properties[65, 69] by way of modulating redox reactions[66] for instance.

Thoughtful arrangement of side group substituents on the porphyrin can have a large influence on the self-assembly on surfaces, dictating the geometry of individual porphyrins with respect to its neighbors. For example, unreactive *meso* substituents, such as phenyl groups, were found to produce dense, tetragonal networks[70] and contrastingly

bulkier *meso* substituents, such as tert-butylphenyl, produce close-packed hexagonal[43, 71] or tetragonal units.[72] Through side group substituents, porphyrin self-assembly often relies upon non-covalent interactions such as pi-stacking,[19] hydrogen bonding interactions, solvophobic interactions, van der Waals interactions,[70] and electrostatic in combination with hydrophobic interactions.[73-74] It is opportune to rely on such interactions because thermodynamically stable structures are formed with the opportunity for self-repair.[43] Yet, constructing a pre-designed assembly in this way requires the careful choice and arrangement of side substituents. Through side group substituents, porphyrin self-assembly can also rely upon stronger covalent interactions.[75-76] This is beneficial because stable structures are formed in which the organization is "locked" in place by pre-defined binding locations and the opportunity to use the covalently bound structure as a template for hierarchical construction of high functioning nanostructures via coordination of ions to modulate electron and photon transport.[75] On the other hand, if covalently bound structures are not supremely selective, they may suffer from organizational defects that are challenging to eliminate.

The many porphyrin architectures supported on surfaces found in the literature were fabricated with the purpose to carry-out certain functions relevant in electron mediated transport. Many porphyrin architectures have been fabricated, but less have been investigated for their electronic properties and even fewer pre-designed and constructed to obtain specific electronic functions. Investing the electronic properties of porphyrin assemblies have relied heavily on scanning probe techniques, like AFM and STM because of their ability to form metallic top-contacts while preserving the integrity

of the assembly and to probe certain localized features. Current sensing AFM (cs-AFM)[77-78] facilitates probing local I-V characteristics with the ability to simultaneously obtaining topography and as well as spatially resolved electronic response. Comparative STM imaging[19, 79] provides information on the relative conductance and charge distribution or bias-dependant STM imaging reveals the charge distribution of occupied and unoccupied states.[80] Likewise, scanning tunneling spectroscopy (STS) facilitates probing local I-V characteristics and furthermore spatially resolved STS is used to obtain information on occupied and unoccupied states but through a wide range of bias.[81] Besides scanning probe, other methods are employed to investigate the electronic properties of assemblies for example cross-wire junctions,[19] nanopores,[82] and forming junctions with polymer top-contacts,[83] The complex nature of porphyrins assemblies on surfaces poses challenges in understand such experimental data, therefore, DFT-based calculations are often carried-out to compliment and further the understanding of the electronic properties of porphyrin assemblies.

From these types of measurements, it was found that the electronic properties of porphyrin assemblies include rectification,[84] charge hopping,[66, 85] Coulomb blockade,[19, 86] and redox reactions[48] Furthermore, it was found that porphyrin architectures have the ability to function as active components in electron donors and acceptors,[87-89] switches,[90] rectifiers,[91] memory storage,[48, 92] and capacitors[19, 92-94]. The organization and therefore the "communication" between neighboring porphyrins influence the resulting electronic properties of the porphyrin structure and electronic functions.[69, 84-85, 95] One exemplary study demonstrated the importance of the relationships between the chemical structure of

individual porphyrins, the assembly of such porphyrins on surfaces, and the resulting electronic properties. The choice of subsistent side groups (dodecyl vs. triethylene gycol) decorating a Cu-metalloporphyrin complex altered the charge transport from n-type to p-type wherein the differing substituents did not affect the pi conjugated macrocycle, but rather affected the stacking organization of the macrocycles.[95] Likewise, this relationship was reinforced not by examine different substituents, but by examining different conformations of individual porphyrin molecules through computational methods resulting in different porphyrin organizations affecting the electron transfer rates.[96] Another exemplary study demonstrated the importance between the organization of porphyrins and their resulting electronic properties. Porphyrins-based donor-spacer-acceptor molecules were synthesized with alkenylated anline spacers with differing alkenyl chain lengths (chains containing 6 and 11 carbons) and the system containing the longer was more densely packed on the surface and exhibited a rectification ratio 10^5 greater than the system with the shorter spacer.[84]

Two notable electronic functions to come out of porphyrin architectures are charge storage and switching which can be used in memory[51], capacitors[19, 93] and transistors.[97-98] Charge is stored in porphyrins by oxidizing the neutral porphyrins forming a mono-pi-cation radical; termed "writing" for memory applications. The reverse reaction, converting a mono-pi-cation radical to a neutral porphyrin, discharges the porphyrin; termed "reading" for memory applications.[51] Porphyrin complexes assembled on surfaces were found to be particularly suited for charge storage for a number of reasons. Triple-decker, lanthanide-containing porphyrin complexes were

demonstrated to simultaneously store more than one bit of information due to the availability of four cationic states at low potentials wherein these states can tuned by choice of center metal ion and side group substituents.[47, 99-101] Porphyrins have exhibited charge storage for extended periods of time, on the order of minutes, without applied potentials.[102-105] Pi-cation radicals formed from porphyrins were stable in possible operational device conditions.[47, 51] However, the performance of porphyrin-containing memory seems to be limited by the rate of charge transport (rate at which charge can be stored and discharged), which is on the order of 10s of kHz compared to the much faster GHz rates in dynamic random access memory (DRAM).[51, 106] Switching is another important function for electronics described by a change in electronic properties due to external stimuli, yet there are limited reports of switching in porphyrins assemblies on surfaces.[19, 107-109] Switching is more often considered within single porphyrin molecules[110-113] and in supramolecular architectures containing porphyrin, but without the consideration of an electrode surface.[114-115] Porphyrin assemblies attached to electrode surfaces are becoming important components in transistors[97] (see Section 1.2.3) and since switching is one of the main functions carried out by transistors, the switching capabilities of porphyrin assemblies on surfaces must be explored further.

1.2.3 Porphyrins for Use in Devices

A far reaching goal of molecular/organic electronics is to develop devices from the bottom-up using single molecules where the associated components are included within the molecule during synthesis. The prospect of this goal is driven by realization of a device entirely integrated within a single molecule in which the components of the

device are included as ligands, side groups, and substituent species for instance during synthesis. In an effort to evaluate the possibility of this, a NEGF-DFT study examined the charge transport trough a Fe-porphyrin between carbon nanotube electrodes. The results show the electron transfer solely occurring through the chelated Fe ion, due to molecular orbital coupling of the carbon nanotubes with the Fe ion and lack of that with the tetra pyrroles of the porphyrin. Therefore transport can be controlled by the redox state as an internal gate with little to no current leakage lending this system to be a possible single molecule transistor.[32] While these results seem promising, such systems require experimental exploration of which, many technical challenges arise such as control over contact geometry, molecular conformation, and low junction yields to mention a few.

A goal attainable in the near future entails incorporating molecular components into silicon-based/CMOS technology, expanding and enhancing the function of current electronic devices resulting in next generation molecule/semiconductor hybrid devices. Hybrid devices will be fabricated with combinations of bottom-up and solution processing methods amenable to molecular/organic materials, the extensive semiconductor infrastructure, and advanced photolithographic methods. Although still in development, a few key devices have been enhanced by the incorporation of porphyrin assemblies; namely dye sensitized solar cells (DSC),[116-118] memory devices,[51, 119] and organic field effect transistors (OFET).[46, 97, 120] Importantly, all of these devices are based on porphyrin assemblies and the advancement of which relies upon tuning the molecular structure of porphyrins for certain functions. In DSCs use of porphyrins has

advanced the understanding of the role of molecular sensitizer structure on device performance. Zn porphyrin sensitizers with iodide/triiodide redox electrolytes yielded power conversation efficiencies at approximately 11%[121] while other porphyrin sensitizers at the time yielded efficiencies at approximately 8% or below.[122-124] The increased efficiency is attributed to the porphyrin integrated within the light harvesting donor-pi-acceptor system where the Zn porphyrin itself serves as the pi-bridge. Through careful chemical modification of Zn porphyrin sensitizers, it was found that side group substituents consisting of phenyl rings at every *meso* position containing two octyloxy groups and in combination with a Co-redox based electrolyte as a co-sensitizer, the charge recombination rate was reduced by increasing the distance of the back reaction by which yielded benchmark power conversion efficiencies of over 12%.[116] Furthermore the power conversion efficiencies have improved to 13% without a co-sensitizer achieved by further modifying the benchmark Zn porphyrin species reported before[116] but incorporating a proquinoidal benzothiadiazole acceptor group which allows for improved green (500-600 nm) and red (up to 800 nm) light harvesting.[15] Currently, power conversion efficiencies have reached an impressive 20% with perovskite-type light harvesters[125-126] and even though DSC with porphyrin sensitizers has not been as efficient, the ability to carefully modify porphyrins to improve device performance has been exemplified.

Porphyrins in OFETs as part of charge transport layers has been less researched than for use in DSCs, but in both devices porphyrins have been useful to study the relationships between molecular structure, assembly organization, and device

performance.[97-98] These relationships are particularly important for OFETs because enhanced charge carrier mobility is integral to enhance device performance and charge carrier mobility in OFETs was found to strongly depend on the intrinsic properties of molecules in the charge transport layer as well as on the molecular morphology; including factors such as grain size, layer thickness, interface modifications, and molecular structure modifications.[127-128] For example, OFETs performance is superior when the transport layer is well-ordered rather than amorphous.[127] Additionally, modifications of Zn-porphyrins by adding different conjugated peripheral arms of varying length affected OFET device performance. The origin lies in the molecular organization; wherein the carrier mobility increased from 0.32 to 3.1 $cm^2\ V^{-1}\ s^{-1}$ when the distance between porphyrin macrocycles decreases due to the more compact pi-stacked organization. The attribute of pi-stacking, common in porphyrins, and low dimensionality have been beneficial in OFETs specifically effecting charge carrier mobilities.[97, 120, 129] In polymer-based OFETs, porphyrins are used as chemical dopants to tune and direct the polymer morphology and by this it was found that introducing only a small amount (approximately 0.1 mol. %) of pi-stacking porphyrins was required to significantly decrease domain boundaries size thereby increasing the carrier mobility by an order of magnitude to $2.4 \times 10^{-4}\ cm^2\ V^{-1}\ s^{-1}$ and OFET performance.[129] Beyond charge transport layer morphology, porphyrins offer the ability to control electron transport in OFETs by responding to external stimuli through light absorption.[130-131] Research on porphyrin/metal and porphyrin/semiconductor systems have investigated the use of electron transport from photoexcited electrons from the porphyrins to inorganic support

matierlas.[46-47, 132-133] By this, the functionality of conventional electronics has been enhanced to include hybrid memory/transistor devices[46, 107, 134] in which information storage is induced by light illumination.

1.3 The Effect of Small Chemical Variations on Charge Transport Through Organic Materials

Early on, one reason why molecule/organic electronics was attractive because it seemingly offered almost limitless possibilities in which active molecular components could be fabricated and combined rendering an almost limitless possibilities of electronic functions that can be finely tuned through small chemical variations. To do this, a thorough understanding must be developed of what chemical group substituents affect certain electronic properties and the underlying mechanisms. It was found that altering chemical variations in molecules sometimes resulted in a meaningful change in the electronic properties, but other times it did not. Therefore, this notion of wide synthetic and chemical freedom in molecular/organic electronics is more limited than once thought and it is complex to find where these limits lie. Altering the molecular structure has resulted in meaningful changes in the electronic properties for cases involving single molecule junctions,[135-138] molecular assemblies,[139-144] and molecules incorporated into devices.[138-139, 145-146] However, other times there was no meaningful change for cases involving molecular assemblies,[147-149] molecules incorporated into devices[150] and rarely for single molecules.[151]

Molecular structure/ electronic properties relationship studied in single molecule junctions eliminates nearest neighbor and “bulk” effects whereupon the ability of the

molecule to modulate the electronic properties is solely examined. There are reports describing molecular perturbations impacting the electronic properties of the junctions, but such reports in which molecular perturbations do not impact the electronic properties are scant and the limits of electronic tunability based molecular perturbations is yet unclear. A particular report focused on the effect of Cu(I) metal coordination in molecular wires consisting of 1,10-phenanthroline for metal-binding and different substituent anchoring groups (acetylthiol, pyridine, and ethynyl).[135] It was found that Cu(I) coordination decreased the HOMO-LUMO energy gaps compared to the un-coordinated wire analogue. Nevertheless, exemplifying the complexity of understanding the molecular structure/ electronic properties relationship, the conductance did not follow a distinct trend and the conductance of the wires did not always increase upon Cu(I) coordination, opposite to other metal coordination studies. The delicate interplay between Cu(I) coordination and subsistent anchoring groups shifted the molecular levels involved in charge transport with respect to the electrodes' Fermi level thereby altering the conductance and such shifts are expected to occur for different metals and different side group substituents. Conversely, adding a metal center does not always produce an observation change in the electronic properties compared to the non-metal analogue [19-20]

Molecular structure/ electronic properties relationship is studied most heavily in molecular assemblies seeing as they have the most imminent potential to be incorporated into devices. When small molecular structure perturbations affect the electronic properties of a molecular assembly, it is largely due to organizational nearest neighbor interactions. For example, SAMs with an odd verse even number of repeating units

terminated by CH_3,[147] phenyl,[143] and ferrocene groups[146] were found to have different tunneling rates because of differences in the geometrical conformation of the SAM. Additionally, the sublet exchange of the terminal C-H for N atom in oligophenylene SAMs resulted in an approximate 0.3 V difference in transition voltage.[152] Beyond organizational effects, another strategy is to alter the molecular dipole moment to affect the barrier height of the assembly[142, 153-154] or the transition voltage.[155] On the contrary; the electronic properties of similar molecular assemblies are not affected by molecular structure perturbations. For example, the tunneling rates in SAMs terminated with commonplace aromatic,[147] polar,[156] and acidic[157] groups are insensitive to such modifications. Similarly in another study of bi-layer SAMs found that when one layer includes either alkane, aromatic, and redox-active molecules, the current density and tunneling decay constants remained unaffected.[158]

The complexity of the molecular structure/ electronic properties relationship continues in studies of devices with molecular components. Since the understanding of this relationship requires further development in the single molecule and molecular assembly stage, there are limited but meaningful reports. Pi-conjugated peptide molecules within the charge carrier layer in a bottom-gated OFET was shown to have varying charge carrier motilities by up to three orders of magnitude (from 0.02 to up to $5x10^{-5}$ cm^2 V^{-1} s^{-1}) by simply altering the amino acid sequence adjacent to the pi-electron core.[139] Small mobilities result from more bulky amino acids that seem to assembly in such a way hindering hole-transport where as large mobilities result from amino acids with the strongest intermolecular electronic couplings. An even more subtle change in

the molecular structures by just a few atoms has lead to a dramatic change in device performance. Within a SAM-based molecular diode, the addition of just one CH_2 group resulted in a 10-fold increase in rectification efficiency and 10% increase in device yield.[146] The improvements are due to the even-odd effects in alkanethiol SAMs and with chains with an odd number of repeating CH_2 units, benefited from more favorable van der Waals interactions. Therefore, small modification can, but does not always have a large impact.

1.4 Charge Transport Through Single Molecules vs. Molecular Assemblies

Early on in molecular/organic electronics, it was perceived that electronic properties inherent to single molecules would carry-over to molecular assemblies. However, the properties of single molecules can differ from assemblies[159] due to complex nearest neighbor interactions involving geometrical organization,[19, 160] collective electrostatic effects,[140, 161-164] cooperative quantum-mechanical coupling,[165-166] and charge trapping.[19, 167] Charge trapping is a particularly interesting electronic property to emerge from a collection of molecules on a surface. Typically charge trapping has been observed in quantum dots,[168-169] but recently it has been observed in small assemblies of Zn porphyrin-thiols (ca. 5-10 nm in lateral dimension or approximately 6-20 molecules) on Au(111)[19] and in small assemblies ferrocene dicarboxylic acid (ca. 150 nm^2 or approximately 185 molecules) on calcite[167]. In the case of the Zn porphyrin-thiols, the assembly forms a Coulomb island wherein charge is stabilized within the molecular states of the pi-stacked porphyrin macrocycles and then by applying a sufficiently large bias, the porphyrins are discharged through the thiol binding group to

the underlying Au surface. Remarkably the Coulomb island is a result of the Zn porphyrin assembly involving as little as 6 molecules; in single molecules charge is not stabilized and simply tunnels to the underlying Au surface. In the case of ferrocene dicarboxylic acid, charge is injected and stabilized on an assembly, but then is discharged in favor of occupying another near-by ferrocene dicarboxylic acid assembly. Again, this is an assembly affect where charge is only stabilized on ferrocene dicarboxylic acid assembly and not on single ferrocene moieties. In both porphyrin and ferrocene systems, the assemblies function as molecular capacitors that can be charged with one charge at a time and both lose this ability as single molecules.

However, single molecules do not always have electronic properties that vary from their molecular assemblies, furthermore highlighting the complexity of the relationship between molecular structure, molecular assembly, and electronic properties. As an example, in a break-junction set-up, the tunneling decay constant for dithiol Zn porphyrin oligomers was found to be an impressive 0.0034 $Å^{-1}$ which is among one of the lowest for thiol terminated single molecules.[39] Assemblies of dithiol Zn porphyrin oligomers were fabricated by nanotransfer printing (nTP) onto Au surfaces and the tunneling decay constant remained relatively unchanged. These results indicate nTP as a possible method to fabricate assemblies on surfaces while maintaining the inherent electronic properties of single molecules. Additionally, these results do not agree with other studies of densely packed dithiol monolayers. Specifically in dithiol phenylnes, the tunneling decay coefficient severally suffers in molecular assemblies verses single molecule junctions.[170-171] The change arises from intermolecular interactions wherein

molecular states and charge transport pathways become available upon assembling and are not necessarily relevant in single molecule charge transport. Contrastingly, it is supposed that the tunneling decay constant remains unchanged for single molecules and molecule assemblies of dithiol Zn porphyrin oligomers because the intermolecular interactions sterically hinder such transport pathways in densely packed assemblies.

Molecular assemblies have a combinatorial capacity to a degree that single molecules do not. Molecular assemblies can be built with more than one type of molecule in which the individual properties of each constituent molecule contributes to the over-all property or function of the assembly.[172] Mixed monolayers are often assembled by phase segregation[173] and by this combinations of alkanethiols/ fluorinated alkanethiols were found to tune the surface workfunction in a predictable manner as a function of the combination ratio.[174] In more complex systems, phthalocyanines and nanocarbon species, like as fullerenes and carbon nanotubes, have been a popular choice for combinatorial molecule assemblies because of the phthalocyanines with vast redox chemistry and energy level tunability in addition to nanocarbon species with ballistics charge transport and high mobilties[175] In combination, intriguing function have been displayed like photoinduced charge separation for phthalocyanine/ carbon nanotube assemblies[176-177] and photoinduced charge transfer for phthalocyanine/ fullerene assemblies.[178] However, fabrication of complex combinatorial molecular assemblies is challenging because of the delicate balancing and control over intermolecular interactions from multiple components to produce pre-designed structures.

1.5 Pattering Organic Materials on Surfaces for Specific Electronic Properties

Monolayers on the surface are known to alter the properties[179] of surfaces but the properties can be finely controlled by controlling the absorbed monolayer. Therefore careful patterning of materials absorbed on the surface is required. The purpose of patterning is to control nearest neighbor interactions. As was discussed above, nearest neighbor interactions are important and certain electronic properties emerge from certain arrangements of organic materials. The ultimate goal is to use the knowledge acquired from studies on transport through molecular assemblies of molecules but achieving this necessitates execute a pre-designed array of organic components onto electrode surfaces.

1.5.1 Pattering Methods

Most patterning methods involving organic/molecular components arrive from building-up materials on a surface by selectively and continuously adding individual components to form a hierarchical structure. This approach is called bottom-up fabrication. Conversely, top-down fabrication involves cutting away a starting material and the desired pattern emerges from larger, "bulk" material and is the typical method used to pattern electronic devices from conventional silicon-based and CMOS materials. The advantage of using bottom-up fabrications lies in ability of organic/molecular materials to be broken down into smaller components from which in nano-sized structures can be produced, solution processing can be applied which is usually cost effective, and only the necessary quantities of materials are used. Controlled bottom-up fabrication can lead to applications in molecular/organic electronics,[180] sensors,[181] nanolithography,[182] and solar cells[183] to note a few. Some bottom-up fabrication

strategies for organic/molecular are controlled self-assembly and AFM nanografting among others like dip pen lithography[182] and Langmuir Blodgett films.[184]

Self-assembled monolayers (SAM) are a single layer of well ordered, closely packed molecules that spontaneously form on a surface through surface-molecule and intermolecular interactions.[179, 185] The phrase "monolayer films that assemble themselves" or more commonly, "self-assembling monolayer" was introduced in 1983[186] illustrating the work of Netzer and Sagiv involving fabrication of multi-layer films with chemical control.[187-188] But this method for absorbate assembly on surfaces has been known since 1946 with the work of Zisman and coworkers involving assembled oleophobic (long-chained, polar hydrocarbons) monolayers on polar surfaces.[189-190] Since then, the versatility of SAMs has been realized and numerous absorbate/surface combinations have been explored.[191-192] By thoughtfully controlling the surface-molecule interaction as well as the intermolecular interactions one can control the self-assembly of these monolayers into diverse architectures with ease and in parallel which is suitable for batch processing in industrial applications.[179] In an outstanding case, Rothemund reported on folding DNA molecules to create shapes on mica beyond simple patterns.[193] This was possible because the many available design combinations due to diverse and specific interactions provided by the specificity of Watson-Crick base pairing. However, these many design combinations seem to be unique to DNA and self-assembling complex structures from other types of molecules is an on-going challenge. To create more complex patterns using bottom-up approaches, Scanning Probe Microcopy (SPM) techniques are often used.

SPM, not only allows for the visualization of surfaces on the nanoscale, but also for manipulation of materials on the nanoscale, equipping the ability to place single atoms and molecules on the surface as well as to monitor the surface modifications in situ. One SPM patterning technique used for the manipulation of SAMs is nanografting, originating from the work of Gang-yu Liu and coworkers.[194-195] Nanografting is a so-called "film growth then patterning"[196] method in which first, a SAM is formed on the surface and second, nanografting is used to manipulate the existing SAM structure. The nanografting method is carried out by Atomic Force Microcopy where the tip (~ 10 nm in radius) applies a sufficiently large load to the surface to break the bonds between the SAM end groups and the surface, selectively removing the SAM at specific locations and exposing the underlying surface. When this is done in an inert environment such as, ethanol, nitrogen, or air in some cases depending on the reactivity of the underlying surface, the SAM is simply selectively removed. This is referred to as nanoshaving.[194] Furthermore, when this is done in a reactive environment, commonly in a solution of target molecules that can bond with the underlying substrate, the pre-formed SAM is removed (via nanoshaving) but then the target molecules in the solution bind to the newly exposed surface forming a SAM of mixed domains. These domains can be controlled in terms of arrangements, shape, and size by controlling the AFM tip. There are technical challenges to create the desired; domain patterns; for instance the size and shape of the domains are limited by the size of the AFM tip and the large loads required that eventually wear away and blunt the tips. AFM tips are commercially available with 10 nm nominal tip radius of curvature and ultrasharp tips with 2 nm nominal tip radius

of curvature, but these significantly suffer from wear and blunting under typical nanografting loads. Nanografted features have been as small as a reported 2 x 4 nm^2 dot-type pattern composed of approximately 32 alkanethiol molecules.[197] Typically, square and line patterns are nanografted on the surface,[195, 198] but more complex patterns are possible such as concentric rings,[198] "mouse ears",[198] stars (Figure 51 in Appendix C), and an even an intricate university seal.[195] Indeed, a wide variety of pattern designs can be nanografted by placing the tip and applying a sufficiently large load at the appropriate positions on the surface, perhaps with the automation of computer scripting.

The patterns produced by nanografting alone have been limited to target molecules that are compatible with the method, i.e. soluble in mild, solvents with low vapor pressure; hence the plethora of nanografting reports that include mainly alkanethiol-type molecules.[195, 198-201]. However, to expand beyond this to use more complex molecules to fabricate patterned surfaces, hybrid approaches are needed where nanografting is used not as means to an end, but as the foundation of hierarchical patterns. This can be done by nanografting a reactive template then using self-assembly directed by the nanografted template. Although this is not "one-pot" fabrication, but rather a multistep fabrication in which each step is done with relative ease taking advantage of the strengths of nanografting and controlled self-assembly

Even though nanografting has been and continues to be useful in expanding surface patterning in the laboratory, it is largely incongruent with industrial applications because patterns are fabricated in serial, one line at a time. It has been suggested to use many AFM tips simultaneously to parallelize patterning, but there are technical

considerations that need to be optimized and automated for industrial applications.[198] Therefore, nanografting remains a method for laboratory research. Alternative patterning methods are being considered to translate what has been researched in the laboratory to industry. One possibility is nanotransfer printing (nTP) which is a stamping process that can fabricate patterns on the nanoscale.[202] A recent report tested the viability of nTP for transferring a laboratory set-up to scalable, bulk electronic devices.[30] A monolayer of dithiol-porphyrins were absorbed onto a surface by nTP and produce very similar tunneling efficiencies as obtained for the same molecules as part of a break-junction showing that nTP can be a viable method. On the contrary, the monolayer consisted of one type of molecule and it is yet to be seen if a mixed monolayer or a specific molecular arrangement (comparable to those produced by nanografting) will be compatible with nTP.

1.5.2 Patterning to Produce Specific Electronic Properties

The organization of molecules/organic components on the surface can dictate the electronic properties and furthermore the performance of a device. Therefore, patterning surfaces is a means to organize molecule/organic components to achieve specific electronic properties and device functions. There have been many reports on patterning methods with the intention of controlling the emergent electronic properties, but with limited electronic property characterization.[182, 193, 203-206] On the other hand, there are reports on molecular/organic structures produced through self assembly and the resulting electronic properties are explored as a function of the assembled molecular organization.[140, 207-209] Although these two approaches are necessary and valuable in

providing intermediate steps towards the ultimate goal of molecular/organic electronics, designing these components into definitive architectures to achieve certain electronic functions,[210] in comparison there is a deficit of work on patterning molecular/organic components into pre-designed structures with an aim to obtain an intended electronic function.[75, 211] As an example, naphthalene-based molecules were pre-designed to assembly during synthesis into a square pattern for fast, hopping electron transport,[212] but this was made possible by intermediary assembly and electronic property exploration.[213-214]

To realize the wide-spread incorporation of molecular/organic components into electronics, the deficiency in pre-designed assembly for a specific electronic property must be filled. A promising concept to realize the wide-spread use of molecular/organic components is that of a "nanobreadboad".[193] The "nanobreadboard" concept is focused on nanoscale surfaces patterning to create sites where organic electro-active components can modularly and selectively be attached through chemical interactions and by this, devices based on molecules/organics can be built-up in a hierarchical fashion. The "nanobreadboad" provides as a basis for the implementation and culmination of the knowledge gained during intermediate molecular/organic patterning studies and structure-electronic function studies. A similar idea has been applied to self-organizing surface-initiated polymerization[215] in combination with template stack exchange[216] in which triad photo-systems are synthesized directly on a surface. This is done first by self-organizing surface-initiated polymerization that provides a basis for the incorporation of secondary and tertiary species, such as fullerenes and phthalocyanines,

at specific orientations through template stack exchange.[211] But similar to the molecule squares example above, this is a based upon the knowledge gained from other intermediary, exploratory work.

1.6 Summary and Outlook

Molecules and organic materials are the fundamental, electro-active materials in the field of molecular/organic electronics used to modulate charge transport in devices. The present goal is to fabricate next generation, hybrid electronic devices by combining molecules/organics with silicon-based and CMOS devices.[6] Hybrid devices benefit from molecular/organic materials because the inherent nanometer scale of molecules, bottom-up and solution-based processing, new functions unattainable with only typical silicon-based/CMOS materials, and exploiting intermolecular interactions for self-assembly during device fabrication. But to achieve hybrid devices, the rational design of molecule/organic components into useful, pre-designed architectures requires extensive development and comprehensive understating of the emergent electronic properties.

Porphyrins are among the most significant electro-active materials for molecular/organic electronics applications because of their distinguished properties.[9, 11-12] They have become a platform to study the chemical structure-function relationship because of their versatile and modular synthetic tailorability to affect surface assembly and electronic properties. For single porphyrin molecules, the electronic properties were found to be varied and dependant on variation in chemical structure based on the type and position (e.g. β or *meso*) of chemical substituents.[20, 31, 33-36, 39] A vast number of porphyrin compounds have been synthesized and knowledge of their electronic

properties is growing. But to fully understand the chemical structure/ electronic function relationship, systematic studies on the influence of small chemical perturbations in porphyrins in tuning the electronic properties are necessary and even more so when with the additional complication of directing porphyrin assemblies where bulk and assembly effects must be considered as well.

Examining assemblies of porphyrin molecules on surfaces has been essential in the development of porphyrin-containing electronic devices because molecular assemblies on electrodes often serve as the operational basis. It was found that careful control of intermolecular interactions[59-61, 69-70, 84-85, 95] as well as the chemistry of the supporting surface[19, 52, 56,41-50] is critical to construct porphyrin assemblies into specific structures and the collective electronic properties is substantially impacted by local order. With these considerations, porphyrin assemblies have been fabricated almost entirely by self-assembly and solution processing to form diverse structures comprising aggregates/islands, close-packed arrays, wires, two- and three-dimensional networks, among many others.[10] Due to the abounding types of individual porphyrin units, self-assembly is facilitated through numerous types of intermolecular interactions such as robust coordination bonds, pi-stacking,[19] hydrogen bonding, solvophobic van der Waals,[70] as well as covalent bonds. Additionally, the atomic structure of the underlying surface supporting porphyrin assemblies was found to strongly influence the molecular structures that form atop, revealing the potential for controlling surface structure at the atomic level to template the organization porphyrin assemblies on surfaces. [52, 56] The collective electronic properties of porphyrin assemblies were found to include

rectification,[84] charge hopping,[66, 85] Coulomb blockade,[19, 86] and redox reactions[48] with notable functions such as charge storage[51, 102-105] and switching.[107-109] The plethora or electronic properties and functions originate from local order and thus the "communication" between neighboring porphyrins.[69, 84-85, 95] When incorporated into devices, porphyrin assemblies have been a leading actor in DCSs[116-118, 121] that recently reached an impressive 13% efficiency.[116] Although less researched, porphyrins have been incorporated into charge transport layers in OFETs to study the relationships between molecular structure, assembly organization, and device performance. [46, 97-98, 120] In new current directions, the unique photonic properties of porphyrins are providing enhance functionality to OFETs and memory/transistor devices by offer the potential to control charge transport by light absorption.[46, 107, 130-131, 134]

Likewise, relationships between molecular structure, assembly organization, and device performance have been the subject of investigation focused on molecular/organic materials beyond porphyrins. These investigations are common across many types of molecular and organics owning to one the original promises of molecular/organic electrons to provide a limitless potential for electronic functions, finely tuned through chemical variations, due to the almost limitless ways in which molecules and organics can be constructed during synthesis. After all, it was found that there are limits and small chemical variations do not always lead to meaningful changes in the electron properties. [147-150, 156-158] However, finding where these limits lie is complex and requires a comprehensive understanding of what chemical group substituents affect (and just as important do not affect) certain electronic properties with the underlying mechanisms. It

has been commonly conjectured that chemical variations most often affect the electronic properties of molecular assemblies when nearest neighbor interactions are strongly perturbed producing different assembly organizations.[19, 139, 143, 146-147] For single molecules, it has been more challenging the find the limits of electronic tunability by chemical variations because reports describing chemical variations that do not affect the electronic properties are infrequent.

Even though electronic properties are inherent within certain molecules, these properties do not necessarily carry-over to assemblies of these molecules on surfaces.[159] Oftentimes, the electronic properties of single molecules and assemblies differ due to complex nearest neighbor interactions in which collective and cooperative effects are significant.[19, 140, 160-167] Sometimes these collective and cooperative effects can arise from a difference of only a few molecules like in the case of forming Coulomb islands from porphryin-thiols on Au(111).[19] On the contrary, single molecules do not always have electronic properties that differ from their molecular assemblies as in the case of dithiol Zn porphyrin oligomers where assemblies were fabricated by nTP.[30] Beyond assemblies composed of one type of molecular units, mixed assemblies benefit from combinatorial freedom where the individual properties of each type of molecule cooperates to influence the collective property or function of the assembly.[172] For example, workfunction tunability in mixed monolayers alkanethiols/ fluorinated alkanethiols[174] and in more complex systems, photoinduced charge separation/transfer in mixed assemblies of phthalocyanines/ nanocarbon species.[176-177] Though the electronic properties and functions arising from complex mixed assemblies and the combinatorial

potential is intriguing, delicate control over intermolecular interactions from multiple components required to fabricate such assemblies remains a challenge.

To employ the electronic properties that arise from certain, specific molecular organizations, it is necessary to fabricate pre-designed assemblies of molecular/organic units onto electrode surfaces with an aim to achieve intended electronic functions. Self-assembly has proven to be a versatile method to fabricate molecular assemblies by controlling the surface-molecule and intermolecular interactions to direct the molecular/organic materials into diverse architectures.[179, 189-190, 193] However, to fabricate complex assemblies there must be many available design combinations with diverse and specific interactions; such is the case with DNA[193] but not so with other types of molecular/organic materials. To fabricate complex assemblies, SPM techniques are used; specifically nanografting by AFM where small numbers of molecules ($\leq$ 32 thiol molecules) are controllably placed on the surface with the ability to monitor modifications in situ.[194-195] But nanografting is limited to molecules that are soluble in mild solvents with low vapor pressure (e.g. alkanethiols)[195, 198-201] and to go beyond this hybrid approaches are needed in which nanografting provides a template for a hierarchical assembly acting as a "nanobreadboard"[193] for instance. There have been many reports on assembly methods with limited electronic property characterization.[182, 193, 203-206] and when the electronic properties are explored it is done as a function of the assembled molecular organization.[140, 207-209] On the other hand, there is far less work on assembling molecular/organic components into pre-designed structures with an aim to obtain an intended electronic function.[75, 211]

From the discussions in this review, it is clear that there are many open questions in the study of molecular/organic materials for wide spread use in electronic devices. One of the most important questions involves the delicate relationships between chemical structure, assembly organization, and the emergent electronic properties. At each level, there are opportunities for design to produce specific properties, but to do so is complex. In the following chapters, three questions are address with the purpose to systematically understand these complex relationships enabling molecular/organic devices to be engineered at the molecular level with specific functions. *1) How do systematic perturbations in the molecular structure of porphyrins affect the resulting electronic properties? 2) How does molecular assembly affect the cooperative electronic properties of porphyrins on surfaces? 3) How can the assembly of porphyrins be pre-designed and directed into specific architectures to produce a specific, targeted electronic property?*

CHAPTER II

TRANSPORT THROUGH SINGLE AND FEW MOLECULE ASSEMBLIES OF PORPHYRIN-THIOLS WITH VARYING CHEMICAL IDENTITY ON AU

2.1 Introduction

Incorporating active molecular components into current Complementary Metal Oxide Semiconductor (CMOS) and silicon-based technology has the potential to expand the functionality of electronic devices in terms of biocompatibility, flexibility, and to produce functions yet unrealized by conventional materials.[6] There are generalities known about the relation between molecular structure and electronics properties. For instance, saturated hydrocarbons were found to be insulating because all electrons are used in chemical bonding and therefore are localized; such as the case of alkanethiols with a low tunneling efficiency of 1.2 $Å^{-1}$.[217-218] When a pi-system is extended over the entire molecule, as is the case of highly conjugated aromatic molecules, the tunneling efficiency was found to be high (0.2 to 0.6 $Å^{-1}$)[8, 137, 219]. Specifically, porphyrins are highly conjugated aromatic molecules and have attracted much interest in terms of molecular/organic electronics for memory or photo-devices.[9, 51, 105, 220-222] However, the detailed relation between structure of porphyrin-based molecules and electronic properties is lacking and without first understanding this, porphyrin-containing devices cannot be intelligibly designed.

Recently, the finer details of the molecular structure/electronic properties relation have begun to be examined in specific molecular systems by making small perturbations to the molecular structure and studying the resulting electronic properties.[20, 137, 146-147, 223] Molecular/organic electronics is tantalizing in this respect because of the imaginably infinite amount of ways to construct a molecule and thus, it is perceived that the electronic properties of a molecule can be tuned by making small perturbations to the molecular structure. With this idea, it seems that there is molecule for every kind of function and functions yet unknown. In some cases, small molecular structure changes lead to meaningful changes in electron transport.[137, 224-226] However, the notion of unlimited tune-ability is becoming more conservative because the work of Whitesides and coworkers have shown that small perturbations to the molecular structure of individual molecules that are incorporated into a molecular assembly does not necessarily lead to a change in the electronic properties.[147, 227-228] Therefore, tuning the electronic properties of a molecular or a molecular-containing device must be designed more thoughtfully than previously perceived. From work on alkanethiol based junctions,[146-147, 152, 224, 229-230] it seems that transport is affected only when redox reactions or hopping occurs. Because tunneling occurs exponentially, small perturbations in the molecular structure do not influence the tunneling through the barrier enough to be significant for the overall junction. It is thought that functional groups that can alter the transport to involve hopping may have a more noticeable effect.[224]

The finer details of the molecular structure/electronic properties relation for porphyrins in particular have begun to be examined.[9, 20, 51, 220-222, 231] Chen, Schuckmann

and coworkers, investigated two porphyrinoid molecules consisting of a porphyrin macrocycle, phenyl linker, and thiol tether where the porphyrin macrocycle included a chelated Zn ion (metalated)[19] or did not (free base).[20] As single molecules, it was found that charge transport takes place via tunneling and the metalated and free base porphyrin-thiols did not have any significant differences in the electronic properties in terms of tunneling efficiency and I-V characteristics. On the contrary, the charge transport for ensembles of these porphyrin-thiols was found to be different than that of single molecules because for ensembles, the transport was found to involve hopping.

In this chapter, the molecular structure/electronic properties relation is further elucidated by reporting on four porphyrinoid molecules similar to that discussed above where perturbations to the molecular structures have been done to alter the extent of pi-conjugation and nearest neighbor. To do this, a dodecanethiol (C12) self assembled monolayer (SAM) was used as template in which one or a few porphyrin-thiol molecules insert and incorporate into the SAM. The mixed SAM system was physically characterized by Atomic Force Microscopy and the electronic properties were examined by Density Functional Theory (DFT) calculations, Scanning Tunneling Microscopy (STM), and Scanning Tunneling Spectroscopy (STS). The differences in electronic properties that results from the small structural changes in the porphyrin based molecules are discussed herein.

2.2 Experimental Methods

2.2.1 Synthesis of Porphyrin-Thiol Derivatives of Varying Chemical Identity

The 5,10,15-tri(4-pyridyl)-20-(4-(1',5'-dithiopentyl)-2,3,5,6-tetrahydrophenyl) porphyrin (H-Pyridyl), 5,10,15-tri(4-pyridyl)-20-(4-(1',5'-dithiopentyl)-2,3,5,6-tetraflourophenyl) porphyrin (F-Pyridyl), 5,10,15-tri(4-phenyl)-20-(4-(1',5'-dithiopentyl)-2,3,5,6-tetraflourophenyl) porphyrin (F-Phenyl) was synthesized in two steps as detailed in previously published procedures.[19-20] A chelated Zn(II) ion was incorporated into the macrocycle of the above porphyrins (Zn H-Pyridyl, Zn F-Pyridyl, and Zn F-Phenyl) as formally described[19] to form the metaled analogue of the molecules

2.2.2 Materials

All the mixed SAMs were prepared on flame annealed, 200 nm thick Au(111) films on mica from Phasis (Geneva, Switzerland). Dodecainthiol (C12) used in SAM preparation was also used as received from Aldrich (98% purity).

2.2.3 Density Functional Theory Calculations

Electronic and geometric structure calculations were performed with the Gaussian Software Package, using the TPSS DFT functional with the 6-31+g(d') basis set. Localized density of states analysis was performed using the AOMix software package. This is similar to a previously published method and further details can be found there.[19-20]

2.2.4 Mixed Self-Assembled Monolayer (SAM) Preparation

The Au(111) on mica substrates were cleaned by exposure to in two cycles of UV/ozone for 10 minutes, rinsing the Au film with high purity water (18.2 MΩ•cm)

(NANOpure Diamond, Barnstead), further rinsing with ethanol, and drying under streaming nitrogen. The cycle was repeated again with just 5 minutes UV/ozone exposure. Then, to assembly the SAM, the substrate was immersed in a 1 mM C12 solution for one day. Afterwards, the substrate was rinsed with ethanol and immersed in the porphyrin solution with the concentration of 0.5 mM or 0.05 mM for the free base or the Zn metalated porphyrin respectively for one, three, or five days. The concentration of the Zn metalated porphyrin-thiol was reduced because of excess aggregation in solution and in the mixed SAM.

2.2.5 Atomic Force Microscopy (AFM)

Atomic Force Microscopy (AFM) images used to determine the physical structure of the mixed SAM were obtained using a Keysight 5500 AFM/SPM (Keysight, Santa Rosa, CA). All samples were imaged in an ethanol liquid cell with a force of 0.015 to 0.050 nN using a Si_3Ni_2 tips (Bruker AFM Probes, MSCT, Sunnyvale, CA). Imaging a $SrTiO_3$ standard surface was used to acquire the tip radii and it were typically 10 nm.[232] The Sader method was used to acquire the lever spring constants were typically 0.03 N/m.[233]

2.2.6 Scanning Tunneling Microscopy (STM)

Scanning Tunneling Microscopy (STM) was used to study the relative conductance and Scanning Tunneling Spectroscopy (STS) to study I-V characteristics. These were collected with an Omicron UHV-XA STM system and analyzed with Scanning Probe Image Processor (SPIP) software (version 6.0.2, Image Metrology,

Lyngby, Denmark). The images used to study the relative conductance were collected at 1.4 V and 20 pA and the I-V spectra were obtained in the range of 2 to -2 V.

2.3 Results and Discussion

2.3.1 Porphyrin-Thiol Derivatives of Varying Chemical Identity

The basic molecular structure of the porphyrin-thiol studied herein consists of a porphyrin macrocycle, phenyl linker, and a thiol tether that serves to bind the molecule to Au(111) surfaces (Figure 2). The molecular structure of the porphyrin-thiol has been systematically altered to control 1) molecular connectivity within a single molecule and 2) intermolecular interactions between molecules in an ensemble. To control 1, the subsistent on the phenyl linker has been changed from –F to –H. To control 2, a chelated Zn ion incorporated in the porphyrin macrocycle had been changed to $2H^+$ and the pyridyl groups on the macrocycle have been changed to phenyl groups. These changes affect intermolecular interactions because the Zn ion and the pyridyl groups interact via coordination and the porphyrin-thiols organize via macrocycle edge-face. To eliminate edge-face organization and to drive pi-stacking, Zn has been changed to 2H+, pyridyl groups have been changed to phenyl groups, or both substitutions have been made. In total, six porphyrin-thiols have been investigated. The F-Pyridyl[20] and Zn F-Pyridyl[19] porphyrin-thiols have been reported before. Here the remaining four are reported to complete the extensive series of porphyrin-thiols.

A)

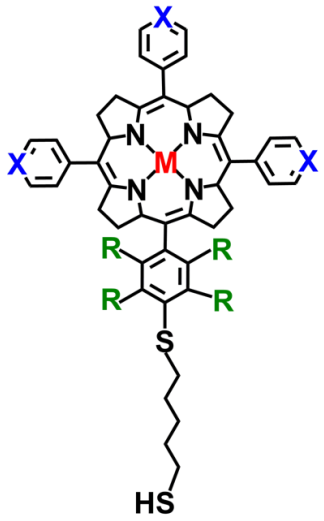

Molecule	M	R	X
H-Pyridyl	$2H^+$	-H	N:
F-Phenyl		-F	-CH
F-Pyridyl		-F	-CH
Zn H-Pyridyl	Zn^{2+}	-H	N:
Zn F-Phenyl		-F	-CH
Zn F-Pyridyl		-F	N:

B)

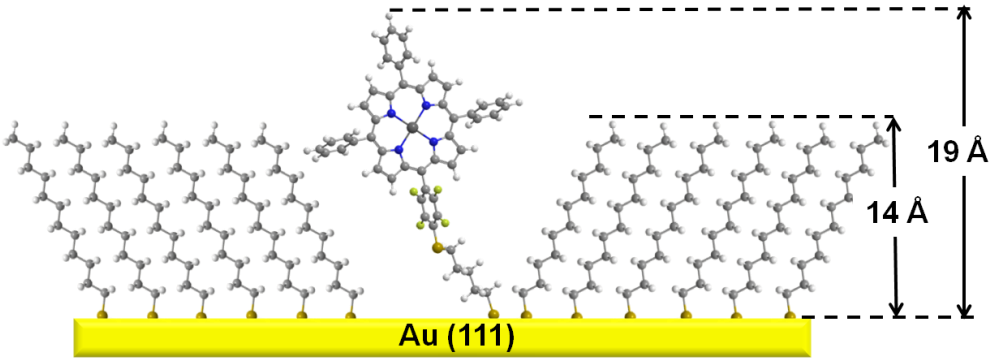

Figure 2. A) The basic molecular structure of the porphyrin-thiols studied herein. The corresponding table shows the substituents for X, M, and R. The molecules in grey have been reported on previously.[19-20] B) A model of the mixed SAM structure. The porphyrin-thiol randomly inserts into the background of dodecanethiol and is not standing up-right, but tilted with respect to the surface normal.

2.3.2 Electronic and Geometric Structure Calculations

In the optimized geometry of the molecule with R= -H, the linker phenyl ring was found to be rotated 67^o with respect to the macrocycle (Figure 3(A)). The optimized geometry of the free molecule with R= -F, the linker phenyl ring was found to be rotated 81^o with respect to the macrocycle. Therefore, a small chemical change results in a

change in the geometry of the linker group. The electronic structure calculations revealed that the increase in the co-planarity of the macrocycle and the linker leads to an extension of the pi-system into the linker (Figure 3). From this, it is hypothesized that an electron will have a smaller potential barrier to tunnel through over a larger portion of the tunnel gap in the R= -H than the R= -F system. Besides this, the electronic structure analysis was found to be quite similar for both R=-H and R=-F substituents in terms of band gap and orbital energies (Table 1). These are unpublished results carried out by Dr. Bradley Ewers.

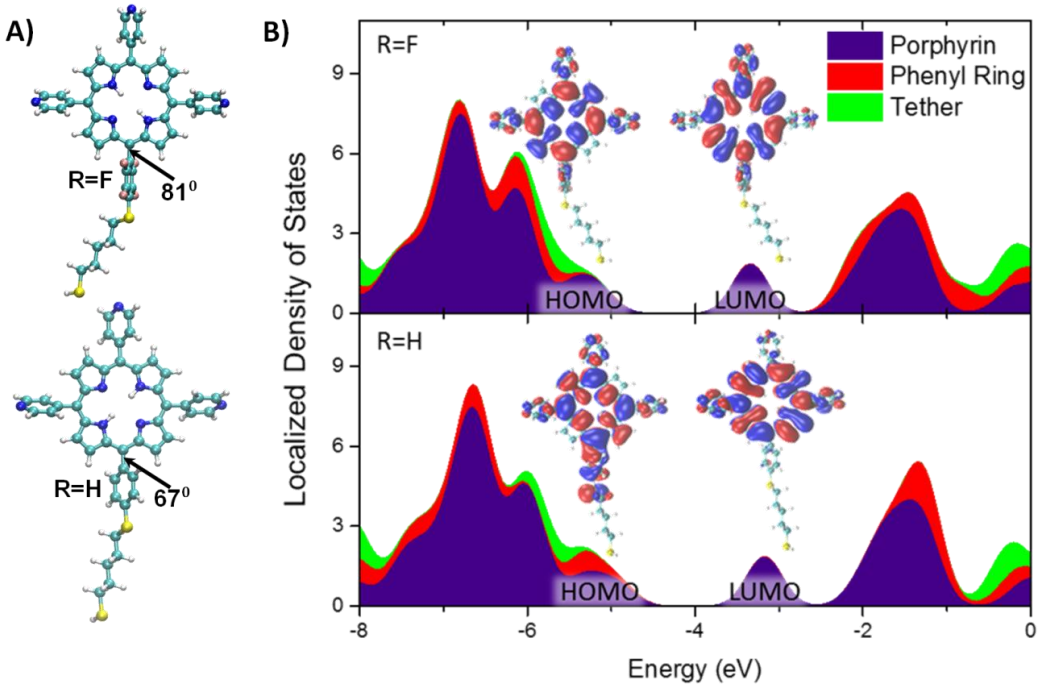

Figure 3. A) Optimized geometry and the corresponding HOMO levels of the porphyrin-thiol with –F and –H substituent on the phenyl linker. The phenyl ring was found to be more co-planer for the –H than the –F substituents due to steric effects. Because the phenyl linker for the –H substituted porphyrin-thiol was found to be more co-planer, the delocalization extends more than that of the –F substituted. B) HOMO and LUMO levels of the –F and –H substituted porphyrin-thiols by DFT calculations. These calculations were carried out by Dr. Bradley Ewers.

Molecule	HOMO (eV)	LUMO (eV)	Band Gap (eV)
F-Phenyl	-5.27	-3.44	1.83
Zn F-Phenyl	-5.37	-3.38	1.99
H-Pyridyl	-4.94	-3.18	1.76
Zn H-Pyridyl	-4.92	-3.11	1.81

Table 1. The location of the HOMO and LUMO levels and the band gap between them for the porphyrin-thiols, from DFT calculations, were found to be similar for all porphyrin-thiols derivatives. These calculations were carried out by Dr. Bradley Ewers.

2.3.3 Physical Structure Determination

AFM was used to determine the assembly structure of the mixed SAMs. In the AFM images, the porphyrins appeared as bright features and were mainly located near etch pits or defect sites in the C12 SAM. The existence of porphyrins in the SAM were confirmed X-Ray Photoelectron Spectroscopy (XPS) as reported previously.[20] On average, the bright features protruded a few angstroms, 5±2 Å, from the background C12 (Figure 4(A) and Figure 4(C)). The height difference between the background C12 and the maximum of the porphyrin feature is called the physical height. The physical height of many porphyrin features obtained from multiple samples and AFM tips, was recorded in a histogram shown in Figure 5(A). The histogram peak was taken to be the representative physical height of the porphyrin-thiol and the error was taken to be the full with at half the maximum (FWHM) of the histogram scaled with number of trails. For all porphyrin-thiol solution soak durations, the physical height did not change. The physical height for

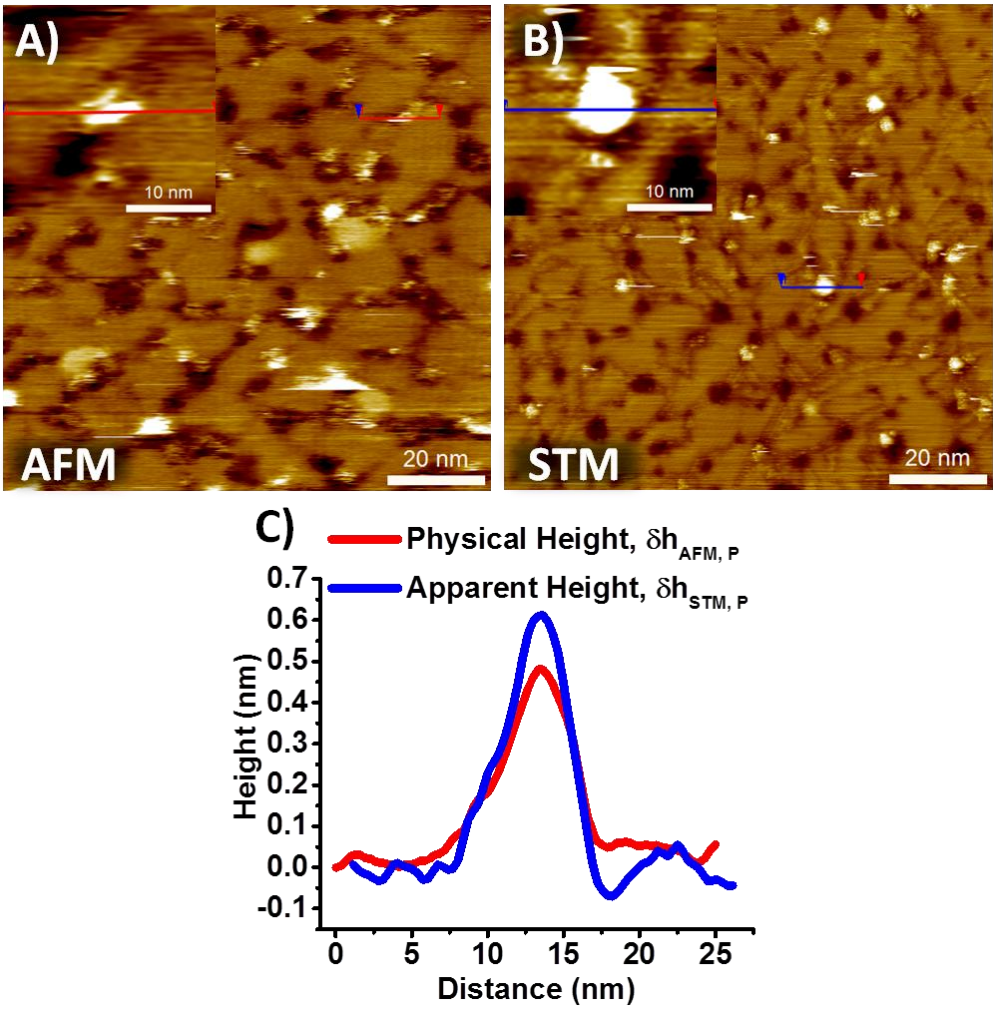

Figure 4. A) Topographic AFM image of the mixed SAM in which the bright features are porphyrin-thiols inserted into the background of C12. B) Topographic STM image of the mixed SAM and likewise, the bright features are porphyrin-thiols inserted into the background of C12. C) Line trace of a porphyrin-thiol feature observed in AFM and another porphyrin-thiol feature observed in STM where both have similar widths. These were not the from the same porphyrin-thiol insertion because it is challenging relocate a randomly inserted porphyrin-thiol in STM that has imaged in AFM. Different porphyrin-thiols of the same width were found to have similar properties and therefore, these two porphyrin-thiol features are compared here. The line trace shows that the porphyrin-thiol feature was found to have a larger height in STM than in AFM where this increase is due to the local electron density in a vicinity of the porphyrin-thiols.

all molecules studied herein as well as two similar molecules discussed previously in the literature, F-Pyridyl[20] and Zn F-Pyridyl[19], were tabulated in Table 4 in Appendix A. Because the porphyrin features protruded from the C12, the porphyrins were found not to insert face-down, but were held upright by the surrounding C12 SAM. Even though the porphyrins were upright, they were not parallel to the surface normal; they were tilted at an angle. This is because the length of the optimized structure of the porphyrin, 24.5 Å,[20] is larger than the physical height plus the height of the dodecanethiol,[234] 19 Å. A model of the mixed SAM is shown in Figure 2(B) where a single H-Pyridyl porphyrin is inserted into C12. The model as depicted in Figure 2(B) is most appropriate for the mixed SAM after one day porphyrin solution immersion duration since single molecule porphyrin-thiol insertions were likely. For longer immersion durations, the porphyrin-thiols were found to insert as few molecule assemblies. Increasing the immersion duration effectively increased the assembly size. To understand this, the width of the porphyrin-thiol features were measured as the longest dimension of the feature as it appears in STM images. For this, STM images were used because the lateral resolution is superior to AFM. The width of many porphyrins across different samples and STM tips were recorded in a histogram according to porphyrin-thiol solution immersion duration and shown in Figure 5(C). The peaks of the histogram were taken to be the representative lateral dimension of the porphyrin-thiol features for certain immersion durations and the spread was taken to be the FWHM scaled with the number of trials. All of the lateral dimensions of all varieties of porphyrin-thiols studied herein were tabulated and is shown in Table 4 in Appendix A. The smallest porphyrin-thiol features observed

has a width of 20 Å. The footprint of a single porphyrin-thiol on the surface is estimated to be 11 Å from optimized structure calculations and STM images.[19] But because of the broadening due to the tip, the observed lateral dimension of 20 Å was taken to be due to a single porphyrin-thiol in the mixed SAM. Features between 20 and 30 Å in lateral dimension, were considered to be small clusters of porphyrins-thiols. Larger features, 50 Å in lateral dimension and above, were considered large assemblies of porphyrins-thiols. The lateral dimensions of the porphyrin-thiol features were found to become more spread towards larger values for increasing porphyrin-thiol solution immersion duration. This indicates that as the porphyrin-thiol immersion duration increased, the porphyrin-thiol feature dimensions became more mixed and therefore there was the formation of some large assemblies alongside single and small clusters porphyrins-thiols. Although the lateral dimension increased, the physical height remained the same for single molecules and small clusters and large clusters.

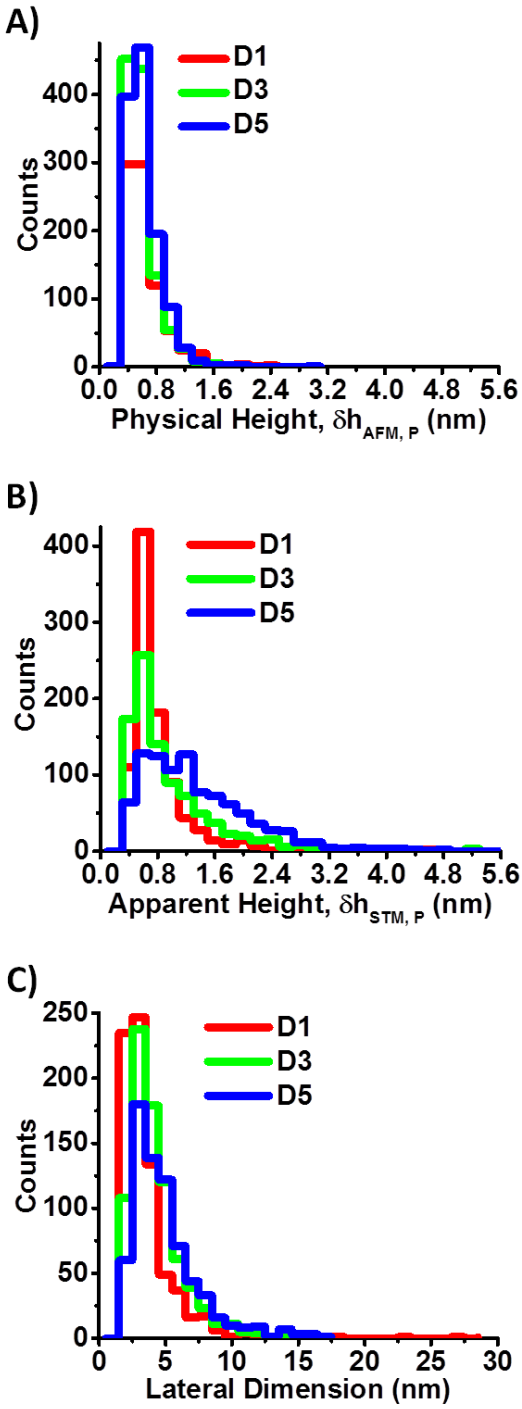

Figure 5. Representative histograms of the A) physical height (from AFM), B) apparent height (from STM) and C) lateral dimension (from STM) of the porphryin-thiols within the C12 SAM for one (D1), three (D3), and five (D5) days immersion duration in the porphyrin solution.

2.3.4 Relative Conductance

The crux of this study is to compare the molecular conductance, between all the porphyrin-thiol varieties using C12 as an internal reference. Previously, the Double-Layer Tunnel Junction Model (DLTJ) had been used to obtain a value for tunneling efficiency (which indicates the rate at which the electronic wavefunction decays within a certain barrier) and that served a point of comparison.[19-20] However, here, when the DLTJ model was applied, negative un-physical values were obtained for some porphyrin-thiol features; particularly for porphyrin-thiol features with large lateral dimensions suggesting that this model was not appropriate over the entirety of this extensive series of porphyrin-thiol derivatives. Instead an apparent height ratio between the porphryin-thiols and C12 SAM is used as a point of comparison. The apparent height ratio quantifies the change in height of the porphyrin-thiol features between AFM and STM images (Δh_p) with respect to the change in height of the C12 SAM between STM and AFM images (Δh_{C12}). The apparent height ratio is defined as

$$\frac{\Delta h_P}{\Delta h_{C12}} = \frac{\delta h_{STM,P} - \delta h_{AFM,P}}{\delta h_{STM,C12} - \delta h_{AFM,C12}} = \delta h_{STM,P} - \delta h_{AFM,P} \qquad \text{(Equation 1)}$$

where $\delta h_{STM,P}$ is the apparent porphyrin height extracted from STM measured with respect to the C12 SAM and $\delta h_{AFM,P}$ is the physical porphyrin height extracted from STM measured with respect to the C12 SAM. The denominator $\delta h_{STM,C12} - \delta h_{AFM,C12}$ is normalized to one since the porphyrins heights are always measured with respect to the C12 SAM with the aim to quantify the magnitude of porphyrin-thiol height increase with respect to the relatively insulation C12 SAM.

The height difference between the porphyrin and the C12 imaged by STM ($\delta h_{STM,P}$) is called the apparent height because in STM images, features are a convolution of topography and electron density. In the STM images of the mixed SAMs, the porphyrin-thiols appeared as bright features where the contrast between the features indicates relative degrees of conductance as well as topography (Figure 2(B)). The background C12 appeared dark and is less conductive than the porphyrin-thiols. The apparent height was measured in the same way as the physical height; over many samples and STM tips (Figure 2(C)). A representative histogram of the apparent height is shown in Figure 5(B). The error of the peak was taken to be the FWHM of the histogram scaled with the number of counts. The peak and the error of the apparent height histogram for all porphyrin-thiol varieties were tabulated in Table 4 in Appendix A. The apparent heights of the porphyrin-thiols were found to become more spread towards larger values for increasing porphyrin-thiol solution immersion durations. This indicates that as the porphyrin-thiol immersion duration increased, the apparent height of the porphyrin-thiols become more mixed and therefore there were an increasing number of porphyrin-thiol features with an apparent height larger than the peak histogram value. This same trend was observed for the lateral dimensions of the porphyrin-thiol features with increasing porphyrin-thiol solution immersion duration. However, as stated previously this trend was not observed for the physical height and stayed the same for all porphyrin-thiol regardless of lateral dimension. Comparing the apparent and physical height of a given porphyrin-thiol gives insight into the electron density. When the apparent height is found to be larger than the physical height, this difference can be

attributed to a large electron density in the vicinity of the molecule. Therefore, since the physical height was found to be the same but the apparent height and lateral dimension was found to increase for increasing porphyrin-thiol solution immersion duration, the increase in apparent height is related to the increase of the porphyrin-thiol lateral dimension (Figure 6).

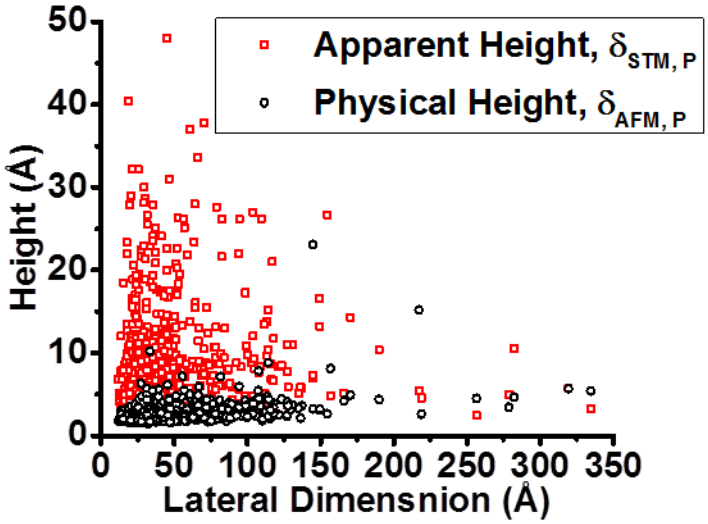

Figure 6. The apparent height and physical height of porphyrin-thiol molecules within a C12 SAM as a function of lateral porphyrin-thiol feature dimension.

Using Equation 1, the apparent ($\delta h_{STM,P}$) and physical ($\delta h_{AFM,P}$) height, the apparent height ratio was calculated for the porphyrin-thiols as a function of the lateral dimensions and solution immersion duration (Figure 7). The apparent height ratio is shown in two plots; for entire set of data in Figure 7(A) and for single and small clusters (lateral dimension ≤ 30 Å) in Figure 7(B). This is because the apparent height ratio for

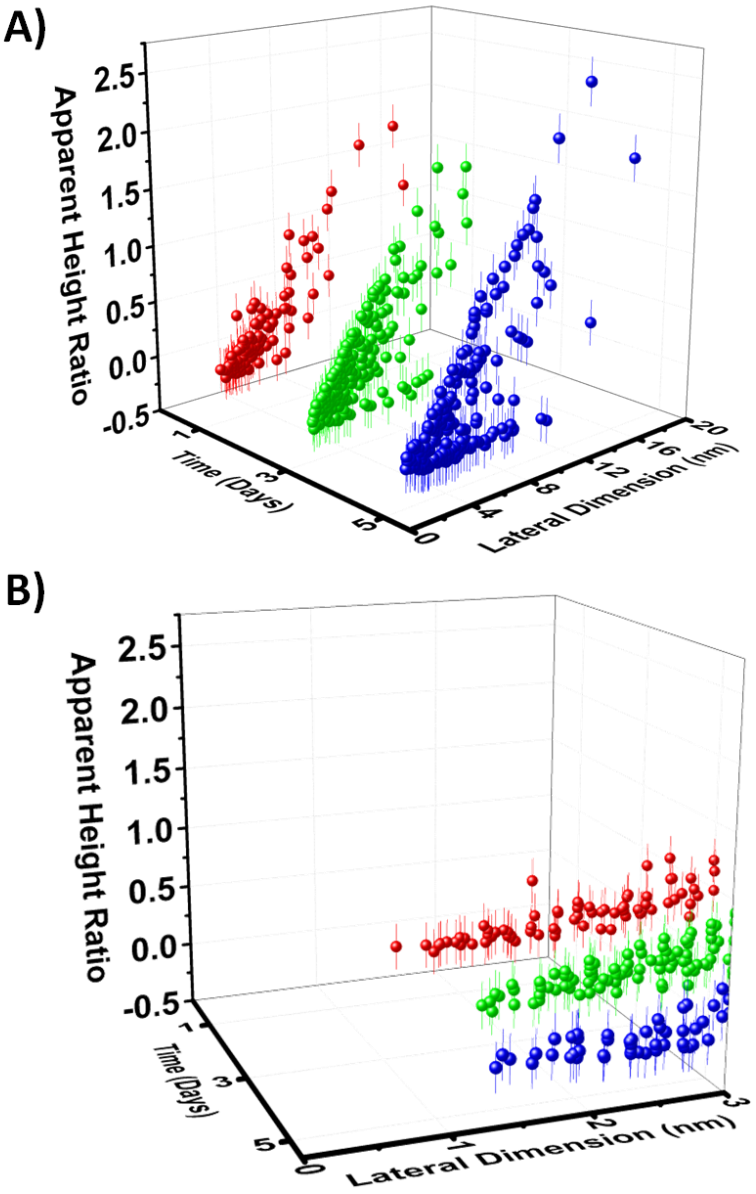

Figure 7. Representative three-dimension plots of the apparent height ratio, as calculated from Equation 1 for porphryin-thiols as a function of assembly time (one, three, or five days) and lateral porphyrin-thiol dimensions. In A) the entire data set is shown and in B) only data for single molecules and small clusters (lateral dimension ≤ 30 Å) are shown at a different perspective for clarity. Similar plots for all varieties of porphyrin-thiols appear comparable and are located in Appendix A.

single molecules and small clusters was found to be different than for large aggregates of porphyrin-thiols.

The apparent height ratio of single molecules and small clusters of porphyrin-thiols of all varieties was found to be zero. It was hypothesized that when –F was replaced by –H in the phenyl linker, thereby increasing the extent of electron delocalization (Figure 3), the –H substituted variety would have a higher conductance. It was found that there is no measurable difference in the apparent height ratio for –F versus –H substituted varieties. Furthermore, there is no measurable difference in the apparent height ratio for the Zn^{2+} versus $2H^{+}$ or for the –N: versus –CH substituents. Accordingly, it was suspected there would be no major variation in the conductance for these because the electronic structure analysis showed no considerable difference between these varieties of porphyrin-thiols; all demonstrating similar band gaps and orbital energies. Therefore, it was found that there is no measurable difference in the apparent height ratio of single porphyrin-thiols of all varieties studied herein. This result is consistent with works by Whitesides and coworkers in which they found that there is no measurable difference in current density[147] or charge transport rate[156] for alkyl-based molecular SAMs of the same length that have been slightly altered to incorporate different functional groups.

Furthermore, since the apparent height ratio is zero for single porphryin-thiols of all varieties, the conductance of the porphyrin-thiols and C12 are comparable. For other conjugated systems,[8, 137, 219] the conductance is found to be greater than that of C12.[235-239] Therefore, it seems that the transport through the porphyrin-thiol is dominated by the

thiol and the variation in chemical identity within the porphyrin macrocycle and linker (Figure 2(A)) does little to modulate the charge transport resulting in the same conductance properties for all varieties of single porphyrin-thiol molecules of every variety studied herein.

The apparent height ratio departs from zero when porphryin-thiols grow in lateral dimensions within the mixed SAM. In general, the apparent height ratio steadily increases with increasing porphyrin-thiol lateral dimension (Figure 7). At this point, the transport is no longer dominated by the thiol tether opening the opportunity for small chemical modifications to modulate charge transport in porphyrin-thiols. Although the apparent height ratio increases for increasing lateral dimension, the spread in the data is large and becomes larger for increasing lateral dimension. This increasing spread can be explained because larger porphyrin-thiol assemblies have more ways in which the individual porphyrin-thiols molecules can organize and therefore varying nearest neighbor interactions which can produce varying electronic properties. [143, 146-147] This is explored further in Chapter III that discusses the effect of mixed SAM organization and porphyrin assembly time on the emergent electronic properties.

2.3.5 I-V Characteristics

To investigate the differences in charge transport of single molecules and small clusters of porphyrin-thiols versus large aggregates, STS was carried out to obtain I-V characteristics for these. It was found that there are two distinct I-V curves characteristic of the single molecule and small clusters and characteristic of large aggregates of porphyrin-thiols. A representative set of data displaying these two classes is shown in

Figure 8. Here all the I-V curves that were collected are shown where immediately before and after, I-V response representative of C12 as reported in the literature,[240-242] was obtained so as to minimize effects due to the tip. Further details on STS are described in Appendix D. The C12 I-V curves are also shown in Figure 8 to serve as a reference for the I-V of the porphyrin-thiols. For single molecules and small clusters of porphyrin-thiols, the I-V response was found to be very similar to C12. This corroborates with transport dominated by the thiol-tether and within the tunnelling regime. The I-V response for large aggregates of porphyrin-thiols was found to be different compared to C12 and single molecules and small clusters of porphyrin-thiols. The I-V response of large aggregates exhibited a gap opening near low bias where little current flows through the STM, porphyrin-thiol junction. When the bias was increased, to a larger onset voltage, more current was allowed to flow through the STM, porphyrin-thiol junction. This I-V behavior is indicative of Coulomb blockade[243] which has also been observed in other molecular systems[26, 244-245] and in quantum dots.[246-247] Here the I-V characteristics of large aggregates suggest the porphyrin-thiol aggregates are Coulomb islands capable of stabilizing charge meaning that when the applied bias is large enough to overcome the charging energy of the porphyrins, electrons hop from the STM tip to the region of delocalization, formed by the aggregates of porphyrins, and then subsequently hops to the Au(111) surface.

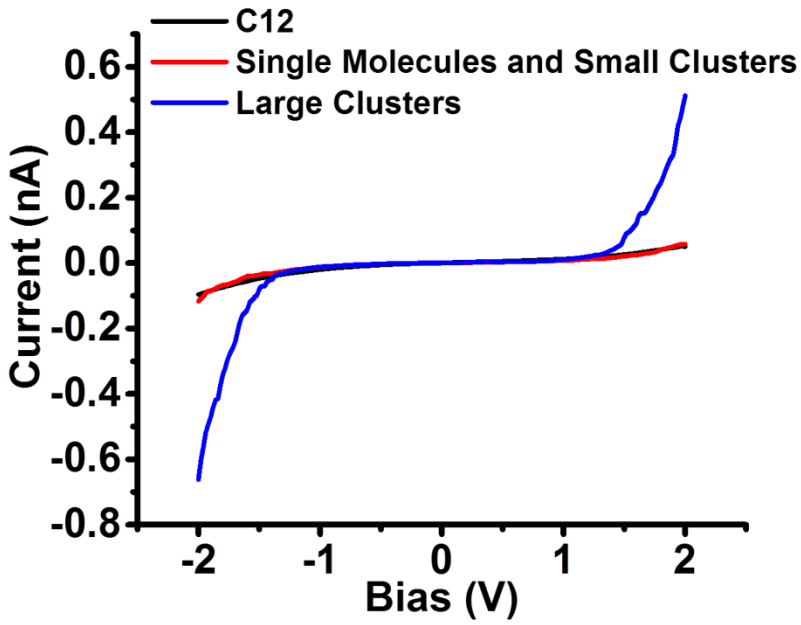

Figure 8. Representative I-V curves for single molecules and small clusters of porphryin-thiols, large clusters of porphyrin-thiols, and the surrounding C12 for comparison. The curves shown are a geometric mean of, 191 curves for single molecules and small clusters, 209 curves for large clusters, and 186 curves for C12. The I-V curve for C12 lies behind that for single molecules and small clusters.

To rationalize why Coulomb blockade is observed for aggregates and not for single molecules and small clusters of porphyrins, an estimate to first order is considered. For Coulomb blockage a single electron is added to the porphyrin island at a time where the change in the Coulomb energy is given by the capacitance (C) and the change in electrostatic energy is given by the charging energy (E_C). There are three conditions for Coulomb blockage to be observed here. First, the tunnel resistances of the barriers (R_T) must be larger than the resistance quantum or tunneling events due to quantum fluctuations must be minimal:

$$R_T >> \frac{h}{e^2} \quad \text{(Equation 2)}$$

where h is plank's constant and e is the charge of an electron. This condition is satisfied for weak electrode/ molecule coupling and is met in the case presented herein because of the alkanethiol tether that separates the porphyrin from the Au surface and the vacuum gap that separates the porphyrin from the STM tip. Second, the charging energy (E_c) must be sufficiently large:

$$E_C >> \frac{k_B}{T} \quad \text{(Equation 3)}$$

where k_B is Boltzmann's constant and T is temperature. At room temperature the relation becomes

$$E_C >> 0.025\ eV \quad \text{(Equation 4)}$$

and to test the satisfaction of this condition, the charging energy must be larger than 0.025 eV. This is sufficiently satisfied for the single molecules and small clusters as well as the large aggregates observed herein (Table 2). However, for porphyrin islands that are much larger (150 nm in lateral dimension), that is much larger than those observed here, Equation 4 may not be sufficiently met (Table 2) and perhaps this presents an upper bound to the Coulomb blockage behavior, but this is yet to explored. To estimate the charging energy in the case presented here, the porphyrin islands are simply assumed to be spheres with a radius equal to half the width of the porphyrin features as they appear in STM. The charging energy of a sphere is give by

$$E_C = \frac{e^2}{C} = \frac{e^2}{4\pi\varepsilon r} \quad \text{(Equation 5)}$$

where C is the capacitance, ε is the permittivity of the dialectic medium, and r is the radius of the porphyrin island. The charging energy is evaluated for the different porphyrin island sizes and presented in Table 2. Third and lastly, for the porphyrin islands to be capable of stabilizing charge and consequently displaying Coulomb blockade herein, the HOMO-LUMO gap plus the charging energy must be less than the potential available during STS (2 eV). The value for the HOMO-LUMO gap is approximately 1.8 eV according the results of DFT calculations shown in Table 1.

According to this model, the third condition is met only for large aggregates of porphyrins with an island diameter of 10 nm and larger due to the sufficiently small energies required for charging the porphyrin islands and hence charge can be stabilized on these large islands exhibiting Coulomb blockade. Conversely, this third condition is not met for single molecules and small clusters of porphyrins with an island diameter between 2 nm to 5 nm because the charging energy is too large and hence, the electrons tunnel through the entire molecule. The results of this capacitor model qualitatively corroborates with the experimental data which is quite astounding considering the simplicity of the model. The differences between the experimental data and model arise in the porphyrin island sizes that show Coulomb blockade behavior. In experiment, Coulomb blockade has been observed for islands as small as approximately 5 nm while the model predicts that Coulomb blockage should not be apparent for this island size and only so at an island size above approximately 10 nm with a possible limitation below 150 nm.

Observed Island Diameter (nm)	2	3	5	10	150, not actually observed here
Estimated Number of Molecules	1	3	6	9	200
Projected Actual Island Diameter (nm)	1	2	4	12	100
E_c (eV)	3	1.5	0.7	0.15	0.029
HOMO,LUMO Gap +E_c (eV)	**4.8**	3.3	2.5	**1.95**	1.83
Coulomb Blockade Possible	**No**	No	No	**Yes**	Yes, but Equation 4 may not be sufficiently satisfied

Table 2. Rationalizing Coulomb blockage behavior in porphyrin islands. A) By using the energy level alignment data presented in Table 1 and a simple spherical capacitor model, the possibility of Coulomb blockade is estimated. The estimated number of molecules and projected actual island diameter in a given observed island diameter is based upon previous reports[19-20] where the approximate smallest porphyrin-thiol feature observed in STM images is 2 nm which is assumed to correspond to one porphyrin-thiol molecule with a projected diameter of approximately 1 nm. Furthermore, in a pi-stacked aggregate, the porphyrin-thiol molecules are separated by a distance of approximately 0.6 nm. E_c is calculated from Equation 5 and to assess whether Coulomb blockage is possible the HOMO, LUMO Gap (Table 1) is added to E_c.

From experimental data and qualitative agreement with a simple model, charge transport was found to be different for single molecules and small clusters than for large aggregates of porphyrin-thiols. It was suggested by Whitesides and coworkers that small changes the molecular structure may significantly affect the electronic properties when the transport mechanism is not simply tunneling.[156] This is, in fact, the circumstance here. When the transport mechanism is altered from tunneling, in single and small

cluster of porphyrin-thiols, to hopping, in large clusters of porphyrin-thiols, it was found that there is indeed a difference in the electronic properties.

2.4 Conclusion

When the idea of using molecules as electronics components first arose, it was thought that there exists an almost infinite amount of possibilities due to the numerous ways in which molecules can be chemically constructed and therefore produce unique electronic properties.[7] However, in this study, it was shown that a small chemical perturbation does not necessarily produced unique electronic properties. The tunneling efficiency of all single porphyrins-thiols in this extensive series was shown to be the same. After the DFT calculations showed that the pi system extended well into the linker group for R= -H as opposed to only slightly for R= -F, it was suspected that the apparent height ratio would be greater the R= -H porphyrin-thiols. However, it seems that the extent of orbital overlap does not produce a significant difference only that there is, in fact, an overlap.

The electronic properties of the single porphyrin molecules are altered when they are assembled in aggregates large enough to so that the aggregates can stabilize charge. This is evident in the differences in apparent height ratio and I-V characteristics of single porphryin-thiols versus aggregates of porphyrin-thiols. The opening of a low bias gap in the I-V response suggests that the charge transport mechanism is not in the tunneling regime as is the case for single porphyrin-thiols. Instead for aggregates, the I-V response indicates Coulomb blockade where the electrons tunnel from the STM tip, occupy the states on porphyrins, then subsequently tunnels to the Au substrate.

CHAPTER III

THE INFLUENCE OF SELF-ASSEMBLY DURATION ON THE CHARGE TRANSPORT OF PORPHYRIN CLUSTERS

3.1 Introduction

The vision of molecular electronics considers molecules as the ultimate nano-metric building blocks with batch synthesis of moles of identical copies. Since nuclear motion is easier in organic molecules, than in similar inorganic materials like quantum dots, electron-phonon coupling is far more important for molecular conductors than for inorganic (semi)conductors.[248] Charge transport is therefore carried by polarons in organic systems rather than free carriers in inorganic materials.[249] The strong electron-phonon coupling regime of polaron-mediated transport is characterized by nuclear reorganization or electronic polarization in response to charge transfer. Nuclear reorganization stabilizes the charged states by shifting the electron density and molecular orbital energy levels. The polaron mechanism can explain the rich transport behavior of molecular systems, including negative differential resistance (NDR) and hysteresis[248, 250-252] yet experimental demonstration of strong vibronic effects is rare. In one instance, an isolated conjugated molecular wire of oligo phenylene ethynylene (OPE) with higher vibrational freedom enables the wire to become charged and conduct by hopping contrary to transport by inefficient tunneling with restricted vibrational motion across the dense OPE monolayer [253]

Although polaron formation considers minor rearrangements within atoms, there are even larger conformational changes that have a drastic effect on transport. For example, upon heating single alkanedithiol conformers buckle, thereby shorting the tunneling length.[254] Alternative binding configurations of tetra-phenyl porphyrin (TPP) derivatives within mechanical break junctions showed conductance fluctuations of up to four orders of magnitude.[255] Within the semi-stable state very fast "noise" in the conductance of up to ×2-3 G/G_0 is observed, which is attributed to vibronic states in the porphyrin.[255]

Likewise, fast stochastic fluctuations in conductance can also be explained by vibronic coupling, which shifts the nearest molecular orbital energy away from the Fermi level, and "switches off" the molecular conductivity. Thermal fluctuations can release the charge to switch the conductance "on" or "off."[250] Stochastic switching is well known in the STM-measured apparent height (i.e., a combination of physical height and conductivity) of OPE,[256] ferrocene, and viologen insertions into thiol monolayers.[257] Initially stochastic switching was observed by comparing consecutive STM images over a few-minutes time intervals[256] and later, direct current-time recording indicated that "on/off" switching, observed as 4 Å changes in the apparent STM height, occurring within a millisecond or less.[258] It was found through these studies that increasing the density of the host monolayer reduces the probability of stochastic switching, and supports the importance of local order on vibronic effects.[259]

Bias-induced current switching is also important in organic molecular wires because it is a method to modulated charge transport without the addition of junction

components and simply done through the existing contacts. When the bias is controlled the electro-active unit can be switched between and high conductive or "on" state to a low conductive or "off" state. Bias-induced switching has been reported to primarily originate in conformational changes[260-262] with suggestions to be associated with polaronic transport.[260, 263] To a lesser extent bias-induced switching involves redox processes[264-265] as well as redox processes that can possibly alter conformation.[266] For example, in fast (0.64 ms) mechanical break-junction measurements of a bipyridyl-dinitro derivative of OPE displayed bias-induced current switching that is intrinsic to the molecular component and conjectured to be due to conformational changes of the molecule.[260] Furthermore, bias-induced current fluctuations between only two levels were observed for transport across mixed monolayers composted of approximately 85% surface coverage of dodecanethiol (C12) and approximately 15% surface coverage ferrocenyl hexanethiol and measured in junctions contacted by suspended wires. Contrastingly, no fluctuations in the redox center were observed and the mechanism attributed to bias both the electronic properties of the background C12 monolayer and the ferrocenyl hexanethiol itself.[265]

The emergent understanding is that structural dynamics makes conductance switching in molecular wires less stable than in inorganic materials, and fast recording rates (cf. vibronic frequency) are required to reveal conductance switching rather than apparent fluctuations arising from molecular dynamics. Since molecular charging occurs while atoms are in motion, the local order is critical. Local order and structural effects is also critical in thin-film organic electronics, where the carrier mobility of molecularly

identical substance can vary by several orders of magnitudes for different processing conditions.[267] Although local order and structural effects are not completely comparable between molecular and thin-film organic electronics, structural effects on the polaron formation should be in common. In thin-film organic electronics, polaron formation is often facilitated by aggregation, especially pi-stacking, as is the case of red shift of dye-aggregates[268-269] or enhanced field-effect mobility in denser packing of conductive oligomers.[270] Efficient pi-stacking delocalizes molecular orbitals between non-covalently bonded pi-systems, thereby reducing the polarization energy requiring less energy to charge the molecules.

Recently, we have been working to elucidate the complex role of intermolecular interactions driven by specific design elements, especially those driving pi-stacking, in supramolecular systems of thiol-tethered porphyrins on molecular charge transport properties.[9] We use porphyrin derivatives as a platform because they have great potential as molecular device components for studies of the role of supramolecular organization on transport properties.[9, 271] Porphyrins are aromatic macrocycles that are chromophore cofactors involved in variety of biological process, such as energy and electron transfer in photosynthesis, redox catalysts, and respiration. The aromaticity implies high electrical conductivity across the dye,[272] the frontier orbitals (HOMO-LUMO) are within approximately 2 eV from the Fermi level of common electrodes, and core metallic atom can be redox active.[273] The chemical diversity of the peripheral sites and choice of chelated metallic cation afford means to engineer porphyrin derivatives with tuned

HOMO-LUMO gaps, large dipoles, diverse spin properties, and moieties that drive self-assembly and self-organization.[274]

Because of the strong affinity of the macrocycle toward Au(111)[255, 271, 275] porphyrin derivatives do not form a uniform monolayer in a standing-up orientation.[9, 276] Consequently, porphyrin derivatives were extensively studied by STM where the macrocycles are lying flat on the metallic substrate and therefore strongly coupled to the metallic states.[271] Decoupling the molecular and metallic substrate states, longitudinal transport across the *ca.* 1 nm single porphyrin molecules is often studied by a break-junction configuration,[255, 272, 275, 277-278] but here we focus on revealing effects of many porphyrin molecules within a molecular cluster on transport using STM imaging. To achieve a standing-up orientation, allowing STM imaging for study of longitudinal transport, some surface templating methods have been developed to stabilize the porphyrins on Au(111).[279-280] But here, the standing-up orientation was achieved by allowing the porphyrin derivatives to self-insert into a defects sites in a preformed monolayer of dodecanethiol (C12) on Au(111).[19-20, 256-259]

Our previous studies on 5,10,15-tri(4-pyridyl)-20-(4-(1′ ,5′ -dithiopentyl)-2,3,5,6-tetra-fluorophenyl) porphyrin and its Zn(II) metaled analogue revealed pyridyl-group coordination to the Zn(II) center of a neighboring metalloporphyrin, and this competes with pi-stacking. We found that small pi-stacked clusters are formed if the substrates are immersed for one day in the porphyrin solution, and the clusters grow up to 30 nm in lateral dimension, composed of approximately 20 molecules, after immersing the substrates for five days.[19-20] The lateral dimension of the clusters changes

the electrical transport behavior from simple tunneling for small clusters to rich switching behavior for large clusters.[19-20] The self-assembled clusters, driven by pyridyl coordination, exhibited greater conductance switching compared to those driven by pi-stacking.

Here we report new molecular engineering strategies for molecular charge transport in few-molecule clusters of porphyrins in a host monolayer through delicate self-organization over prolonged assembly time. The *meso* pyridyl groups, along with other chemical choices during synthesis such as to chelate metal ions and the pendant phenyl linker substituents, can drive self-assembly of the porphyrins in the clusters into diverse architectures. We controlled the chemical nature of the thiol-tethered tetra phenyl porphyrins to systematically investigate the effect of inter-molecular interactions, over prolonged self-assembly times, on the resulting electronic properties. For all of the molecules in the series, we observe that in general, there is a stark change in the conductance magnitude of a series of thiol-derived tetra phenyl porphyrins inserted within a preformed monolayer of dodecanethiol (C12) on Au(111). This conductance switching cannot be explained exclusively by cluster size as before[19] but can be explained by further considering the internal organization of porphyrins within individual clusters and nearest neighbor interactions with the surrounding host monolayer. Cluster size, internal molecular organization, and nearest neighbor interactions with the host monolayer are driven by the assembly time. To untangle these, one particular thiol-tethered tetra phenyl porphyrin derivative in the series is examined, [(5,10,15-tri(4-phenyl)-20-(4-[(5-mercaptopentyl)thio)]-2,3,5,6-

tetrafluorophenyl)porphyrinato) zinc(II) ($ZnTPPF_4$-SC_5SH), with a detailed investigation comparing clusters of approximate similar sizes formed over different assembly intervals. Reinforcing the trend observed for variation in only assembly time, the same rational is applied to a statistical data set regardless of lateral dimension and generally obtain the same trend.

We have chosen to feature $ZnTPPF_4$-SC_5SH here because it is analogous to the molecule studied in Suchkmann et al.[19] with one variation; the pyridyl groups are replaced with phenyl groups (Figure 9). The variation eliminates the axial coordination of the Zn(II) by pyridyl groups on neighboring porphyrins and favors pi-stacking of the porphyrin macrocycles. This subtle chemical change inhibits the lateral growth of the porphyrins clusters because one pathway is repressed, but eventually large clusters of the porphyrin are observed in the C12 monolayer after prolonged immersion in a solution of the porphyrin. The larger clusters exhibit enhanced transport and we suggest that the switching is due to delicate optimization of the mixed monolayer molecular packing that reduces the polaron reorganization energy.

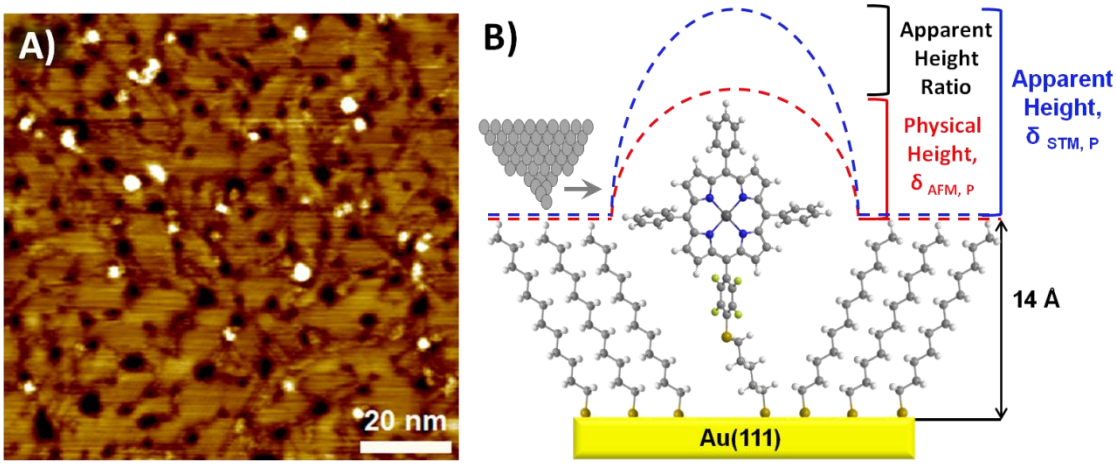

Figure 9. $ZnTPPF_4$-SC_5SH within the C12 matrix, showing A) STM image with height contrast at set point of 20 pA at 1.4 V. and B) Schematic side view illustrates that the measured heights are relative to the surrounding matrix, with a height of 14 Å.

3.2 Experimental Methods

3.2.1 Synthesis of $ZnTPPF_4$-SC_5SH

5,10,15-tri(4-phenyl)-20-(4-(1',5'-dithiopentyl)-2,3,5,6-tetraflourophenyl) porphyrin was synthesized in two steps similar to a previously published procedure.[20] This was followed by chelation of Zn(II) ion in a procedure formally detailed[19] to form [(5,10,15-tri(4-phenyl)-20-(4-[(5-mercaptopentyl)thio)]-2,3,5,6-tetrafluorophenyl)porphyrinato)zinc(II) ($ZnTPPF_4$-SC_5SH).

3.2.2 Mixed Self-Assembled Monolayer (SAM) Preparation

The mixed monolayers were adsorbed onto 200 nm thick, flamed annealed Au(111) films on mica (Phasis, Geneva, Switzerland). Before mixed monolayer absorption, the Au(111) films were cleaned by UV/ozone for 10 minutes, rinsed with deionized (18.2 MΩ·cm) water (NANOpure Diamond, Barnstead), rinsed with ethanol,

and dried under streaming N_2; then UV/ozone for another 5 minutes and rinsed and dried with the same sequence described above. The substrates were subsequently immersed in a 1 mM dodecantihol (Aldrich, 98%, used as received) in ethanol solution for 24 hours. The substrates were rinsed with ethanol and immersed in 0.05 mM of $ZnTPPF_4$-SC_5SH in dichloromethane for one, three, or five days. The concentration of $ZnTPPF_4$-SC_5SH was smaller than what has been previously used[19-20] to avoid monomers aggregation in solution, resulting in highly crowded clusters on the Au(111) surface. After one, three, or five days, the substrates were removed from the $ZnTPPF_4$-SC_5SH solution, rinsed with dichloromethane, and dried under streaming N_2.

3.2.3 Scanning Tunneling Microscopy (STM)

STM images and I-V spectroscopy were collected with an Omicron UHV-XA STM system (< 3 x 10^{-10} Torr) using mechanically cut Pt/Ir (80/20) tips and analyzed with Scanning Probe Image Processor (SPIP) software (version 6.0.2, Image Metrology, Lyngby, Denmark). Images were collected at 1.4 V and 20 pA in which 100-350 $ZnTPPF_4$-SC_5SH clusters were imaged for each immersion time (one, three, and five days) and their dimensions were extracted using grain analysis. I-V spectroscopy was collected over several clusters on different samples with different tips. 100 consecutive I-V spectra were collected above selected $ZnTPPF_4$-SC_5SH clusters, by scanning the bias from -2 to +2 V (300 data points, 0.1 ms per point, see Figure 58 in Appendix D for detailed bias-scan timing). The feedback loop was activated before each scan to maintain the tip height according to a set point of 20 pA at 1.4 V. To avoid spurious tip effects, 100 scans were also collected on a near-by C12 matrix immediately before and after the

$ZnTPPF_4$-SC_5SH spectroscopy. If these reference spectra were of wide distribution or highly asymmetric, the results were discarded (Figure 59 in Appendix D). I-V data was also discarded in cases where re-imaging the insertion area was much distorted. Further data statistics was done using MatLab.

3.2.4 Atomic Force Microscopy (AFM)

AFM images were obtained with an Agilent 5500 AFM using, commercially available, Si_3N_4 tips (Bruker AFM Probes, MSCT, Sunnyvale, CA) with nominal 10 nm radii and 0.03 N/m spring constants. Samples were imaged an ethanol liquid cell using contact mode with forces between 0.015 and 0.050 nN. Low imaging forces were used to minimize compression of the $ZnTPPF_4$-SC_5SH into the mixed monolayer. Between 100 and 350 $ZnTPPF_4$-SC_5SH clusters were imaged by AFM and for each immersion time (one, three, and five days) and their dimensions were extracted using grain analysis.

3.3 Results and Discussion

3.3.1 Subtle Change in Mixed Monolayer Morphology with Reorganization Time

A typical STM topography image is shown in Figure 9(A) wherein the bright features are $ZnTPPF_4$-SC_5SH and the dark features are etch pits characteristics of alkanethiols on Au(111). Similar images were obtained by AFM though with poorer lateral resolution. A comparison between AFM and STM images is given in the Appendix. The height measured by either AFM or STM is the height difference relative to the surrounding C12 matrix, as schematically shown in Figure 9. The AFM height, $\delta_{AFM,P}$, is the difference in physical height. Generally, the height and lateral dimension of the $ZnTPPF_4$-SC_5SH clusters were widely distributed. Full histograms and statistical

analysis is provided in Appendix B. The mean and standard deviation are not adequate for asymmetric distributions thus Table 3 summarizes the location and spread of the distribution using the median and half of the interquartile range (IQR) of all imaged clusters. The time evolution of the clusters is statistical in nature and that the large spread in values implies that not all evolved in the same manner.

We can further use $\delta_{AFM,P}$ to estimate the orientation of the $ZnTPPF_4$-SC_5SH clusters, expressed as tilt angle, α of the $ZnTPPF_4$-SC_5SH long axis with respect to surface normal:

$$cos\,\alpha = \frac{\delta_{AFM,P}+1.4}{2.3} \qquad \text{(Equation 6)}$$

Where 1.4 nm and 2.3 nm are the height of the C12[281] and the nominal length of the $ZnTPPF_4$-SC_5SH thiol derivative respectively. The tilt angles derived from Equation 6 are given in Table 3. The $ZnTPPF_4$-SC_5SH clusters are at an angle of approximately 41-45° with respect to the surface normal, which is reasonable compared to a tilt angle of approximately 30° for alkyl thiols on Au(111).

The lateral dimension of the $ZnTPPF_4$-SC_5SH clusters was determined by STM due to superior lateral resolution. The distribution was rather broad but there is a trend of 30-60% *reduction* in the lateral cluster dimension after prolonged immersion time (Figure 42 in Appendix B). A rough estimate for the number of $ZnTPPF_4$-SC_5SH molecules per cluster is made using the 1.6 nm diameter of a $ZnTPPF_4$-SC_5SH and 0.6 nm as the distance between pi-stacked porphyrins.[19] Thus the minimal cluster size of 1-2 nm is most likely a single $ZnTPPF_4$-SC_5SH and the large clusters, 10 nm in lateral

Immersion Time	(Days)	1	3	5
AFM Height	(nm)	0.24 ± 0.04	0.30 ± 0.06	0.31 ± 0.05
Tilt Angle[b]	(Degree)	44.6 ± 1.5	42.6 ± 1.9	41.9 ± 1.7
Lateral Dimension	(nm)	5.2 ± 1.9	3.5 ± 1.6	3.3 ± 1. 7
STM App. Height	(nm)	0.62 ± 0.3	1.04 ± 0.6	0.45 ± 0.2
Apparent height ratio[c]	(Ratio)	0.38	0.74	0.14

Table 3. Statistics on cluster morphology[a]. A) Values are the median of the distribution and error is half of the interquartile range (25 to 75% of the population); B) Relative to the surface normal; computed by Equation 1 C) Computed according to Equation 1, with median values of physical and apparent heights.

dimension (approximately 100 nm^2), can contain a range of 30 loosely packed to 120 tightly packed $ZnTPPF_4$-SC_5SH molecules. The trend of reducing cluster size with immersion time is opposed to what we observed with the pyridyl Zn porphyrin derivative, where the size of the inserted clusters increased considerably from approximately 5 nm for one day to 3 nm on average for three and five days.[276] The difference in the self-organization is attributed primarily to the lack of Zn metalloporphyrin coordination by the pyridyl groups on neighboring molecules in the cluster. Other differences between the $ZnTPPF_4$-SC_5SH clusters presented herein and the previously reported pyridyl Zn porphyrin derivative include the 10x lower concentration of $ZnTPPF_4$-SC_5SH molecules in the immersion solution to limit aggregation in solution as well as the negation of pyridine additives in the $ZnTPPF_4$-SC_5SH immersion solution. Pyridine had been added previously in the pyridyl Zn porphyrin derivative solution and acted to stabilize the porphyrin clusters allowing for molecular resolved STM images.[19]

Considering the large amount of $ZnTPPF_4$-SC_5SH molecules in the immersion solution compared to the lack of C12, one would expect continued exchange between desorbed C12 and adsorbed porphyrin to cause a gradual increase in the cluster size with immersion time, as opposed to the observed size reduction. It is suggested that the size reduction observed from one to five days originates from reorganization of $ZnTPPF_4$-SC_5SH molecules within individual clusters. Despite their strong surface binding, adsorbed thiols diffuse on Au surfaces quite easily and the Au surface atoms diffuse to relax lattice strain.[282] Reducing the intermolecular distance might be driven by pi-stacking between the aromatic macrocycles, which results in ≤ 0.5 nm distances between the mean planes. Considering that it takes approximately 24 hours for flexible alkyl-thiols to achieve their optimal surface organization, it is probable that it would take three to times longer for rigid and more bulky $ZnTPPF_4$-SC_5SH to reach organizational equilibrium.

Furthermore, subtle changes are also observed in the C12 SAM in the vicinity of the $ZnTPPF_4$-SC_5SH clusters with immersion time. Any morphological change in the C12 is important because the C12 stabilizes the standing-up orientation of the ZnTPPF4-SC5SH molecules and any change in the C12 is likely to affect the $ZnTPPF_4$-SC_5SH clusters through a change in nearest-neighbor interactions.[256] The subtle changes observed here is that C12 desorbs from the sample surface and since the mixed monolayer is immersed in a solution with a lack of C12, there is no exchange as is typical in a solution with sufficient concentration,[283] but a depletion of the C12 SAM from the surface. An indication of C12 depletion is shown in the STM image featuring a

particular $ZnTPPF_4$-SC_5SH cluster formed after immersion of five days (Figure 10). A lying-down, striped phase emerges in the C12 surrounding this $ZnTPPF_4$-SC_5SH cluster. The lying-down, striped phase is formed with a lower density of alkanethiols on the surface than the high density standing-up phase.[284] Evidence of the C12 standing-up phase surrounding the $ZnTPPF_4$-SC_5SH cluster shown in the one day and three day image is not apparent and the emergence of the striped-phase is also not completely clear. This is because the STM tip used to obtain stable, repeatable I-V spectra is generally blunt and usually does not allow or only allows limited simultaneous molecular level resolution. To clarify the C12 organization in the vicinity of the $ZnTPPF_4$-SC_5SH clusters used in the I-V analyses presented herein, Figure 11 shows typical images, where both reasonable resolution and I-V spectra were achieved. After one day immersion, the C12 appears to be in the densely-packed, standing-up orientation while after three days immersion the development of some low-density, lying-down phase appears and is further developed after five days immersion.

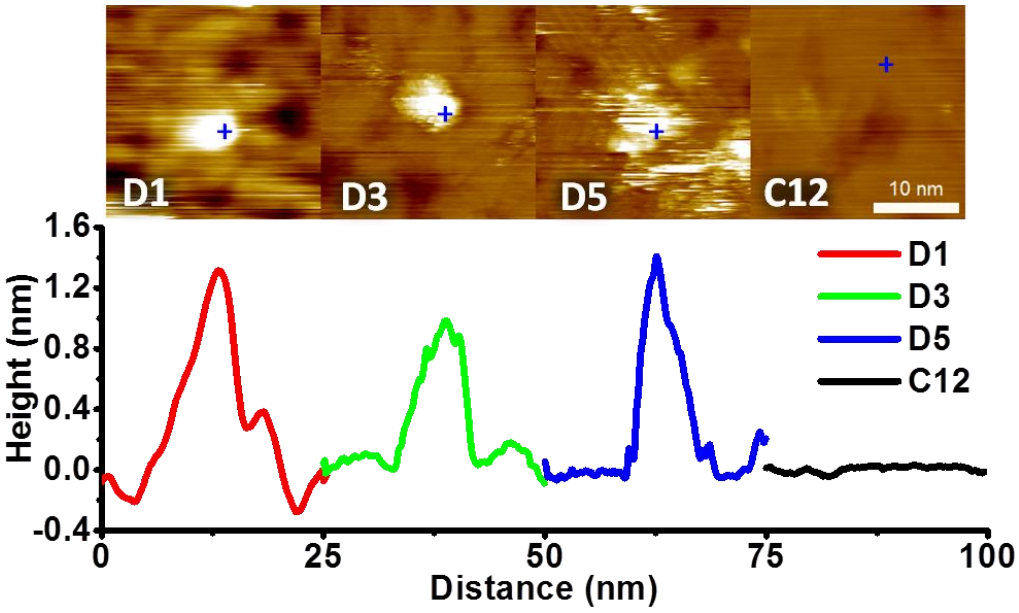

Figure 10. STM topography, showing a 25x25 nm images (top), and corresponding line profiles (bottom) of selected $ZnTPPF_4$-SC_5SH clusters, showing from left to right, clusters from one, three, and five days in addition to the neat C12 matrix. Blue crosses indicate the approximate (due to drift) locations where I-V scans were recorded.

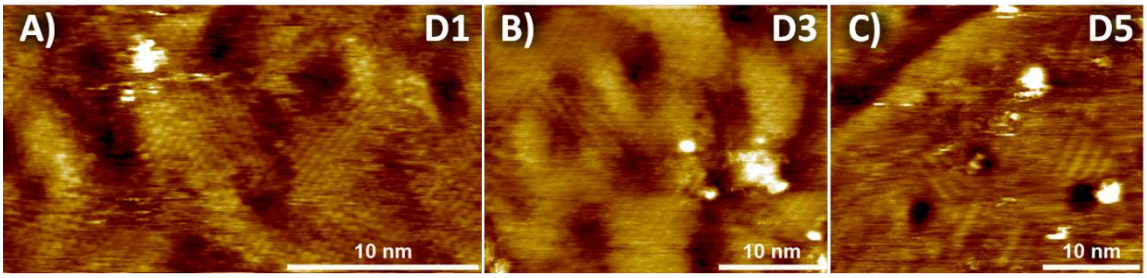

Figure 11. Typical STM topography images of the C12 SAM quality surrounding the $ZnTPPF_4$-SC_5SH clusters. STS on these particular $ZnTPPF_4$-SC_5SH clusters have been included in the intensity maps shown in Figure 12 as well as in the statistical data treatment. A) The C12 monolayer after one day immersion in the $ZnTPPF_4$-SC_5SH solution appears to be well-ordered in the vicinity of the $ZnTPPF_4$-SC_5SH clusters. However evidence of SAM degradation appears after B) three days immersion and even more so after C) five days immersion with the emergence of a striped or laying down phase.

3.3.2 Variation in Conductivity with Reorganization Time

Overall, Table 3 indicates that increasing the immersion time has a little effect on the physical dimensions of the ZnTPPF$_4$-SC$_5$SH clusters. In contrast, the STM apparent height changes markedly by 0.4 nm upon increasing immersion time from one to three days, which is similar to values reported for stochastic switching of OPE molecular clusters.[258] The scheme in Figure 9 illustrates that the apparent STM height, $\delta h_{STM,P}$, is the sum of the physical height difference, $\delta h_{AFM,C12}$, and a variation in the vacuum gap to compensate for changes in the conductivity of ZnTPPF$_4$-SC$_5$SH clusters compared to that of the surrounding C12 matrix, to maintain the set point current. The range in apparent height values is the greatest for the clusters after three days immersion, and the range narrows after five days immersion. After five days, the apparent height is the smallest, indicating the conductance is "switched-off" in these clusters. The change in apparent height can be used to quantify the relative conductance the apparent height ratio of the of the ZnTPPF$_4$-SC$_5$SH clusters, Δh_P, to the surrounding matrix, Δh_{C12}:

$$\frac{\Delta h_P}{\Delta h_{C12}} = \frac{\delta h_{STM,P} - \delta h_{AFM,P}}{\delta h_{STM,C12} - \delta h_{AFM,C12}} = \delta h_{STM,P} - \delta h_{AFM,P} \qquad \text{(Equation 1)}$$

where $\delta h_{STM,P}$ is the apparent porphyrin height extracted from STM measured with respect to the C12 SAM and $\delta h_{AFM,P}$ is the physical porphyrin height extracted from STM measured with respect to the C12 SAM. The denominator $\delta h_{STM,C12} - \delta h_{AFM,C12}$ is normalized to one since the porphyrin height is always measured with respect to the C12 SAM (Table 3). The full data set of the apparent height ratio as a function of immersion time is shown in the Figure 40 in Appendix B. In general, the apparent height

ratio increase for increasing lateral cluster dimension as was described in Chapter II, but the spread in the apparent height ratio with lateral cluster dimensions is large and becomes larger as the lateral cluster dimension increases suggesting that lateral dimension is not the solitary factor impacting the electronic properties. As the lateral cluster dimension increases, the possibilities of internal porphyrin organization within a particular cluster increases as well which is likely to be the origin of the large spread with larger lateral cluster dimensions. To interrogate this possibility, the electronic properties of clusters formed over different immersion times with approximately similar lateral dimensions were investigated.

3.3.3 Current–Voltage Intensity Maps

We focus on three $ZnTPPF_4$-SC_5SH clusters, formed after one, three, and five days of approximately similar lateral dimension, and one on a neat C12 monolayer (Figure 10). As summarized in Table 3 the $ZnTPPF_4$-SC_5SH clusters appear similar however, their current-voltage spectroscopy (I-V) differs markedly. The lateral dimensions of the clusters are not a priori representative of the general population, and the $ZnTPPF_4$-SC_5SH clusters chosen for spectroscopy where amongst the wide-end of the population. To manage the large variance in the measured I-V, we show intensity maps in Figure 13 of 100 successive scans recorded over the specific $ZnTPPF_4$-SC_5SH clusters shown in Figure 10. The intensity I-V map over a neat C12 monolayer is also shown for comparison. The pure C12 matrix also included a low density of apparent low-contrast C12 islands. I-V scans were taken both over background and C12 “islands” and were identical. Figure 12 reveals a prominent change in the transport characteristic

solely as a function of immersion time and consequently, reorganization of the mixed monolayer.

Transport across a $ZnTPPF_4$-SC_5SH cluster grown for one day is qualitatively similar to the neat C12. Both I-V intensity maps have a narrow data distribution and are continuous across zero bias. In contrast, transport across a $ZnTPPF_4$-SC_5SH cluster, grown for three and five days results in drastically different I-V intensity maps. The data has a wide distribution containing current variations of orders of magnitude (note the semi log-scale of Figure 12). There is a more understated, but meaningful, difference in the transport between the $ZnTPPF_4$-SC_5SH cluster grown for three and five days. For the three day cluster, the I-V intensity map has a conductance gap at low bias indicating bias-induced switching, while for the five day cluster the I-V intensity map has a narrower conductance gap and the widest data distribution indicating stochastic switching (Figure 12).

There is a gradual increase in maximum current between the four samples. The maximum current does not exceed 100 pA for the neat C12 and the one day cluster, while there is a considerable increase in the maximum current reaching 1 nA for the three day cluster, and an even further increase for the five day cluster, often reaching the compliance limit of the current amplifier (3 nA). Rather than the current maximum simply increasing for the three and five day clusters, the number of current data counts becomes more intense in the low current range (< 1pA) suggesting conductivity switching.

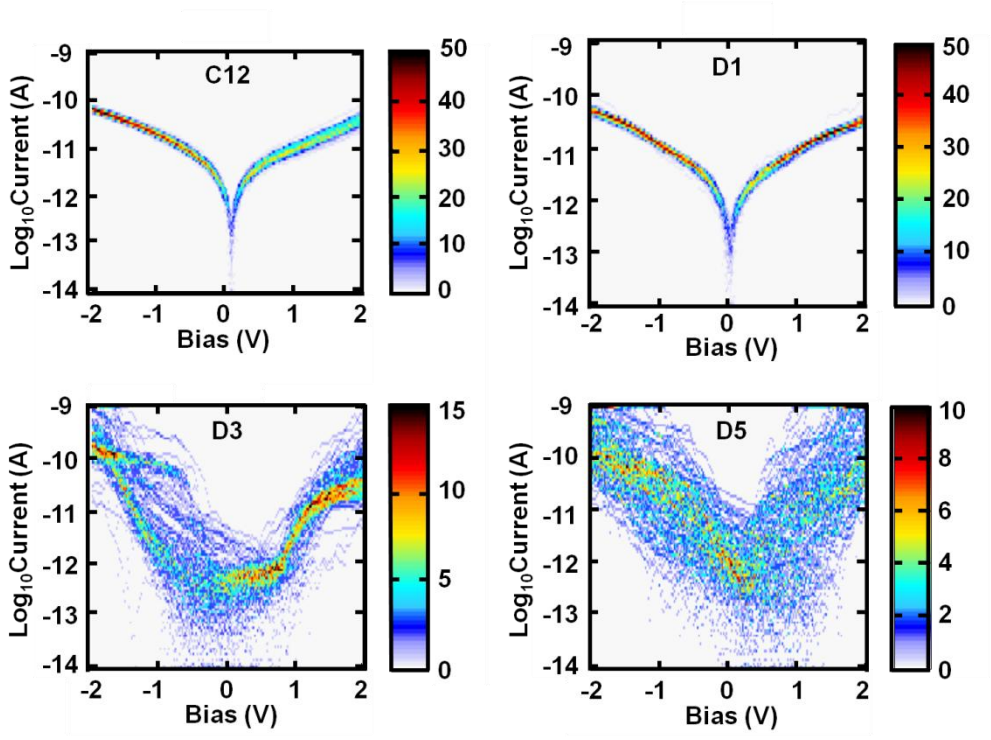

Figure 12. Current intensity maps for neat C12 matrix (C12), $ZnTPPF_4$-SC_5SH clusters after one day (D1), three days (D3) and five days (D5) on a semi-log scale against the applied bias. The color scale represents the recorded counts out of 100 replicas (note the different color scale bars for top and bottom plots).

3.3.4 Characteristic I-V Curves

To illustrate the observed trend in Figure 12, typical I-V curves are shown in Figure 13 Because of the large variance within consecutively measured I-V curves, especially for the longer immersion times, it is challenging to select a single, "representative" curve. To do this the I-V curve nearest to the median was chosen to be the "representative" rather than the average. The median eliminates the effect of outliers and answers the need to average both over log-normal distribution at high bias[285] and noisy, varying polarity near low bias. Different approaches to define a "representative"

curve are described in Appendix B. The single cubic polynomial fits of the clusters for the one day cluster and the neat C12 (continuous lines in Figure 13) indicates a generic, single tunneling mechanism[286] over the entire ±2V bias range. In contrast, the I-V curves recorded over the three and five day clusters could not be generally fitted to a polynomial relation, except over a limited range near zero bias (see green and blue lines in Figure 13). Thus, what appears to be a conductance gap in the I-V intensity maps shown in Figure 12 is actually an onset of an additional transport channel.

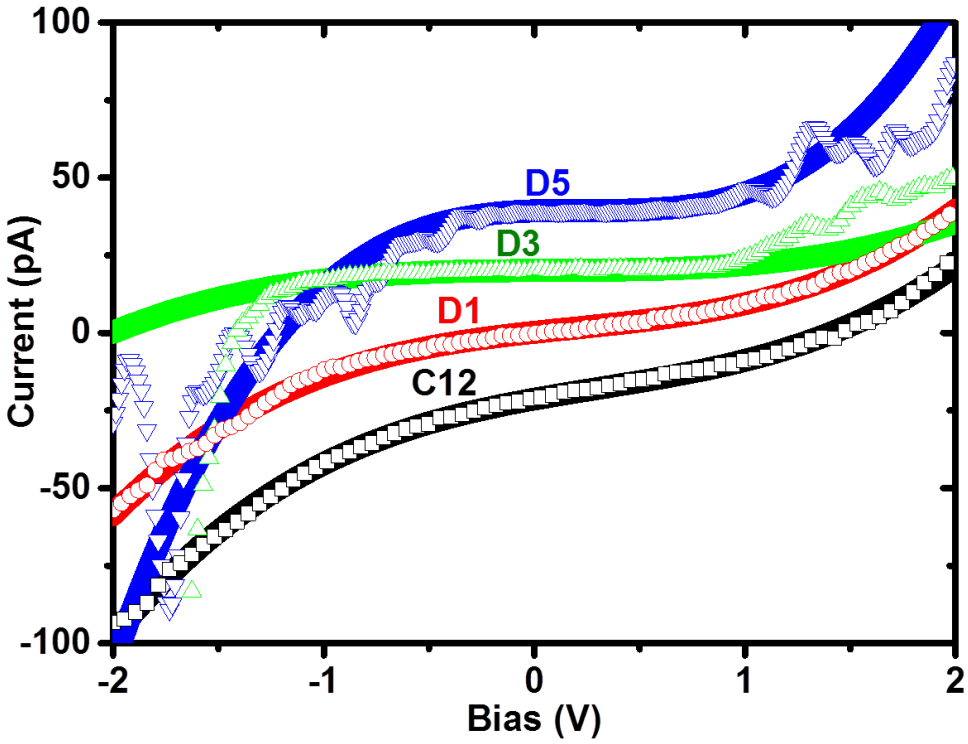

Figure 13. I-V curves for the different equilibration times and the C12 matrix that is nearest to the median. The symbols are the data and the solid lines are fits to a third order polynomial relation. Curves are shifted vertically (by 20 pA each) for clarity.

The additional, high-bias conductance channel behaves differently for the three and five day clusters. For the three day cluster, the second channel is characterized by a huge conductance onset, above approximately ±1V, or a *bias-induced switching* of conductivity. For the five day cluster, the onset occurs at lower bias (< 1V) but leads to a rather noisy conductance of moderate magnitude. This noisy I-V curve in Figure 13 qualitatively agrees with the wide intensity spread in Figure 12. In particular, this noise is not simply between consecutive scans but also within each individual scan. Both observations point to *stochastic switching* of conductivity. Stochastic switching was also observed as a function of imaging time and STM set-point (Figure 44 in Appendix B).

3.3.5 Statistics Quantifying Bias-Induced and Stochastic Switching

Overall, Figure 12 and Figure 13 indicate that prolonged assembly of $ZnTPPF_4$-SC_5SH clusters within the C12 matrix induces both bias-induced switching (conductance onset) and stochastic switching (noise). Ideally we would like to extend the qualitative observations of Figure 12 and Figure 13 over all measured clusters and this requires defining quantitative parameters to compare between data sets. Among a large variety of optional quantification approaches, three parameters were deemed appropriate since they contain the essence of the above qualitative observation. Two parameters are used to quantify bias-induced switching and one parameter is used to quantify stochastic switching.

3.3.5.1 Quantifying Bias-Induced Switching

The concept of bias-induced switching is represented by two possible parameters: 1) the fraction of noise-level current and 2) the onset of high-conductance.

The noise level is set to a value of 0.5 pA based on the observed noise in measured current (i.e. 2.5% of the set-point current and 0.02% of the amplifier saturation). For convenience, the current count below the noise level is expressed as an "effective bias gap" (V_{noise}) by multiplying with the bias interval (δV = 13.3 mV):

$$V_{noise} = \delta V \cdot [\sum_{all\,V}(|I| < 5 \cdot 10^{-13}) - 1] \quad (8)$$

where the square brackets term is the sum of intervals. Equation 8 is approximated because it does not differentiate between a continuous low state and stochastic turn-offs, and cannot account for differences in tip-sample distance. The advantages of the V_{noise} approach are directness and simplicity. We have extracted V_{noise} for all measured I-V sets over all measured clusters (cf. specific clusters in Figure 10) and the distribution in this parameter for the different samples is shown in Figure 14(A). Figure 14 confirms the evolution of low-conductance region with assembly time. The mean effective noise-region is 0.09 V for C12 and double for one day ZnTPPF$_4$-SC$_5$SH clusters. Further increasing the immersion time considerably increases the noise region up to 0.54 V on average for the five day clusters. The width of the distribution also increases considerably with immersion time. The extension of the low current region for five day clusters is in accordance with the trend of lower STM height for the longest immersion time (Table 3).

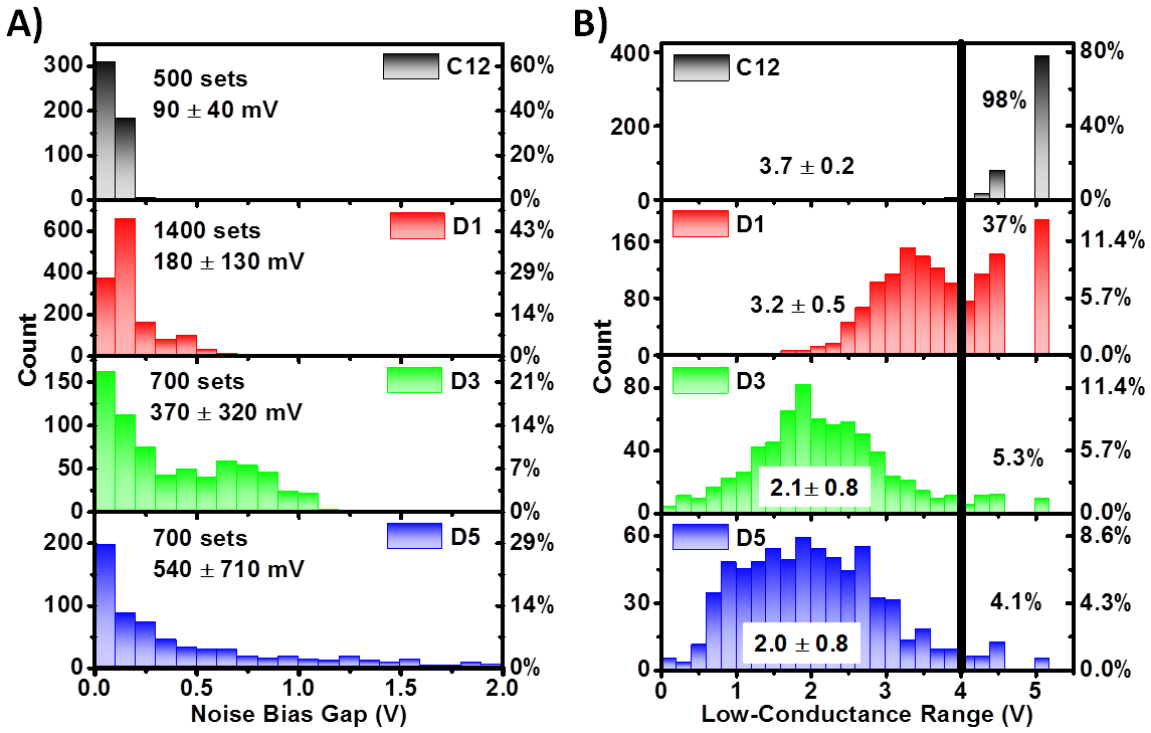

Figure 14. Histograms of the two parameters used to quantify bias-induced switching. A) Noise gap histograms for all measured I-V sets. The x-axis shows the effective gap width, computed by Equation 8 with an absolute threshold value of $|I| \leq 0.5$ pA. The left y-axis is the net counts of I-V sets and the right y-axis is the percentage. B) Histograms of low-conductance range, determined as the difference between the positive and negative onset bias, where the numerical conductance exceeds 10 times its value near zero V (Equation 9). The left y-axis is the absolute counts of I-V sets and the right y-axis is the percentage. A range of 4 V (vertical line) is the full bias scan; any value larger than this indicates that at least over one polarity all conductance points are $< 10 \cdot G_{Eq}$ and an arbitrary onset value of ±2.5 V is designated.

To obtain a cleaner separation between the bias-induced and stochastic switching, a parameter that is more specific to the bias effect on the shape of the I-V curves, rather than the magnitude, is defined. The onset of a second transport channel is identified by a relative increase in conductance. The conductance was computed

numerically ($\frac{dI}{dV}$, after smoothing) and the onset bias (V_P, V_N) was set to a bias where the derivative exceeds an arbitrarily threshold of 10 folds of its ~ 0 V value (G_{Eq}):

$$V_{P(N)} = \text{lowest (highest) bias where } \frac{dI}{dV} \geq 10 \cdot G_{Eq} \qquad \text{(Equation 9)}$$

The equilibrium conductance, G_{Eq} near 0 V is the mean of the numerical conductance for the four values nearest to 0 V (i.e., at V = ± 7 mV, ± 20 mV). Histograms of G_{Eq} are shown in Figure 43 in Appendix B. Within this view, the tunneling range (V_{tunn}) is the bias range where the conductance is smaller than tenfold its value near zero V ($G_{Eq} \approx$ minimum value) or the difference between the positive and negative onsets:

$$V_{tunn} = V_P - V_N \qquad \text{(Equation 10)}$$

In cases where none of the $\frac{dI}{dV}$ values exceed $10G_{Eq}$, the value of $V_{N(P)}$ is set to ±2.5 V making it distinctly different than the measured range of ±2 V.

As above, the values of V_{tunn} were extracted for all measured I-V sets and shown as histograms in Figure 14(B). It shows that 78% of the neat C12 I-V curves had no onset of high conductance at either positive or negative bias (i.e. V_{tunn} = 5 V) and only 2% of the curves reached $10G_{Eq}$ on both polarities. Onset of high conductance was much more frequent for $ZnTPPF_4$-SC_5SH clusters and 2/3 of the curves showed a conductance onset on both bias polarities. Increasing the immersion time to three and five days reduces the gap to approximately 2 V or onsets at approximately ±1 V. The mean of the distribution was similar for both three and a five day clusters, however, the distribution of the five day clusters' low-conductance range is flatter (less Gaussian) and wider than

that of the three day clusters', due to enhanced stochastic switching for longer immersion times.

Comparing Figure 14(A) and Figure 14(B), the neat C12 has the smallest noise range, V_{noise} but the largest tunneling range, V_{tunn} This is because of the nature of the STM measurement. The conductivity of C12 has a moderate variation with bias and therefore setting the STM tip height at 1.4 V is sufficiently close to the substrate to measure a non-noise current over almost the full range. However, for the long-immersed $ZnTPPF_4$-SC_5SH clusters, the second transport channel induces a huge dynamic range of transport. The tip-sample distance in these samples is set at a bias where the second conductance channel is most often active, mandating a large vacuum gap. Therefore, sensitivity is lost toward the low end of the dynamic conductance range and the tunneling regime appears as a noise regime. This trend is apparent also from the lower G_{Eq} values obtained for longer immersion time (Figure 43 in Appendix B).

Other methods were pursed to describe the bias effect on the shape of the I-V curves with inadequate results. Transition voltage spectroscopy[3, 286] yielded widely spread values with weak correlation to immersion time. Figure 13 shows that the C12 and the one day I-V curves can be fitted to a cubic polynomial, but no such single polynomial could be fitted for the I-V curves of the longer immersion times. Technically it is possible to fit the I-V curves to a sum of two polynomials, representing additional tunneling channels, but such an approach inflates the amount of free fitting parameters and is time consuming.

3.3.5.2 Quantifying Stochastic Switching

Parameters 1) and 2) have been used to quantify bias-induced switching and now the concept of stochastic switching is quantified by parameter 3) describing the ratio between the measured current and nominal set-point current. Using a single parameter is challenging because the magnitude of the current depends on the height of the STM tip; which is set arbitrarily to yield a certain set-point value. For example, in our measurement procedure the height of the STM tip was re-adjusted before each I-V scan to yield a current of 20 pA at a bias of +1.4 V, and then the bias was swept from -2 V to +2 V over approximately 40 ms (Appendix D). The time between turning-off the feedback loop and scanning the bias back to 1.4 V is approximately 35 ms; if any stochastic switching occurred during this time interval the current re-measured at 1.4 V would differ from the set-point of 20 pA. Therefore we define the set-point ratio, P_{sp} as:

$$P_{sp} = \frac{I(1.4V)}{20pA} \qquad \text{(Equation 11)}$$

Following the evolution in P_{sp} for 100 consecutive sets reveals no trend (Figure 44 in Appendix B), namely the time evolution of this noise or stochastic switching is completely random. As above, we further apply this analysis over all measured I-V sets, and summarize the results as a histogram in Figure 15, where the x-axis is the $log_{10}(P_{sp})$. In all four cases the histograms are centered at zero which is the stable or non-switching case (P_{sp} = 1). However, the distribution in P_{sp} becomes much wider for three day clusters and reaches even three orders of magnitudes for five day clusters. The reasonable uniformity in P_{sp} of the neat C12 and the one day clusters confirms that the noise is a true molecular feature and not a measurement artifact. The trend in Figure 15

agrees well with the qualitative observation of the large spread in the I-V intensity maps (Figure 12) for the three and five day clusters.

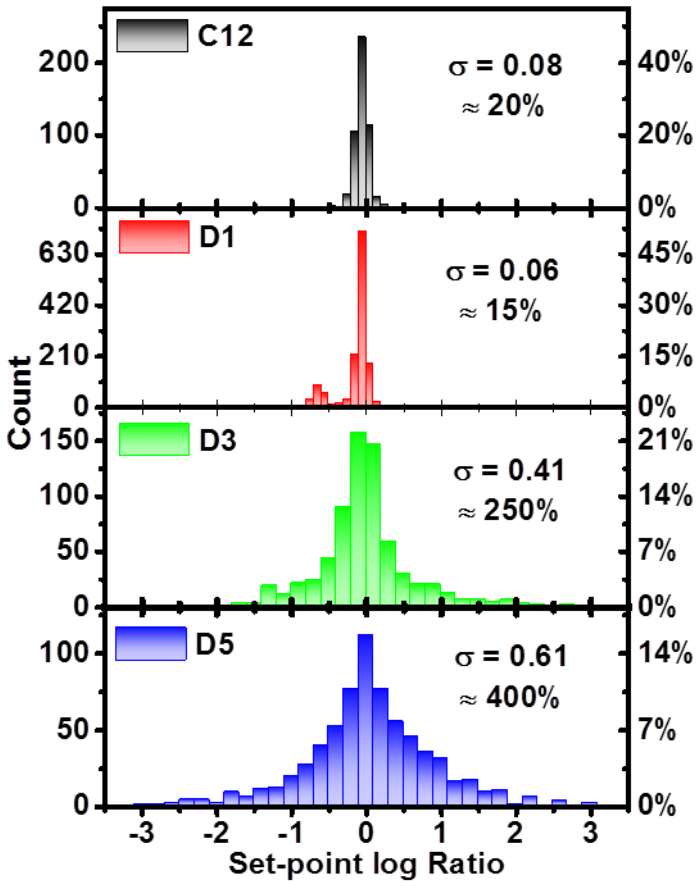

Figure 15. Histograms of the parameter used to quantify stochastic switching; the ratio between measured current and nominal set-point current for all measured P_{sp} data, see Equation 11. Log_{10} of this ratio is used as the bins axis.

Finally, the observed distribution in the extracted parameters (Figure 14 and Figure 15) is not due to cluster to cluster variation, but occurs within each individual cluster or measurement set. This is demonstrated by averaging the 100 values V_{tunn} of extracted for a given cluster and plotting them against the lateral dimension of the cluster

(Figure 16(A)) extracted from STM topography images (Table 3 and Figure 11). Figure 16(A) shows a clear difference in the tunneling gap between the one day clusters and the three-five day clusters. However, the standard variation within each cluster is similar or larger than the difference between clusters of the same immersion time. Figure 16(B) tests this concept for the variance in the stochastic current ratio, P_{sp} within each location. Also here, there is a clear trend in increasing stochastic variance, but no trend with the lateral cluster dimension. The lateral cluster dimension used in Figure 10 is specifically determined for the clusters where the I-V spectroscopy was performed, in contrast to Table 3 which refers to a much larger set of imaged clusters. The fact that both parameters (Figure 16) show no dependence on lateral cluster dimension provides strong evidence that the change in transport mechanism cannot be induced by a geometrical effect, and must originate in a more subtle structural change.

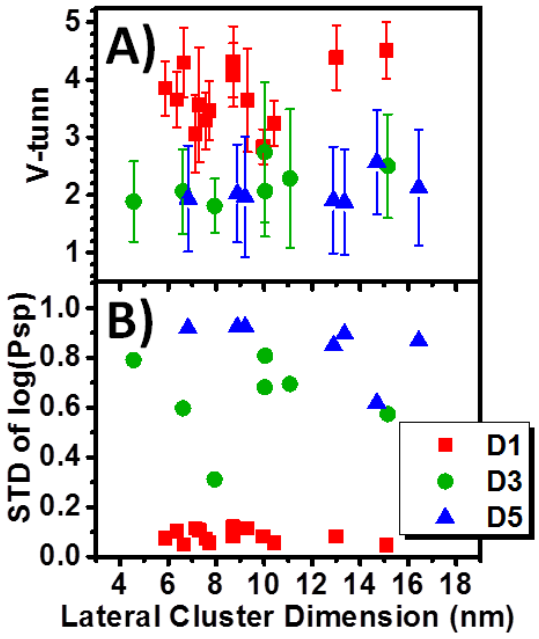

Figure 16. Averaged parameters as a function of lateral cluster dimension, showing A) the low-conductance range, V_{tunn} (Equation 10 and Figure 14) and B) the standard deviation of stochastic switching, $log_{10}(P_{sp})$ (Equation 11 and Figure 15). The measured lateral cluster dimension is larger than the average (Table 3) because we measured tunneling spectroscopy on larger clusters to minimize the tip drifting away from the $ZnTPPF_4$-SC_5SH clusters.

3.3.6 Discussion

Our statistical analyses shows that allowing the $ZnTPPF_4$-SC_5SH/ C12 SAM mixed monolayer an extended period of time to re-arrange, the net electrical conductivity of the $ZnTPPF_4$-SC_5SH molecules drastically changes (Table 3 and Figure 12) with emergence of both bias-induced (D3) and stochastic switching (D5). Bias-induced switching is clear after immersion for three days and then overruled by stochastic switching (Figure 12) for immersion after five days. On the other hand the structural changes in the mixed monolayer (Table 3 and Figure 11) are subtle and not easily discerned with room-temperature STM. The apparent trend is that the clusters

laterally squeeze to reduce in size and depletion of the C12 matrix with immersion time. A model to summarize our findings is presented in Figure 17.

3.3.6.1 Lateral Cluster Reduction and the Effect on Net Conductance

Increasing the immersion time from one day to three days squeezes the clusters by 1.7 nm on average (estimated 54% area reduction) and between three and five days there is less reduction in size; 0.2 nm on average (estimated 6% area reduction) further of the original (one day) cluster size. It seems improbable that the net amount of $ZnTPPF_4$-SC_5SH molecules is reduced by desorption against the high $ZnTPPF_4$-SC_5SH concentration in the immersion solution. A more probable explanation is slow surface diffusion reducing the net energy of the system. The two possible driving forces for slow surface diffusion are 1) improved pi-stacking of the aromatic macro-cycles and, 2) less likely strain relaxation of binding Au atoms. Improved pi-stacking is the most likely, but both possibilities are explored below.

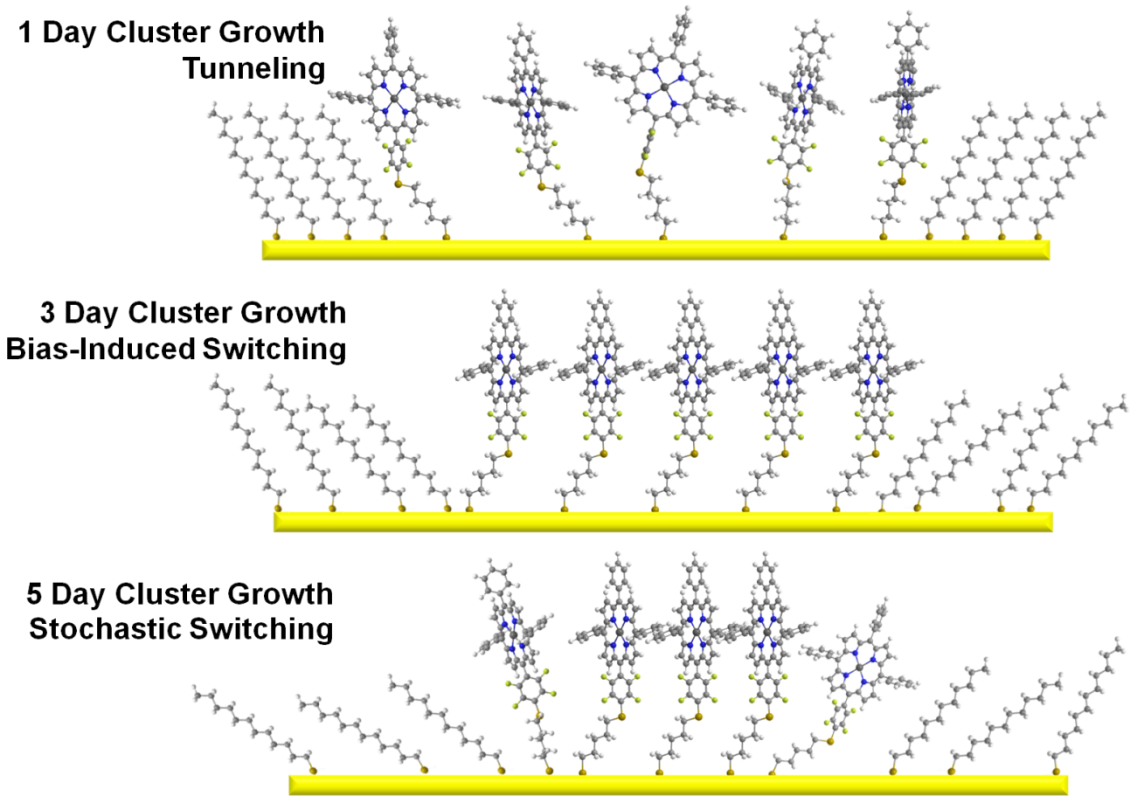

Figure 17. Model of the reorganization of the $ZnTPPF_4$-SC_5SH clusters formed after one, three, and five days. After one day, the clusters are fairly isolated from their neighbors while the clusters formed after three represent strong to medium inter-molecular interactions and finally after five days, due to the depletion of the surrounding C12, the clusters become more disordered and still interacting but not as uniformly as in the three day clusters.

The most probable mechanism that can account for reduction in cluster size and increased conductivity is improved pi-stacking that stabilizes the molecular energy levels or reduces the polaron formation energy. Dye molecules in general, and porphyrin derivatives specifically, are known to form aggregates in solutions, with drastic effect on photo-physical properties like absorption shifts and fluorescence quenching. Two-dimensional aggregation of porphyrins was specifically studied at the air-water interface

using Langmuir-Blodgett (LB) trough. For example, Miyake and coworkers compared LB films of Zn tetra pyridyl porphyrin (ZnTPyP) with or without Cd^{2+} ions in the trough's water (sub-phase).[194] The Cd^{2+} ions are coordinated between the pyridyl units and thus increase the area per monomer from 0.65 nm^2 to 1.9 nm^2 (i.e., a 66% area difference). Interestingly, the molecular tilt was approximately 30° from the surface normal, for both phases,[194] in a qualitative agreement with the lack of orientation change observed here (Table 3 and Figure 41 in Appendix B). The closely packed ZnTPyP LB film (0.65 nm^2) has a stronger red shift of the Soret band and very strong quenching of fluorescence compared to the loosely packed, $ZnTPyPCd^{2+}$, which behaved similar to the dilute solution.[194] A different LB experiment was done with free-base H_2TPP (methyl-phenyl) where one phenyl is tethered to a carboxylic acid. The nature of the tether was used to control the area per TPP from 0.87 nm^2 to 0.25 nm^2 (i.e., a change of 71% in area per porphyrin).[269] The red-shift of the Soret band increased linearly with the reduction of area per molecule.[269] In addition, the closer packing induced stronger quenching of fluorescence on an insulating substrate (quartz) and even further quenching on a semiconductor (SnO_2), indicating more efficient injection of the excited electron into the substrate. The effect of packing was so dramatic, that the electron injection was more efficient with a propyl tether than for directly-bound carboxylic acid, despite the longer tunneling distance, because the packing of the first was much closer.[269]

Based on these LB examples we deduce that the apparent reduction of $ZnTPPF_4$-SC_5SH cluster size with extended immersion time (Table 3) is well within reported values for LB films of similar porphyrins. Moreover, the LB experiments showed that

the aggregation driving force can be cancelled by, and therefore is comparable in magnitude to, other self-assembly forces like alkyl-chains flexibility[269] or metallic coordination.[194] Considering the slower diffusion on Au than on water (as in LB), the slow organization times observed herein are reasonable. Optical effects differ from charge transport since they are electrically neutral excited states. Still, they involve similar energy levels and charge propagation mechanism. Thus, the aggregation-induced red-shift in the Soret band implies a smaller HOMO-LUMO gap or smaller barrier for charge transport. Similarly, the stronger fluorescence quenching is due to more efficient spatial delocalization of the optically excited state. In principle, wider exciton delocalization should be similar to polaron delocalization as in charge transport.

In order to gain support for the pi-stacking explanation, it was attempted to induce stronger aggregation by increasing the concentration of $ZnTPPF_4$-SC_5SH in the immersion solution from 0.05 mM to 0.5 mM. The 10x higher concentration yielded over-crowding of $ZnTPPF_4$-SC_5SH clusters, and physical deposition (molecular clusters which are weakly-bound to the substrate and easily adsorbed onto the STM tip). About 30% of the $ZnTPPF_4$-SC_5SH clusters formed after one day in high-concentration $ZnTPPF_4$-SC_5SH showed I-V behavior very similar to that of aged clusters formed after three days in the low-concentration $ZnTPPF_4$-SC_5SH solution (Appendix B.2). The fact that increased solution concentration induces behavior similar to that achieved by slow surface cluster growth, suggests that the driving force for this process originates in molecular interactions rather than other mechanisms such as rearrangement of surface adatoms, which should not be affected by the solution concentration.

Although Maksymovych et al., have stressed the role of Au adatoms in dictating the fine structure of thiol monolayers on gold[282], strain relaxation of binding Au atoms seems to be a less likely mechanism to explain the one to five day evolution in morphology and net conductance. While the most stable conformer for alkyl thiols is a dimer of R-S-Au-S-R, where Au is a surface adatom, it is not clear if and how similar dimers are formed for bulkier molecules, as in our case.[282] It is possible that the prolonged immersion times (three to five days) allows for such a slow diffusion to occur toward stabilization of the adsorbed $ZnTPPF_4$-SC_5SH. The position of Au adatoms with respect to lattice and binding S is also used to explain large changes in the conductance of alkyl dithiols in single molecule STM break-junction experiments.[287] However, the three distinctly different conductance states of alkyl or biphenyl dithiols were attributed mostly to changes in the S-Au contact resistance without a marked difference in the barrier height for transport or the shape of the I-V curves,[288] which is inconsistent with the marked change in the shape of the I-V observed here. Therefore, the richness of transport evolution with immersion time reported herein is beyond a single adatom arrangement.

Thus we suggest that the one day clusters are composed of $ZnTPPF_4$-SC_5SH molecules that are fairly isolated from their neighbors while the three and five days clusters represent medium to strong inter-molecular interactions (Figure 17). Based on the change in lateral cluster dimensions (Table 3) and assuming that the $ZnTPPF_4$-SC_5SH in the clusters formed after three days are pi-stacked with a separation of 0.6 nm,[19] the $ZnTPPF_4$-SC_5SH separation after one day immersion is estimated to be 0.9 nm

which is larger than the typical van der Waals interaction length, supporting that after one day the $ZnTPPF_4$-SC_5SH molecules are fairly isolated. After five days of immersion, the $ZnTPPF_4$-SC_5SH separation is estimated to be 0.5 nm which is within the typical van der Waals interaction length and slightly smaller than the $ZnTPPF_4$-SC_5SH separation after three days immersion supporting that after three and five days immersion, the $ZnTPPF_4$-SC_5SH clusters have medium to strong inter-molecular interactions. Closer pi-stacking impacts the electronic properties by reducing the polarization energy, thereby opening a second conductance channel with an actual charging of the $ZnTPPF_4$-SC_5SH clusters formed after three and five days.

A phenomenon that has been related to polaron mediated transport is negative differential resistance (NDR).[289-290] Intriguingly, NDR was reported to emerge by much weaker, side-by-side interaction between flat-laying Rose Bengal in dimers and trimers, an effect that is explained by the creation of new pseudo energy levels by much weaker, interactions between the neighboring monomers.[291] While NDR or hysteresis was not specifically sought, Figure 13 shows that the three days sample is characterized by sharp conductance onsets, which is required for hysteresis. On the other hand, the five day I-V curve in Figure 13 shows multiple peaks, which can be viewed as ill-developed NDR. The absolute reproducibility of these noisy peaks in terms of bias (energy) and intensity was rather poor, but their abundance was a clear characteristic of the five day clusters; conductance noise was much weaker or none for the one to three day clusters.

It was suggested that both NDR and hysteresis originate in a redox event of charging of the molecular wire. If the charged state is long lived, as for e.g., isolated

molecule, it will appear as a stable switching or hysteresis, while the presence of an electrolyte will reduce the reorganization energy and increase the fluctuations of the charged state, which appears as NDR.[292] In analogy with this concept, and in view of the continues red-shift of the optical gap with aggregation,[269] we can attribute the evolution of the sharp conductance onset (three days) into multiple small peaks (five days) as a further reduction in the polaron energy for the five days clusters (e.g., by closer pi-stacking). The medium polaron energy of the three day is accessible by bias up to 2 V, but discharging is restricted. The even lower polaron energy of the five day clusters requires smaller onset bias (Figure 13 and Figure 14(A)) and is also less stable. The fluctuations in the charged state appear as multiple peaks in the I-V curves (Figure 13), large spreading of the intensity maps (Figure 12) and large distribution of the onset current (Figure 15).

3.3.6.2 Depletion of C12 SAM and the Effect on Net Conductance

Increasing the immersion time from one to five days influences the entire mixed monolayer and not simply the electro-active, guest molecule. Accordingly, the surrounding C12 monolayer depletes with immersion time and is consistent with other SAM morphology studies in organic solvents over an extended period of time.[283, 293] This depletion causes the C12 monolayer morphology to evolve from a densely-packed standing-up organization after one day, to the development of some less-dense lying down domains after three days, and to more prevalent lying down domains after five days (Figure 11). In this mixed monolayer system, the role of the C12 monolayer is to stabilize the $ZnTPPF_4$-SC_5SH clusters and since the morphology is evolving with

immersion time, it is likely that the interaction between the surrounding C12 and $ZnTPPF_4$-SC_5SH clusters is also evolving; providing less stabilization with immersion time leading to more $ZnTPPF_4$-SC_5SH conformational variations[294] within a particular cluster. Conformational variations in molecules[294-295], nanoclusters[296] and morphological changes of the background SAM in mixed monolayers[297-298] are known to impact the electronic characteristics. In particular guest molecules within a host SAM[256] similar to the $ZnTPPF_4$-SC_5SH clusters presented herein, was found to switch stochastically when the host SAM was disordered. Therefore, it is conjectured that the stochastic switching, dominant in the five day clusters (Figure 12), can originate from further squeezing of the $ZnTPPF_4$-SC_5SH clusters as discussed above accompanied by the depletion of the surrounding C12 monolayer after five days immersion.

3.4 Conclusion

The STM measured charge transport characteristics across $ZnTPPF_4$-SC_5SH clusters within a C12 monolayer changes drastically over an extended self-assembly time. The accompanying structural changes are rather minor and indicate for a surprising effect of an averaged 30% reduction in lateral cluster area with longer assembly times. Here, it is propose that slow aggregation of the adsorbed porphyrin derivatives explains the reduction in lateral cluster dimension and can account for the conductance evolution from tunneling (one day) to bias-switching (three days). In addition to in lateral cluster dimension, the morphology of the stabilizing C12 monolayer depletes and this becomes most apparent for the longest immersion time where the transport of the clusters are dominated by stochastic-switching (five days). Similar to the prominent effect of

aggregation on optical properties, it is highly probable that pi-stacking would affect transport across dye-molecules, even-though the charge transport direction is perpendicular to the stacking. The work presented herein suggests that few molecule clusters have drastically different conductance characteristics than single of identical chemistry and that it is not necessarily the size of the molecular cluster as was suggested before, but the organization and inter-molecular interactions within in the clusters.

CHAPTER IV

STUDIES OF THE STRUCTURE AND PHASE TRANSITIONS OF NANO-CONFINED PENTANEDITHIOL AND ITS APPLICATION IN DIRECTING HIERARCHICAL MOLECULAR ASSEMBLIES ON AU(111)*

4.1 Introduction

The idea of using molecules in electronic devices has been studied since the 1950s,[1-3, 299-300] and more specifically, since the seminal work of Aviram and Ratner on a molecule rectifier.[1] Molecular electronics is attractive because it offers low-cost, simultaneous production of numerous nanometer-sized "devices" that may be tuned in a facile manner through synthetic modification. Directing the assembly of such molecular devices into pre-designed integrated electronic circuits, while enforcing selectivity and hierarchy is an inherent challenge. It is perceived that organic synthesis could be used to tailor molecules for a host of electronic functions (switching, amplification, rectification, etc.). These expectations have since become more reserved as it has been shown that tuning chemical functionality in a molecular junction does not necessarily lead to a well-defined change in the charge transport characteristics of the junction, especially when the transport is limited to the tunneling regime.[147, 227-228] We have recently shown that

*Part of this chapter is reprinted from Pawlicki, A.; Avery, E.; Jurow, M.; Ewers, B.; Vilan, A.; Drain, C. M.; Batteas, J., Studies of the Structure and Phase Transitions of Nano-Confined Pentanedithiol and Its Application in Directing Hierarchical Molecular Assemblies on Au(111). J. Phys.-Cond. Matt. **2016**, *28* (9), 094013 with permission from IOPscience.

through the controlled assembly of nanoscale islands of molecules, this can be overcome,[19, 147] as nearest-neighbor interactions within assemblies of molecules can strongly affect transport across molecular junctions, making it possible to recover effects of chemical functionality in tuning charge transport.[19, 146]

As part of our ongoing work on the relation between chemical structure and charge transport characteristics of molecules at interfaces, we have previously examined the transport properties of porphryin-thiols on Au.[19-20] Charge transfer through the length of this molecule is achieved by bracing it upward with a dodecanethiol (C12) self-assembled monolayer, producing a mixed monolayer. An interesting behavior was observed when the porphryin-thiols were driven to aggregate on the surface by pi-stacking, whereby a seemingly size dependent change in the charge transport characteristics occurred, with single and few molecule clusters demonstrating tunneling dominated charge transport, while large clusters (>5 nm in diameter) transitioned to transport characteristic of a "hopping" mechanism.[19] These results indicate that the structure-function relationship goes beyond consideration of the chemical structure of a molecule to include interactions with neighbors, the dimensions of aggregates that may form, and the internal architecture of these aggregates. Reliability in function and behavior therefore depends on control over the configuration of molecules on the electrode surface, and as molecular complexity increases, this becomes a greater challenge. To systematically study the influence of these variables, control over the formation of aggregates, their architectures, and their dimensions, is crucial. In this work we seek to address these challenges using our model porphyrin system.

To establish control of the insertion process, we initially sought to nanograft the porphyrin- thiol molecules directly into the alkanethiol film. Nanografting is one of several scanning probe lithography methods[301] where an AFM tip is used to selectively displace a pre-formed SAM in the presence of another molecule which immediately binds to the newly exposed Au surface. This technique has successfully been applied in the attachment of a variety of molecular species, most commonly studied has been the replacement of one alkanethiol with another of different length or termination,[302] but can be extended to patterned placement of proteins[303] and other complex molecules on surfaces.[304-305] Unfortunately, this approach was not successful, largely because our porphyrin molecule of interest was simply not soluble in solvent routinely compatible with the nanografting process, which generally requires low vapor pressure solvents that are equipment compatible (i.e. water and alcohols). This is not a problem unique to porphyrins, but rather molecules that might be of interest for charge storage and transport at interfaces very often bear functionalities that render them soluble in highly nonpolar organic solvents.[272, 306-307]

To overcome this challenge, here we have sought to leverage the click-chemistry employed in the synthesis of our tethered porphyrin,[9, 20] specifically the attachment of the dithiol tether to the porphyrin macrocycle (Figure 18). The mild conditions and absence of any highly reactive reagents required to attach the dithiol suggest that such a reaction would be suitable for surface film modification, and dithiols are much more amenable to techniques like nanografting.[308] More specifically, we have sought to determine if this click-chemical reaction would be a suitable alternative for direct

covalent attachment of the thiol-tethered porphyrin molecule to the surface, and subsequently if nanografting could be employed to direct, or template, the assembly of the porphyrins on the surface in predetermined geometries, thereby facilitating systematic evaluation of how nearest-neighbor interactions and aggregate formation influence charge transport through these molecules.

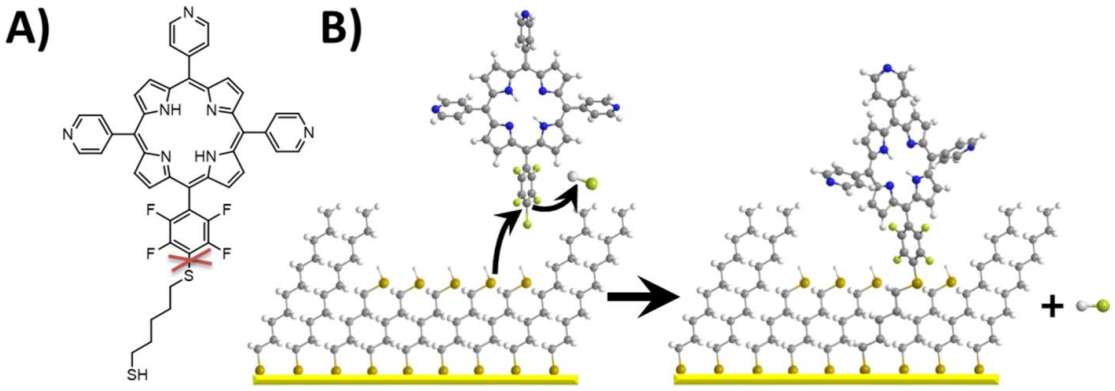

Figure 18. A schematic of the functionalization approach used in this work for the porphyrin molecule (A) that has been used in prior studies. Herein, we consider the molecule in its constituent parts, demarcated by the red 'X'. By first functionalizing the surface with the alkanedithiol, the attachment of the porphyrin to the surface can be directed to form aggregates of specific geometry and dimension.

To evaluate the viability of the dithiol linkage reaction conducted at the surface, we have employed co-adsorption of dithiol, 1,5-pentanedithiol (C5DT) and dodecanethiol (C12) to create domains of C5DT. Subsequent reaction of the C5DT with 5,10,15-tris(4'-pyridyl)-20-2,3,4,5,6-pentaflourophenyl) porphyrin (TPPF5) would then effectively produce the same molecule that we have considered in previous studies.[19-20] We begin by first characterizing the C5DT domains formed by co-adsorption as well as

nanografting by Atomic Force Microscopy (AFM) and Scanning Tunneling Microscopy (STM) to verify their structural characteristics and molecular scale order. Interestingly, this allowed for characterization of the molecular structure of the C5DT domains in great detail showing that domain size is strongly influenced the local structure (phase) of the C5DT whose local packing density was dramatically impacted by the interactions between the C5DT and C12 at the domain boundaries. The results of which will be discussed in detail below. Following detailed characterization of the C5DT linker group, attachment of TPPF5 via a click-reaction was conducted and verified, to demonstrate the ability of this approach to create hierarchical assemblies of porphyrin-thiols on Au. This two-step assembly process, prepares the means for further studies of the transport properties of these assemblies, and demonstrates this as a general approach for attaching complex molecules to surfaces in a directed fashion.

4.2 Experimental Methods

4.2.1 Synthesis of the Porphyrin Compound

5,10,15-tris(4'-pyridyl)-20-2,3,4,5,6-pentaflourophenyl) porphyrin (TPPF5) was synthesized using a previously published method[20] but was limited to the first step; synthesizing the macrocycle. Here the second step, attachment to a thiol tether, was done on the surface as described below.

4.2.2 Formation of Mixed Monolayers of Pentanedithiol and Dodecanethiol by Co-absorption

All monolayers were prepared on 200 nm thick, flame annealed, Au(111) films on mica (Phasis, Geneva, Switzerland). Before SAM formation, the Au(111) samples

were then placed under UV/Ozone for 10 minutes, followed by an ultrapure water rinse (18.2 MΩ·cm) (NANOpure Diamond, Barnstead), an ethanol rinse, and immediate drying with streaming nitrogen. The process was then repeated with only 5 minutes of UV/Ozone. To form islands of 1,5-pentanedithiol (C5DT) (Aldrich, 96%) in a matrix of dodecanethiol (C12) (Aldrich, 98%) by co-absorption, the Au(111) films were immersed in ethanol with 10:1 mM ratio of C5DT to C12 for 24 hours at room temperature.

4.2.3 In Situ Attachment of TPPF5 to Surface Bound C5DT

SAMs containing both C5DT and C12, prepared by either co-adsorption or nanografting, were then subjected to TPPF5 for attachment. The monolayers were immersed in a 1 mM solution of TPPF5 in dichloromethane, chloroform, methanol, and diethylamine (4:4:1:0.001 v/v) at room temperature. After immersion, all samples were rinsed with dichloromethane before examination by AFM and/or STM. The co-absorbed samples were immersed in the TPPF5 solution for three hours. The nanografted samples were immersed for three (3) to twenty-one (21) hours. Between each immersion interval, the same nanografted features were imaged by AFM to monitor the assembly of the TPPF5 islands.

4.2.4 Scanning Tunneling Microscopy (STM)

High resolution STM images and scanning tunneling spectroscopy (STS) data were acquired using an Omicron UHV-XA STM system with a base pressure of $< 3\times10^{-10}$ mbar. The STM tips were mechanically cut using Pt/Ir (80/20) wire. Images were obtained at 20 pA and 1.4 V. For the purposes of investigating the effect of bias on reacted TPPF5 islands, STS was collected on the reacted TPPF5 islands as well as the

surrounding C12 matrix to use as an internal reference to avoid artifacts from the tip, similar to a previously published procedure.[19] Briefly, STS was done by sweeping the voltage from -2 V to 2 V and measuring the resulting tunneling current (300 points at 0.1 ms per point). Prior to recording spectra, the tip was position at the point of measurement with feedback loop parameters of 20 pA and 1.4 V, and during spectra collection the feedback loop was inactive.

4.2.5 Atomic Force Microscopy (AFM) and Nanografting

AFM imaging and nanografting were carried out with a Keysight 5500 AFM/SPM (Keysight, Santa Rosa, CA). Images were obtained of the mixed monolayer (co-absorbed and nanografted) before and after the TPPF5 reaction in an ethanol liquid cell using a Si_3N_4 tip (Bruker AFM Probes, MSCT, Sunnyvale, CA) with an applied load at or below 1 nN. The radii of the tips were obtained by imaging a $SrTiO_3$ standard and were typically in the range of 10-20 nm.[232] The lever spring constants were obtained using the Sader method and ranged between 0.05-0.7 N/m.[233] The tips with lower spring constants were used for imaging and the tips with higher spring constants were used for nanografting.

For the purposes of nanografting, the Au(111) films were cleaned as stated above and immersed in 1mM of C12 for 24 hours. Then the C12 monolayer was rinsed with ethanol and immersed in 1 mM C5DT in ethanol, which serves as the target molecule for nanografting. To nanograft, a large load was applied that varied between 8-11 nN and the line step varied between 0.25-0.5 nm. These line steps correspond to a contact-radius-to-linestep ratio of 2-4,[309] such that all points in the nanografted area experience

tip sliding 4-8 times to ensure a clean graft. The load and line step depend on variations in the specific experimental set-up; primarily arising from variations in tip geometry. To determine the minimum or threshold load as well as the maximum line step, load and line step were varied until the minimal load and maximal line step necessary to achieve a complete graft was determined, indicated by complete replacement of the C12 by C5DT in the grafted area. Excessively exceeding these optimal parameters could result in wearing of the underlying Au surface. These parameters were continuously monitored and adjusted to account for changes to the tip resulting from the grafting process. To access any tip changes during a grafting experiment, the tip radius was obtained by imaging a $SrTiO_3$ standard before and after the experiment.

4.2.6 Control: C5DT/C12 Monolayer Immersion in Blank Solution

Some mixed C5DT/C12 monolayers were immersed in a blank solution for 3 hours at room temperature. The conditions are the same as in the In Situ Attachment of TPPF5 to Surface Bound C5DT section with one exception. The blank solution is lacking TPPF5 and only consists of dichloromethane, chloroform, methanol, and diethylamine (4:4:1:0.001 v/v). After immersion, the samples were like-wise rinsed with dichloromethane before examination by AFM.

4.2.7 Data Analysis of the AFM and STM Images

The AFM and STM images as well as STS data were analyzed with the help of Scanning Probe Image Processor (SPIP) software (version 6.0.2, Image Metrology, Lyngby, Denmark) and OriginPro software (version 9.0.0, OriginLab Corporation,

Northampton, MA, USA). The grain analysis feature in SPIP was used for the statistics on the C5DT domains and TPPF5 islands.

4.3 Results and Discussion

Previously it was found that when porphyrin were allowed to insert randomly into a matrix of C12, for short deposition times, they would insert predominately as single molecules, while for longer deposition times, they would organize into nanoscopic islands on the order of 5–10 nm in lateral dimension. Moreover, the electronic properties of the inserted porphyrin-thiols were found to depend on island size, with single molecules and small clusters showing simple tunneling behavior, while larger islands (5–10 nm) showed characteristics indicative of charge hopping.[19-20] As these prior experiments relied on random self-organization, to utilize the size selective electronic properties of these islands in any prescribed fashion, it is paramount to develop approaches to control and direct the island formation. To this end, in this work, porphyrin-thiol islands were formed on Au(111) surfaces using a two-step process: first, a tether to the surface, C5DT, was controllably attached to the Au surface by co-absorption[310] or nanografting,[195, 311] then the porphyrin head group (TPPF5) was reacted with the surface-bound C5DT domains to form the entire porphyrin-thiol complex attached to the substrate via reaction between the pendant pentafluorophenyl ring with surface thiols. Here we will first describe the assembly of the C5DT linker by co-adsorption and nanografting to understand the organization of the C5DT template on the surface, then we will discuss the surface reaction of TPPF5 with the C5DT, and the structures formed from this process.

4.3.1 Formation of C5DT Domains via Co-Absorption with C12

As noted above, in previous studies porphyrin-thiol assemblies were formed by allowing the molecules to randomly insert into a background of C12, where the immersion time and interactions of the porphyrin macrocycles dictated the sizes of the inserted islands.[19-20] Here, we attempt to control the sizes of these islands by first co-absorbing from solution C5DT and C12 onto Au(111) exploiting their spontaneous phase segregation to act as a template for the subsequent attachment of TPPF5. Prior studies of self-assembled monolayers of mixed thiols on Au have shown that phase segregation can occur for two alkanethiols with differences in chain length of *ca.* eight methylene units,[312] with different head groups,[310] and with symmetric versus asymmetric disulfides,[313] allowing for domains to be formed. The sizes of the phase segregated domains could be controlled by solution immersion time, temperature, relative concentrations of the two components, and by annealing after formation of the mixed SAMs.[311-312] Here we have found that domains of C5DT inside a matrix of C12 could be readily formed by co-absorption in a solution with 10:1 molar ratio of C12 to C5DT for 24 hours at room temperature. AFM and STM images of the domains are shown in Figure 19.

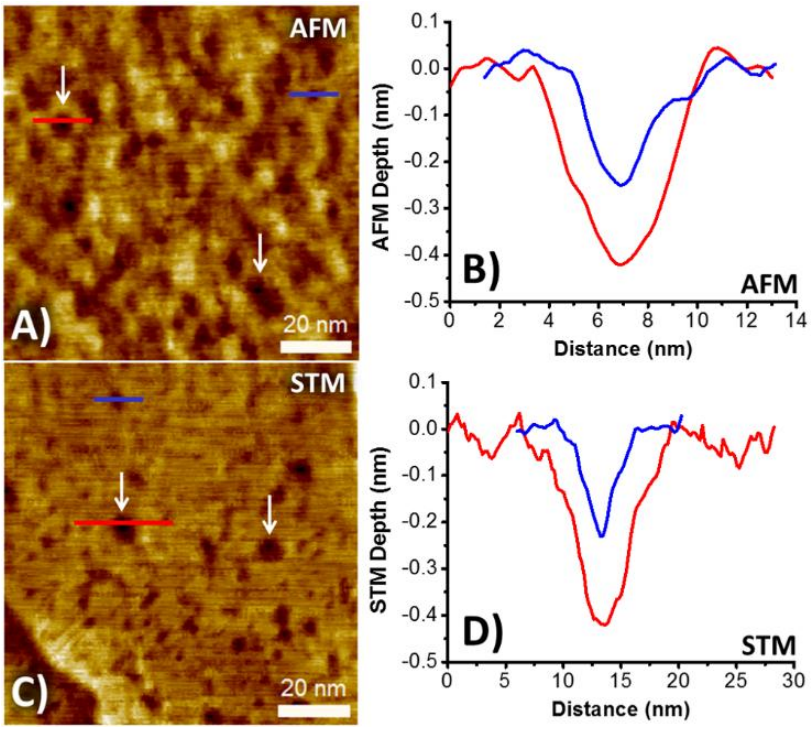

Figure 19. AFM topography image (A) and corresponding cross-sections (B) of a C5DT domain and etch pit for comparison. STM image (D) and corresponding cross-sections (E) of a C5DT domain and etch pit for comparison.

At a glance, the C5DT domains may be confused with etch pits that are characteristic of alkanethiol monolayers assembled on Au(111).[314] However, by examining the cross-sections, the C5DT domains are seen to be deeper and larger than the typical size of etch pits, which have a depth of one interlayer atomic spacing of the Au(111) surface (0.23 nm). On average the C5DT domains were determined to be 0.4±0.1 nm deep from both AFM and STM images. Assuming that both C5DT and C12 are in a standing-up orientation and tilted at 30° from the surface normal (as is typical for an alkanethiol SAM),[185] the theoretical depth of the island should be 0.6 nm. As the average depth is smaller, it could possibly suggest that the C5DT is standing more

upright. However, this may also be due to the inability of the tip to completely probe the domain since the tip and domain are of comparable size (especially in the case of the AFM tip). There was no evidence of multilayer formation in STM or AFM at the C5DT domains, as has been occasionally observed in some cases for dithiolate SAMs.[315-316] This may be due to intra-layer binding being inhibited by spatial confinement of the dithiol,[317] given that the terminal thiols of C5DT would be directed normal to the surface,[318] yielding additional steric hindrance for assembly.

On average, the widths of the C5DT domains were determined to be on the order of 11 nm from AFM images and nearly half of that at (~5 nm) from STM images (Figure 19(B) and Figure 19(D)). It is likely that the domains appear smaller in STM due to an increase in lateral resolution and some small domains in AFM appear clustered as a large one. This is supported by the fact that on average, only 26 domains per 100 nm^2 were routinely counted in AFM images, while on average more than triple that (82 domains per 100 nm^2) were observed in STM images. From the images, the C5DT domains were found to cover approximately 5-10% of the total area of the surface. This will be used in the following section to consider the extent of the reaction with TPPF5.

The molecular organization of the co-absorbed samples was examined using STM. In Figure 20 both the internal structure of a C5DT phase separated domain as well as the surrounding C12 is shown. In both the C5DT domain and the surrounding C12, the characteristic $(\sqrt{3}\times\sqrt{3})R30°$ structure of thiols on Au(111) was observed.[319] Using band-pass filtering to remove the topographic variation of the domain, (Figure 20C) it can be seen that C5DT molecules appear ordered at the center of the island. Lattice

agreement between the C5DT domain and surrounding C12 was observed, both in terms of dimension and orientation, clearly indicating that the C12 is driving the organization of the C5DT. The images are blurry at the boundaries, which may be a reflection of the greater freedom of motion of the less confined C12 at the boundary (Figure 20). For comparison, a homogenous C5DT monolayer was also imaged. The homogenous monolayer of C5DT produces a striped lying-down phase (Figure 21) as is typical for short chain thiols[284] and similar to 1,6-hexanedithiol[320-321] due to competition between van der Waals interactions and the relatively strong S-Au interaction.

Based on this data, it is clear that when the C5DT is confined in regions of C12, the C5DT organizes in a standing-up phase via a "lateral epitaxy," as evidenced by atomic resolution STM images (Figure 20(C)). It seems that in the confined regions, C5DT takes on the molecular organization of the surrounding C12. The longer chain lengths and spatial confinement provided by the C12 however, introduces sufficient van der Waals interactions to stabilize a standing-up phase through-out the ~5 nm C5DT domain. These results are consistent with prior studies of co-adsorption[312] and indicate that the C5DT domains provide well-ordered structures suitable for attachment of TPPF5.

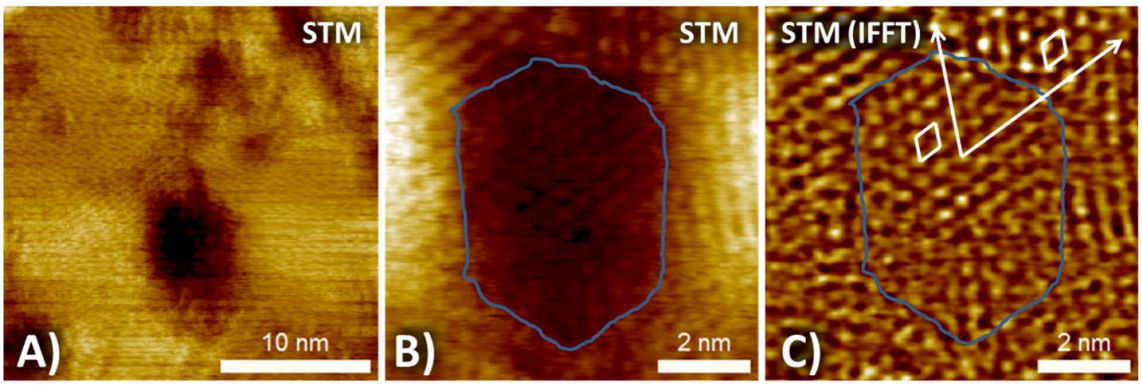

Figure 20. STM image (A) of a co-absorbed C5DT domain and surrounding C12 matrix. (B) High resolution STM image of the same co-absorbed C5DT domain, outlined in blue. Band-pass filtering (C) shows identical lattice dimensions as well as lattice alignment of the C5DT domain to the surrounding C12.

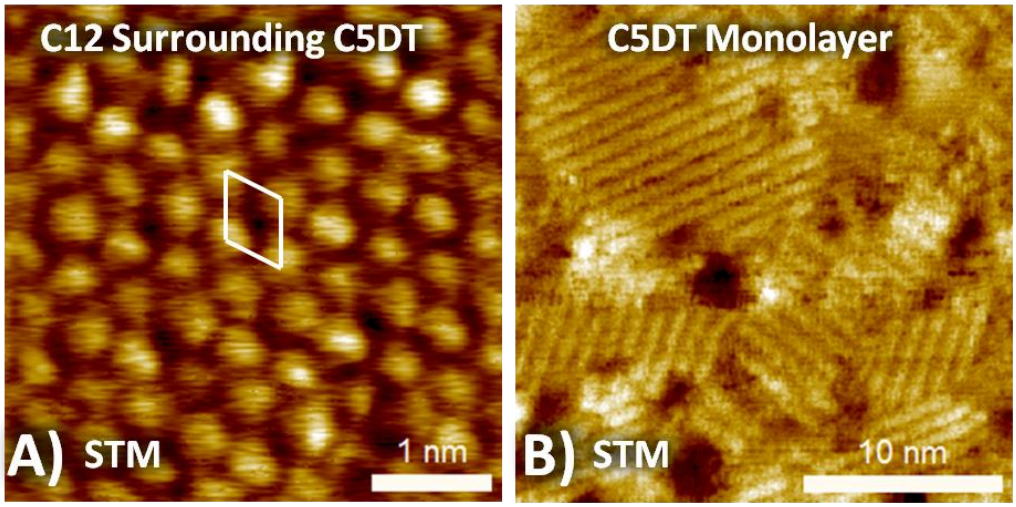

Figure 21. Reference STM images. (A) Atomic resolution of the C12 near a C5DT graft. The unit cell is drawn in white (0.49×0.49±0.01 nm). (B) Molecular organization of a homogenous C5DT monolayer. When C5DT is un-confined, the molecules arrange in the lying-down, striped phase.

4.3.2 Nanografting of Pentanedithiol (C5DT) into Dodecanethiol (C12)

While phase separation provides one route to fabricate assembled templates of C5DT in C12, the island size depends upon the deposition conditions and there is no ability to spatially control the positions of the islands. To achieve control of the island sizes of C5DT in C12, with the intention to later direct the assembly of TPPF5 islands, patterning the template is necessary. To accomplish this, C5DT was nanografted[195] into a C12 monolayer. Using this method, the size shape, and location of the C5DT domains could be controlled. Square features of the C5DT ranging from approximately 10 nm to 100 nm in lateral dimension were nanografted into C12. Figure 22 shows topographic and lateral force images of the grafted structures, indicating that the grafted features appear as depressions with stark friction contrast owing to the greater interactions between the thiol headgroup and the AFM tip.[322-323]

Similarly to the co-adsorbed structures, the C5DT nanografts were found to exhibit a depth between 0.4 nm to 0.6 nm below that of the surrounding C12 monolayer (Figure 22(C)).

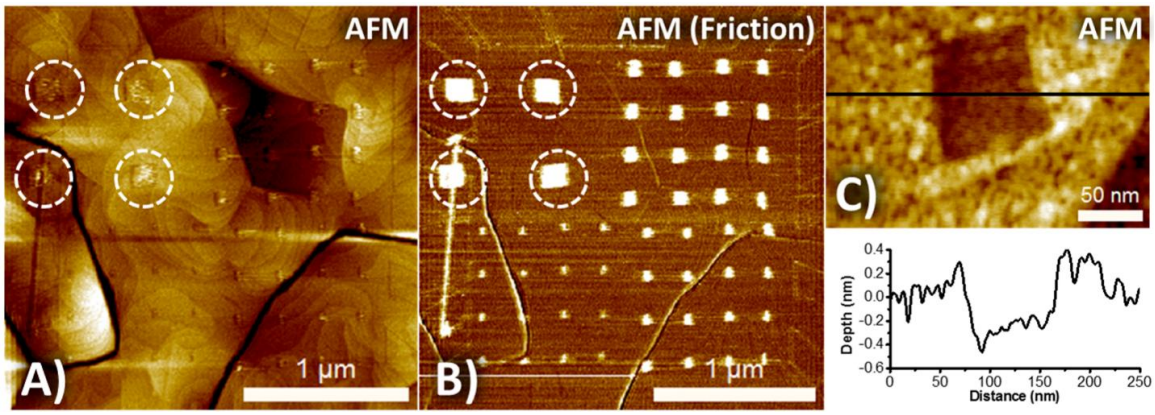

Figure 22. AFM topography (A) and friction contrast image (B) of C5DT grafts, which appear as topographic depressions with increased friction owing to the thiol termination. Features are 100, 50, 25, and 10 nm boxes. Surrounding grafted lines are part of the pattern used for relocation. A closer view of a 50 nm box (C) indicates a depression depth of 0.4 nm.

The smaller patterned features (<50 nm) tended to have a shallower depth, nearer 0.4 nm, while the larger patterned features structures (>50 nm) exhibited depths nearer 0.6 nm. This subtle variation with graft size suggested that the size of the C5DT graft could affect its internal molecular arrangement. These height differences can be attributed to a combination of changes in molecular tilt and mechanical rigidity as the packing density within the grafted structures changes, indicating that, in the smaller grafts, the molecules are more tightly packed, potentially into a more upright and rigid configuration, compared to the larger grafts.

To further explore this supposition, we examined the molecular structure of the grafts in detail by STM. Similar to the co-absorbed samples, it appears that the matrix of C12 surrounding the C5DT grafts also influences their molecular organization, with the C12 matrix helping to stabilize the C5DT in a standing-up arrangement. Evidence of this

is shown in STM images of a 40 nm square of C5DT grafted into C12 (Figure 23). In this graft, it was observed that the C5DT was more ordered near the boundaries of the grafted region than towards the center, where image blurriness is an indicator of greater disorder, and/or freedom of motion. This suggests that the stabilizing effect of the C12 is limited to a range of ~10 nm from the sidewalls of the graft.

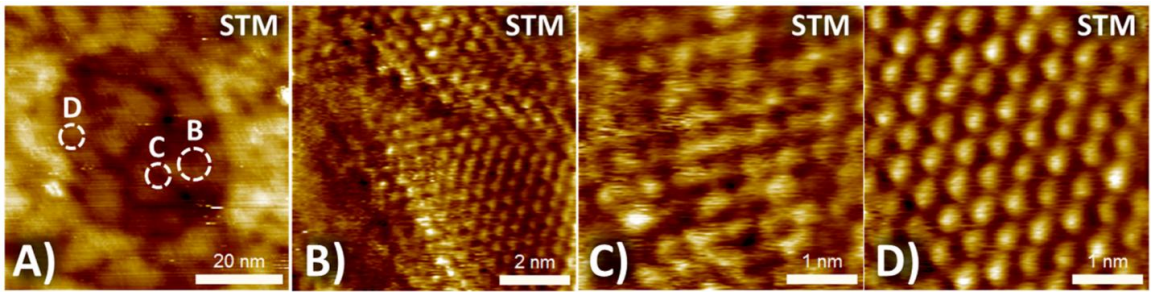

Figure 23. A C5DT graft (A) imaged by STM, with molecular resolution images (B-D) at the positions indicated. At positions B and D, near the edge of the graft, ordered domains were very clearly visible, while towards the center of the graft, a blurred image indicative of disorder was observed.

To fully investigate the extent of C12's influence on the internal structure of different size C5DT grafts, STM images were obtained and compared for *ca*. 40 nm, 50 nm, and 120 nm in lateral dimension grafted C5DT squares (Figure 24). Across all structures, generally the same behavior was observed, with ordered C5DT near the boundaries of the grafts, regardless of size, and disorder in the center. However, the extent of disorder was generally found to be greater for larger grafts, for which images near the center contained few discernible features, reflective of greater disorder. The disorder in the larger graft also had an intriguing effect on the lattice dimensions near its

border, where, rather than the (√3×√3)R30° structure typical of alkanethiols (0.5x0.5 nm), dimensions consistent with a (2x2) expanded adlattice were observed (0.6x0.6 nm).

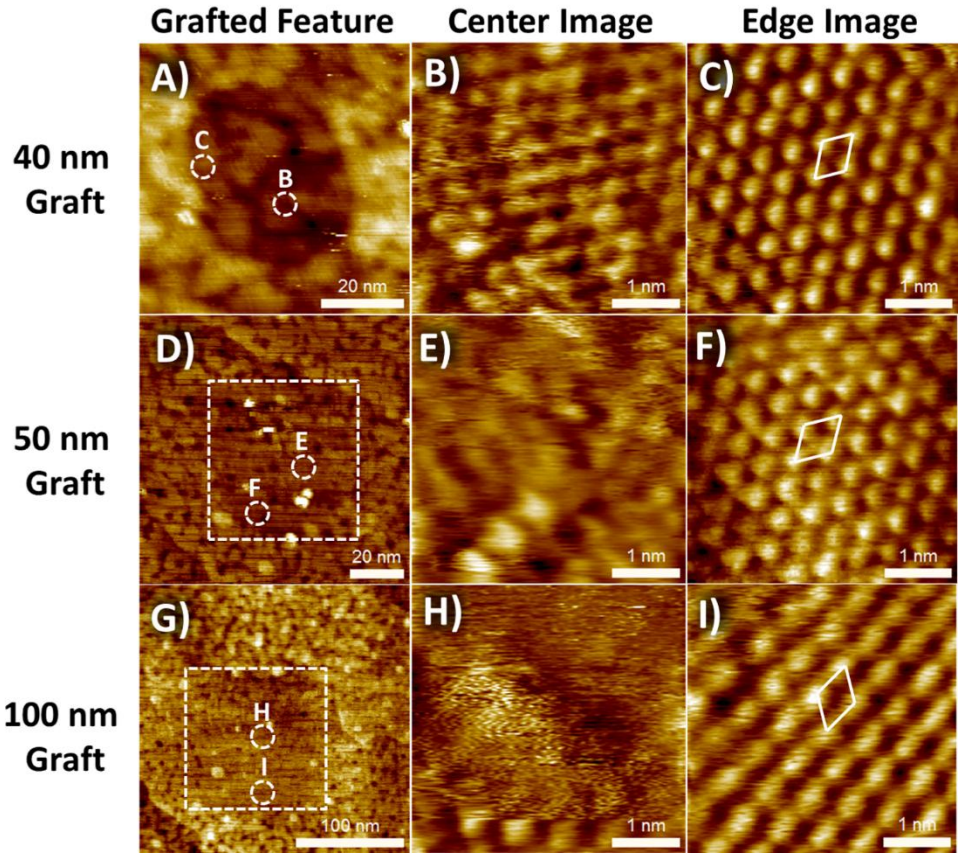

Figure 24. STM images comparing the structural organization of 40 nm (A-C), 50 nm (D-F) and 120 nm (G-I) grafts. Images collected near the center of the graft showed increasing disorder with increasing graft size, reflecting the fact that these points receive less stabilization from the surrounding matrix. Ordering is readily apparent near the edges of the grafts, though the dimension of the C5DT lattice near the edge of the 100 nm graft (I) are consistent with a (2x2) expanded phase. The stark change in appearance observed in (H) was observed through repeated imaging and is therefore not attributable to a tip change.

While the differences are small, the measurements were conducted side-by-side and taken across the entire lattice, so it is a distinct difference in boundary lattice structure amongst the different sized grafts, with larger grafts exhibiting reduced density near the boundary. We surmise that the reduced density at the boundary of the larger grafts results from a surface concentration gradient away from the graft boundary. Because larger grafts exhibit a smaller perimeter-to-area ratio and corresponding greater mean distance from points within the graft to the boundary, we would expect the density at the center of larger grafts to be lower for larger grafts, a point supported by their greater depth observed by AFM. This greater depletion at the center of the graft can facilitate depletion from the boundaries, resulting in a boundary (2x2) phase for larger grafts. In the interest of homogeneity, this implies there is a clear upper limit for graft size, which for C5DT is on the order of a few 10's of nm, and is presumably greater for longer, more self-stabilizing grafted molecules.

4.3.3 Assembly of TPPF5 on Co-Absorbed and Nanografted C5DT

Placement of the C5DT on the surface affords us reaction sites to which we can link the TPPF5 to the substrate via a click reaction between the pendant pentafluorophenyl group on the porphyrin macrocycle with the surface bound thiol. While the solution based protocol for this is reasonably straight forward,[20] carrying out attachment to the surface bound C5DT using *in situ* adsorption is not necessarily transferable and there are technical considerations. The surface of the C5DT domains represents a more sterically hindered reaction substrate than the dissolved thiol, and this is exacerbated as more TPPF5 molecules bind to the domain. Additionally, depletion of

the SAM in the reaction solution is a possibility and necessitates optimizing reaction times and conditions.

To form islands of attached TPPF5, the two-component film was immersed in 1 mM TPPF5 solution for three hours. AFM and STM images of a co-adsorption substrate after three hours of immersion in 1 mM TPPF5 is shown in Figure 25 as compared to the images of the co-absorbed template before immersion shown early in Figure 19(A) and Figure 19(C). After immersion in the TPPF5 solution, bright features appear in the images due to the attachment of the TPPF5 to the domains of C5DT. Grain analysis of the AFM images before the reaction yielded 16 and 9 counts per 100 nm^2 in AFM and STM images, respectively. After the reaction, 96 and 23 counts per 100 nm^2 in AFM and STM images respectively were detected, clearly indicating that reaction on the C5DT has occurred. On average, the physical height of the TPPF5 islands was found to be 0.4±0.1 nm above the C12 background, as extracted from AFM measurements. This is similar, but slightly smaller, than the physical height expected from prior studies of these molecules with the thiol tether already attached, when they were allowed to randomly insert into a surrounding matrix of C12.[20] From STM, the apparent height of the TPPF5 was on average 0.3±0.2 nm. Again, this was similar, but slightly smaller than the apparent height of these molecules when they were allowed to randomly insert into the surrounding C12.[20]

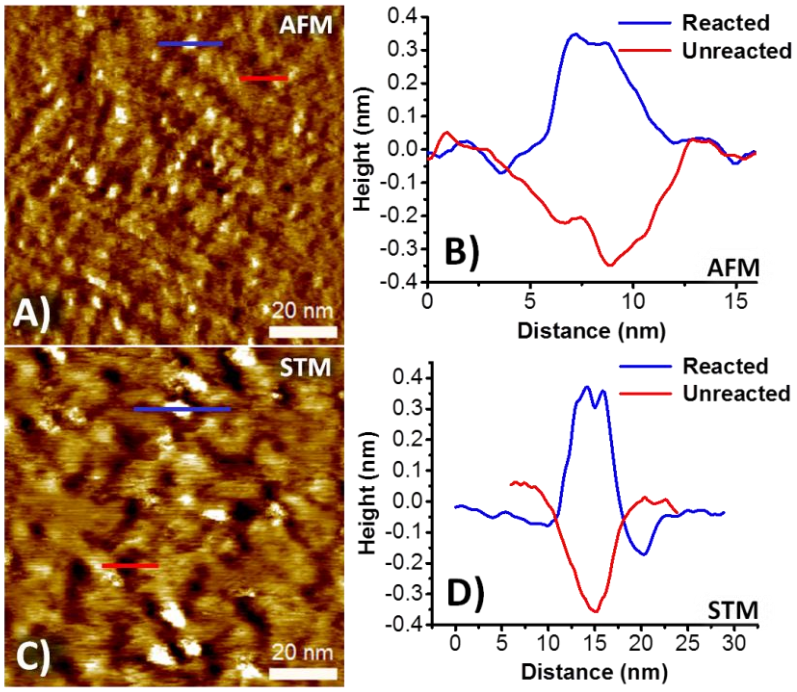

Figure 25. AFM topography image (A) showing the reacted TPPF5 islands which appear as bright protrusions and corresponding AFM cross-sections (B) of a TPPF5 island as well as an unreacted C5DT domain. Similarly an STM image (C) is shown with corresponding cross-sections (D) of a TPPF5 island and unreacted C5DT domain.

Though several islands were observed, unreacted domains of C5DT were still present after the three hour immersion time. To increase the amount of TPPF5 that reacted with C5DT, the immersion time in the TPPF5 could be increased or the TPPF5 solution concentration could be increased. To more systematically explore the development of these TPPF5 islands, the addition of TPPF5 to C5DT nanografts as a function of time was examined.

After C5DT features were fabricated by nanografting, the samples were immersed in the TPPF5 solution. AFM images of the grafted structures before and after 3, 18, and 21 hours of immersion are shown in Figure 26. There was a clear change in

topography, where the nanografted structures transform from depressions with the C5DT into protrusions following immersion in the TPPF5.

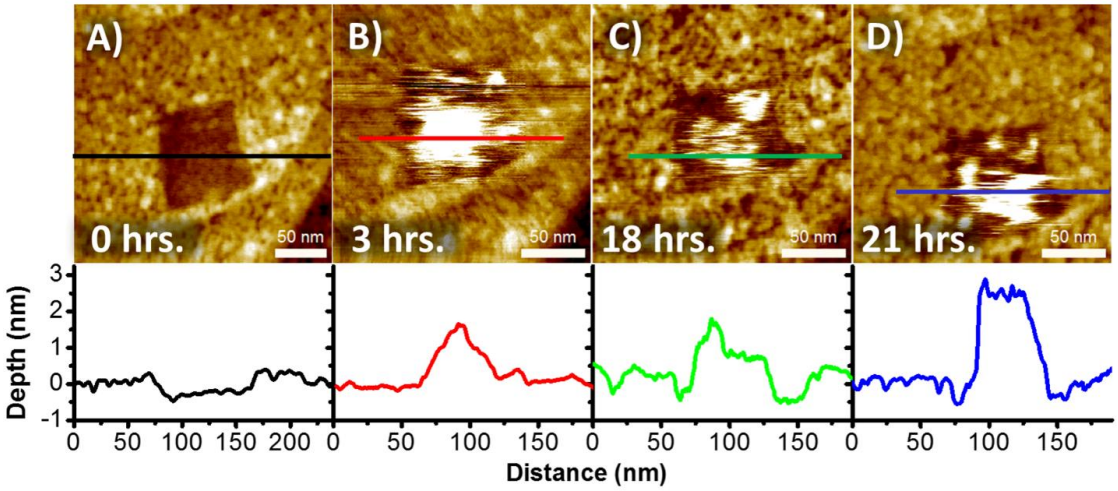

Figure 26. AFM topography images of a C5DT graft (A) after 3, 18, and 21 hours (B-D respectively) immersion in TPPF5 solution. Corresponding cross sections indicate the evolution from the depression, corresponding to the graft, to an increasing feature height of 2.5 nm after 21 hours of immersion.

Importantly, the change in topography only appeared at the locations of the grafted structures and not in the background C12; consequently the attachment appears to indeed be selective to the location of the C5DT. With increasing immersion time, the island was observed to increase in height relative to the background matrix, from 1.6 nm to 2.5 nm. While depletion of the surrounding matrix could contribute to the increasing height difference, and changes are apparent in the surrounding C12 matrix, this would result in decreased spatial confinement of the graft, whereas the localization of the island did not change over time. Rather, the increasing height of these structures with time

likely results from intercalation of dissolved TPPF5 into the covalently bound TPPF5 via pi-stacking and static dipole interactions, owing to the highly electronegative perflouro substituent, which would stabilize such a structure, as proposed in Figure 27.

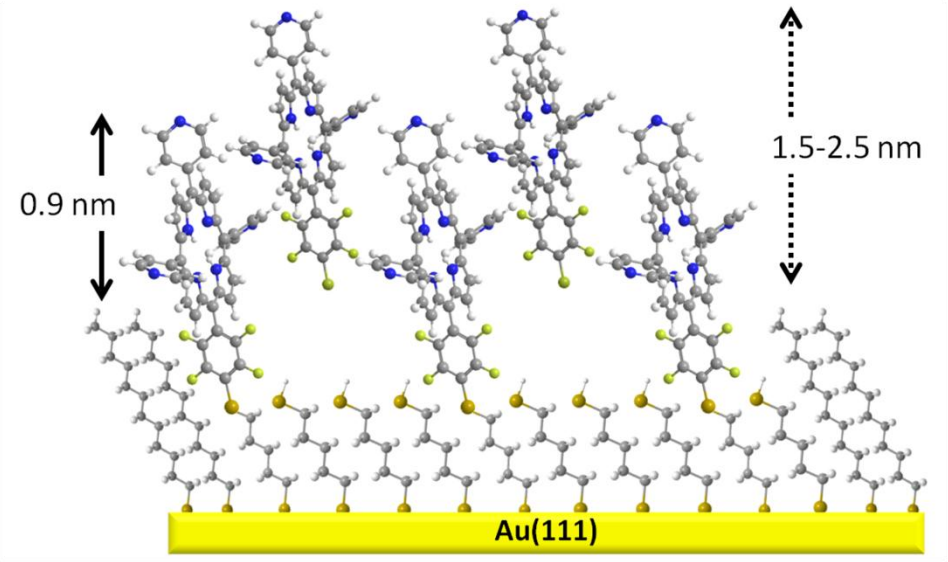

Figure 27. Proposed model of the C5DT domains and the organization of the TPPF5 on the C5DT. The C5DT is in a standing-up orientation similar to the surrounding C12. The TPPF5 binds to some of the C5DT and others intercalate to pi-stack between.

STM was used to interrogate the final, TPPF5 islands on the surface, and Figure 28(A) shows one such island. Thus far, molecular resolution of any internal organization has not been achieved, but STS was employed as a preliminary verification of their identity. Figure 28(B) shows representative current-voltage (I-V) characteristics of the bright features and the C12. I-V characteristics on the bright feature are comparable to those previously reported for porphyrin-thiols inserted into defects in a homogenous C12 monolayer.[20]

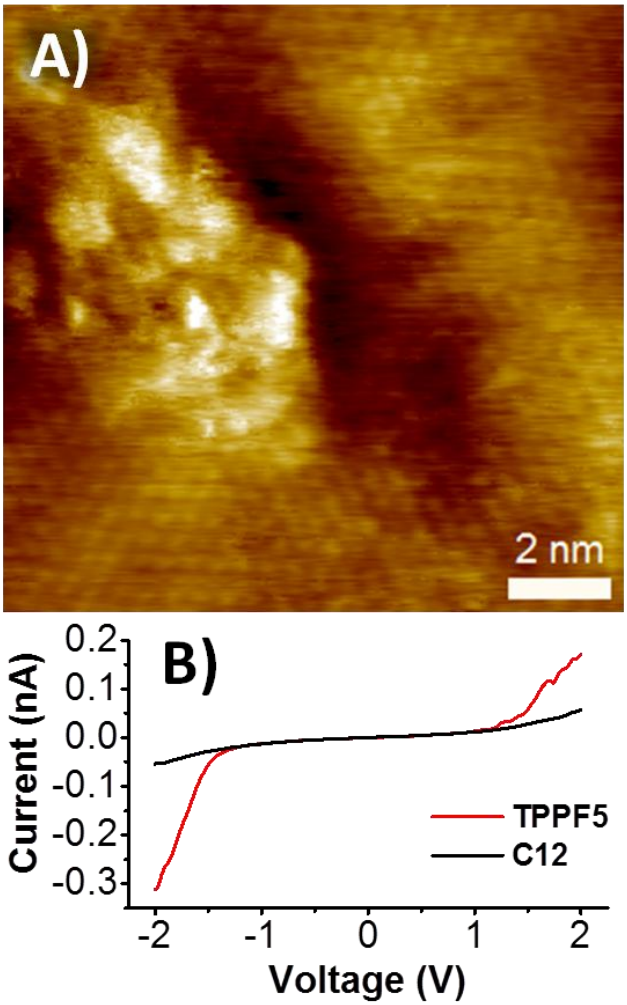

Figure 28. STM image (A) of a TPPF5 island on a C5DT graft. The molecular organization of the surrounding C12 is visible; however, the organization of the TPPF5 island is unclear. Average I-V curve of 100 collected spectra of the island and the C12 background for reference shows behavior consistent with tethered TPPF5.

Accordingly, since the I-V signatures are the same, it seems that the bright features on C5DT have similar identity to the previously reported inserted porphyrin-thiols and supports that these bight features are the reacted TPPF5.

4.3.4 Control: Nanografted C5DT Structures Immersed in a Blank Solution

As a control, the C5DT/C12 mixed monolayers were immersion in a blank soultuion with out TPPF5. AFM topgrpahic and firction contrast images showing grafted C5DT domains before and after immersion for three hours is presented in Figure 29. For closer inspection, a particualr C5DT grafted domain before and after the immersion is shown in Figure 30 with the corrisponding cross section. There is no change in the C5DT domains after immersion in the blank solution and the cross-section in Figure 30(C) is the regmains unchanged. Accordinly, the presence of TPPF5 in the immersion soultion accounts for the dramtic change in the C5DT domains after immesion as discussed above.

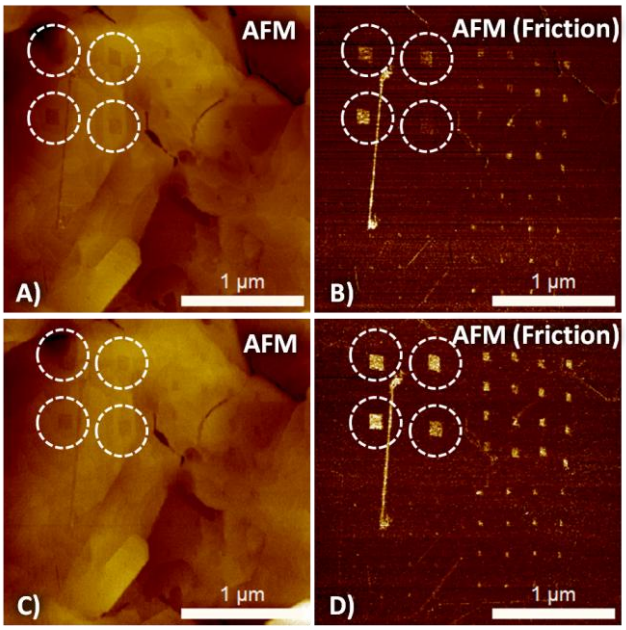

Figure 29. AFM topography (A, D) and friction contrast image (B, D) of C5DT grafts. In A and B the grafts were imaged immediately after fabrication. In C and D the grafts were imaged after immersion for 3 hours in the blank solution (without TPPF5). There is no change after immersion in a blank solution.

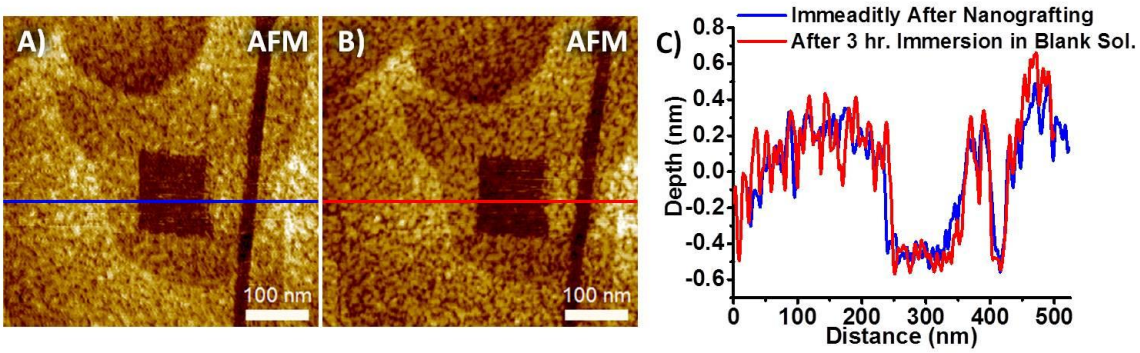

Figure 30. AFM topography images and corresponding cross-sections of the same C5DT grafted structure immediately after fabrication (A, blue line) and after immersion for 3 hours in a blank solution (B, red line). There is no difference in topography before and after immersion.

4.4 Conclusion

Patterned domains of C5DT in a background of C12 were generated by two methods, co-adsorption and nanografting. In both methods, it was found not only could the size of the C5DT domains be controlled but also the organization of the individual molecules inside the island. This control was facilitated by the interactions between the surrounding C12 matrix and the confined C5DT. While a homogenous monolayer of C5DT is organized in the striped-lying down phase, when confined in a C12 matrix, the C5DT adopts a densely-packed, standing-up phase similar to its C12 neighbors via "lateral epitaxy." It has been shown that the phase of C5DT transitions from a highly dense, $(\sqrt{3}\times\sqrt{3})R30°$ phase, to a sparser (2×2) phase, to a disordered molecular arrangement with increasing C5DT domain size (from ~5-100 nm in lateral dimension). The C5DT domains were used as a template for the surface attachment of a porphyrin derivative, TPPF5, via a "click" reaction. A model of the assembled system is proposed

where the C5DT molecules are in a standing-up orientation and TPPF5 selectively reacts with the C5DT head groups to achieve binding to the surface, with additional unreacted TPPF5 intercalating by pi-stacking.

The work presented herein provides a basis to study lateral patterning at the nanometer scale of functional self-assembled monolayers. It is specifically relevant for exploring the effect of assembly size on the emergent electronic properties. As a proof of principle, the two-step method was applied to work done with porphyrin derivatives, for which it had previously been found that the electronic properties of islands on the surface varied with dimension[19] and internal organization (Chapter III). However, the work presented herein is not limited to porphyrin attachment. Metal ions or nanoparticles can bind to the thiol head group as well to provide an organizational template for other types of assemblies.[324] In a broader perspective, creating assemblies of molecules/organic materials with controlled organization will serve different purposes in devices because nearest neighbor interactions can be more readily controlled and therefore the stability, size, and electronic properties of such assemblies can be controlled. [51, 146]

CHAPTER V

SUMMARY AND OUTLOOK

5.1 Summary

In summary, the work presented herein examined porphyrin molecules as electro-active materials to modulate charge on Au(111) surfaces in terms of single molecules, molecular assemblies fabricated through self-assembly, and pre-designed molecular assemblies that achieved a desired electronic property fabricated through template-directed assembly. Porphyrins have been among the most important materials for electronic applications and many interesting properties have been studied and exploited in the work here. Because of their remarkable electronic and physical properties and importantly their synthetic tailorability and modularity, porphyrins were used as platform to study relationships and challenges broadly common with the use of molecular/organic materials for electronics by researching the following questions: *1) How do systematic perturbations in the molecular structure of porphyrins affect the resulting electronic properties? 2) How does molecular assembly affect the cooperative electronic properties of porphyrins on surfaces? 3) How can the assembly of porphyrins be pre-designed and directed into specific architectures to produce a specific, targeted electronic property?* The impact of this work presented here expands further than exclusively for porphyrins molecules and has provided knowledge necessary to engineer molecular/organic electronic devices with pre-designed functions at the molecular level. Following these studies and results are summarized.

In Chapter II, systematic perturbations in the molecular structure of porphyrin-thiols the resulting electronic properties were investigated. This was done by considering a series of porphyrin-thiols with a combination of substituents by replacing –F with –H in the phenyl linker group, converting pyridal to phenyl groups at the *meso* positions, and chelating a Zn ion or not. The porphyrin-thiols were assembled onto Au(111) surfaces with a pre-formed C12 SAM where they inserted into the SAM at defect sites and near etch pits to covalently bond to the underlying Au through their thiol tether. The porphryin-thiols were allowed to self-assemble in this way for durations of one, three, or five days during which single porphyrin-thiol molecules tended to insert into the C12 SAM for one day durations while small assemblies of porphyrin-thiols formed for three and five day durations. The physical properties of the porphyrin-thiol/C12 mixed SAM was examined though AFM imaging and the electronic properties were examined though comparative STM imaging with respect to the background C12 SAM to obtain a apparent height ratio and STS though examination of I-V characteristics. Contrary to one of the original promises of molecular electronics of ultimate electronic tunability based on the almost limitless combinations in which molecules can be constructed during synthesis, here it was found that the chemical structure perturbations did not lead to any observable variations in the relative conductance nor in the I-V characteristics for single porphryin-thiols. All of the single porphryin-thiols in the series exhibited a apparent height ratio of approximately 1 and I-V characteristics similar to that of alkanethiols suggesting a tunneling transport mechanism in which the alkanethiol tether dominates the overall transport. There are some reports on the limits of electronic tunability due to

chemical perturbations in molecular assemblies and in device configurations that predominantly originate in nearest neighbor effects, but reports on the limits for single molecules, thereby minimizing nearest neighbor effects, are infrequent. From this work, one of the limits to electronic tunability with chemical perturbations was found to originate from the tunneling transport mechanism dominated by the alkanethiol tether. To have a meaningful affect on the electronic properties through chemical perturbations, the transport mechanism must deviate from tunneling. This is done so in assemblies of porphyrin-thiols large enough to stabilize charge on the porphyrin macrocycles which can be as little as a 6-10 porphyrin-thiol molecule containing assembly. In porphyrin-thiol assemblies the apparent height ratio departed from 1 and generally increased with increasing lateral assembly dimension with I-V characteristic of Coulomb blockade suggesting a charge hopping transport mechanism. By this the ability to tune the electronic properties through chemical perturbations was recovered. However, the apparent height ratio did not strictly increase with increasing lateral assembly dimension and the apparent height ratio displayed a large spread in the data. Therefore the increase in apparent height ratio cannot be exclusively due assembly dimension which prompted the research following.

In Chapter IV, the porphryin-thiols were examined with the focus on of the detailed effect of self-assembly time on the electronic properties. As before, the porphyrin-thiols were inserted into a pre-formed C12 SAM and allowed to self-assemble for one, three, or five days. The physical properties were examined through though AFM and molecularly resolved STM imaging and the electronic properties were examined

though comparative STM imaging. STS was also used to examine the electronic properties but to a greater extent discerning the details in the I-V characteristics for assemblies formed after different durations. It was found that there was a stark difference in the I-V characteristics for porphyrin-thiol assemblies formed after one, three, and five days with a gradual increase in the maximum current for increasing durations. For the one day assemblies, the I-V traces are comparable to that of alkanethiols similar to single porphyrin-thiol molecules. For three day assemblies, the I-V traces show a conductance gap at low bias indicating bias-induced switching. Finally, for the five day assemblies, the conductance gap narrows and the I-V traces are highly spread indicating stochastic switching. Accompanying this, the morphology of the background C12 SAM was observed to deplete in the vicinity of porphyrin-thiol assemblies from a densely-packed, standing-up orientation after one day with the development of some low-density, lying-down phase after three days and even more so after five days. These data suggest that for the porphyrin-thiol assemblies formed after one day, the constituent molecules are weakly interacting and act as single molecules. Then the assemblies formed after three days are allowed enough time to re-arrange into a closely-packed and possibly pi-stacked arrangement in which the porphyrin-thiols are strongly interacting Finally, after five days, the assemblies begin disorganize and to lose their closely-packed arrangement due to the depleting of the surrounding C12 SAM which can no longer stabilize the porphyrin-thiol assemblies. This work has demonstrated that extremely subtle organizational differences in porphyrin-thiol assemblies on Au(111) surfaces have an abounding impact on the electronic properties

with the loss of the useful property of bias-induced switching for stochastic or little switching capability. With this understanding, research to controllably fabricate porphyrin-thiol assemblies with specific electronic properties follows.

It is essential to control and direct the assembly of porphyrin-thiols to utilize their electronic properties that depend on lateral assembly dimension and internal organization, previously found here and elsewhere, in any pre-defined manor. Therefore, Chapter IV describes a method that has been developed to fabricate porphyrin-thiol assemblies on Au(111) surfaces with two steps. First the surface tether, C5DT, was controllably attached to the Au(111) surface co-absorption from a mixed C5DT/C12 solution or nanografting with AFM. Second a porphyrin derivative was selectively attached to the surface bound C5DT by a click reaction. The organization of the C5DT template was examined by AFM and STM with molecular-level resolution and the porphyrin head group attachment was monitored at time intervals of 3, 18, and 21 hours with AFM and the electronic properties were investigated by STM as well as STS to obtain I-V characteristics. It was found that contrary to a simple C5DT monolayer, domains of C5DT within the C12 background formed a standing-up phase via a "lateral epitaxy," and the internal organization could be controlled by varying the size of the domains from approximately 5 nm, 40 nm, 50 nm, and 120 nm. The C5DT domains undergo a phase transition from the most densely packed $(\sqrt{3}\times\sqrt{3})R30°$, to a less dense (2×2), and finally to a disordered phase with increasing domain size. Such detailed, molecular-level understanding of the placement of the C5DT on the surface provides specific reaction sites to which active head groups can be attached. In this work,

porphyrin head groups with a pendant pentafluorophenyl ring were bound to the C5DT domains by leveraging a “click” reaction between with the pentafluorophenyl ring and the exposed thiol on the surface. It was found that the porphyrins derivatives selectively reacted with the C5DT domains and overtime there was a hierarchical build-up of porphyrins on the C5DT domains where some porphyrins were directly bound to the exposed thiols and other intercalated to pi stack between. The resulting I-V characteristic of was the same as that observed for porphyrin-thiol assemblies formed through random self-assembly. There have been many reports describing assembly methods, less that examine the resulting electronic properties of the assembled structures, and far fewer in which a fabrication method is designed to achieve a pre-desired electronic property. Here a facile two-step method was devised to controllably direct porphyrin derivatives into pre-defined, pi-stacked geometries to produce a certain electronic property. Beyond porphyrin derivatives, this two-step method is versatile and can be applied to direct the assembly of variety of other types of systems, such as quantum dots, DNA, and other complex molecules requiring immobilization on surfaces into specific geometries by tuning the interactions between the targets and head groups of the surface-bound thiols.

The research described here examined porphyrin molecules as electro-active materials to modulate charge on Au(111). From this it was found that in single porphyrin-thiol molecules, there as limits to electronic tunability and this limitation was surmounted in assemblies of porphryin-thiols. The electronic properties in porphyrin-thiol assemblies was found to be extremely sensitive to local molecular re-arrangements by way of differing self-assembly durations. Finally, to utilize the electronic properties

of porphryin-thiols, a directed two-step fabrication method was designed in which hierarchical pi-stacked porphyrin structures were produced that displayed the intended electronic property.

5.2 Outlook

5.2.1 Future Directions for Electronic Investigations of Porphyrin-Thiols on Surfaces

The knowledge and understanding acquired in the studies of porphyrin molecules as electro-active materials to modulate charge on Au(111) surfaces as single molecules, assemblies, and as directed hierarchical assemblies has been paramount. This work has provided a foundation for future investigations of porphyrin-thiols on Au surfaces. Distinctly, the two-step fabrication method developed herein expanded the possibilities for further investigations making it possible to direct the assembly of porphyrins on surfaces opening the potential for greater morphological control and the ability to design complex, multi-component structures. To further future investigations, recent innovations in experimental techniques such as thermovoltage and direct transmission function (*T(E)*) measurements can assist to illuminate the fine electronic details expected to differentiate complex molecular structures.

The electronic properties of porphyrin-thiol assemblies were found to depend on the assembly size as well as the local organization, within and surrounding the assemblies and with greater morphological control these electronic properties can be better understood and thereafter utilized in a prescribed way. In single porphyrin-thiol molecules and small clusters (*ca.* <3 nm in lateral dimension) charge was transported via tunneling, however in large assemblies (*ca.* >5 nm in lateral dimension) charge was

transported via hopping, but the distinct transition between these transport mechanism has not yet been observed and additionally it is not been discerned whether there is an upper bound on assembly size for charge hopping behavior. In other reports on differing transport properties, observing the transition between the properties has been useful in understanding the structure-function relationship and it would be so in this case as well. For fine control of the porphyrin-thiol assembly size, the two-step fabrication method would be ideal for controlling the size of the assemblies in the first nanografting step and by this a series of porphyrin-thiol assemblies could be created with finely varied sizes; for instance 4 nm to 20 nm in 2 nm increments. Incrementing the size by 2 nm translate to incrementing the porphyrin-thiol assemblies by one porphyrin-thiol molecule and from this the molecular-level understanding of the collective electronic properties could be gained. Yet, there are anticipated challenges in nanografting such small C5DT domains differing by only a few nanometers, seeing as nanografted features have been reported down to a 2x4 nm line consisting of only 32 alkanethiol molecules.[197] To achieve this carful optimization of nanografting parameters is required by considering the applied load, contact radius to line step (CRLS),[309] and size of the AFM tip. Additionally, changes in the organization of alkanethiol SAM surrounding the porphyrin-thiol assembles affect the electronic properties with the loss of bias-induced switching for a stochastic switching with SAM depletion for prolonged self-assembly durations, rendering the surrounding SAM less able to stabilize the porphyrin-thiol assembly. Even when the surrounding alkanethiol SAM is fully intact the bonds to the surface are not uniform, forming on atop adatoms or at threefold hollow sites for

instance, and can diffuse on the surface and it may not provide the necessarily stabilization, possibly responsible for some of the spread in the data shown herein.[314] Stabilization is an area that needs advancement for molecular/organic electronic in general and here specifically the porphyrin-thiols assemblies can be more effectively stabilized by replacing the alkanethiol SAM with a diacetylene-containing alkanethiol SAM. The diacetylene-containing alkanethiol SAM in comparable to the simple alkanethiol SAM and is seemingly compatible with two-step fabrication method. The difference arises when the diacetylene-containing alkanethiol SAM is exposed to UV-vis light and form robust cross-linking bonds upon that can "lock-in" the assembled porphyrins after carrying out the two-step fabrication method.

Multi-component molecular assembles appears to one of the promising areas for advancement in molecular/organic electronics because of the immense combinatorial capacity in which the individual properties of each constituent molecule contributes to the over-all property or function of the assembly.[172] Appropriate fabrication methods have been lacking, but the development of two-step fabrication method has provided potential for designing and directing the assembly of multi-component structures. In Chapter IV, as a proof of principle, one type of porphyrin derivative with a pendant pentafluorophenyl ring was directed into a hierarchical structure in which some porphyrin bonded directly to the underlying C5DT template and others did not. Those that did not directly bind to the C5DT intercalated between the bound porphyrins to pi stack and were stabilized by the "book ends" of the directly bound porphyrins. In fact, it appeared that over time, this pi-stacking structure grew upwards with multiple pi-stacked

layers. Leveraging these “book ends”, a multitude of different molecular species could be incorporated into the hierarchical structure and potentially with a different molecular species in each pi-stacked layer. The applications of such hierarchical molecular structures could extend to spintroins, molecular magnets, and advanced functional materials depending on the choice of secondary and tertiary molecular materials. The “book ends” need not necessarily be porphyrin molecules but simply containing flouro groups to react via click chemistry with the exposed thiol group of in the surface bound C5DT domains. Beyond flouro-thiol chemistry, the head group of the template alkanethiols could be optimized to react with alternative groups of the target molecule. Moreover, any secondary and tertiary molecular components indented to be incorporated between the “book ends” do not require reactive flouro groups since they need not be directly bound and are instead stabilized by the initial molecular species that are directly bound to the surface.

Achieving multi-component molecular assembles through the two-step fabrication method will require further research to better understand the details of the assembly process. Specifically, it would be advantageous to understand the formation of each pi-stacked layer through in-situ AFM imaging to monitor the assembly one molecule at a time. Preliminary data on the on the affects of the reactions conditions has been collected with similar experimental methods as described in Chapter IV but with two different variations. First, the solution concentration was reduced by 10x and monitored with shorter, more frequent time intervals. Second, the versatility of the

fabrication method was tested by replacing volatile and harsh TPPF5 solvent with simply ethanol.

In an effort to examine the process of porphyrin assembly, the C5DT domains were nanografted as before (Chapter IV) and then immersed in the TPPF5 solution but with a 0.1 mM concentration (10x lower than before). The immersion was carried out directly in the vessel utilized for liquid AFM imaging and AFM images were recorded at 1 hour intervals (Figure 31). Imaging in the environment of the reaction solution is challenging because the solvents that compose the reaction solution, especially DCM, are highly volatile and can degrade the materials of the AFM components causing enormous drift. To mitigate this, glass and Teflon AFM components are used where possible. Figure 31 displays topographic and corresponding frictional force AFM images of the reaction of C5DT domains with TPPF5 while immersed in a 0.1 mM solution from 0-5 hours. The images are of various sizes and quality, due to the enormous drift, but provide preliminary information on the detailed TPPF5 assembly. The TPPF5 does not react with the C5DT domains until immersion duration of 4 hrs. at which protrusions appear in the topography in Figure 31(E) and become more apparent after 5 hours in Figure 31(F). Previously, with the more highly concentrated 1 mM TPPF5 solution, TPPF5 reacted with C5DT domains in as little as 3 hours. Therefore, it seems that reaction duration is dependent on TPPF5 concentration. Furthermore, the TPPF5 seems to react more readily with the lager C5DT domains as evidence in the appearance of protrusions on the largest C5DT domains first (Figure 31(E)) then later on the second largest C5DT domains (Figure 31(F)). After 4 hours of immersion, large and small

C5DT domains were examined more closely in Figure 32 showing some reacted TPPF5 near the boundaries of the large C5DT domains and none on the small C5DT domains. Therefore, it seems that the reaction may also depend on the surface area of the C5DT domain. The first appearance of reacted TPPF5 domains at 4 hours (Figure 31(E)) was more closely examined in Figure 33 and shows that TPPF5 reacted near the C5DT domain boundaries. The reacted TPPF5 features vary in height from approximately 1-3 nm. A representative cross-section of a reacted TPPF5 feature is shown in Figure 33(C). These data suggests that TPPF5 first reacts near the boundaries of the C5DT domains in the well-ordered regions, as described in Chapter IV, and then nucleates from there to eventually cover the majority of the C5DT domain, resulting in reacted TPPF5 domains as observed in Chapter IV.

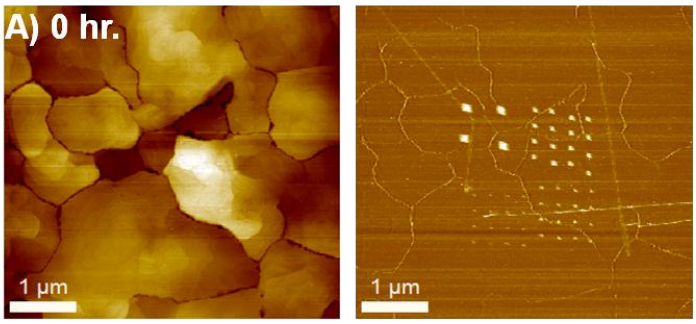

Figure 31. Nanografted C5DT domains were immersed in 0.1 mM TPPF5 and in-situ AFM images were recorded at 1 hour intervals. On the right is the topography image and on the left image is the corresponding friction image. A) AFM images immediately after nanografting C5DT domains. While not visible in the topography image, the C5DT domains are highly apparent in the friction image. B)-D) There is no change in the topography images indicating no reaction between the C5DT domains and TPPF5. E) and F) Reacted TPPF5 become apparent in the topography image in the location of the large C5DT domains.

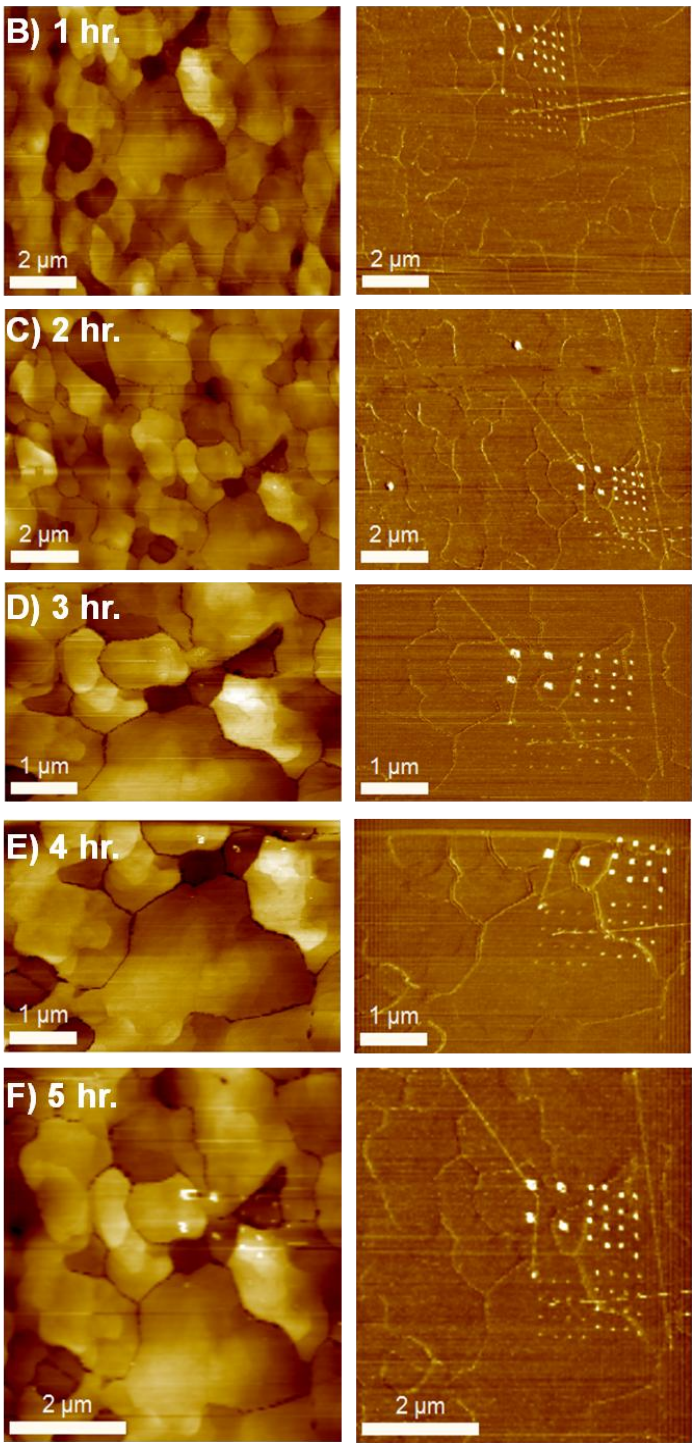

Figure 31. Continued.

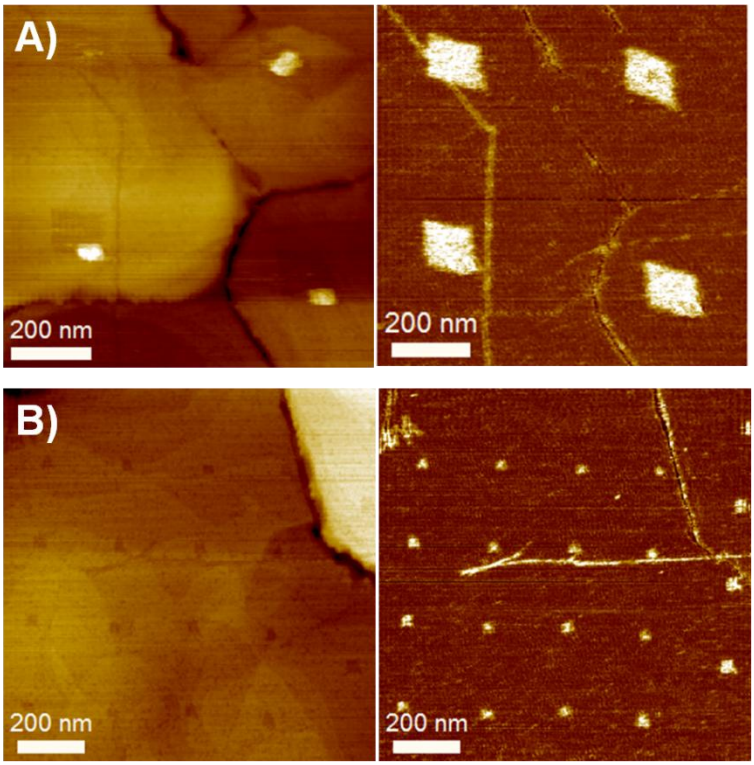

Figure 32. AFM topographic (left) and frictional force (right) images after nanografted C5DT domains were immersed in 0.1 mM TPPF5 for 4 hours. A) Protrusions appear near the boundaries of the C5DT domains indicating that TPPF5 begins to react with the large C5DT domains but B) does not yet do so with the small C5DT domains.

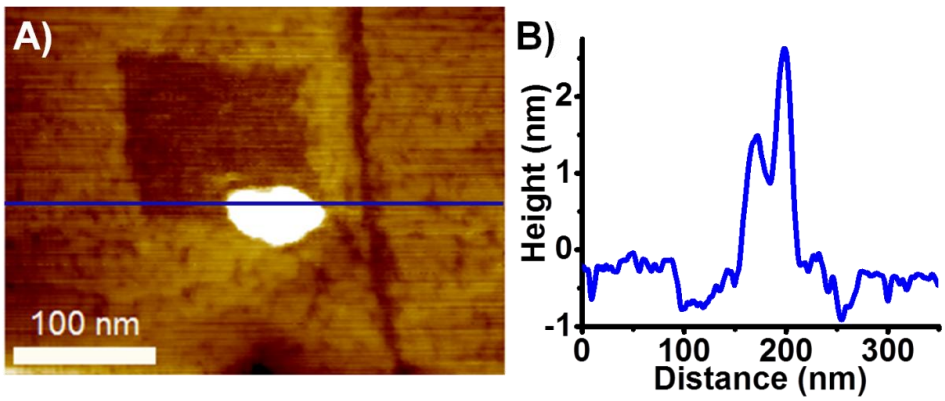

Figure 33. Large C5DT domain and reacted TPPF5 after 4 hours of immersion in 0.1 mM TPPF5 solution. A) AFM topography image and B) corresponding cross-section.

Because of the challenges that arise using such highly volatile and harsh solvents, the second variation involved replacing the TPPF5, DCM-based, solvent by ethanol. To do this, a co-absorbed C12/C5DT SAM was formed and characterized with AFM and STM with equivalent results as presented in Chapter IV and in Figure 19. Then, a 1 mM TPPF5 solution was sonciated for 10 minutes to disperse the insoluble TPPF5 in the ethanol. Finally, the co-absorbed C12/C5DT SAM was immersed in the 1 mM TPPF5 solution for 3 hours. AFM and STM images after immersion are shown in Figure 34. Similar to the DCM-based solution used in Chapter IV, after 3 hours immersion in the ethanol-based solution, bright features appear in the AFM and STM images indicating attachment of the TPPF5 to the C5DT domains. While some C5DT domains reacted with the TPPF5, others remained unreacted (Figure 34(B) and Figure 34(D)). Grain analysis of the AFM and STM images after the reaction yielded 107 and 38 detected TPPF5 features per 100 nm^2, respectively. On average the physical (extracted from AFM images) and apparent height (extracted from STM images) of the TPPF5 domains reacted from an ethanol solution was found to be 0.3±0.1 nm and 0.4±0.2 nm above the background C12 respectively. Additionally, on average the lateral dimension (extracted from STM images) of the TPPF5 domains reacted from an ethanol solution was found to be 2.9±1.4 nm. These TPPF5 dimensions and the number of detected TPPF5 features after 3 hours immersion are comparable to those obtained for the reaction in the DCM-based solution (Chapter IV). Therefore, these results indicate the possible versatility of the reaction of TPPF5 with surface bound C5DT that does not necessarily require a DCM-based solution. However, because TPPF5 is not soluble in ethanol, *in situ* AFM

was not possible because the 1 mM TPPF5 solution in ethanol dispersed the incident laser path resulting in insufficient laser signal on the photodiode and the inability to monitor the AFM tip.

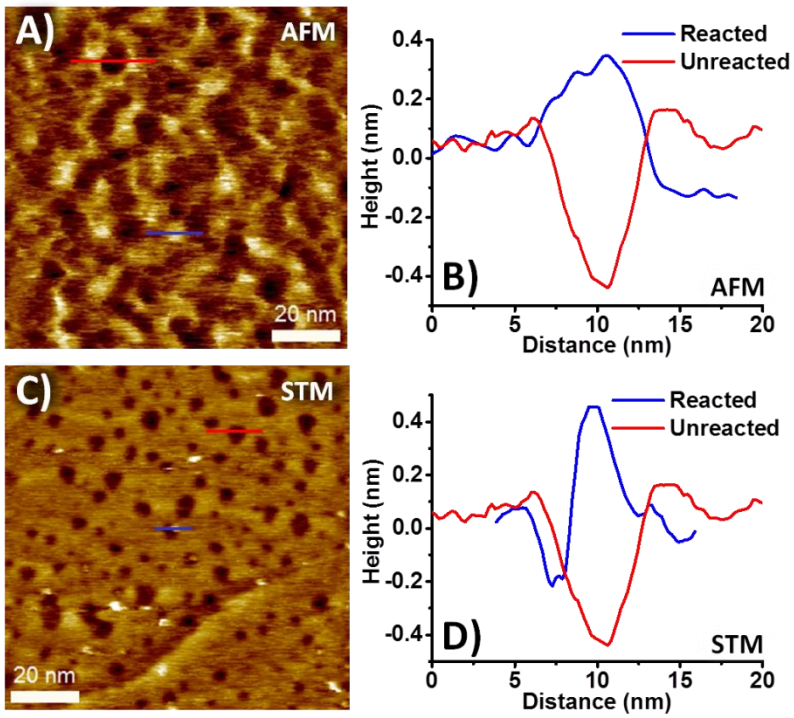

Figure 34. Co-absorbed C12/C5DT SAM after 3 hours immersion in 1 mM TPPF5 ethanol AFM topography image (A) showing the reacted TPPF5 islands which appear as bright protrusions and corresponding AFM cross-sections (B) of a TPPF5 domain as well as an unreacted C5DT domain. Similarly an STM image (C) is shown with corresponding cross-sections (D) of a TPPF5 domain and unreacted C5DT domain.

With the potential for complex porphyrin-containing materials and for molecular/organic materials in general, further future electronic investigations will call for new experimental techniques to elucidate the fine details of molecular transport. Previously and presently I-V characteristics have been and still are integral in

understating the electronic properties in molecular/organic materials, but are effected by atomistic details of the electrical contacts[225, 325-326] that are unclear during measurement and cannot be used to distinctly discern details such the dominance of hole or electron transport and energy level alignment.[327-329] In recent years, thermovoltage measurements have been decisive in elucidating the fine details of molecular transport unattainable from I-V characteristics alone.[330-333] For example, after much uncertainty using other methods, thermovoltage measurements of benzenethiol were robust enough to finally shown that the charge transport is dominated by holes and that the relative energy level alignment can be altered by perturbations in molecular structure, shifting the HOMO closer to the Fermi level by 1.2 eV.[327, 330, 334-337] Therefore, by this it is possible to examine the structure-function relationship of molecular assemblies fabricated though the two-step method in terms of HOMO-LUMO level alignment or "doping", which has been indispensable for traditional semi-conductors, to design a host of finely tuned molecular/organic structures. Thermovoltage measurements are usually carried-out by home-built adaptations to existing STM or AFM systems with either local point measurements in a break-junction configuration[330, 337] or through more advanced mapping.[338-339] The STM and AFM systems currently residing in the Batteas Research Group have the capacity to be adapted by utilizing the available heating stages and introducing a differential amplifier circuitry, but would require careful circuit design.[340-341] Alternatively the user facility at the Center for Nanophase Materials Science within Oak Ridge National Laboratory is available for advance thermovoltage mapping. Thermovoltage measurement have been a tool to access fundamental information

considering the charge transport, but recently there was a report on a method to acquire even more fundamental information; namely the transmission function (T(E)) within a molecular break-junction.[342] By directly measuring the transmission function, a detailed transmission map can be acquired instead of only providing a limited amount of data that is later related to the transmission function like in the case of I-V[343] and thermovoltage measurements.[330-331, 333] While there is potential for direct transmission function mapping, it is quite new and its applicability has yet to be seen.

5.2.2 Future Directions for Molecular/Organic Electronics

The farthermost limit of electronic device controllable design and miniaturization is directing the constituent components at the atomic level and this is possible with molecular/organic materials.[3, 344] Therefore, there is abounding work on using molecules and organics for electronic applications (see Chapter I and the references therein). The aim is to modify existing silicon-based and CMOS technology by incorporating molecular/organics as charge modulating components with future aims directed towards devices composed exclusively of molecular/organic materials and ultimately single molecule devices.[6, 180] Presently, it seems that molecular/organic materials will not replace silicon and semiconductor materials, but rather suited to compliment current technology with their inherent nanoscopic dimensions and increased, new functionality. Despite developments, there are areas requiring future advancement to achieve wide spread use of molecular/organic materials in electronic applications; namely in situ measurements,[345-346] device stability,[347-349] and fabrication techniques for integration.[196, 350-351]

In the work presented herein as well in other works, in situ measurements would be advantageous in providing valuable information on the electronic properties and the related physical properties during the charge transport process. Oftentimes, physical properties are characterized immediately before and after electronic measurements. But because of the reduced dimensions, molecular junctions are sensitive to atomistic details and local environment that can be perturbed during electronic measurements.[138, 330, 348-349] Without in situ physical characterization, the detailed structure-function relationship cannot be completely illuminated. As an example in the work presented herein, Chapter III described bias-induced and stochastic switching in porphyrin-thiol assemblies observed through fast (in comparison to STM imaging) STS I-V measurements. Although the assemblies were imaged before and after, the response of the assemblies under a sweeping applied bias could not be imaged. The need for fast, simultaneous imaging in other works as well. In nanogap junctions, TEM (Transmission Electron Microscopy) images could only be obtained after electromigration, leaving conductance changes and mechanisms related to physical changes during the electromigration process unclear.[345] Furthermore, molecules underwent a cis to trans conformation change when irradiated by ultra violet and visible light and IETS (Inelastic Tunneling Spectroscopy) measurements revealed isomer-identifying vibrational spectra.[345] But IETS could only be performed ex situ and the transition from cis to trans transformation could be not resolved.

Device stability is essential when evaluating the integrity of device function in addition to device to device variation. Instabilities arise from molecular and atomic-level

details such as nearest neighbor interactions, local environment, and atomistic details, especially in contacts at metal-molecule interface.[348-349] These molecular and atomic-level details are challenging to control, regularly leading to variations in assembled devices from sample to sample.[347] In an effort for control, fabrication methods and processing has been an area of research (see Section 1.5 and the references therein). For example, in Chapter III of this work the importance of nearest neighbor interactions and local environment of the elecro-active molecules was displayed with the loss of bias-induced switching in favor of stochastic switching in porphyrin-thiol assemblies when the stabilizing background alkanethiol SAM degraded. In fact, SAMs and Langmuir–Blodgett films are widely used to construct junctions and the bonds of which are labile introducing instabilities.[352] To improve stability in the work herein, in the future, alkanethiol SAM can be replaced with diacetylene-containing alkanethiols that will form robust cross-linking bonds upon UV-vis exposure.[353-355] Another strategy to improve stability is in the use of nanocarbon species such as carbon nanotubes and graphene to connect molecules to electrode surfaces.[351, 356-357] Contrary to their metallic counter parts, nanocarbon species are mechanically stable at the atomic level and are inherently functional at their edges. Nanocarbon species can be lithographically patterned into point contacts and functionalized at their edges with carboxyl acid and though amine tethers covalently bind molecules to the electrode surfaces. These types of contacts contribute to device stability by withstanding processing conditions like chemical treatments and operating conditions like applied, external stimuli. As a demonstration of stability, in

test-bed devices graphene was used to connect Cu phthalocyanine SAMs in a field effect transistor configuration with almost 100% reproducibility.[358]

Foreseeably, next generation electronic devices will be composed of networks of interfaces that dictate the functionality and molecules absorbed on these interfaces will be a means of functionality control. Therefore integrating molecules and organics into device configurations is paramount but methods merging silicon and semiconducting materials with molecules and organics are lacking.[350, 359] Bottom-up methods have been choice for processing molecules and organics and conversely, top-down methods have been choice for silicon-based and CMOS materials. A promising method to bridge these two methods is a combinatorial approach termed top-down assisted bottom-up or template-directed assembly in which structure, size, and local order is directed by using chemical templates.[196] The potential of template-directed assembly has been demonstrated in some reports where notably pre-designed electronic properties were achieved (see Chapter IV).[280] Another promising way to bridge silicon and semiconducting materials with molecules and organics is by using nanocarbon species like carbon nanotubes and graphene because they are suited for small molecular level contact, though their inherently functional edges, and can be indefinitely large, allowing contact to large macroscopic circuitry.[351, 356-357] The potential is evident is the fabrication of a new variety of hybrid field effect transistor where graphene bridged a Cu phthalocyanine SAM and metallic contacts which operated with large carrier motilities of 0.04 $cm^2 V^{-1} s^{-1}$ and high "on/off" ratio of 10^6 through an impressively small single monolayer, approximately 1 nm thick.[358]

5.3 Conclusion

Certainly, molecular/organic electronics will have a distinguished place in new and developing technology. However, at present molecular/organic materials have only been implemented in niche applications and in laboratory settings and research must still continue at the intersection of physics, engineering, materials science, and chemistry. To realize the potential of molecules and organics for electronics applications, the work presented herein has been concentrated on the fundamental electronic properties of molecular/organic materials and the utilization these electronic properties in a prescribed manner with strategies to controllably construct molecular/organic assembles. With this completion of this work, valuable questions have been researched in the directions of the limitations of electronic tunability by way of chemical subsistent in single porphyrin-thiol molecules, the effects of local order on the electronic properties of porphyrin-thiol assemblies, and finally a facile, template-directed fabrication method for molecular materials on surfaces which has produced a pre-designed electronic property when applied to porphyrin molecules. This work has advanced of molecular/organic electronics by providing knowledge essential for molecular-level device engineering with pre-designed functions. The impact of the acquired knowledge will continue into the future, especially with the foundation of the two-step template-directed assembly method with its versatility and immense combinatorial potential in engineering complex, multi-component molecular structures.

REFERENCES

1. Aviram, A.; Ratner, M. A., Molecular Rectifiers. *Chem. Phys. Lett.* **1974,** *29* (2), 277-283.

2. Talham, D. R., Conducting and Magnetic Langmuir-Blodgett Films. *Chem. Rev.* **2004,** *104* (11), 5479-5501.

3. Cuevas, J. C.; Scheer, E., *Molecular Electronics: An Introduction to Theory and Experiment*. World Scientific: Singapore, Singapore, **2010**; *1*, 1-726.

4. Binnig, G.; Rohrer, H., Scanning Tunneling Microscopy. *IBM J. Res. Dev.* **1986,** *30* (4), 355-369.

5. Binnig, G. K., Atomic-Force Microscopy. *Phys. Scr.* **1987,** *T19A*, 53-54.

6. Zhang, X. G.; Bauerle, P.; Aida, T.; Skabara, P.; Kagan, C., *Organic Electronics for a Better Tomorrow: Innovation, Accessibility, Sustainability*. Chemical Sciences and Society Summit (CS3): San Francisco, California, United States, **2012**; 1-34.

7. Son, J. Y.; Song, H., Molecular Scale Electronic Devices Using Single Molecules and Molecular Monolayers. *Curr. App. Phys.* **2013,** *13* (7), 1157-1171.

8. Salomon, A.; Cahen, D.; Lindsay, S.; Tomfohr, J.; Engelkes, V. B.; Frisbie, C. D., Comparison of Electronic Transport Measurements on Organic Molecules. *Adv. Mater.* **2003,** *15* (22), 1881-1890.

9. Jurow, M.; Schuckman, A. E.; Batteas, J. D.; Drain, C. M., Porphyrins as Molecular Electronic Components of Functional Devices. *Coord. Chem. Rev.* **2010,** *254* (19-20), 2297-2310.

10. Auwarter, W.; Ecija, D.; Klappenberger, F.; Barth, J. V., Porphyrins at Interfaces. *Nat. Chem.* **2015,** *7* (2), 105-120.

11. Smith, K. M., *Porphyrins and Metalloporphyrins: A New Edition Based on the Original Volume by J. E. Falk.* Elsevier: Amsterdam, New York, **1975**; 1-910.

12. Tanaka, T.; Osuka, A., Conjugated Porphyrin Arrays: Synthesis, Properties and Applications for Functional Materials. *Chem. Soc. Rev.* **2015,** *44* (4), 943-969.

13. Mauzerall, D., *Photosynthesis I: Porphyrins, Chlorophyll, and Photosynthesis*. Springer-Verlag Berlin Heidelberg: Berlin and Heidelberg, Germany, **1977**; *5*, 117-124.

14. Martinez-Diaz, M. V.; de la Torrea, G.; Torres, T., Lighting Porphyrins and Phthalocyanines for Molecular Photovoltaics. *Chem. Commun.* **2010,** *46* (38), 7090-7108.

15. Mathew, S.; Yella, A.; Gao, P.; Humphry-Baker, R.; Curchod, B. F. E.; Ashari-Astani, N.; Tavernelli, I.; Rothlisberger, U.; Nazeeruddin, M. K.; Gratzel, M., Dye-Sensitized Solar Cells with 13% Efficiency Achieved through the Molecular Engineering of Porphyrin Sensitizers. *Nat. Chem.* **2014,** *6* (3), 242-247.

16. Calvete, M.; Yang, G. Y.; Hanack, M., Porphyrins and Phthalocyanines as Materials for Optical Limiting. *Synth. Met.* **2004,** *141* (3), 231-243.

17. Imahori, H., Porphyrin-Fullerene Linked Systems as Artificial Photosynthetic Mimics. *Org. Biomol. Chem.* **2004,** *2* (10), 1425-1433.

18. Xie, Y. S.; Hill, J. P.; Charvet, R.; Ariga, K., Porphyrin Colorimetric Indicators in Molecular and Nano-Architectures. *J. Nanosci. Nanotechnol.* **2007,** *7* (9), 2969-2993.

19. Schuckman, A. E.; Ewers, B. W.; Yu, L. H.; Tome, J. P. C.; Perez, L. M.; Drain, C. M.; Kushmerick, J. G.; Batteas, J. D., Utilizing Nearest-Neighbor Interactions to Alter Charge Transport Mechanisms in Molecular Assemblies of Porphyrins on Surfaces. *J. Phys. Chem. C* **2015,** *119* (24), 13569-13579.

20. Chan, Y.-H.; Schuckman, A. E.; Pérez, L. M.; Vinodu, M.; Drain, C. M.; Batteas, J. D., Synthesis and Characterization of a Thiol-Tethered Tripyridyl Porphyrin on Au(111). *J. Phys. Chem. C* **2008,** *112* (15), 6110-6118.

21. Reed, M. A.; Zhou, C.; Muller, C. J.; Burgin, T. P.; Tour, J. M., Conductance of a Molecular Junction. *Sci.* **1997,** *278* (5336), 252-254.

22. Natelson, D., Mechanical Break Junctions: Enormous Information in a Nanoscale Package. *ACS Nano* **2012,** *6* (4), 2871-2876.

23. Xu, B. Q.; Tao, N. J. J., Measurement of Single-Molecule Resistance by Repeated Formation of Molecular Junctions. *Sci.* **2003,** *301* (5637), 1221-1223.

24. Chen, F.; Hihath, J.; Huang, Z. F.; Li, X. L.; Tao, N. J., Measurement of Single-Molecule Conductance. *Ann. Rev. Phys. Chem.* **2007,** *58*, 535-564.

25. Park, H.; Lim, A. K. L.; Alivisatos, A. P.; Park, J.; McEuen, P. L., Fabrication of Metallic Electrodes with Nanometer Separation by Electromigration. *Appl. Phys. Lett.* **1999,** *75* (2), 301-303.

26. Dadosh, T.; Gordin, Y.; Krahne, R.; Khivrich, I.; Mahalu, D.; Frydman, V.; Sperling, J.; Yacoby, A.; Bar-Joseph, I., Measurement of the Conductance of Single Conjugated Molecules. *Nat.* **2005,** *436* (7051), 677-680.

27. Kohn, W.; Sham, L. J., Self-Consistent Equations Including Exchange and Correlation Effects. *Phys. Rev.* **1965,** *140* (4A), 1133-&.

28. Hohenberg, P.; Kohn, W., Inhomogeneous Electron Gas. *Phys. Rev. B* **1964,** *136* (3B), B864.

29. Pecchia, A.; Di Carlo, A., Atomistic Theory of Transport in Organic and Inorganic Nanostructures. *Rep. Prog. Phys.* **2004,** *67* (8), 1497-1561.

30. Bruce, R. C.; Wang, R. B.; Rawson, J.; Therien, M. J.; You, W., Valence Band Dependent Charge Transport in Bulk Molecular Electronic Devices Incorporating Highly Conjugated Multi- (Porphinato)Metal Oligomers. *J. Am. Chem. Soc.* **2016,** *138* (7), 2078-2081.

31. Sedghi, G.; Garcia-Suarez, V. M.; Esdaile, L. J.; Anderson, H. L.; Lambert, C. J.; Martin, S.; Bethell, D.; Higgins, S. J.; Elliott, M.; Bennett, N.; Macdonald, J. E.; Nichols, R. J., Long-Range Electron Tunnelling in Oligo-Porphyrin Molecular Wires. *Nat. Nanotechnol.* **2011,** *6* (8), 517-523.

32. Lebedev, N.; Griva, I.; Blom, A., Internal Control of Electron Transfer through a Single Iron Atom by Chelating Porphyrin. *J. Phys. Chem. C* **2013,** *117* (14), 6933-6939.

33. Li, Z. H.; Borguet, E., Determining Charge Transport Pathways through Single Porphyrin Molecules Using Scanning Tunneling Microscopy Break Junctions. *J. Am. Chem. Soc.* **2012,** *134* (1), 63-66.

34. Tai, C. K.; Chuang, W. H.; Wang, B. C., Substituted Group and Side Chain Effects for the Porphyrin and Zinc(Ii)-Porphyrin Derivatives: A DFT and TD-DFT Study. *J. Lumines.* **2013,** *142*, 8-16.

35. Goh, Y. M.; Nam, W. W., Significant Electronic Effect of Porphyrin Ligand on the Reactivities of High-Valent Iron(IV) Oxo Porphyrin Cation Radical Complexes. *Inorg. Chem.* **1999,** *38* (5), 914-920.

36. Kiguchi, M.; Takahashi, T.; Kanehara, M.; Teranishi, T.; Murakoshi, K., Effect of End Group Position on the Formation of a Single Porphyrin Molecular Junction. *J. Phys. Chem. C* **2009,** *113* (21), 9014-9017.

37. Liu, Z. F.; Wei, S. J.; Yoon, H.; Adak, O.; Ponce, I.; Jiang, Y.; Jang, W. D.; Campos, L. M.; Venkataraman, L.; Neaton, J. B., Control of Single-Molecule Junction Conductance of Porphyrins Via a Transition-Metal Center. *Nano Lett.* **2014,** *14* (9), 5365-5370.

38. Sadeghi, H.; Sangtarash, S.; Lambert, C. J., Electron and Heat Transport in Porphyrin-Based Single-Molecule Transistors with Electro-Burnt Graphene Electrodes. *Beilstein J. Nanotechnol.* **2015,** *6*, 1413-1420.

39. Li, Z.; Park, T.-H.; Rawson, J.; Therien, M. J.; Borguet, E., Quasi-Ohmic Single Molecule Charge Transport through Highly Conjugated Meso-to-Meso Ethyne-Bridged Porphyrin Wires. *Nano Lett.* **2012,** *12* (6), 2722-2727.

40. Chiang, C. L.; Xu, C.; Han, Z. M.; Ho, W., Real-Space Imaging of Molecular Structure and Chemical Bonding by Single-Molecule Inelastic Tunneling Probe. *Sci.* **2014,** *344* (6186), 885-888.

41. Elemans, J.; Van Hameren, R.; Nolte, R. J. M.; Rowan, A. E., Molecular Materials by Self-Assembly of Porphyrins, Phthalocyanines, and Perylenes. *Adv. Mater.* **2006,** *18* (10), 1251-1266.

42. Jiao, J.; Nordfund, E.; Lindsey, J. S.; Bocian, D. F., Effects of Counterion Mobility, Surface Morphology, and Charge Screening on the Electron-Transfer Rates of Porphyrin Monolayers. *J. Phys. Chem. C* **2008,** *112* (15), 6173-6180.

43. Yokoyama, T.; Yokoyama, S.; Kamikado, T.; Okuno, Y.; Mashiko, S., Selective Assembly on a Surface of Supramolecular Aggregates with Controlled Size and Shape. *Nat.* **2001,** *413* (6856), 619-621.

44. Anariba, F.; Schmidt, L.; Muresan, A. Z.; Lindsey, J. S.; Bocian, D. F., Metal-Molecule Interactions Upon Deposition of Copper Overlayers on Reactively Functionalized Porphyrin Monolayers on Si(100). *Lang.* **2008,** *24* (13), 6698-6704.

45. Smith, A. R. G.; Ruggles, J. L.; Yu, A.; Gentle, I. R., Multilayer Nanostructured Porphyrin Arrays Constructed by Layer-by-Layer Self-Assembly. *Lang.* **2009,** *25* (17), 9873-9878.

46. Seol, M. L.; Choi, S. J.; Kim, C. H.; Moon, D. I.; Choi, Y. K., Porphyrin-Silicon Hybrid Field-Effect Transistor with Individually Addressable Top-Gate Structure. *ACS Nano* **2012,** *6* (1), 183-189.

47. Liu, Z. M.; Yasseri, A. A.; Lindsey, J. S.; Bocian, D. F., Molecular Memories That Survive Silicon Device Processing and Real-World Operation. *Sci.* **2003,** *302* (5650), 1543-1545.

48. Fabre, B., Ferrocene-Terminated Monolayers Covalently Bound to Hydrogen-Terminated Silicon Surfaces. Toward the Development of Charge Storage and Communication Devices. *Accounts Chem. Res.* **2010,** *43* (12), 1509-1518.

49. Mao, B. Y.; Calatayud, D. G.; Mirabello, V.; Hodges, B. J.; Martins, J. A. R.; Botchway, S. W.; Mitchels, J. M.; Pascu, S. I., Interactions between an Aryl Thioacetate-Functionalized Zn(II) Porphyrin and Graphene Oxide. *Adv. Funct. Mater.* **2016,** *26* (5), 687-697.

50. Montes, C. J.; Ojeda, M. L.; Gonzalez, F.; Garcia-Sanchez, M. A.; Rojas, F.; Velasquez, C., On Trapping Porphyrin Free-Bases between Graphene Oxide Plates. *Nan.* **2015,** *10* (4), 12.

51. Lindsey, J. S.; Bocian, D. F., Molecules for Charge-Based Information Storage. *Accounts Chem. Res.* **2011,** *44* (8), 638-650.

52. Suto, K.; Yoshimoto, S.; Itaya, K., Two-Dimensional Self-Organization of Phthalocyanine and Porphyrin: Dependence on the Crystallographic Orientation of Au. *J. Am. Chem. Soc.* **2003,** *125* (49), 14976-14977.

53. Jarvis, S. P.; Taylor, S.; Baran, J. D.; Thompson, D.; Saywell, A.; Mangham, B.; Champness, N. R.; Larsson, J. A.; Moriarty, P., Physisorption Controls the Conformation and Density of States of an Adsorbed Porphyrin. *J. Phys. Chem. C* **2015,** *119* (50), 27982-27994.

54. Qiu, X. H.; Nazin, G. V.; Ho, W., Vibrationally Resolved Fluorescence Excited with Submolecular Precision. *Sci.* **2003,** *299* (5606), 542-546.

55. Wang, A. J.; Yu, W.; Huang, Z. P.; Zhou, F.; Song, J. B.; Song, Y. L.; Long, L. L.; Cifuentes, M. P.; Humphrey, M. G.; Zhang, L.; Shao, J. D.; Zhang, C., Covalent Functionalization of Reduced Graphene Oxide with Porphyrin by Means of Diazonium Chemistry for Nonlinear Optical Performance. *Sci Rep* **2016,** *6*, 12.

56. Yoshimoto, S.; Higa, N.; Itaya, K., Two-Dimensional Supramolecular Organization of Copper Octaethylporphyrin and Cobalt Phthalocyanine on Au(111): Molecular Assembly Control at an Electrochemical Interface. *J. Am. Chem. Soc.* **2004,** *126* (27), 8540-8545.

57. Biswas, S.; Ahn, H.-Y.; Bondar, M. V.; Belfield, K. D., Two-Photon Absorption Enhancement of Polymer-Templated Porphyrin-Based J-Aggregates. *Lang.* **2012,** *28* (2), 1515-1522.

58. den Boer, D.; Habets, T.; Coenen, M. J. J.; van der Maas, M.; Peters, T. P. J.; Crossley, M. J.; Khoury, T.; Rowan, A. E.; Nolte, R. J. M.; Speller, S.; Elemans, J., Controlled Templating of Porphyrins by a Molecular Command Layer. *Lang.* **2011,** *27* (6), 2644-2651.

59. Li, Y.; Xiao, J.; Shubina, T. E.; Chen, M.; Shi, Z. L.; Schmid, M.; Steinruck, H. P.; Gottfried, J. M.; Lin, N., Coordination and Metalation Bifunctionality of Cu with 5,10,15,20-Tetra(4-Pyridyl)Porphyrin: Toward a Mixed-Valence Two-Dimensional Coordination Network. *J. Am. Chem. Soc.* **2012,** *134* (14), 6401-6408.

60. Fendt, L. A.; Stohr, M.; Wintjes, N.; Enache, M.; Jung, T. A.; Diederich, F., Modification of Supramolecular Binding Motifs Induced by Substrate Registry: Formation of Self-Assembled Macrocycles and Chain-Like Patterns. *Chem.-Eur. J.* **2009,** *15* (42), 11139-11150.

61. Drain, C. M.; Nifiatis, F.; Vasenko, A.; Batteas, J. D., Porphyrin Tessellation by Design: Metal-Mediated Self-Assembly of Large Arrays and Tapes. *Angew. Chem. Int. Ed.* **1998,** *37* (17), 2344-2347.

62. Heim, D.; Ecija, D.; Seutert, K.; Auwarter, W.; Aurisicchio, C.; Fabbro, C.; Bonifazi, D.; Barth, J. V., Self-Assembly of Flexible One-Dimensional Coordination Polymers on Metal Surfaces. *J. Am. Chem. Soc.* **2010,** *132* (19), 6783-6790.

63. Shi, Z. L.; Lin, N., Porphyrin-Based Two-Dimensional Coordination Kagome Lattice Self-Assembled on a Au(111) Surface. *J. Am. Chem. Soc.* **2009,** *131* (15), 5376.

64. Klappenberger, F.; Weber-Bargioni, A.; Auwarter, W.; Marschall, M.; Schiffrin, A.; Barth, J. V., Temperature Dependence of Conformation, Chemical State, and Metal-Directed Assembly of Tetrapyridyl-Porphyrin on Cu(111). *J. Chem. Phys.* **2008,** *129* (21).

65. Li, F. R.; Gentemann, S.; Kalsbeck, W. A.; Seth, J.; Lindsey, J. S.; Holten, D.; Bocian, D. F., Effects of Central Metal Ion (Mg, Zn) and Solvent on Singlet Excited-State Energy Flow in Porphyrin-Based Nanostructures. *J. Mater. Chem.* **1997,** *7* (7), 1245-1262.

66. Ahrenholtz, S. R.; Epley, C. C.; Morris, A. J., Solvothermal Preparation of an Electrocatalytic Metalloporphyrin Mof Thin Film and Its Redox Hopping Charge-Transfer Mechanism. *J. Am. Chem. Soc.* **2014,** *136* (6), 2464-2472.

67. Haq, S.; Hanke, F.; Dyer, M. S.; Persson, M.; Iavicoli, P.; Amabilino, D. B.; Raval, R., Clean Coupling of Unfunctionalized Porphyrins at Surfaces to Give Highly Oriented Organometallic Oligomers. *J. Am. Chem. Soc.* **2011,** *133* (31), 12031-12039.

68. Ecija, D.; Auwaerter, W.; Vijayaraghavan, S.; Seufert, K.; Bischoff, F.; Tashiro, K.; Barth, J. V., Assembly and Manipulation of Rotatable Cerium Porphyrinato Sandwich Complexes on a Surface. *Angew. Chem. Int. Ed.* **2011,** *50* (17), 3872-3877.

69. Yang, S. I.; Prathapan, S.; Miller, M. A.; Seth, J.; Bocian, D. F.; Lindsey, J. S.; Holten, D., Synthesis and Excited-State Photodynamics in Perylene-Porphyrin Dyads 2. Effects of Porphyrin Metalation State on the Energy-Transfer, Charge-Transfer, and Deactivation Channels. *J. Phys. Chem. B* **2001,** *105* (34), 8249-8258.

70. Rojas, G.; Chen, X.; Bravo, C.; Kim, J. H.; Kim, J. S.; Xiao, J.; Dowben, P. A.; Gao, Y.; Zeng, X. C.; Choe, W.; Enders, A., Self-Assembly and Properties of Nonmetalated Tetraphenyl-Porphyrin on Metal Substrates. *J. Phys. Chem. C* **2010,** *114* (20), 9408-9415.

71. Yokoyama, T.; Yokoyama, S.; Kamikado, T.; Mashiko, S., Nonplanar Adsorption and Orientational Ordering of Porphyrin Molecules on Au(111). *J. Chem. Phys.* **2001,** *115* (8), 3814-3818.

72. Jung, T. A.; Schlittler, R. R.; Gimzewski, J. K., Conformational Identification of Individual Adsorbed Molecules with the STM. *Nat.* **1997,** *386* (6626), 696-698.

73. Ribo, J. M.; Crusats, J.; Sagues, F.; Claret, J.; Rubires, R., Chiral Sign Induction by Vortices During the Formation of Mesophases in Stirred Solutions. *Sci.* **2001,** *292* (5524), 2063-2066.

74. Schwab, A. D.; Smith, D. E.; Rich, C. S.; Young, E. R.; Smith, W. F.; de Paula, J. C., Porphyrin Nanorods. *J. Phys. Chem. B* **2003,** *107* (41), 11339-11345.

75. Grill, L.; Dyer, M.; Lafferentz, L.; Persson, M.; Peters, M. V.; Hecht, S., Nano-Architectures by Covalent Assembly of Molecular Building Blocks. *Nat. Nanotechnol.* **2007,** *2* (11), 687-691.

76. Yang, H.; Zhang, S. L.; Han, L. H.; Zhang, Z.; Xue, Z.; Gao, J.; Li, Y. J.; Huang, C. S.; Yi, Y. P.; Liu, H. B.; Li, Y. L., High Conductive Two-Dimensional Covalent Organic Framework for Lithium Storage with Large Capacity. *ACS Appl. Mater. Interfaces* **2016,** *8* (8), 5366-5375.

77. Siles, P. F.; Bufon, C. C. B.; Grimm, D.; Jalil, A. R.; Mende, C.; Lungwitz, F.; Salvan, G.; Zahn, D. R. T.; Lang, H.; Schmidt, O. G., Morphology and Local Transport Characteristics of Metalloporphyrin Thin Films. *Org. Electron.* **2014,** *15* (7), 1432-1439.

78. Garai, A.; Kumar, M.; Sinha, W.; Chatterjee, S.; Purohit, C.; Som, T.; Kar, S., Synthesis, Electron Transport, and Charge Storage Properties of Fullerene–Zinc Porphyrin Hybrid Nanodiscs. *RSC Adv.* **2014,** *4* (109), 64119-64127.

79. Wang, C. S.; Bryce, M. R.; Gigon, J.; Ashwell, G. J.; Grace, I.; Lambert, C. J., Synthesis and Properties of Functionalized 4 nm Scale Molecular Wires with Thiolated Termini for Self-Assembly onto Metal Surfaces. *J. Org. Chem.* **2008,** *73* (13), 4810-4818.

80. Liljeroth, P.; Repp, J.; Meyer, G., Current-Induced Hydrogen Tautomerization and Conductance Switching of Naphthalocyanine Molecules. *Sci.* **2007,** *317* (5842), 1203-1206.

81. Auwarter, W.; Seufert, K.; Klappenberger, F.; Reichert, J.; Weber-Bargioni, A.; Verdini, A.; Cvetko, D.; Dell'Angela, M.; Floreano, L.; Cossaro, A.; Bavdek, G.; Morgante, A.; Seitsonen, A. P.; Barth, J. V., Site-Specific Electronic and Geometric Interface Structure of Co-Tetraphenyl-Porphyrin Layers on Ag(111). *Phys. Rev. B* **2010,** *81* (24).

82. Ralls, K. S.; Buhrman, R. A.; Tiberio, R. C., Fabrication of Thin-Film Metal Nanobridges. *Appl. Phys. Lett.* **1989,** *55* (23), 2459-2461.

83. Akkerman, H. B.; Blom, P. W. M.; de Leeuw, D. M.; de Boer, B., Towards Molecular Electronics with Large-Area Molecular Junctions. *Nat.* **2006,** *441* (7089), 69-72.

84. Garg, K.; Majumder, C.; Gupta, S. K.; Aswal, D. K.; Nayak, S. K.; Chattopadhyay, S., A Novel Design for Porphyrin Based D-S-A Systems as Molecular Rectifiers. *Chem. Sci.* **2016,** *7* (2), 1548-1557.

85. Strachan, J. P.; Gentemann, S.; Seth, J.; Kalsbeck, W. A.; Lindsey, J. S.; Holten, D.; Bocian, D. F., Effects of Orbital Ordering on Electronic Communication in Multiporphyrin Arrays. *J. Am. Chem. Soc.* **1997,** *119* (46), 11191-11201.

86. Wakayama, Y.; Kubota, T.; Suzuki, H.; Kamikado, T.; Mashiko, S., Molecular Coulomb Islands for Single-Electron Tunneling in Sio2/Molecular Layer/SiO2 Multilayers on Si(100). *J. Appl. Phys.* **2003,** *94* (7), 4711-4713.

87. D'Souza, F.; Ito, O., Supramolecular Donor-Acceptor Hybrids of Porphyrins/Phthalocyanines with Fullerenes/Carbon Nanotubes: Electron Transfer, Sensing, Switching, and Catalytic Applications. *Chem. Commun.* **2009,** (33), 4913-4928.

88. Hasobe, T.; Fukuzumi, S.; Kamat, P. V., Organized Assemblies of Single Wall Carbon Nanotubes and Porphyrin for Photochemical Solar Cells: Charge Injection from Excited Porphyrin into Single-Walled Carbon Nanotubes. *J. Phys. Chem. B* **2006,** *110* (50), 25477-25484.

89. Damrauer, N. H.; Hodgkiss, J. M.; Rosenthal, J.; Nocera, D. G., Observation of Proton-Coupled Electron Transfer by Transient Absorption Spectroscopy in a Hydrogen-Bonded, Porphyrin Donor-Acceptor Assembly. *J. Phys. Chem. B* **2004,** *108* (20), 6315-6321.

90. Wende, H.; Bernien, M.; Luo, J.; Sorg, C.; Ponpandian, N.; Kurde, J.; Miguel, J.; Piantek, M.; Xu, X.; Eckhold, P.; Kuch, W.; Baberschke, K.; Panchmatia, P. M.; Sanyal, B.; Oppeneer, P. M.; Eriksson, O., Substrate-Induced Magnetic Ordering and Switching of Iron Porphyrin Molecules. *Nat. Mater.* **2007,** *6* (7), 516-520.

91. Matino, F.; Arima, V.; Piacenza, M.; Della Sala, F.; Maruccio, G.; Phaneuf, R. J.; Del Sole, R.; Mele, G.; Vasapollo, G.; Gigli, G.; Cingolani, R.; Rinaldi, R., Rectification in Supramolecular Zinc Porphyrin/Fulleropyrrolidine Dyads Self-Organized on Gold(111). *Chem. Phys. Chem* **2009,** *10* (15), 2633-2641.

92. Li, Q. L.; Surthi, S.; Mathur, G.; Gowda, S.; Zhao, Q.; Sorenson, T. A.; Tenent, R. C.; Muthukumaran, K.; Lindsey, J. S.; Misra, V., Multiple-Bit Storage Properties of Porphyrin Monolayers on SiO2. *Appl. Phys. Lett.* **2004,** *85* (10), 1829-1831.

93. Zhang, H. H.; Zhang, Y. N.; Gu, C.; Ma, Y. G., Electropolymerized Conjugated Microporous Poly(Zinc-Porphyrin) Films as Potential Electrode Materials in Supercapacitors. *Adv. Energy Mater.* **2015,** *5* (10), 6.

94. Lysenko, A. B.; Thamyongkit, P.; Schmidt, I.; Diers, J. R.; Bocian, D. F.; Lindsey, J. S., Diverse Porphyrin Dimers as Candidates for High-Density Charge-Storage Molecules. *J. Porphyr. Phthalocyanines* **2006,** *10* (1), 22-32.

95. Sakurai, T.; Tashiro, K.; Honsho, Y.; Saeki, A.; Seki, S.; Osuka, A.; Muranaka, A.; Uchiyama, M.; Kim, J.; Ha, S.; Kato, K.; Takata, M.; Aida, T., Electron- or Hole-Transporting Nature Selected by Side-Chain-Directed Pi-Stacking Geometry: Liquid Crystalline Fused Metalloporphyrin Dimers. *J. Am. Chem. Soc.* **2011,** *133* (17), 6537-6540.

96. Niskanen, M.; Kuisma, M.; Cramariuc, O.; Golovanov, V.; Hukka, T. I.; Tkachenko, N.; Rantala, T. T., Porphyrin Adsorbed on the (1010) Surface of the Wurtzite Structure of Zno - Conformation Induced Effects on the Electron Transfer Characteristics. *Phys. Chem. Chem. Phys.* **2013,** *15* (40), 17408-17418.

97. Hoang, M. H.; Kim, Y.; Kim, M.; Kim, K. H.; Lee, T. W.; Nguyen, D. N.; Kim, S. J.; Lee, K.; Lee, S. J.; Choi, D. H., Unusually High-Performing Organic Field-Effect Transistors Based on Pi-Extended Semiconducting Porphyrins. *Adv. Mater.* **2012,** *24* (39), 5363-5367.

98. Hoang, M. H.; Ngo, T. T.; Nguyen, D. N., Effect of Molecular Packing of Zinc(II) Porphyrins on the Performance of Field-Effect Transistors. *Adv. Nat. Sci.-Nanosci. Nanotechnol.* **2014,** *5* (4), 6.

99. Li, J. Z.; Gryko, D.; Dabke, R. B.; Diers, J. R.; Bocian, D. F.; Kuhr, W. G.; Lindsey, J. S., Synthesis of Thiol-Derivatized Europium Porphyrinic Triple-Decker Sandwich Complexes for Multibit Molecular Information Storage. *J. Org. Chem.* **2000,** *65* (22), 7379-7390.

100. Balakumar, A.; Lysenko, A. B.; Carcel, C.; Malinovskii, V. L.; Gryko, D. T.; Schweikart, K. H.; Loewe, R. S.; Yasseri, A. A.; Liu, Z. M.; Bocian, D. F.; Lindsey, J. S., Diverse Redox-Active Molecules Bearing O-, S-, or Se-Terminated Tethers for Attachment to Silicon in Studies of Molecular Information Storage. *J. Org. Chem.* **2004,** *69* (5), 1435-1443.

101. Padmaja, K.; Youngblood, W. J.; Wei, L. Y.; Bocian, D. F.; Lindsey, J. S., Triple-Decker Sandwich Compounds Bearing Compact Triallyl Tripods for Molecular Information Storage Applications. *Inorg. Chem.* **2006,** *45* (14), 5479-5492.

102. Roth, K. M.; Liu, Z. M.; Gryko, D. T.; Clausen, C.; Lindsey, J. S.; Bocian, D. F.; Kuhr, W. G., *Molecules as Components of Electronic Devices: Charge-Retention Characteristics of Self-Assembled Monolayers of Molecular-Wire-Linked Porphyrins on Gold.* Symposium Series, American Chemical Society: Washington, DC, United States, **2003**; *844*, 51-61.

103. Li, Q. L.; Mathur, G.; Homsi, M.; Surthi, S.; Misra, V.; Malinovskii, V.; Schweikart, K. H.; Yu, L. H.; Lindsey, J. S.; Liu, Z. M.; Dabke, R. B.; Yasseri, A.; Bocian, D. F.; Kuhr, W. G., Capacitance and Conductance Characterization of Ferrocene-Containing Self-Assembled Monolayers on Silicon Surfaces for Memory Applications. *Appl. Phys. Lett.* **2002,** *81* (8), 1494-1496.

104. Wei, L. Y.; Syomin, D.; Loewe, R. S.; Lindsey, J. S.; Zaera, F.; Bocian, D. F., Structural and Electron-Transfer Characteristics of Carbon-Tethered Porphyrin Monolayers on Si(100). *J. Phys. Chem. B* **2005,** *109* (13), 6323-6330.

105. Padmaja, K.; Wei, L. Y.; Lindsey, J. S.; Bocian, D. F., A Compact All-Carbon Tripodal Tether Affords High Coverage of Porphyrins on Silicon Surfaces. *J. Org. Chem.* **2005,** *70* (20), 7972-7978.

106. Carroll, R. L.; Gorman, C. B., The Genesis of Molecular Electronics. *Angew. Chem. Int. Ed.* **2002,** *41* (23), 4379-4400.

107. Winkelmann, C. B.; Ionica, I.; Chevalier, X.; Royal, G.; Bucher, C.; Bouchiat, V., Optical Switching of Porphyrin-Coated Silicon Nanowire Field Effect Transistors. *Nano Lett.* **2007,** *7* (6), 1454-1458.

108. Thanopulos, I.; Paspalakis, E.; Yannopapas, V., Optical Switching of Electric Charge Transfer Pathways in Porphyrin: A Light-Controlled Nanoscale Current Router. *Nanotechnol.* **2008,** *19* (44), 14.

109. Vijayaraghavan, S.; Ecija, D.; Auwarter, W.; Joshi, S.; Seufert, K.; Seitsonen, A. P.; Tashiro, K.; Barth, J. V., Selective Supramolecular Fullerene-Porphyrin Interactions and Switching in Surface-Confined C-60-Ce(TPP)(2) Dyads. *Nano Lett.* **2012,** *12* (8), 4077-4083.

110. Ambroise, A.; Wagner, R. W.; Rao, P. D.; Riggs, J. A.; Hascoat, P.; Diers, J. R.; Seth, J.; Lammi, R. K.; Bocian, D. F.; Holten, D.; Lindsey, J. S., Design and Synthesis of Porphyrin-Based Optoelectronic Gates. *Chem. Mat.* **2001,** *13* (3), 1023-1034.

111. Zhou, Y. Z.; Ngo, K. T.; Zhang, B.; Feng, Y. Q.; Rochford, J., Synthesis, Electronic and Photophysical Characterization of Pi-Conjugated Meso-Ferrocenyl-Porphyrin Fluorescent Redox Switches. *Organometal.* **2014,** *33* (24), 7078-7090.

112. Li, Z. H.; Smeu, M.; Park, T. H.; Rawson, J.; Xing, Y. J.; Therien, M. J.; Ratner, M. A.; Borguet, E., Hapticity-Dependent Charge Transport through Carbodithioate-Terminated 5,15-Bis(Phenylethynyl)Porphinato Zinc(II) Complexes in Metal-Molecule-Metal Junctions. *Nano Lett.* **2014,** *14* (10), 5493-5499.

113. Wu, S. W.; Ogawa, N.; Nazin, G. V.; Ho, W., Conductance Hysteresis and Switching in a Single-Molecule Junction. *J. Phys. Chem. C* **2008,** *112* (14), 5241-5244.

114. Mondal, P.; Rath, S. P., Cyclic Zinc(Ii) Bisporphyrin-Based Molecular Switches: Supramolecular Control of Complexation-Mediated Conformational Switching and Photoinduced Electron Transfer. *Chem.-Eur. J.* **2016,** *22* (16), 5607-5619.

115. Feng, X.; Liu, L. L.; Honsho, Y.; Saeki, A.; Seki, S.; Irle, S.; Dong, Y. P.; Nagai, A.; Jiang, D. L., High-Rate Charge-Carrier Transport in Porphyrin Covalent Organic Frameworks: Switching from Hole to Electron to Ambipolar Conduction. *Angew. Chem. Int. Ed.* **2012,** *51* (11), 2618-2622.

116. Yella, A.; Lee, H. W.; Tsao, H. N.; Yi, C. Y.; Chandiran, A. K.; Nazeeruddin, M. K.; Diau, E. W. G.; Yeh, C. Y.; Zakeeruddin, S. M.; Gratzel, M., Porphyrin-Sensitized Solar Cells with Cobalt (II/III)-Based Redox Electrolyte Exceed 12% Efficiency. *Sci.* **2011,** *334* (6056), 629-634.

117. Li, L. L.; Diau, E. W. G., Porphyrin-Sensitized Solar Cells. *Chem. Soc. Rev.* **2013,** *42* (1), 291-304.

118. Zhao, L.; Wagner, P.; van der Salm, H.; Gordon, K. C.; Mori, S.; Mozer, A. J., Enhanced Electron Lifetimes in Dye-Sensitized Solar Cells Using a Dichromophoric Porphyrin: The Utility of Intermolecular Forces. *ACS Appl. Mater. Interfaces* **2015,** *7* (39), 22078-22083.

119. Roth, K. M.; Dontha, N.; Dabke, R. B.; Gryko, D. T.; Clausen, C.; Lindsey, J. S.; Bocian, D. F.; Kuhr, W. G., Molecular Approach toward Information Storage Based on the Redox Properties of Porphyrins in Self-Assembled Monolayers. *J. Vac. Sci. Technol. B* **2000,** *18* (5), 2359-2364.

120. Ma, P.; Chen, Y. L.; Cai, X.; Wang, H. L.; Zhang, Y. X.; Gao, Y. N.; Jiang, J. Z., Organic Field Effect Transistors Based on 5,10,15,20-Tetrakis(4-Pentyloxyphenyl)Porphyrin Single Crystal. *Synth. Met.* **2010,** *160* (5-6), 510-515.

121. Bessho, T.; Zakeeruddin, S. M.; Yeh, C.-Y.; Diau, E. W.-G.; Graetzel, M., Highly Efficient Mesoscopic Dye-Sensitized Solar Cells Based on Donor-Acceptor-Substituted Porphyrins. *Angew. Chem. Int. Ed.* **2010,** *49* (37), 6646-6649.

122. Borgström, M.; Blart, E.; Boschloo, G.; Mukhtar, E.; Hagfeldt, A.; Hammarström, L.; Odobel, F., Sensitized Hole Injection of Phosphorus Porphyrin into Nio: Toward New Photovoltaic Devices. *J. Phys. Chem. B* **2005,** *109* (48), 22928-22934.

123. Lee, C.-W.; Lu, H.-P.; Lan, C.-M.; Huang, Y.-L.; Liang, Y.-R.; Yen, W.-N.; Liu, Y.-C.; Lin, Y.-S.; Diau, E. W.-G.; Yeh, C.-Y., Novel Zinc Porphyrin Sensitizers for Dye-Sensitized Solar Cells: Synthesis and Spectral, Electrochemical, and Photovoltaic Properties. *Chem.-Eur. J.* **2009,** *15* (6), 1403-1412.

124. Lu, H.-P.; Tsai, C.-Y.; Yen, W.-N.; Hsieh, C.-P.; Lee, C.-W.; Yeh, C.-Y.; Diau, E. W.-G., Control of Dye Aggregation and Electron Injection for Highly Efficient Porphyrin Sensitizers Adsorbed on Semiconductor Films with Varying Ratios of Coadsorbate. *J. Phys. Chem. C* **2009,** *113* (49), 20990-20997.

125. Bi, D. Q.; Xu, B.; Gao, P.; Sun, L. C.; Graetzel, M.; Hagfeldt, A., Facile Synthesized Organic Hole Transporting Material for Perovskite Solar Cell with Efficiency of 19.8%. *Nano Enrg.* **2016,** *23*, 138-144.

126. Carli, S.; Baena, J. P. C.; Marianetti, G.; Marchetti, N.; Lessi, M.; Abate, A.; Caramori, S.; Graetzel, M.; Bellina, F.; Bignozzi, C. A.; Hagfeldt, A., A New 1,3,4-Oxadiazole-Based Hole-Transport Material for Efficient CH3NH3PbBr3 Perovskite Solar Cells. *Chem. Sus. Chem.* **2016,** *9* (7), 657-661.

127. Minari, T.; Seto, M.; Nemoto, T.; Isoda, S.; Tsukagoshi, K.; Aoyagi, Y., Molecular-Packing-Enhanced Charge Transport in Organic Field-Effect Transistors Based on Semiconducting Porphyrin Crystals. *Appl. Phys. Lett.* **2007,** *91* (12), 123501.

128. Payne, M. M.; Parkin, S. R.; Anthony, J. E.; Kuo, C.-C.; Jackson, T. N., Organic Field-Effect Transistors from Solution-Deposited Functionalized Acenes with Mobilities as High as 1 cm2/V·s. *J. Am. Chem. Soc.* **2005,** *127* (14), 4986-4987.

129. Andernach, R. E.; Rossbauer, S.; Ashraf, R. S.; Faber, H.; Anthopoulos, T. D.; McCulloch, I.; Heeney, M.; Bronstein, H. A., Conjugated Polymer-Porphyrin Complexes for Organic Electronics. *Chem. Phys. Chem.* **2015,** *16* (6), 1223-1230.

130. Baek, E.; Pregl, S.; Shaygan, M.; Romhildt, L.; Weber, W. M.; Mikolajick, T.; Ryndyk, D. A.; Baraban, L.; Cuniberti, G., Optoelectronic Switching of Nanowire-Based Hybrid Organic/Oxide/Semiconductor Field-Effect Transistors. *Nano Res.* **2015,** *8* (4), 1229-1240.

131. Choi, S.-J.; Lee, Y.-C.; Seol, M.-L.; Ahn, J.-H.; Kim, S.; Moon, D.-I.; Han, J.-W.; Mann, S.; Yang, J.-W.; Choi, Y.-K., Bio-Inspired Complementary Photoconductor by Porphyrin-Coated Silicon Nanowires. *Adv. Mater.* **2011,** *23* (34), 3979.

132. Seol, M.-L.; Choi, S.-J.; Choi, J.-M.; Ahn, J.-H.; Choi, Y.-K., Hybrid Porphyrin–Silicon Nanowire Field-Effect Transistor by Opto-Electrical Excitation. *ACS Nano* **2012,** *6* (9), 7885-7892.

133. Li, C.; Ly, J.; Lei, B.; Fan, W.; Zhang, D. H.; Han, J.; Meyyappan, M.; Thompson, M.; Zhou, C. W., Data Storage Studies on Nanowire Transistors with Self-Assembled Porphyrin Molecules. *J. Phys. Chem. B* **2004,** *108* (28), 9646-9649.

134. Star, A.; Lu, Y.; Bradley, K.; Gruner, G., Nanotube Optoelectronic Memory Devices. *Nano Lett.* **2004,** *4* (9), 1587-1591.

135. Ponce, J.; Arroyo, C. R.; Tatay, S.; Frisenda, R.; Gaviña, P.; Aravena, D.; Ruiz, E.; van der Zant, H. S. J.; Coronado, E., Effect of Metal Complexation on the Conductance of Single-Molecular Wires Measured at Room Temperature. *J. Am. Chem. Soc.* **2014,** *136* (23), 8314-8322.

136. Venkataraman, L.; Park, Y. S.; Whalley, A. C.; Nuckolls, C.; Hybertsen, M. S.; Steigerwald, M. L., Electronics and Chemistry: Varying Single-Molecule Junction Conductance Using Chemical Substituents. *Nano Lett.* **2007,** *7* (2), 502-506.

137. Choi, S. H.; Kim, B.; Frisbie, C. D., Electrical Resistance of Long Conjugated Molecular Wires. *Sci.* **2008,** *320* (5882), 1482-1486.

138. Park, J.; Pasupathy, A. N.; Goldsmith, J. I.; Chang, C.; Yaish, Y.; Petta, J. R.; Rinkoski, M.; Sethna, J. P.; Abruna, H. D.; McEuen, P. L.; Ralph, D. C., Coulomb Blockade and the Kondo Effect in Single-Atom Transistors. *Nat.* **2002,** *417* (6890), 722-725.

139. Besar, K.; Ardona, H. A. M.; Tovar, J. D.; Katz, H. E., Demonstration of Hole Transport and Voltage Equilibration in Self-Assembled Pi-Conjugated Peptide Nanostructures Using Field-Effect Transistor Architectures. *ACS Nano* **2015,** *9* (12), 12401-12409.

140. Kretz, B.; Egger, D. A.; Zojer, E., A Toolbox for Controlling the Energetics and Localization of Electronic States in Self-Assembled Organic Monolayers. *Adv. Sci.* **2015,** *2* (3).

141. Kroger, M.; Hamwi, S.; Meyer, J.; Riedl, T.; Kowalsky, W.; Kahn, A., P-Type Doping of Organic Wide Band Gap Materials by Transition Metal Oxides: A Case-Study on Molybdenum Trioxide. *Org. Electron.* **2009,** *10* (5), 932-938.

142. Vilan, A.; Ghabboun, J.; Cahen, D., Molecule−Metal Polarization at Rectifying GaAs Interfaces. *J. Phys. Chem. B* **2003,** *107* (26), 6360-6376.

143. Toledano, T.; Sazan, H.; Mukhopadhyay, S.; Alon, H.; Lerman, K.; Bendikov, T.; Major, D. T.; Sukenik, C. N.; Vilan, A.; Cahen, D., Odd-Even Effect in Molecular Electronic Transport Via an Aromatic Ring. *Lang.* **2014,** *30* (45), 13596-13605.

144. Wang, D. D.; Fracasso, D.; Nurbawono, A.; Annadata, H. V.; Sangeeth, C. S. S.; Yuan, L.; Nijhuis, C. A., Tuning the Tunneling Rate and Dielectric Response of SAM-Based Junctions Via a Single Polarizable Atom. *Adv. Mater.* **2015,** *27* (42), 6689.

145. Jones, B. A.; Facchetti, A.; Wasielewski, M. R.; Marks, T. J., Tuning Orbital Energetics in Arylene Diimide Semiconductors. Materials Design for Ambient Stability of N-Type Charge Transport. *J. Am. Chem. Soc.* **2007,** *129* (49), 15259-15278.

146. Nerngchamnong, N.; Yuan, L.; Qi, D.-C.; Li, J.; Thompson, D.; Nijhuis, C. A., The Role of Van Der Waals Forces in the Performance of Molecular Diodes. *Nat. Nanotechnol.* **2013,** *8* (2), 113-118.

147. Yoon, H. J.; Shapiro, N. D.; Park, K. M.; Thuo, M. M.; Soh, S.; Whitesides, G. M., The Rate of Charge Tunneling through Self-Assembled Monolayers Is Insensitive to Many Functional Group Substitutions. *Angew. Chem. Int. Ed.* **2012,** *51* (19), 4658-4661.

148. Kong, G. D.; Kim, M.; Jang, H.-J.; Liao, K.-C.; Yoon, H. J., Influence of Halogen Substitutions on Rates of Charge Tunneling across SAM-Based Large-Area Junctions. *Phys. Chem. Chem. Phys.* **2015,** *17* (21), 13804-13807.

149. Bowers, C. M.; Liao, K.-C.; Yoon, H. J.; Rappoport, D.; Baghbanzadeh, M.; Simeone, F. C.; Whitesides, G. M., Introducing Ionic and/or Hydrogen Bonds into the SAM//Ga2O3 Top-Interface of Ag-TS/S(CH2)(N)T//Ga2O3/EGain Junctions. *Nano Lett.* **2014,** *14* (6), 3521-3526.

150. Mandal, B.; Sarkar, S.; Sarkar, P., Exploring the Electronic Structure of Graphene Quantum Dots. *J. Nanopart. Res.* **2012,** *14* (12), 8.

151. Miguel, D.; Álvarez de Cienfuegos, L.; Martín-Lasanta, A.; Morcillo, S. P.; Zotti, L. A.; Leary, E.; Bürkle, M.; Asai, Y.; Jurado, R.; Cárdenas, D. J.; Rubio-Bollinger, G.; Agraït, N.; Cuerva, J. M.; González, M. T., Toward Multiple Conductance Pathways with Heterocycle-Based Oligo(Phenyleneethynylene) Derivatives. *J. Am. Chem. Soc.* **2015,** *137* (43), 13818-13826.

152. Fracasso, D.; Muglali, M. I.; Rohwerder, M.; Terfort, A.; Chiechi, R. C., Influence of an Atom in EGain/Ga2O3 Tunneling Junctions Comprising Self-Assembled Monolayers. *J. Phys. Chem. C* **2013,** *117* (21), 11367-11376.

153. Vilan, A.; Shanzer, A.; Cahen, D., Molecular Control over Au/GaAs Diodes. *Nat.* **2000,** *404* (6774), 166-168.

154. Toledano, T.; Biller, A.; Bendikov, T.; Cohen, H.; Vilan, A.; Cahen, D., Controlling Space Charge of Oxide-Free Si by in Situ Modification of Dipolar Alkyl Monolayers. *J. Phys. Chem C* **2012,** *116* (21), 11434-11443.

155. Kovalchuk, A.; Abu-Husein, T.; Fracasso, D.; Egger, D. A.; Zojer, E.; Zharnikov, M.; Terfort, A.; Chiechi, R. C., Transition Voltages Respond to Synthetic Reorientation of Embedded Dipoles in Self-Assembled Monolayers. *Chem. Sci.* **2016,** *7* (1), 781-787.

156. Yoon, H. J.; Bowers, C. M.; Baghbanzadeh, M.; Whitesides, G. M., The Rate of Charge Tunneling Is Insensitive to Polar Terminal Groups in Self-Assembled Monolayers in (AgS)-S-Ts(CH2)(N)M(CH2)(M)T//Ga2O3/EGain Junctions. *J. Am. Chem. Soc.* **2014,** *136* (1), 16-19.

157. Bowers, C. M.; Liao, K. C.; Yoon, H. J.; Rappoport, D.; Baghbanzadeh, M.; Simeone, F. C.; Whitesides, G. M., Introducing Ionic and/or Hydrogen Bonds into the Sam//Ga2o3 Top-Interface of Ag-TS/S(CH2)(N)T//Ga2O3/EGain Junctions. *Nano Lett.* **2014,** *14* (6), 3521-3526.

158. Sayed, S. Y.; Bayat, A.; Kondratenko, M.; Leroux, Y.; Hapiot, P.; McCreery, R. L., Bilayer Molecular Electronics: All-Carbon Electronic Junctions Containing Molecular Bilayers Made with "Click" Chemistry. *J. Am. Chem. Soc.* **2013,** *135* (35), 12972-12975.

159. Selzer, Y.; Cai, L. T.; Cabassi, M. A.; Yao, Y. X.; Tour, J. M.; Mayer, T. S.; Allara, D. L., Effect of Local Environment on Molecular Conduction: Isolated Molecule Versus Self-Assembled Monolayer. *Nano Lett.* **2005,** *5* (1), 61-65.

160. Pathak, A.; Bora, A.; Liao, K. C.; Schmolke, H.; Jung, A.; Klages, C. P.; Schwartz, J.; Tornow, M., Disorder-Derived, Strong Tunneling Attenuation in Bis-Phosphonate Monolayers. *J. Phys.-Cond. Matt.* **2016,** *28* (9), 12.

161. Heimel, G.; Rissner, F.; Zojer, E., Modeling the Electronic Properties of Pi-Conjugated Self-Assembled Monolayers. *Adv. Mater.* **2010,** *22* (23), 2494-2513.

162. Wang, L. J.; Rangger, G. M.; Romaner, L.; Heimel, G.; Bucko, T.; Ma, Z. Y.; Li, Q. K.; Shuai, Z.; Zojer, E., Electronic Structure of Self-Assembled Monolayers on Au(111) Surfaces: The Impact of Backbone Polarizability. *Adv. Funct. Mater.* **2009,** *19* (23), 3766-3775.

163. Romaner, L.; Heimel, G.; Zojer, E., Electronic Structure of Thiol-Bonded Self-Assembled Monolayers: Impact of Coverage. *Phys. Rev. B* **2008,** *77* (4).

164. Romaner, L.; Heimel, G.; Ambrosch-Draxl, C.; Zojer, E., The Dielectric Constant of Self-Assembled Monolayers. *Adv. Funct. Mater.* **2008,** *18* (24), 3999-4006.

165. Reuter, M. G.; Seideman, T.; Ratner, M. A., Molecular Conduction through Adlayers: Cooperative Effects Can Help or Hamper Electron Transport. *Nano Lett.* **2011,** *11* (11), 4693-4696.

166. Reuter, M. G.; Hersam, M. C.; Seideman, T.; Ratner, M. A., Signatures of Cooperative Effects and Transport Mechanisms in Conductance Histograms. *Nano Lett.* **2012,** *12* (5), 2243-2248.

167. Rahe, P.; Steele, R. P.; Williams, C. C., Consecutive Charging of a Molecule-on-Insulator Ensemble Using Single Electron Tunnelling Methods. *Nano Lett.* **2016,** *16* (2), 911-916.

168. Hummon, M. R.; Stollenwerk, A. J.; Narayanamurti, V.; Anikeeva, P. O.; Panzer, M. J.; Wood, V.; Bulovic, V., Measuring Charge Trap Occupation and Energy Level in CdSe/ZnS Quantum Dots Using a Scanning Tunneling Microscope. *Phys. Rev. B* **2010,** *81* (11).

169. Zheng, N.; Johnson, J. P.; Williams, C. C.; Wang, G., Electronic Characterization of Individual Monolayer Protected Au Clusters by Single Electron Tunneling Force Spectroscopy. *Nanotechnol.* **2010,** *21* (29).

170. Wold, D. J.; Haag, R.; Rampi, M. A.; Frisbie, C. D., Distance Dependence of Electron Tunneling through Self-Assembled Monolayers Measured by Conducting Probe Atomic Force Microscopy: Unsaturated Versus Saturated Molecular Junctions. *J. Phys. Chem. B* **2002,** *106* (11), 2813-2816.

171. Kronemeijer, A. J.; Huisman, E. H.; Akkerman, H. B.; Goossens, A. M.; Katsouras, I.; van Hal, P. A.; Geuns, T. C. T.; van der Molen, S. J.; Blom, P. W. M.; de Leeuw, D. M., Electrical Characteristics of Conjugated Self-Assembled Monolayers in Large-Area Molecular Junctions. *Appl. Phys. Lett.* **2010,** *97* (17).

172. Rissner, F.; Egger, D. A.; Romaner, L.; Heimel, G.; Zojer, E., The Electronic Structure of Mixed Self-Assembled Monolayers. *ACS Nano* **2010,** *4* (11), 6735-6746.

173. Folkers, J. P.; Laibinis, P. E.; Whitesides, G. M., Self-Assembled Monolayers of Alkanethiols on Gold: Comparisons of Monolayers Containing Mixtures of Short- and Long-Chain Constituents with CH3 and CH2OH Terminal Groups. *Lang.* **1992,** *8* (5), 1330-1341.

174. Wu, K.-Y.; Yu, S.-Y.; Tao, Y.-T., Continuous Modulation of Electrode Work Function with Mixed Self-Assembled Monolayers and Its Effect in Charge Injection. *Lang.* **2009,** *25* (11), 6232-6238.

175. Bottari, G.; de la Torre, G.; Torres, T., Phthalocyanine-Nanocarbon Ensembles: From Discrete Molecular and Supramolecular Systems to Hybrid Nanomaterials. *Accounts Chem. Res.* **2015,** *48* (4), 900-910.

176. Bartelmess, J.; Ehli, C.; Cid, J.-J.; Garcia-Iglesias, M.; Vazquez, P.; Torres, T.; Guldi, D. M., Tuning and Optimizing the Intrinsic Interactions between Phthalocyanine-Based PPV Oligomers and Single-Wall Carbon Nanotubes toward N-Type/P-Type. *Chem. Sci.* **2011,** *2* (4), 652-660.

177. Bartelmess, J.; Ehli, C.; Cid, J.-J.; Garcia-Iglesias, M.; Vazquez, P.; Torres, T.; Guldi, D. M., Screening Interactions of Zinc Phthalocyanine-Ppv Oligomers with Single Wall Carbon Nanotubes-a Comparative Study. *J. Mater. Chem.* **2011,** *21* (22), 8014-8020.

178. Salome Rodriguez-Morgade, M.; Plonska-Brzezinska, M. E.; Athans, A. J.; Carbonell, E.; de Miguel, G.; Guldi, D. M.; Echegoyen, L.; Torres, T., Synthesis, Characterization, and Photoinduced Electron Transfer Processes of Orthogonal Ruthenium Phthalocyanine-Fullerene Assemblies. *J. Am. Chem. Soc.* **2009,** *131* (30), 10484-10496.

179. Onclin, S.; Ravoo, B. J.; Reinhoudt, D. N., Engineering Silicon Oxide Surfaces Using Self-Assembled Monolayers. *Angew. Chem. Int. Ed.* **2005,** *44* (39), 6282-6304.

180. Xiang, D.; Wang, X.; Jia, C.; Lee, T.; Guo, X., Molecular-Scale Electronics: From Concept to Function. *Chem. Rev.* **2016,** *116* (7), 4318-440.

181. Wang, L.; Sun, Y. J.; Li, Z.; Wu, A. G.; Wei, G., Bottom-up Synthesis and Sensor Applications of Biomimetic Nanostructures. *Mater.* **2016,** *9* (1), 28.

182. Piner, R. D.; Zhu, J.; Xu, F.; Hong, S. H.; Mirkin, C. A., "Dip-Pen" Nanolithography. *Sci.* **1999,** *283* (5402), 661-663.

183. Zhang, W.; Anaya, M.; Lozano, G.; Calvo, M. E.; Johnston, M. B.; Miguez, H.; Snaith, H. J., Highly Efficient Perovskite Solar Cells with Tunable Structural Color. *Nano Lett.* **2015,** *15* (3), 1698-1702.

184. Chen, X.; Lenhert, S.; Hirtz, M.; Lu, N.; Fuchs, H.; Chi, L., Langmuir-Blodgett Patterning: A Bottom-up Way to Build Mesostructures over Large Areas. *Accounts Chem. Res.* **2007,** *40* (6), 393-401.

185. Love, J. C.; Estroff, L. A.; Kriebel, J. K.; Nuzzo, R. G.; Whitesides, G. M., Self-Assembled Monolayers of Thiolates on Metals as a Form of Nanotechnology. *Chem. Rev.* **2005,** *105* (4), 1103-1170.

186. *Monolayer Films That Assemble Themselves*. New Scientist: United Kingdom, **1983**; *98*, 20.

187. Netzer, L.; Sagiv, J., A New Approach to Construction of Artificial Monolayer Assemblies. *J. Am. Chem. Soc.* **1983,** *105* (3), 674-676.

188. Sagiv, J., Organized Monolayers by Adsorption. 1. Formation and Structure of Oleophobic Mixed Monolayers on Solid Surfaces. *J. Am. Chem. Soc.* **1980,** *102* (1), 92-98.

189. Bigelow, W. C.; Pickett, D. L.; Zisman, W. A., Oleophobic Monolayers. *J. Coll. Sci.* **1946,** *1* (6), 513-538.

190. Bigelow, W. C.; Glass, E.; Zisman, W. A., Oleophobic Monolayers. II. Temperature Effects and Energy of Adsorption. *J. Coll. Sci.* **1947,** *2* (6), 563-591.

191. Love, J. C.; Estroff, L. A.; Kriebel, J. K.; Nuzzo, R. G.; Whitesides, G. M., Self-Assembled Monolayers of Thiolates on Metals as a Form of Nanotechnology. *Chem. Rev.* **2005,** *105* (4), 1103-1169.

192. Hasan, A.; Pandey, L. M., Review: Polymers, Surface-Modified Polymers, and Self Assembled Monolayers as Surface-Modifying Agents for Biomaterials. *Polym.-Plast. Technol. Eng.* **2015,** *54* (13), 1358-1378.

193. Rothemund, P. W. K., Folding DNA to Create Nanoscale Shapes and Patterns. *Nat.* **2006,** *440* (7082), 297-302.

194. Liu, G. Y.; Xu, S.; Qian, Y. L., Nanofabrication of Self-Assembled Monolayers Using Scanning Probe Lithography. *Accounts Chem. Res.* **2000,** *33* (7), 457-466.

195. Liu, M.; Amro, N. A.; Liu, G.-y., Annual Review of Physical Chemistry: Nanografting for Surface Physical Chemistry. *Ann. Rev. Phys. Chem.* **2008,** *59*, 367-386.

196. Wang, W. C.; Chi, L. F., Area-Selective Growth of Functional Molecular Architectures. *Accounts Chem. Res.* **2012,** *45* (10), 1646-1656.

197. Liu, G. Y.; Amro, N. A., Positioning Protein Molecules on Surfaces: A Nanoengineering Approach to Supramolecular Chemistry. *Proceed. Natl. Acad. Sci. USA* **2002,** *99* (8), 5165-5170.

198. Ngunjiri, J. N.; Kelley, A. T.; Lejeune, Z. M.; Li, J. R.; Lewandowski, B. R.; Serem, W. K.; Daniels, S. L.; Lusker, K. L.; Garno, J. C., Achieving Precision and Reproducibility for Writing Patterns of N-Alkanethiol Self-Assembled Monolayers with Automated Nanografting. *Scan.* **2008,** *30* (2), 123-136.

199. Bu, D. L.; Mullen, T. J.; Liu, G. Y., Regulation of Local Structure and Composition of Binary Disulfide and Thiol Self-Assembled Monolayers Using Nanografting. *ACS Nano* **2010,** *4* (11), 6863-6873.

200. Liang, J.; Scoles, G., Nanografting of Alkanethiols by Tapping Mode Atomic Force Microscopy. *Lang.* **2007,** *23* (11), 6142-6147.

201. Yu, J. H.; Ngunjiri, J. N.; Kelley, A. T.; Gano, J. C., Nanografting Versus Solution Self-Assembly of Alpha,Omega-Alkanedithiols on Au(111) Investigated by AFM. *Lang.* **2008,** *24* (20), 11661-11668.

202. Loo, Y. L.; Willett, R. L.; Baldwin, K. W.; Rogers, J. A., Additive, Nanoscale Patterning of Metal Films with a Stamp and a Surface Chemistry Mediated Transfer Process: Applications in Plastic Electronics. *Appl. Phys. Lett.* **2002,** *81* (3), 562-564.

203. Xu, S.; Miller, S.; Laibinis, P. E.; Liu, G. Y., Fabrication of Nanometer Scale Patterns within Self-Assembled Monolayers by Nanografting. *Lang.* **1999,** *15* (21), 7244-7251.

204. Alivisatos, A. P.; Johnsson, K. P.; Peng, X. G.; Wilson, T. E.; Loweth, C. J.; Bruchez, M. P.; Schultz, P. G., Organization of 'Nanocrystal Molecules' Using DNA. *Nat.* **1996,** *382* (6592), 609-611.

205. Whitelam, S., Examples of Molecular Self-Assembly at Surfaces. *Adv. Mater.* **2015,** *27* (38), 5720-5725.

206. Hu, X. Y.; Zha, B.; Wu, Y. C.; Miao, X. R.; Deng, W. L., Effects of the Position and Number of Bromine Substituents on the Concentration-Mediated 2D Self-Assembly of Phenanthrene Derivatives. *Phys. Chem. Chem. Phys.* **2016,** *18* (10), 7208-7215.

207. Aluicio-Sarduy, E.; Singh, R.; Kan, Z. P.; Ye, T. L.; Baidak, A.; Calloni, A.; Berti, G.; Duo, L.; Iosifidis, A.; Beaupre, S.; Leclerc, M.; Butt, H. J.; Floudas, G.; Keivanidis, P. E., Elucidating the Impact of Molecular Packing and Device Architecture on the Performance of Nanostructured Perylene Diimide Solar Cells. *ACS Appl. Mater. Interfaces* **2015,** *7* (16), 8687-8698.

208. Palma, C. A.; Joshi, S.; Hoh, T.; Ecija, D.; Barth, J. V.; Auwarter, W., Two-Level Spatial Modulation of Vibronic Conductance in Conjugated Oligophenylenes on Boron Nitride. *Nano Lett.* **2015,** *15* (4), 2242-2248.

209. Pudzs, K.; Vembris, A.; Grzibovskis, R.; Latvels, J.; Zarins, E., Impact of the Molecular Structure of an Indandione Fragment Containing Azobenzene Derivatives on the Morphology and Electrical Properties of Thin Films. *Mater. Chem. Phys.* **2016,** *173*, 117-125.

210. Joachim, C.; Gimzewski, J. K.; Aviram, A., Electronics Using Hybrid-Molecular and Mono-Molecular Devices. *Nat.* **2000,** *408* (6812), 541-548.

211. Sforazzini, G.; Orentas, E.; Bolag, A.; Sakai, N.; Matile, S., Toward Oriented Surface Architectures with Three Coaxial Charge-Transporting Pathways. *J. Am. Chem. Soc.* **2013,** *135* (32), 12082-12090.

212. Wu, Y. L.; Nalluri, S. K. M.; Young, R. M.; Krzyaniak, M. D.; Margulies, E. A.; Stoddart, J. F.; Wasielewski, M. R., Charge and Spin Transport in an Organic Molecular Square. *Angew. Chem. Int. Ed.* **2015,** *54* (41), 11971-11977.

213. Schneebeli, S. T.; Frasconi, M.; Liu, Z.; Wu, Y.; Gardner, D. M.; Strutt, N. L.; Cheng, C.; Carmieli, R.; Wasielewski, M. R.; Stoddart, J. F., Electron Sharing and Anion-Pi Recognition in Molecular Triangular Prisms. *Angew. Chem. Int. Ed.* **2013,** *52* (49), 13100-13104.

214. Wu, Y.; Frasconi, M.; Gardner, D. M.; McGonigal, P. R.; Schneebeli, S. T.; Wasielewski, M. R.; Stoddart, J. F., Electron Delocalization in a Rigid Cofacial Naphthalene-1,8:4,5-Bis(Dicarboximide) Dimer. *Angew. Chem. Int. Ed.* **2014,** *53* (36), 9476-9481.

215. Sakai, N.; Lista, M.; Kel, O.; Sakurai, S.; Emery, D.; Mareda, J.; Vauthey, E.; Matile, S., Self-Organizing Surface-Initiated Polymerization: Facile Access to Complex Functional Systems. *J. Am. Chem. Soc.* **2011,** *133* (39), 15224-15227.

216. Lista, M.; Orentas, E.; Areephong, J.; Charbonnaz, P.; Wilson, A.; Zhao, Y. J.; Bolag, A.; Sforazzini, G.; Turdean, R.; Hayashi, H.; Domoto, Y.; Sobczuk, A.; Sakai, N.; Matile, S., Self-Organizing Surface-Initiated Polymerization, Templated Self-Sorting and Templated Stack Exchange: Synthetic Methods to Build Complex Systems. *Org. Biomol. Chem.* **2013,** *11* (11), 1754-1765.

217. Engelkes, V. B.; Beebe, J. M.; Frisbie, C. D., Length-Dependent Transport in Molecular Junctions Based on Sams of Alkanethiols and Alkanedithiols: Effect of Metal Work Function and Applied Bias on Tunneling Efficiency and Contact Resistance. *J. Am. Chem. Soc.* **2004,** *126* (43), 14287-14296.

218. Fan, F. R. F.; Yang, J. P.; Cai, L. T.; Price, D. W.; Dirk, S. M.; Kosynkin, D. V.; Yao, Y. X.; Rawlett, A. M.; Tour, J. M.; Bard, A. J., Charge Transport through Self-Assembled Monolayers of Compounds of Interest in Molecular Electronics. *J. Am. Chem. Soc.* **2002,** *124* (19), 5550-5560.

219. Moth-Poulsen, K.; Patrone, L.; Stuhr-Hansen, N.; Christensen, J. B.; Bourgoin, J. P.; Bjornholm, T., Probing the Effects of Conjugation Path on the Electronic Transmission through Single Molecules Using Scanning Tunneling Microscopy. *Nano Lett.* **2005,** *5* (4), 783-785.

220. Lindsey, J. S., Synthetic Routes to Meso-Patterned Porphyrins. *Accounts Chem. Res.* **2010,** *43* (2), 300-311.

221. Jiao, J. Y.; Thamyongkit, P.; Schmidt, I.; Lindsey, J. S.; Bocian, D. F., Characterization of Porphyrin Surface Orientation in Monolayers on Au(111) and Si(100) Using Spectroscopically Labeled Molecules. *J. Phys. Chem. C* **2007,** *111* (34), 12693-12704.

222. Jiao, J. Y.; Taniguchi, M.; Lindsey, J. S.; Bocian, D. F., Activation Energies for Oxidation of Porphyrin Monolayers Anchored to Au(111). *Lang.* **2010,** *26* (20), 15718-15721.

223. Thuo, M. M.; Reus, W. F.; Nijhuis, C. A.; Barber, J. R.; Kim, C.; Schulz, M. D.; Whitesides, G. M., Odd-Even Effects in Charge Transport across Self-Assembled Monolayers. *J. Am. Chem. Soc.* **2011,** *133* (9), 2962-2975.

224. Nijhuis, C. A.; Reus, W. F.; Whitesides, G. M., Mechanism of Rectification in Tunneling Junctions Based on Molecules with Asymmetric Potential Drops. *J. Am. Chem. Soc.* **2010,** *132* (51), 18386-18401.

225. Seminario, J. M.; De La Cruz, C.; Derosa, P. A.; Yan, L. M., Nanometer-Size Conducting and Insulating Molecular Devices. *J. Phys. Chem. B* **2004,** *108* (46), 17879-17885.

226. Landauer, R., Spatial Variation of Currents and Fields Due to Localized Scatterers in Metallic Conduction. *IBM J. Res. Dev.* **1957,** *1* (3), 223-231.

227. Whitesides, G. M.; Lipomi, D. J., Soft Nanotechnology: "Structure" Vs. "Function". *Faraday Discuss.* **2009,** *143*, 373-384.

228. Thuo, M. M.; Reus, W. F.; Simeone, F. C.; Kim, C.; Schulz, M. D.; Yoon, H. J.; Whitesides, G. M., Replacing -CH2CH2- with -CONH- Does Not Significantly Change Rates of Charge Transport through Ag-TS-SAM//Ga2O3/EGain Junctions. *J. Am. Chem. Soc.* **2012,** *134* (26), 10876-10884.

229. Lovrinčić, R.; Kraynis, O.; Har-Lavan, R.; Haj-Yahya, A.-E.; Li, W.; Vilan, A.; Cahen, D., A New Route to Nondestructive Top-Contacts for Molecular Electronics on Si: Pb Evaporated on Organic Monolayers. *J. Phys. Chem. Lett.* **2013,** *4* (3), 426-430.

230. Seferos, D. S.; Blum, A. S.; Kushmerick, J. G.; Bazan, G. C., Single-Molecule Charge-Transport Measurements That Reveal Technique-Dependent Perturbations. *J. Am. Chem. Soc.* **2006,** *128* (34), 11260-11267.

231. Clausen, C.; Gryko, D. T.; Yasseri, A. A.; Diers, J. R.; Bocian, D. F.; Kuhr, W. G.; Lindsey, J. S., Investigation of Tightly Coupled Porphyrin Arrays Comprised of Identical Monomers for Multibit Information Storage. *J. Org. Chem.* **2000,** *65* (22), 7371-7378.

232. Sheiko, S.; Möller, M.; Reuvekamp, E.; Zandbergen, H., Calibration and Evaluation of Scanning-Force-Microscopy Probes. *Phys. Rev. B* **1993,** *48* (8), 5675.

233. Kolb, H. C.; Finn, M.; Sharpless, K. B., Click Chemistry: Diverse Chemical Function from a Few Good Reactions. *Angew. Chem. Int. Ed.* **2001,** *40* (11), 2004-2021.

234. Godin, M.; Williams, P. J.; Tabard-Cossa, V.; Laroche, O.; Beaulieu, L. Y.; Lennox, R. B.; Grütter, P., Surface Stress, Kinetics, and Structure of Alkanethiol Self-Assembled Monolayers. *Lang.* **2004,** *20* (17), 7090-7096.

235. Slowinski, K.; Chamberlain, R. V.; Miller, C. J.; Majda, M., Through-Bond and Chain-to-Chain Coupling. Two Pathways in Electron Tunneling through Liquid Alkanethiol Monolayers on Mercury Electrodes. *J. Am. Chem. Soc.* **1997,** *119* (49), 11910-11919.

236. Engelkes, V. B.; Beebe, J. M.; Frisbie, C. D., Length-Dependent Transport in Molecular Junctions Based on Sams of Alkanethiols and Alkanedithiols: Effect of Metal Work Function and Applied Bias on Tunneling Efficiency and Contact Resistance. *J. Am. Chem. Soc.* **2004,** *126* (43), 14287-14296.

237. Selzer, Y.; Salomon, A.; Cahen, D., The Importance of Chemical Bonding to the Contact for Tunneling through Alkyl Chains. *J. Phys. Chem. B* **2002,** *106* (40), 10432-10439.

238. Bumm, L. A.; Arnold, J. J.; Dunbar, T. D.; Allara, D. L.; Weiss, P. S., Electron Transfer through Organic Molecules. *J. Phys. Chem. B* **1999,** *103* (38), 8122-8127.

239. Salmeron, M.; Neubauer, G.; Folch, A.; Tomitori, M.; Ogletree, D. F.; Sautet, P., Viscoelastic and Electrical Properties of Self-Assembled Monolayers on Gold (111) Films. *Lang.* **1993,** *9* (12), 3600-3611.

240. Wang, W.; Lee, T.; Reed, M. A., Electron Tunnelling in Self-Assembled Monolayers. *Rep. Prog. Phys.* **2005,** *68* (3), 523.

241. Pi, U. H.; Jeong, M. S.; Kim, J. H.; Yu, H. Y.; Park, C. W.; Lee, H.; Choi, S. Y., Current Flow through Different Phases of Dodecanethiol Self-Assembled Monolayer. *Surf. Sci.* **2005,** *583* (1), 88-93.

242. Labonte, A. P.; Tripp, S. L.; Reifenberger, R.; Wei, A., Scanning Tunneling Spectroscopy of Insulating Self-Assembled Monolayers on Au (111). *J. Phys. Chem. B* **2002,** *106* (34), 8721-8725.

243. Likharev, K. K., Single-Electron Devices and Their Applications. *Proceed. IEEE* **1999,** *87* (4), 606-632.

244. Reed, M. A.; Zhou, C.; Muller, C.; Burgin, T.; Tour, J., Conductance of a Molecular Junction. *Sci.* **1997,** *278* (5336), 252-254.

245. Chen, C.-P.; Luo, W.-R.; Chen, C.-N.; Wu, S.-M.; Hsieh, S.; Chiang, C.-M.; Dong, T.-Y., Redox-Active Pi-Conjugated Organometallic Monolayers: Pronounced Coulomb Blockade Characteristic at Room Temperature. *Lang.* **2013,** *29* (9), 3106-3115.

246. Kouwenhoven, L. P.; Marcus, C. M.; McEuen, P. L.; Tarucha, S.; Westervelt, R. M.; Wingreen, N. S., *Mesoscopic Electron Transport: Electron Transport in Quantum Dots.* Springer Netherlands: Dordrecht, Netherlands, **1997**; 105-214.

247. Lee, S.; Lee, Y.; Song, E. B.; Hiramoto, T., Observation of Single Electron Transport Via Multiple Quantum States of a Silicon Quantum Dot at Room Temperature. *Nano Letters* **2013,** *14* (1), 71-77.

248. Galperin, M.; Ratner, M. A.; Nitzan, A.; Troisi, A., Nuclear Coupling and Polarization in Molecular Transport Junctions: Beyond Tunneling to Function. *Sci.* **2008,** *319* (5866), 1056-60.

249. Jin, H.; Erica, S. F.; Larry, A. N.; Nongjian, T.; Stuart, L., Charge Transport in Mesoscopic Conducting Polymer Wires. *J. Phys.-Cond. Matt.* **2008,** *20* (37), 374120.

250. Galperin, M.; Ratner, M. A.; Nitzan, A., Hysteresis, Switching, and Negative Differential Resistance in Molecular Junctions: A Polaron Model. *Nano Lett.* **2005,** *5* (1), 125-130.

251. Galperin, M.; Nitzan, A.; Ratner, M. A., The Non-Linear Response of Molecular Junctions: The Polaron Model Revisited. *J. Phys.-Cond. Matt.* **2008,** *20* (37), 374107.

252. Galperin, M.; Ratner, M. A.; Nitzan, A., Molecular Transport Junctions: Vibrational Effects. *J. Phys.-Cond. Matt.* **2007,** *19* (10), 103201.

253. Selzer, Y.; Cai, L.; Cabassi, M. A.; Yao, Y.; Tour, J. M.; Mayer, T. S.; Allara, D. L., Effect of Local Environment on Molecular Conduction: Isolated Molecule Versus Self-Assembled Monolayer. *Nano Lett.* **2005,** *5* (1), 61-65.

254. Haiss, W.; van Zalinge, H.; Bethell, D.; Ulstrup, J.; Schiffrin, D. J.; Nichols, R. J., Thermal Gating of the Single Molecule Conductance of Alkanedithiols. *Faraday Discuss.* **2006,** *131* (0), 253-264.

255. Perrin, M. L.; Prins, F.; Martin, C. A.; Shaikh, A. J.; Eelkema, R.; van Esch, J. H.; Briza, T.; Kaplanek, R.; Kral, V.; van Ruitenbeek, J. M.; van der Zant, H. S. J.; Dulić, D., Influence of the Chemical Structure on the Stability and Conductance of Porphyrin Single-Molecule Junctions. *Angew. Chem. Int. Ed.* **2011,** *50* (47), 11223-11226.

256. Donhauser, Z. J.; Mantooth, B. A.; Kelly, K. F.; Bumm, L. A.; Monnell, J. D.; Stapleton, J. J.; Price, D. W.; Rawlett, A. M.; Allara, D. L.; Tour, J. M.; Weiss, P. S., Conductance Switching in Single Molecules through Conformational Changes. *Sci.* **2001,** *292* (5525), 2303-2307.

257. Wassel, R. A.; Fuierer, R. R.; Kim, N.; Gorman, C. B., Stochastic Variation in Conductance on the Nanometer Scale: A General Phenomenon. *Nano Lett.* **2003,** *3* (11), 1617-1620.

258. Moore, A. M.; Mantooth, B. A.; Donhauser, Z. J.; Yao, Y.; Tour, J. M.; Weiss, P. S., Real-Time Measurements of Conductance Switching and Motion of Single Oligo(Phenylene Ethynylene) Molecules. *J. Am. Chem. Soc.* **2007,** *129* (34), 10352-10353.

259. Donhauser, Z. J.; Mantooth, B. A.; Pearl, T. P.; Kelly, K. F.; Nanayakkara, S. U.; Weiss, P. S., Matrix-Mediated Control of Stochastic Single Molecule Conductance Switching. *Japanese J. Appl. Phys.* **2002,** *41* (Part 1, No. 7B), 4871-4877.

260. Lörtscher, E.; Ciszek, J. W.; Tour, J.; Riel, H., Reversible and Controllable Switching of a Single-Molecule Junction. *Sml.* **2006,** *2* (8-9), 973-7.

261. Harzmann, G. D.; Frisenda, R.; van der Zant, H. S. J.; Mayor, M., Single-Molecule Spin Switch Based on Voltage-Triggered Distortion of the Coordination Sphere. *Angew. Chem. Int. Ed.* **2015,** *54* (45), 13425-13430.

262. Kitaguchi, Y.; Habuka, S.; Okuyama, H.; Hatta, S.; Aruga, T.; Frederiksen, T.; Paulsson, M.; Ueba, H., Controlled Switching of Single-Molecule Junctions by Mechanical Motion of a Phenyl Ring. *Beilstein J. Nanotechnol.* **2015,** *6*, 2088-2095.

263. Donarini, A.; Yar, A.; Grifoni, M., Vibration Induced Memory Effects and Switching in Ac-Driven Molecular Nanojunctions. *Euro. Phys. J. B* **2012,** *85* (9), 14.

264. Gittins, D. I.; Bethell, D.; Schiffrin, D. J.; Nichols, R. J., A Nanometre-Scale Electronic Switch Consisting of a Metal Cluster and Redox-Addressable Groups. *Nat.* **2000,** *408* (6808), 67-69.

265. Arielly, R.; Vadai, M.; Kardash, D.; Noy, G.; Selzer, Y., Real-Time Detection of Redox Events in Molecular Junctions. *J. Am. Chem. Soc.* **2014,** *136* (6), 2674-80.

266. Derosa, P. A.; Guda, S.; Seminario, J. M., A Programmable Molecular Diode Driven by Charge-Induced Conformational Changes. *J. Am. Chem. Soc.* **2003,** *125* (47), 14240-14241.

267. Salleo, A.; Kline, R. J.; DeLongchamp, D. M.; Chabinyc, M. L., Microstructural Characterization and Charge Transport in Thin Films of Conjugated Polymers. *Adv. Mater.* **2010,** *22* (34), 3812-38.

268. Qian, D.-J.; Nakamura, C.; Miyake, J., Multiporphyrin Array from Interfacial Metal-Mediated Assembly and Its Langmuir−Blodgett Films. *Lang.* **2000,** *16* (24), 9615-9619.

269. Choudhury, B.; Weedon, A. C.; Bolton, J. R., Effects of Molecular Organization on Photophysical Behavior. 1. Steady-State Fluorescence and Fluorescence Quantum Yield Studies of Langmuir−Blodgett Monolayers of Some Surfactant Porphyrins. *Lang.* **1998,** *14* (21), 6192-6198.

270. Österbacka, R.; An, C. P.; Jiang, X. M.; Vardeny, Z. V., Two-Dimensional Electronic Excitations in Self-Assembled Conjugated Polymer Nanocrystals. *Sci.* **2000,** *287* (5454), 839-842.

271. Mohnani, S.; Bonifazi, D., Supramolecular Architectures of Porphyrins on Surfaces: The Structural Evolution from 1d to 2d to 3d to Devices. *Coord. Chem. Rev.* **2010,** *254* (19-20), 2342-2362.

272. Sedghi, G.; Sawada, K.; Esdaile, L. J.; Hoffmann, M.; Anderson, H. L.; Bethell, D.; Haiss, W.; Higgins, S. J.; Nichols, R. J., Single Molecule Conductance of Porphyrin Wires with Ultralow Attenuation. *J. Am. Chem. Soc.* **2008,** *130* (27), 8582-8583.

273. Ruben, M.; Landa, A.; Lörtscher, E.; Riel, H.; Mayor, M.; Görls, H.; Weber, H. B.; Arnold, A.; Evers, F., Charge Transport through a Cardan-Joint Molecule. *Sml.* **2008,** *4* (12), 2229-2235.

274. Drain, C. M.; Varotto, A.; Radivojevic, I., Self-Organized Porphyrinic Materials. *Chem. Rev.* **2009,** *109* (5), 1630-1658.

275. Li, Z.; Borguet, E., Determining Charge Transport Pathways through Single Porphyrin Molecules Using Scanning Tunneling Microscopy Break Junctions. *J. Am. Chem.Soc.* **2012,** *134*, 63−66.

276. Schuckman, A. E., *Charge Transport through Organized Organic Assemblies in Confined Geometries*. Texas A&M University: College Station, Texas, United States, **2011**; 1-263.

277. Sedghi, G.; Garcia-Suarez, V. M.; Esdaile, L. J.; Anderson, H. L.; Lambert, C. J.; Martin, S.; Bethell, D.; Higgins, S. J.; Elliott, M.; Bennett, N.; Macdonald, J. E.; Nichols, R. J., Long-Range Electron Tunnelling in Oligo-Porphyrin Molecular Wires. *Nat. Nano* **2011,** *6* (8), 517-523.

278. Sedghi, G.; Esdaile, L. J.; Anderson, H. L.; Martin, S.; Bethell, D.; Higgins, S. J.; Nichols, R. J., Comparison of the Conductance of Three Types of Porphyrin-Based Molecular Wires: Beta,Meso,Beta-Fused Tapes, Meso-Butadiyne-Linked and Twisted Meso-Meso Linked Oligomers. *Adv. Mater.* **2012,** *24* (5), 653-7.

279. Otte, F. L.; Lemke, S.; Schütt, C.; Krekiehn, N. R.; Jung, U.; Magnussen, O. M.; Herges, R., Ordered Monolayers of Free-Standing Porphyrins on Gold. *J. Am. Chem. Soc.* **2014,** *136* (32), 11248-11251.

280. Pawlicki, A.; Avery, E.; Jurow, M.; Ewers, B.; Vilan, A.; Drain, C. M.; Batteas, J., Studies of the Structure and Phase Transitions of Nano-Confined Pentanedithiol and Its Application in Directing Hierarchical Molecular Assemblies on Au(111). *J. Phys.-Cond. Matt.* **2016,** *28* (9), 094013.

281. Monnell, J. D.; Stapleton, J. J.; Dirk, S. M.; Reinerth, W. A.; Tour, J. M.; Allara, D. L.; Weiss, P. S., Relative Conductances of Alkaneselenolate and Alkanethiolate Monolayers on Au(111). *J. Phys. Chem. B* **2005,** *109* (43), 20343-20349.

282. Maksymovych, P.; Voznyy, O.; Dougherty, D. B.; Sorescu, D. C.; Yates, J. T., Gold Adatom as a Key Structural Component in Self-Assembled Monolayers of Organosulfur Molecules on Au(111). *Prog. Surf. Sci.* **2010,** *85* (5-8), 206-240.

283. Schlenoff, J. B.; Li, M.; Ly, H., Stability and Self-Exchange in Alkanethiol Monolayers. *J. Am. Chem. Soc.* **1995,** *117* (50), 12528-12536.

284. Vericat, C.; Vela, M. E.; Salvarezza, R. C., Self-Assembled Monolayers of Alkanethiols on Au(111): Surface Structures, Defects and Dynamics. *Phys. Chem. Chem. Phys.* **2005,** *7* (18), 3258-3268.

285. Reus, W. F.; Nijhuis, C. A.; Barber, J. R.; Thuo, M. M.; Tricard, S.; Whitesides, G. M., Statistical Tools for Analyzing Measurements of Charge Transport. *J. Phys. Chem. C* **2012,** *116* (11), 6714-6733.

286. Vilan, A.; Cahen, D.; Kraisler, E., Rethinking Transition Voltage Spectroscopy within a Generic Taylor Expansion View. *ACS Nano* **2013,** *7* (1), 695-706.

287. Haiss, W.; Martin, S.; Leary, E.; van Zalinge, H.; Higgins, S. J.; Bouffier, L.; Nichols, R. J., Impact of Junction Formation Method and Surface Roughness on Single Molecule Conductance. *J. Phys. Chem. C* **2009,** *113* (14), 5823-5833.

288. Guo, S.; Hihath, J.; Diez-Perez, I.; Tao, N., Measurement and Statistical Analysis of Single-Molecule Current-Voltage Characteristics, Transition Voltage Spectroscopy, and Tunneling Barrier Height. *J. Am. Chem. Soc.* **2011,** *133* (47), 19189-97.

289. Galperin, M.; Ratner, M. A.; Nitzan, A., Hysteresis, Switching, and Negative Differential Resistance in Molecular Junctions: A Polaron Model. *Nano Lett.* **2005,** *5* (1), 125-130.

290. Wei, J. H.; Xie, S. J.; Mei, L. M.; Berakdar, J.; Yan, Y. J., Charge-Transfer Polaron Induced Negative Differential Resistance and Giant Magnetoresistance in Organic Spin-Valve Systems. *New J. Phys.* **2006,** *8*, 9.

291. Bandyopadhyay, A.; Wakayama, Y., Origin of Negative Differential Resistance in Molecular Junctions of Rose Bengal. *Appl. Phys. Lett.* **2007,** *90* (2), 023512.

292. He, J.; Fu, Q.; Lindsay, S.; Ciszek, J. W.; Tour, J. M., Electrochemical Origin of Voltage-Controlled Molecular Conductance Switching. *J. Am. Chem. Soc.* **2006,** *128* (46), 14828-14835.

293. Noh, J.; Hara, M., Molecular-Scale Desorption Processes and the Alternating Missing-Row Phase of Alkanethiol Self-Assembled Monolayers on Au(111). *Lang.* **2001,** *17* (23), 7280-7285.

294. Wu, H.; Sotthewes, K.; Schon, P. M.; Vancso, G. J.; Zandvliet, H. J. W., Ordering and Dynamics of Oligo(Phenyleneethynylene) Self-Assembled Monolayers on Au(111). *RSC Adv.* **2015,** *5* (52), 42069-42074.

295. Su, T. A.; Li, H. X.; Steigerwald, M. L.; Venkataraman, L.; Nuckolls, C., Stereoelectronic Switching in Single-Molecule Junctions. *Nat. Chem.* **2015,** *7* (3), 215-220.

296. Li, X. G.; Zhang, X. G.; Cheng, H. P., Conformational Electroresistance and Hysteresis in Nanoclusters. *Nano Lett.* **2014,** *14* (8), 4476-4479.

297. Leijnse, M., Interaction Effects in Electric Transport through Self-Assembled Molecular Monolayers. *Phys. Rev. B* **2013,** *87* (12), 9.

298. Jiang, L.; Sangeeth, C. S. S.; Yuan, L.; Thompson, D.; Nijhuis, C. A., One-Nanometer Thin Monolayers Remove the Deleterious Effect of Substrate Defects in Molecular Tunnel Junctions. *Nano Lett.* **2015,** *15* (10), 6643-6649.

299. Kuhn, H., Present Status and Future Prospects of Langmuir-Blodgett Film Research. *Thin Sol. Fil.* **1989,** *178* (1–2), 1-16.

300. Drain, C. M.; Mauzerall, D., An Example of a Working Molecular Charge Sensitive Ion Conductor. *Bioelectrochem. and Bioener.* **1990,** *24* (2), 263-268.

301. Rosa, L. G.; Liang, J., Atomic Force Microscope Nanolithography: Dip-Pen, Nanoshaving, Nanografting, Tapping Mode, Electrochemical and Thermal Nanolithography. *J. Phys.-Cond. Matt.* **2009,** *21* (48).

302. Bu, D.; Riechers, S.; Liang, J.; Liu, G.-y., Impact of Nanografting on the Local Structure of Ternary Self-Assembled Monolayers. *Nano Res.* **2015,** *8* (6), 2102-2114.

303. Hu, Y.; Das, A.; Hecht, M. H.; Scoles, G., Nanografting De Novo Proteins onto Gold Surfaces. *Lang.* **2005,** *21* (20), 9103-9109.

304. Josephs, E. A.; Ye, T., Nanoscale Positioning of Individual DNA Molecules by an Atomic Force Microscope. *J. Am. Chem. Soc.* **2010,** *132* (30), 10236-10238.

305. Castronovo, M.; Scaini, D., The Atomic Force Microscopy as a Lithographic Tool: Nanografting of DNA Nanostructures for Biosensing Applications. *DNA Nanotechnol.: Meth. and Proto.* **2011,** *749*, 209-221.

306. Kowalzik, P.; Atodiresei, N.; Gingras, M.; Caciuc, V.; Blügel, S.; Waser, R.; Karthäuser, S., Single Electron Tunneling through a Tailored Arylthio-Coronene. *J. Phys. Chem. C* **2011,** *115* (18), 9204-9209.

307. Cygan, M. T.; Dunbar, T. D.; Arnold, J. J.; Bumm, L. A.; Shedlock, N. F.; Burgin, T. P.; Jones, L.; Allara, D. L.; Tour, J. M.; Weiss, P. S., Insertion, Conductivity, and Structures of Conjugated Organic Oligomers in Self-Assembled Alkanethiol Monolayers on Au{111}. *J. Am. Chem. Soc.* **1998,** *120* (12), 2721-2732.

308. Yu, J.-H.; Ngunjiri, J. N.; Kelley, A. T.; Gano, J. C., Nanografting Versus Solution Self-Assembly of Alpha,Omega-Alkanedithiols on Au(111) Investigated by AFM. *Lang.* **2008,** *24* (20), 11661-11668.

309. Helt, J. M.; Batteas, J. D., Implications of the Contact Radius to Line Step (CRLS) Ratio in Afm for Nanotribology Measurements. *Lang.* **2006,** *22* (14), 6130-6141.

310. Stranick, S.; Parikh, A.; Tao, Y.-T.; Allara, D.; Weiss, P., Phase Separation of Mixed-Composition Self-Assembled Monolayers into Nanometer Scale Molecular Domains. *J. Phys. Chem.* **1994,** *98* (31), 7636-7646.

311. Bumm, L. A.; Arnold, J. J.; Charles, L. F.; Dunbar, T. D.; Allara, D. L.; Weiss, P. S., Directed Self-Assembly to Create Molecular Terraces with Molecularly Sharp Boundaries in Organic Monolayers. *J. Am. Chem. Soc.* **1999,** *121* (35), 8017-8021.

312. Chen, S.; Li, L.; Boozer, C. L.; Jiang, S., Controlled Chemical and Structural Properties of Mixed Self-Assembled Monolayers of Alkanethiols on Au(111). *Lang.* **2000,** *16* (24), 9287-9293.

313. Chen, S.; Li, L.; Boozer, C. L.; Jiang, S., Controlled Chemical and Structural Properties of Mixed Self-Assembled Monolayers by Coadsorption of Symmetric and Asymmetric Disulfides on Au(111). *J. Phys. Chem. B* **2001,** *105* (15), 2975-2980.

314. Yang, G.; Liu, G.-y., New Insights for Self-Assembled Monolayers of Organothiols on Au(111) Revealed by Scanning Tunneling Microscopy. *J. Phys. Chem. B* **2003,** *107* (34), 8746-8759.

315. Cometto, F. P.; Ruano, G.; Ascolani, H.; Zampieri, G., Adlayers of Alkanedithiols on Au(111): Effect of Disulfide Reducing Agent. *Lang.* **2013,** *29* (5), 1400-1406.

316. Millone, M. A. D.; Hamoudi, H.; Rodríguez, L.; Rubert, A.; Benítez, G. A.; Vela, M. E.; Salvarezza, R. C.; Gayone, J. E.; Sánchez, E. A.; Grizzi, O.; Dablemont, C.; Esaulov, V. A., Self-Assembly of Alkanedithiols on Au(111) from Solution: Effect of Chain Length and Self-Assembly Conditions. *Lang.* **2009,** *25* (22), 12945-12953.

317. Esplandiu, M. J.; Carot, M. L.; Cometto, F. P.; Macagno, V. A.; Patrito, E. M., Electrochemical Stm Investigation of 1,8-Octanedithiol Monolayers on Au(111). Experimental and Theoretical Study. *Surf. Sci.* **2006,** *600* (1), 155-172.

318. Hamoudi, H.; Guo, Z.; Prato, M.; Dablemont, C.; Zheng, W. Q.; Bourguignon, B.; Canepa, M.; Esaulov, V. A., On the Self Assembly of Short Chain Alkanedithiols. *Phys. Chem. Chem. Phys.* **2008,** *10* (45), 6836-6841.

319. Poirier, G.; Pylant, E., The Self-Assembly Mechanism of Alkanethiols on Au (111). *Sci.* **1996,** *272* (5265), 1145-1148.

320. Leung, T. Y. B.; Gerstenberg, M. C.; Lavrich, D. J.; Scoles, G.; Schreiber, F.; Poirier, G. E., 1,6-Hexanedithiol Monolayers on Au(111): A Multitechnique Structural Study. *Lang.* **2000,** *16* (2), 549-561.

321. Kobayashi, K.; Yamada, H.; Horiuchi, T.; Matsushige, K., Uhv-Stm Studies on the Structures of Alkanedithiol Self-Assembled Monolayers. *Appl. Surf. Sci.* **1999,** *144–145*, 435-438.

322. Garno, J. C.; Zangmeister, C. D.; Batteas, J. D., Directed Electroless Growth of Metal Nanostructures on Patterned Self-Assembled Monolayers. *Lang.* **2007,** *23* (14), 7874-7879.

323. Brewer, N. J.; Beake, B. D.; Leggett, G. J., Friction Force Microscopy of Self-Assembled Monolayers: Influence of Adsorbate Alkyl Chain Length, Terminal Group Chemistry, and Scan Velocity. *Lang.* **2001,** *17* (6), 1970-1974.

324. Vericat, C.; Vela, M. E.; Benitez, G.; Carro, P.; Salvarezza, R. C., Self-Assembled Monolayers of Thiols and Dithiols on Gold: New Challenges for a Well-Known System. *Chem. Soc. Rev.* **2010,** *39* (5), 1805-1834.

325. Tovar, R. M.; Johnson, K. P.; Ashline, K.; Seminario, J. M., Effects of Substituents on Molecular Devices. *Int. J. Quant. Chem.* **2008,** *108* (9), 1546-1554.

326. Derosa, P. A.; Seminario, J. M., Electron Transport through Single Molecules: Scattering Treatment Using Density Functional and Green Function Theories. *J. Phys. Chem B* **2001,** *105* (2), 471-481.

327. Damle, P.; Ghosh, A. W.; Datta, S., First-Principles Analysis of Molecular Conduction Using Quantum Chemistry Software. *Chem. Phys.* **2002,** *281* (2-3), 171-187.

328. Paulsson, M.; Datta, S., Thermoelectric Effect in Molecular Electronics. *Phys. Rev. B* **2003,** *67* (24).

329. Zahid, F.; Ghosh, A. W.; Paulsson, M.; Polizzi, E.; Datta, S., Charging-Induced Asymmetry in Molecular Conductors. *Phys. Rev. B* **2004,** *70* (24).

330. Reddy, P.; Jang, S. Y.; Segalman, R. A.; Majumdar, A., Thermoelectricity in Molecular Junctions. *Sci.* **2007,** *315* (5818), 1568-1571.

331. Widawsky, J. R.; Darancet, P.; Neaton, J. B.; Venkataraman, L., Simultaneous Determination of Conductance and Thermopower of Single Molecule Junctions. *Nano Lett.* **2012,** *12* (1), 354-358.

332. Evangeli, C.; Gillemot, K.; Leary, E.; Teresa Gonzalez, M.; Rubio-Bollinger, G.; Lambert, C. J.; Agrait, N., Engineering the Thermopower of C-60 Molecular Junctions. *Nano Lett.* **2013,** *13* (5), 2141-2145.

333. Kim, T.; Darancet, P.; Widawsky, J. R.; Kotiuga, M.; Quek, S. Y.; Neaton, J. B.; Venkataraman, L., Determination of Energy Level Alignment and Coupling Strength in 4,4 '-Bipyridine Single-Molecule Junctions. *Nano Lett.* **2014,** *14* (2), 794-798.

334. Taylor, J.; Brandbyge, M.; Stokbro, K., Theory of Rectification in Tour Wires: The Role of Electrode Coupling. *Phys. Rev. Lett.* **2002,** *89* (13).

335. Kushmerick, J. G.; Holt, D. B.; Yang, J. C.; Naciri, J.; Moore, M. H.; Shashidhar, R., Metal-Molecule Contacts and Charge Transport across Monomolecular Layers: Measurement and Theory. *Phys. Rev. Lett.* **2002,** *89* (8).

336. Di Ventra, M.; Pantelides, S. T.; Lang, N. D., First-Principles Calculation of Transport Properties of a Molecular Device. *Phys. Rev. Lett.* **2000,** *84* (5), 979-982.

337. Baheti, K.; Malen, J. A.; Doak, P.; Reddy, P.; Jang, S. Y.; Tilley, T. D.; Majumdar, A.; Segalman, R. A., Probing the Chemistry of Molecular Heterojunctions Using Thermoelectricity. *Nano Lett.* **2008,** *8* (2), 715-719.

338. Sotthewes, K.; Siekman, M. H.; Zandvliet, H. J. W., A Method to Measure the Thermovoltage with a High Spatial Resolution. *Appl. Phys. Lett.* **2016,** *108* (14), 4.

339. Park, J.; He, G. W.; Feenstra, R. M.; Li, A. P., Atomic-Scale Mapping of Thermoelectric Power on Graphene: Role of Defects and Boundaries. *Nano Lett.* **2013,** *13* (7), 3269-3273.

340. Tan, A.; Sadat, S.; Reddy, P., Measurement of Thermopower and Current-Voltage Characteristics of Molecular Junctions to Identify Orbital Alignment. *Appl. Phys. Lett.* **2010,** *96* (1).

341. Poler, J. C.; Zimmermann, R. M.; Cox, E. C., Scanning Thermopower Microscopy of Guanine Monolayers. *Lang.* **1995,** *11* (7), 2689-2695.

342. Capozzi, B.; Low, J. Z.; Xia, J.; Liu, Z.-F.; Neaton, J. B.; Campos, L. M.; Venkataraman, L., Mapping the Transmission Functions of Single-Molecule Junctions. *Nano Lett.* **2016,** *16* (6), 3949-3954.

343. Frisenda, R.; Perrin, M. L.; Valkenier, H.; Hummelen, J. C.; van der Zant, H. S. J., Statistical Analysis of Single-Molecule Breaking Traces. *Phys. Stat. Sol. B* **2013,** *250* (11), 2431-2436.

344. Ratner, M., A Brief History of Molecular Electronics. *Nat. Nanotechnol.* **2013,** *8* (6), 378-381.

345. Kim, Y.; Garcia-Lekue, A.; Sysoiev, D.; Frederiksen, T.; Groth, U.; Scheer, E., Charge Transport in Azobenzene-Based Single-Molecule Junctions. *Phys. Rev. Lett.* **2012,** *109* (22).

346. Chen, X.; Braunschweig, A. B.; Wiester, M. J.; Yeganeh, S.; Ratner, M. A.; Mirkin, C. A., Spectroscopic Tracking of Molecular Transport Junctions Generated by Using Click Chemistry. *Angew. Chem. Int. Ed.* **2009,** *48* (28), 5178-5181.

347. Moth-Poulsen, K.; Bjornholm, T., Molecular Electronics with Single Molecules in Solid-State Devices. *Nat. Nanotechnol.* **2009,** *4* (9), 551-556.

348. Xiang, D.; Lee, T.; Kim, Y.; Mei, T.; Wang, Q., Origin of Discrete Current Fluctuations in a Single Molecule Junction. *Nanoscal.* **2014,** *6* (22), 13396-13401.

349. Xiang, D.; Sydoruk, V.; Vitusevich, S.; Petrychuk, M. V.; Offenhaeusser, A.; Kochelap, V. A.; Belyaev, A. E.; Mayer, D., Noise Characterization of Metal-Single Molecule Contacts. *Appl. Phys. Lett.* **2015,** *106* (6).

350. Yu, X.; Lovrincic, R.; Kraynis, O.; Man, G.; Ely, T.; Zohar, A.; Toledano, T.; Cahen, D.; Vilan, A., Fabrication of Reproducible, Integration-Compatible Hybrid Molecular/Si Electronics. *Sml.* **2014,** *10* (24), 5151-5160.

351. Jia, C. C.; Ma, B. J.; Xin, N.; Guo, X. F., Carbon Electrode-Molecule Junctions: A Reliable Platform for Molecular Electronics. *Accounts Chem. Res.* **2015,** *48* (9), 2565-2575.

352. Yang, G. H.; Liu, G. Y., New Insights for Self-Assembled Monolayers of Organothiols on Au(111) Revealed by Scanning Tunneling Microscopy. *J. Phys. Chem. B* **2003,** *107* (34), 8746-8759.

353. Kim, T.; Ye, Q.; Sun, L.; Chan, K. C.; Crooks, R. M., Polymeric Self-Assembled Monolayers. 5. Synthesis and Characterization of Ω-Functionalized, Self-Assembled Diacetylenic and Polydiacetylenic Monolayers. *Lang.* **1996,** *12* (25), 6065-6073.

354. Kim, T.; Crooks, R. M.; Tsen, M.; Sun, L., Polymeric Self-Assembled Monolayers. 2. Synthesis and Characterization of Self-Assembled Polydiacetylene Mono- and Multilayers. *J. Am. Chem. Soc.* **1995,** *117* (14), 3963-3967.

355. Kim, T.; Crooks, R. M., Polymeric Self-Assembling Monolayers. 1. Synthesis and Characterization of Y-Functionalized N-Alkanethiols Containing a Conjugated Diacetylene Group. *Tetrahed. Lett.* **1994,** *35* (51), 9501-9504.

356. Feldman, A. K.; Steigerwald, M. L.; Guo, X. F.; Nuckolls, C., Molecular Electronic Devices Based on Single-Walled Carbon Nanotube Electrodes. *Accounts Chem. Res.* **2008,** *41* (12), 1731-1741.

357. Cao, Y.; Dong, S.; Liu, S.; He, L.; Gan, L.; Yu, X.; Steigerwald, M. L.; Wu, X.; Liu, Z.; Guo, X., Building High-Throughput Molecular Junctions Using Indented Graphene Point Contacts. *Angew. Chem. Int. Ed.* **2012,** *51* (49), 12228-12232.

358. Cao, Y.; Wei, Z.; Liu, S.; Gan, L.; Guo, X.; Xu, W.; Steigerwald, M. L.; Liu, Z.; Zhu, D., High-Performance Langmuir-Blodgett Monolayer Transistors with High Responsivity. *Angew. Chem. Int. Ed.* **2010,** *49* (36), 6319-6323.

359. Shen, Q.; Guo, X. F.; Steigerwald, M. L.; Nuckolls, C., Integrating Reaction Chemistry into Molecular Electronic Devices. *Chem.-Asian J.* **2010,** *5* (5), 1040-1057.

APPENDIX A

SUPPLEMENTAL DATA FOR CHAPTER II

A.1 Data Summary for All Porphyrin-Thiols with Varying Chemical Identity

Molecule	Porphyrin-thiol Solution Concentration (mM)	Porphyrin-thiol Solution Immersion Duration (Days)	Physical Height, δh_{AFM} (Å)	Apparent Height, δh_{STM} (Å)	Lateral Dimension (Å)
H-Pyridal	0.5	1	5±2	5±2	32±22
		3	5±2	5±2	53±22
		5	5±2	5±2	49±29
F-Phenyl	0.5	1	3±1	5±3	Bimodal 27±8, 50±25
		3	4±2	4±2	25±14
		5	2±1	5±2	Bimodal 27±6, 47±25
F-Pyridal*	0.5	5	9±5	5±2	Bimodal 50±8,100±10
Zn H-Pyridal	0.05	1	4±2	3±2	29±13
		3	5±2	5±3	31±17
		5	5±2	4±2	33±21

Table 4. Summary of the data collected for all the porphyrin-thiols in the series. Some research on the F-Pyridyl[20] and Zn F-Pyridyl[19] has been done previously. The physical height, apparent height, and lateral dimension values were obtained by fitting the population to an extreme Gaussian function and extracting the peak value. The error of the values reported is the full width at half the maximum of an extreme function (a particular case of the Gumbel probability density function as defined in OriginPro 2013) that was fitted to the data as plotted in a histogram similar to Figure 5.

Zn F-Phenyl	0.05	1	2±1	5±4	Bimodal 33±7, 59±22
		3	3±2	4±2	Bimodal 23±7, 47±19
		5	3±1	4±2	Bimodal 20±5, 38±47
Zn F-Pyridal*	0.05	1	3±1	5±3	Bimodal 31±9, 52±11
		3	3±1	5±2	33±19
		5	3±1	4±2	Bimodal 27±10 45±24

Table 4. Continued.

A.2 Apparent Height Ratio

The apparent height ratio, calculated from Equation 1, is used as a measure of the relative conductance for porphyrin-thiol molecules within a pre-formed C12 SAM. The apparent height ratio for all varieties of porphyrin-thiols studied herein plotted as a function of lateral dimension and assembly time in Figure 35. The apparent height ratio is a value for comparison between all the different porphryin-thiols with varying chemical identity as well as with the C12 SAM. It was found that for single molecules and small clusters (lateral dimension $\leq$3 nm) of all varieties of porphyrin-thiols, the apparent height ratio is approximately zero. This indicates that there is no change in the apparent height and therefore single porphryin-thiols and C12 are equally conductive and that the thiol-tether of the porphyrins dominates the transport. For larger clusters of porphryin-thiols (lateral dimension $\geq$5 nm) the apparent height ratio departs from zero and generally increases by 4-fold for increasing lateral dimension but with a large spread in the data. This indicates that for large clusters of porphryin-thiols, the transport is no

longer dominated by the thiol-theater, providing an opportunity to recover transport modulation with varying chemical identity. The larger spread in the data can be attributed to variations in molecular organization and therefore nearest-neighbor interactions which results in varying electronic properties (see Chapter III).

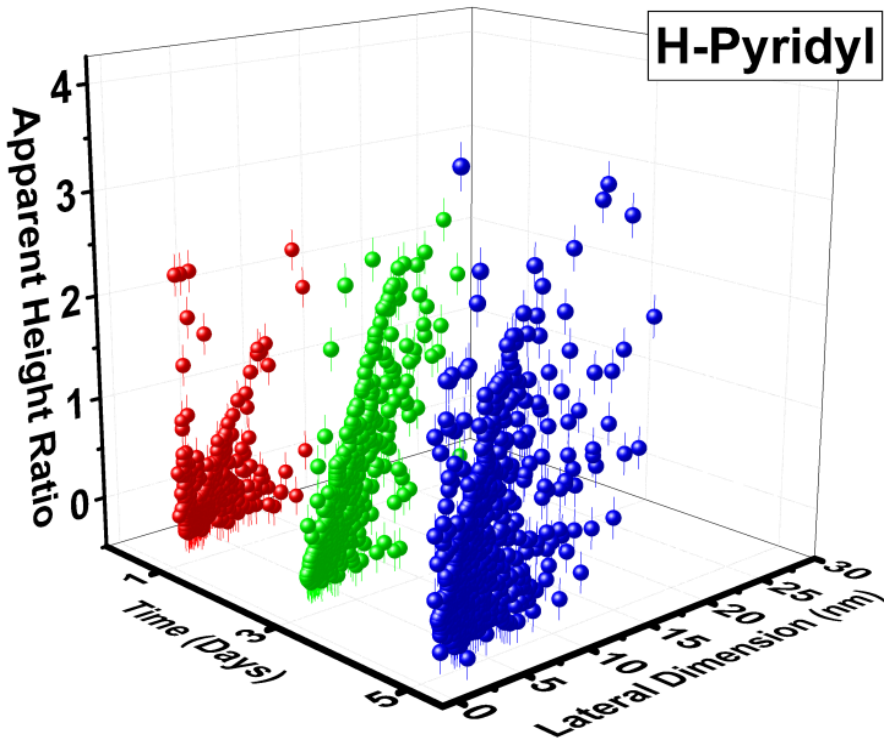

Figure 35. Three dimensional plots of the apparent height ratio, as calculated from Equation 1 for all porphyrin-thiol varieties studied herein as a function of lateral dimension and assembly time.

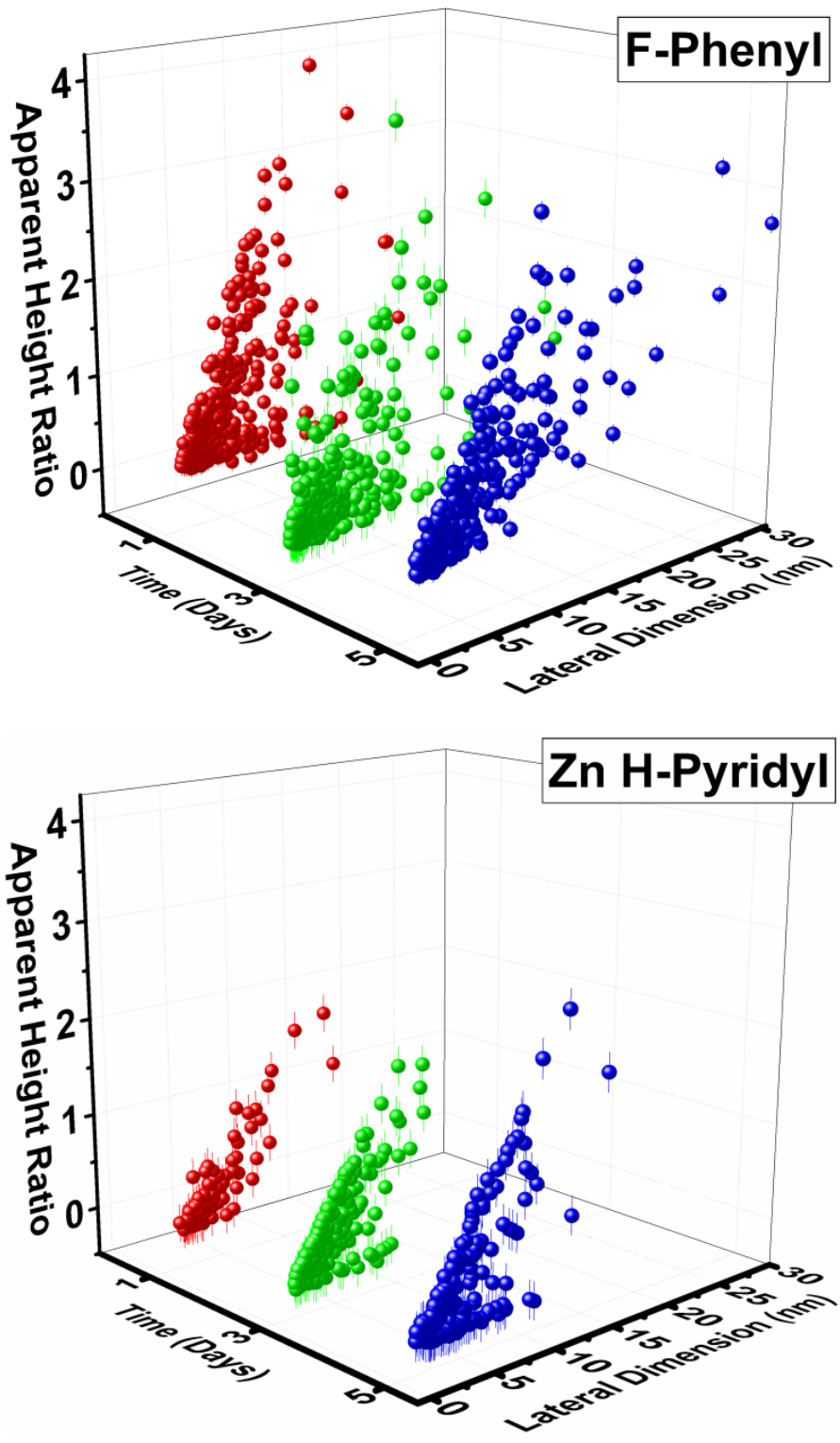

Figure 35. Continued.

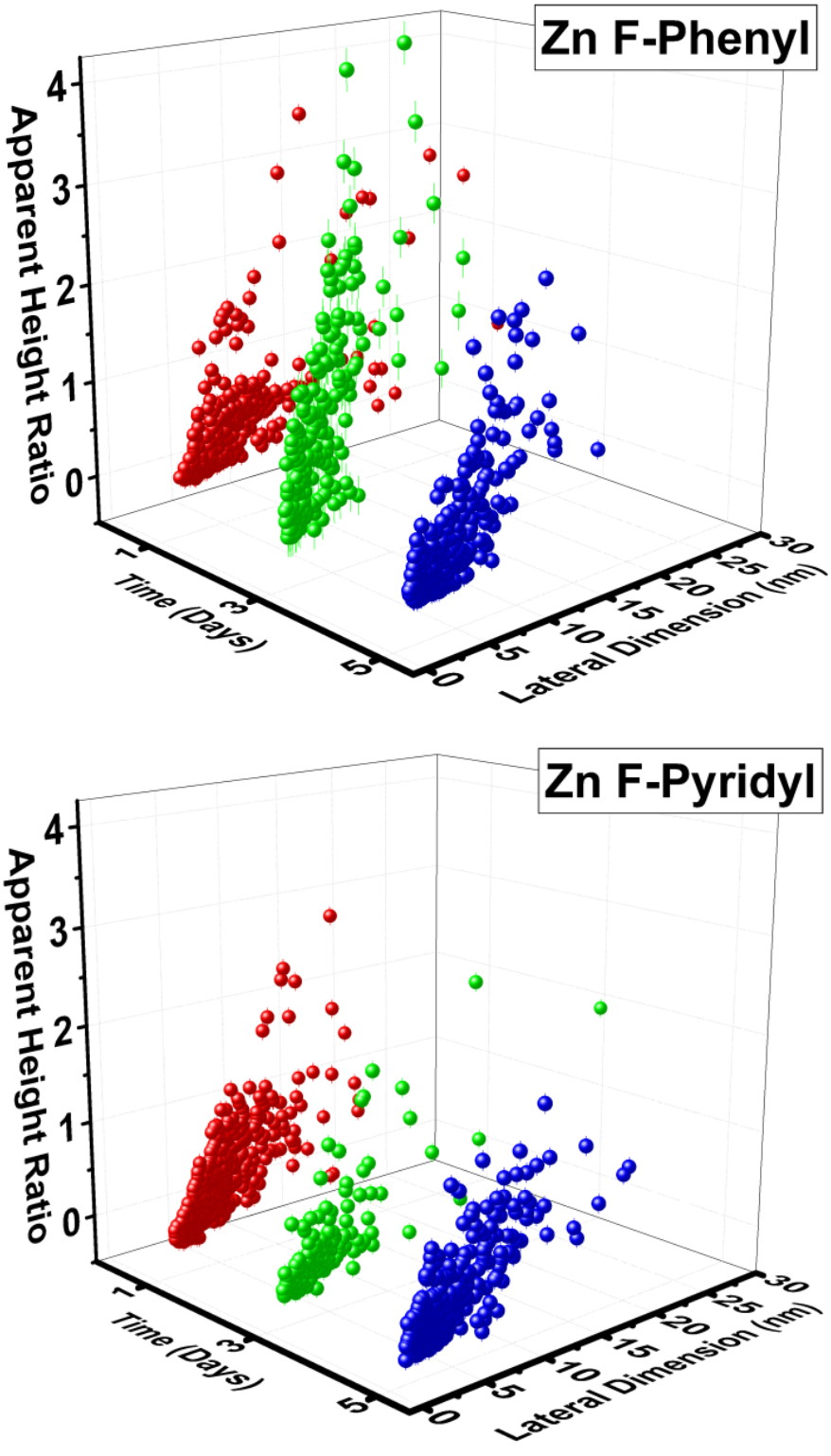

Figure 35. Continued.

A.3 Tunneling Efficiency

An alternative method to compare the relative electronic properties is by using the molecular tunneling efficiency (or tunneling decay constant), which indicates the decay of the electronic wavefunction in the barrier (i.e. molecule or molecular assembly), between all the porphyrin-thiol varieties. To do this, the Double-Layer Tunnel Junction Model (DLTJ)[20, 219] serves as a basis to contrast the well-studied tunneling efficiency of C12 to the previously unknown tunneling efficiency of these porphyrin-thiols. In the DLTJ model assuming that the conductance is the same for C12 and porphyrins,[230, 238] and the tunneling efficiency is given by

$$\beta_P = \frac{\beta_{C12} h_{C12} - \beta_{vac}(\delta h_{STM,P} - \delta h_{AFM,P})}{h_P} \qquad \text{(Equation 12)}$$

where β_{C12} is the tunneling efficiency of C12, h_{C12} is the height of the C12 from the surface of the substrate, β_{vac} is the tunneling efficiency in vacuum, $\delta h_{STM,P}$ is height difference between the porphyrin-thiol and dodecanethiol imaged by STM, and h_P is the height of the porphyrin-thiol from the surface of the substrate. The tunneling efficiency was calculated by using β_{C12} = 1.2 Å^{-1} [239] and h_{C12} = 14 Å.[234] This model was applied by obtaining the following about the porphyrin-thiol in the mixed SAM: the height of the porphyrin from the surface h_P and the physical height $\delta h_{AFM,P}$ obtained from AFM measurements, and the apparent height $\delta h_{STM,P}$ obtained from STM measurements. The tunneling efficiency for all porphyrin-thiol varieties as a function of lateral dimension and assembly time is shown in Figure 36 and Figure 37. The tunneling efficiency of single molecules and small clusters of porphyrin-thiols of all varieties was found to be 0.9±0.2 Å^{-1} (Figure 35). This is larger than the tunneling efficiency of other conjugated

systems; 0.2 to 0.6 $Å^{-1}$.[8, 137, 219] However, the tunneling efficiency for the porphyrin-thiols is within error of that reported for C12, which varies from 0.7 to 1.2 $Å^{-1}$ depending on the method of measurement.[235-239] The tunneling efficiency, using the DLTJ model, for large clusters of porphyrin-thiols produces negative, unphysical values (Figure 36) and this is the reason for the apparent height ratio (Equation 1) to be the method of comparison. Unphysical values suggest that the DLTJ does not apply for large clusters and that the mechanism of charge transport is different than for single and small clusters of porphyrin-thiols.

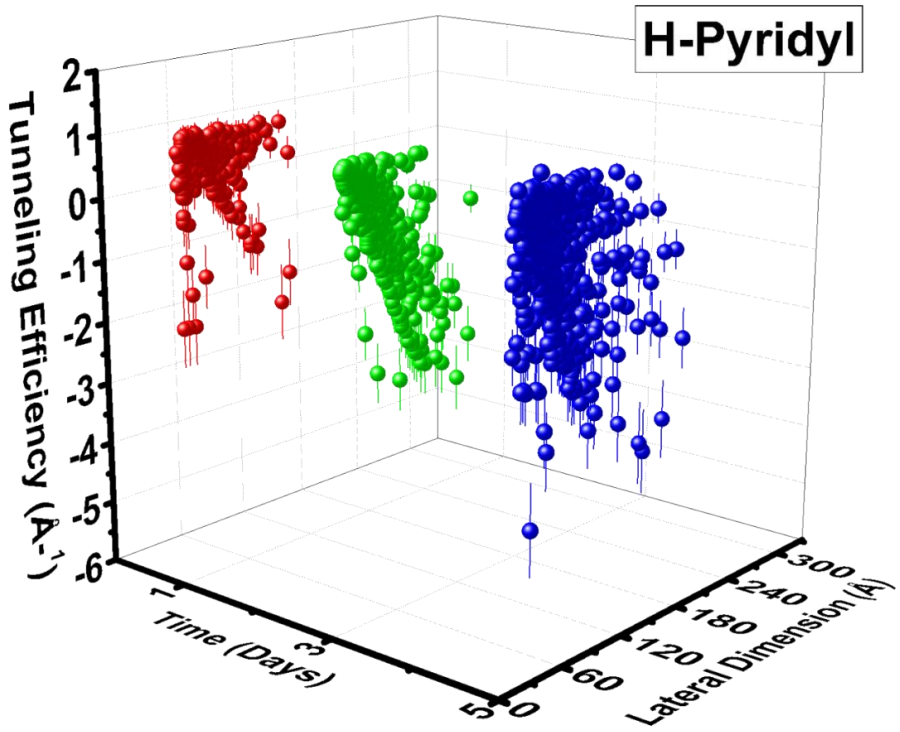

Figure 36. Three dimensional plots of the tunneling efficiency, as calculated from Equation 12 for all porphyrin-thiol varieties studied herein as a function of lateral dimension and assembly time.

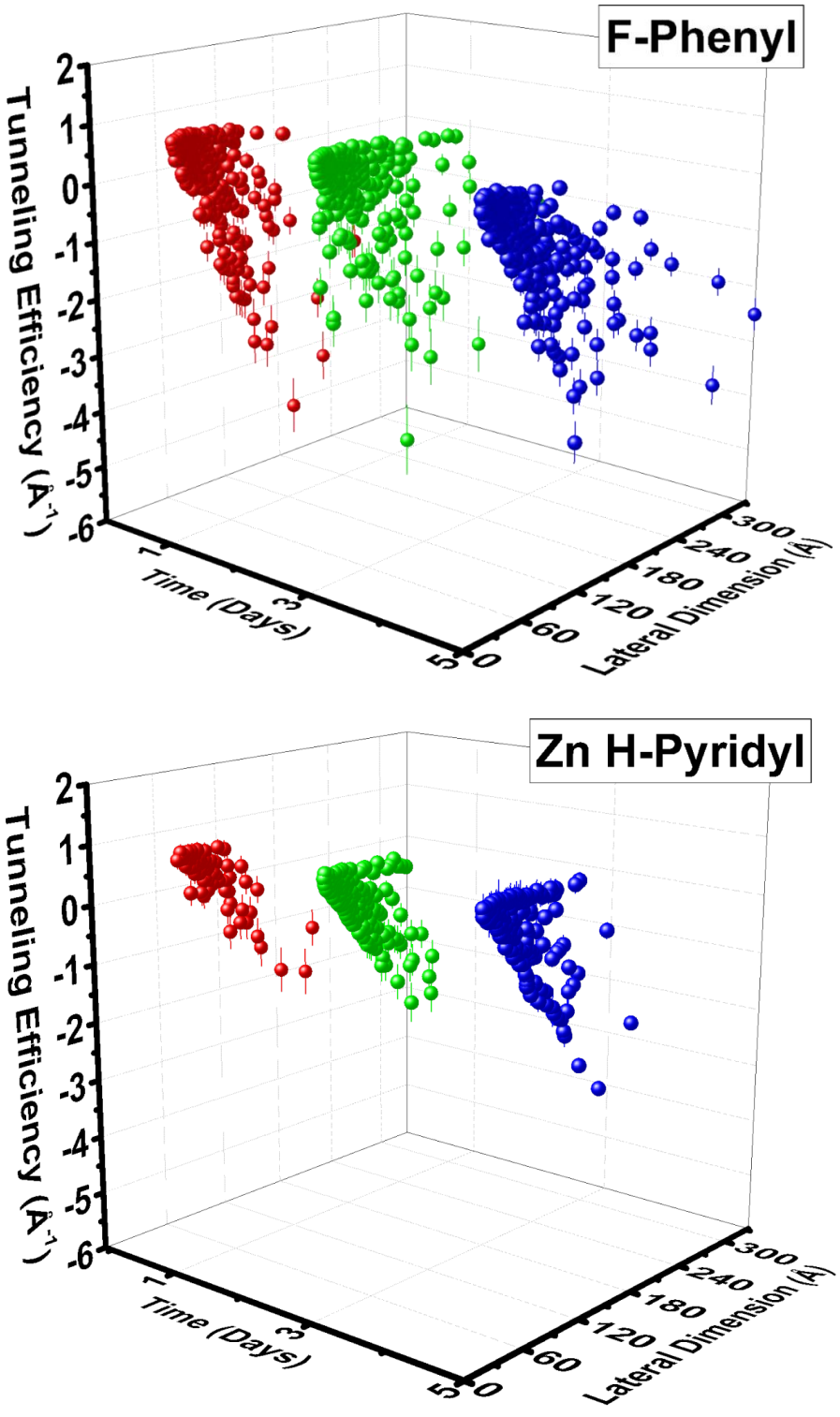

Figure 36. Continued.

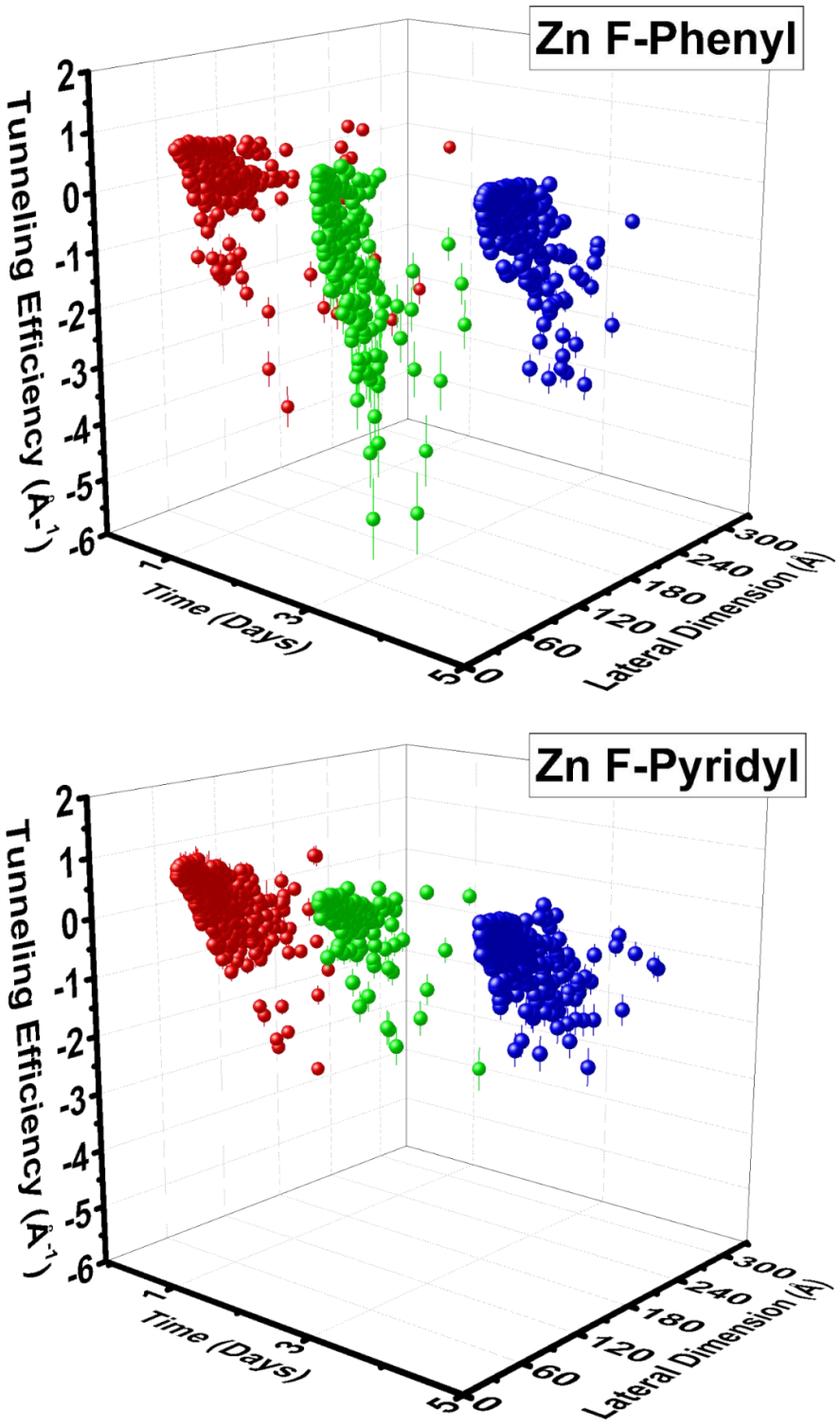

Figure 36. Continued.

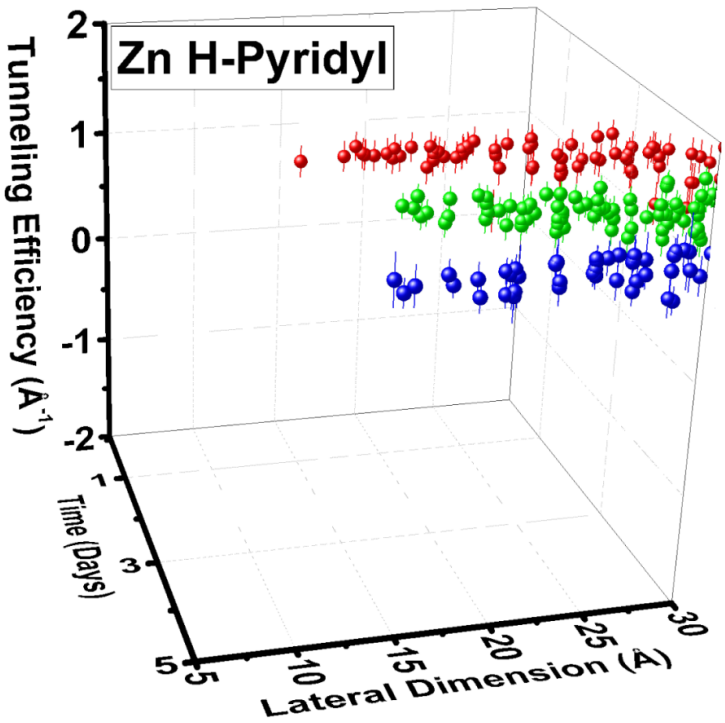

Figure 37. The tunneling efficiency, as calculated from Equation 12 for a particular porphyrin variety as an example, for only single molecules and small clusters at different perspective for clarity. For single molecules and small clusters, the tunneling efficiency is 0.9±0.2 $Å^{-1}$.

APPENDIX B

SUPPLEMENTAL DATA FOR CHAPTER III

B.1 Quantifying Statistics

Statistical treatment of the data presented in Chapter III is described here. These statistics are utilized to quantify the bias-induced switching, observed for porphyrin-thiol clusters formed after three days of self-assembly, and stochastic switching, observed in porphyrin-thiol clusters formed after five days of self-assembly.

B.1.1 Distribution of Geometrical Parameters

The distribution of geometrical parameters, such as the AFM physical height, the estimated molecular tilt derived from the AFM physical height difference, the STM apparent height, and lateral cluster dimension obtained from STM topography all show non-symmetric distributions, which could not be fitted to a normal distribution. Table 5 is an extension of Table 3 in Chapter III, providing the major statistical characteristics of the different parameters.

Property	Location	D1	D3	D5	Shape	D1	D3	D5
AFM Phys. Height (nm)	Mean	0.27	0.36	0.36	STD	0.11	0.19	0.17
	Median	0.24	0.30	0.31	IQR / 2	0.04	0.06	0.05
	Mode	0.21	0.26	0.29	Skew	2.42	3.87	6.70
Tilt Angle (degree)	Mean	43.3	41.0	40.5	STD	4.4	4.6	4.3
	Median	44.6	42.6	41.9	IQR / 2	1.5	1.9	1.7
	Mode	45.5	43.5	43.0	Skew	-2.8	-2.3	-3.1
Lateral Dimension (nm)	Mean	6.16	4.13	4.12	STD	4.06	2.57	2.66
	Median	5.23	3.55	3.28	IQR / 2	1.92	1.57	1.70
	Mode	3.20	2.00	1.80	Skew	2.53	1.95	1.54
STM App. Height (nm)	Mean	0.74	1.30	0.64	STD	0.53	0.87	0.48
	Median	0.62	1.04	0.45	IQR / 2	0.26	0.60	0.20
	Mode	0.35	0.50	0.35	Skew	2.56	1.29	2.09
Conductance Ratio (Eq. 3.2)	Mean	1.3 E4	1.7 E8	266				
	Median	1991	3.0 E6	16				
	Mode	16	122	3				

Table 5. Statistical analysis of the geometric characterization with the parameters as following. Location describes the different ways to extract a characteristic quantity, including the mean defined as arithmetic average over all measured values; median defined as the 50% probability value; mode defined as the highest occurrence value (or highest value of the histogram). The mode was computed on rounded values to 0.01, 0.5, 0.1 and 0.05 for AFM height, tilt, lateral dimension and STM height, respectively. Shape describes the different statistical features of the distribution, including STD defined as the standard deviation of the sampling; IQR / 2: defined as half of the interquartile range which is the difference between the 75% and 25% percentiles, and skew is a measure of the distribution asymmetry that equals 0 for a symmetric distribution.

Two of the parameters in Table 5 are not measured but computed. The estimated tilt angle is extracted from the AFM physical height, compared to nominal $ZnTPPF_4$-SC_5SH and C12 lengths according to Equation 6. The difference between the between the AFM physical height (Figure 38) and STM apparent height (Figure 39) are used to compute the apparent height ratio (Figure 40) according to Equation 7. This comparison is that of a population, because STM and AFM were measured by two different instruments on different locations of the sample. The values in Table 3 refer to

calculations using the difference between the mean, median or mode of the STM apparent height and the same characteristic of the distribution in the AFM physical height. The distribution in relative conductivity as presented in Figure 40 was computed by sorting the two independent populations and comparing pairs of values with the same relative position. For example, the highest STM apparent height value was compared to the highest AFM physical height value, the lowest with lowest, and so on. Figure 40 plots the log of the apparent height ratio because it has an exponential dependence on the height difference. Figure 40 shows a satisfying correlation between the two methods, which strengthen the relevance of the estimated distribution in relative conductance.

Figure 38 to Figure 42 displays the histograms of the different parameters and over them the mean, median and mode as vertical lines. These three parameters coincide for normal distribution, which is clearly not the case here. In all cases, the median (‘2’, magenta) is the central of the three location values, and therefore, better describe gross shifts in the distribution with time. Therefore, this parameter is chosen to represent the location of the distribution. The mode is generally the least sensitive to the behavioral evolution with immersion time, suggesting that there is a significant portion of the clusters that do not evolve much with time.

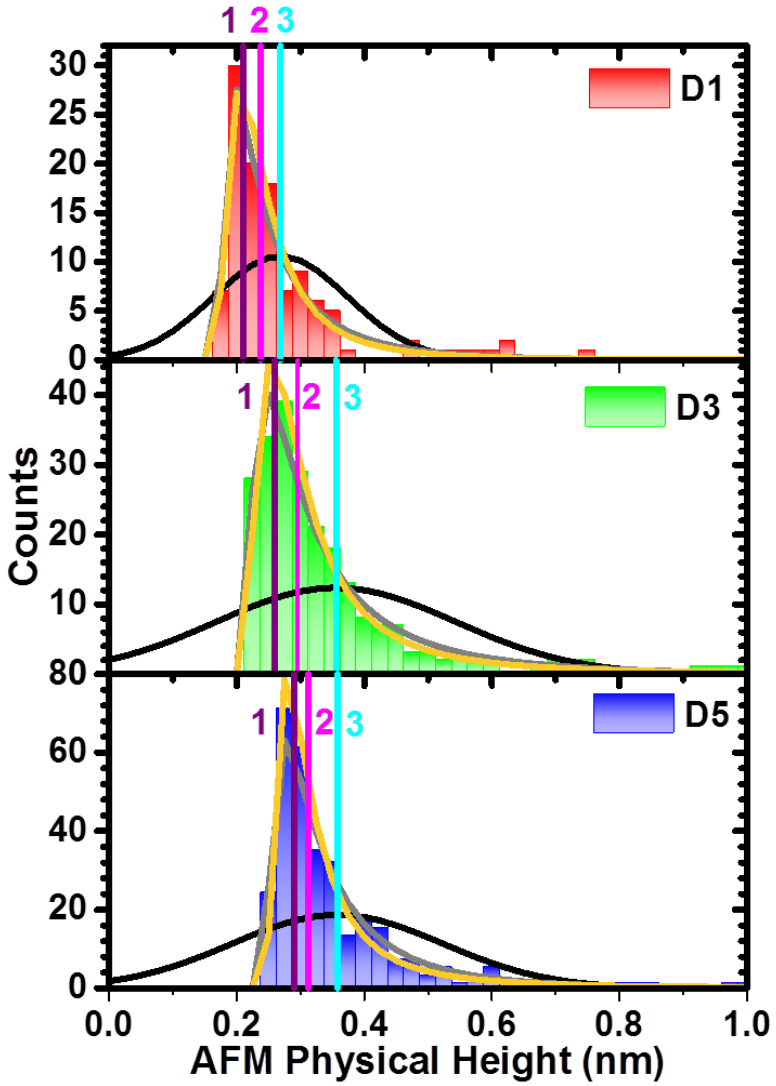

Figure 38. Distribution of the physical heights measured by AFM. Each panel is for a different immersion time; vertical lines show the mode (1), the median (2) and the mean (3). Curves are fits of the raw data (not histograms) to a Gaussian (black), inverse Gaussian (orange) and generalized extreme value (gray) distribution.

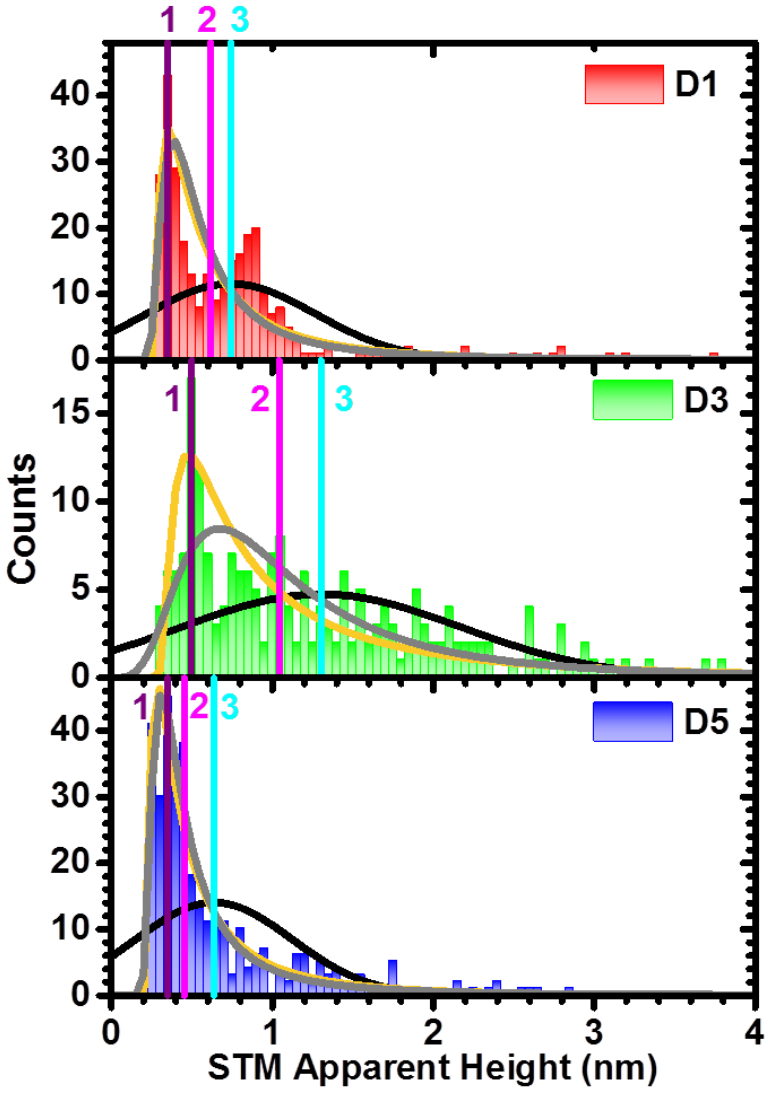

Figure 39. Distribution of the STM apparent heights. Curves and lines are as above.

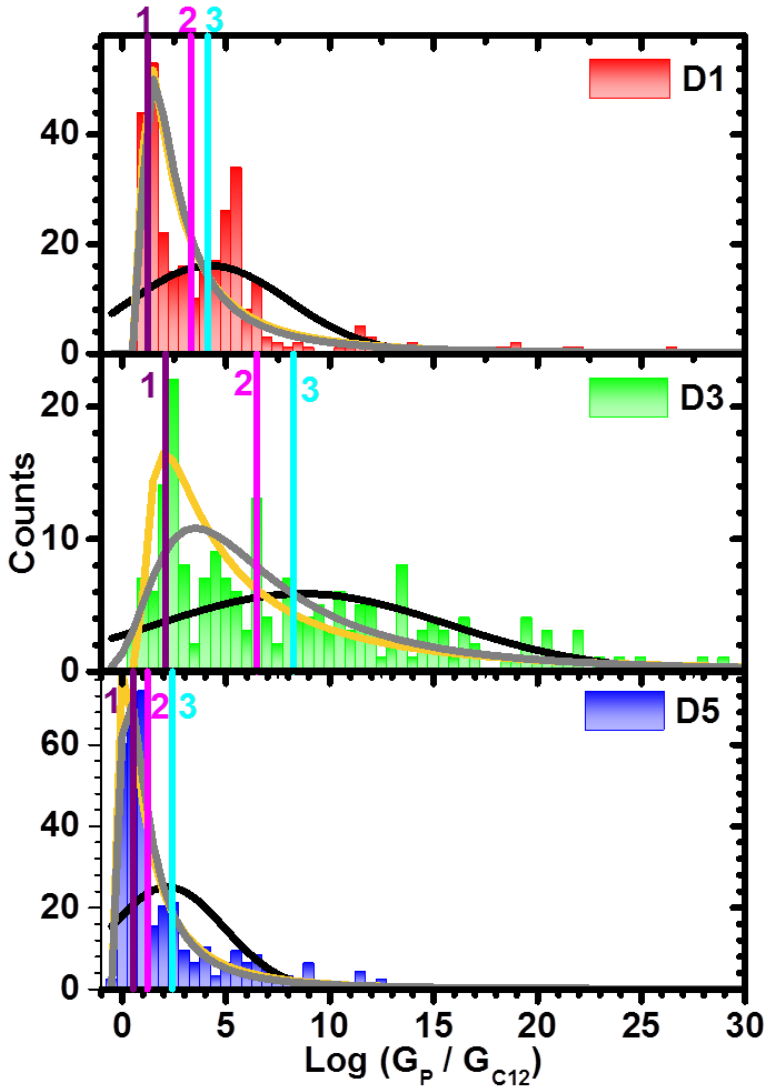

Figure 40. Distribution of the estimated relative conductivities according to Equation 7. Extracting the relative conductivity requires the difference between the STM apparent height and the AFM physical height, as explained Chapter III. Curves and lines are as above, except that lines 1, 2, 3 mark values computed from the mode, median and mean of the two raw populations.

The different sampling arrays were also fitted to three distribution functions: normal (black curve), inverse Gaussian (orange curve) and generalized extreme value (gray curve). As can be seen in Figure 38 to Figure 42, the center of the normal distribution coincides with the mean location (vertical line ‘3’). The width of the normal distribution or the formal standard deviation is much larger than the real width of the distribution. Therefore, we find the interquartile range (IQR) to be a better representation of the width of the distribution than the standard deviation.

The asymmetry of the data is clearly not in accord with a normal distribution. A common distribution to model nonnegative positively skewed data is inverse Gaussian (orange curves), which gave a fairly good fit to the data. However, we fit the data to this model, only after adjusting the data to start rising at 0 (i.e., fitting used $z = x\text{-}min(x)$ as the independent parameter; for negative skew as with tilt values, $z = x\text{-}min(x)$ was used. Another distribution functions that yielded fair description of the data is generalized extreme value (gray curves). This distribution aimed at describing maximum or minimum values within a random variable; this might reflects the variability in lateral cluster dimensions which has a limited minimum value (equals to a single molecule) and an un-bounded upper value.

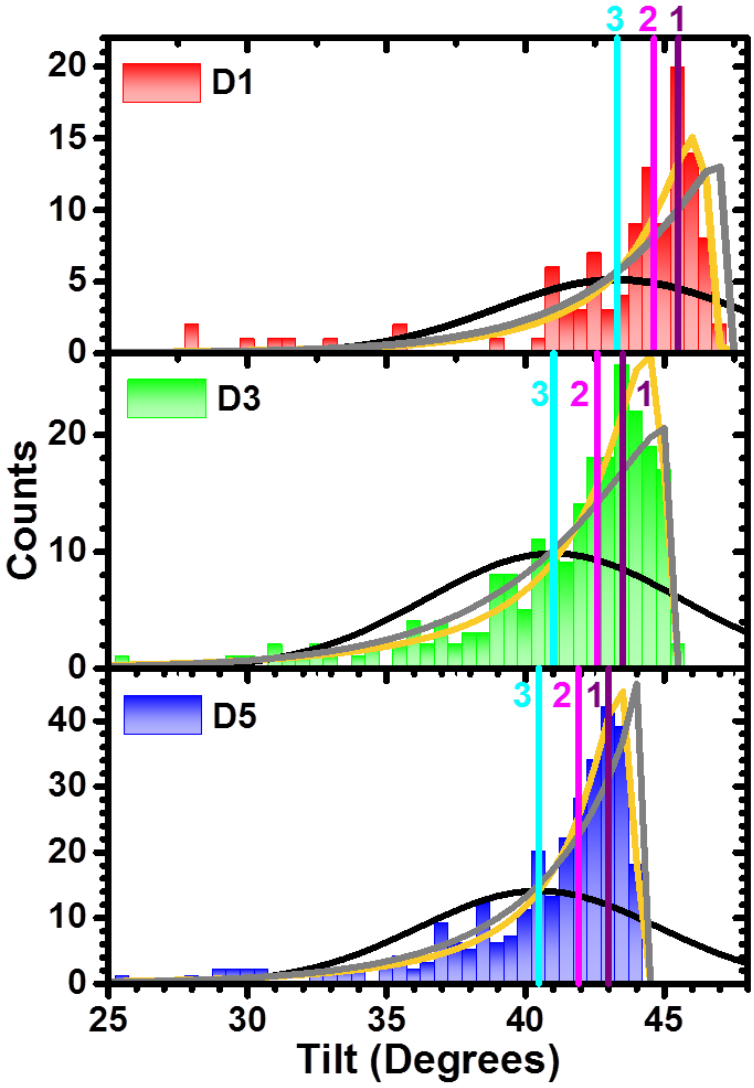

Figure 41. Distribution of the computed tilt angles (Equation 6) from the AFM physical height. Vertical lines show the 1) mode, 2) median and 3) mean. The curves are fits to a Gaussian (black), inverse Gaussian (orange) and generalized extreme value (gray) distribution. Notice that the negatively skewed data was fitted to an inverse Gaussian by using $z = x\text{-}min(x)$.

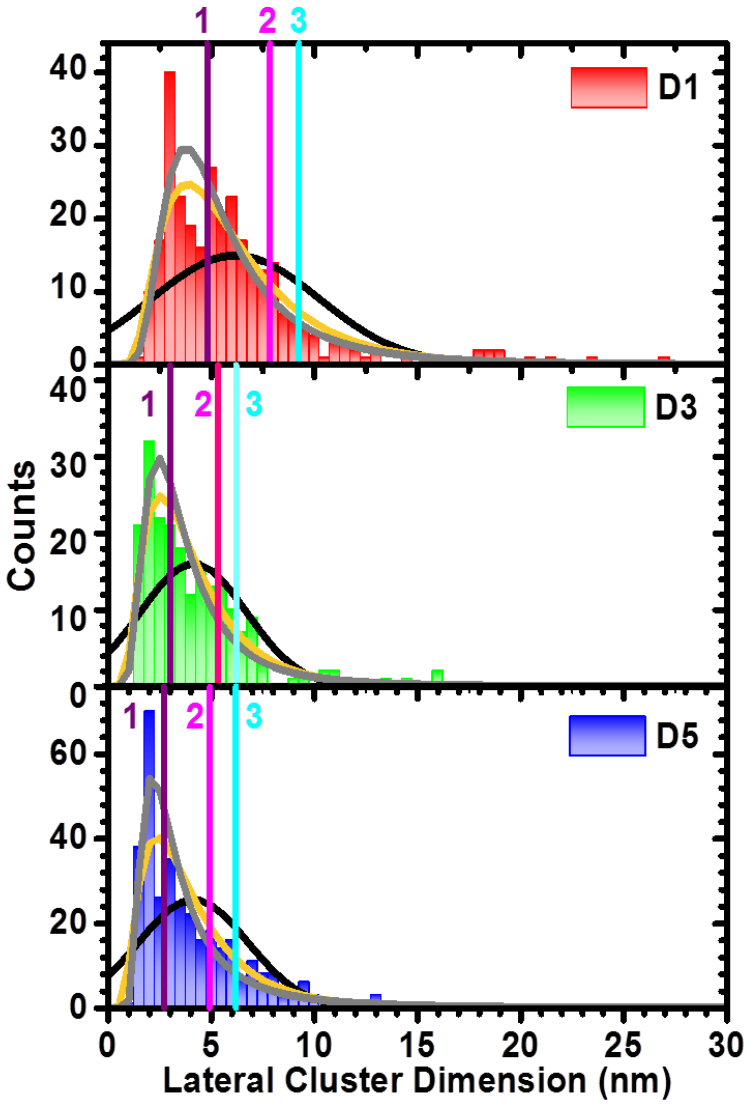

Figure 42. Distribution of the lateral cluster dimension as extracted from STM images. Curves and lines are as above.

B.1.2 Distribution of Equilibrium Conductance

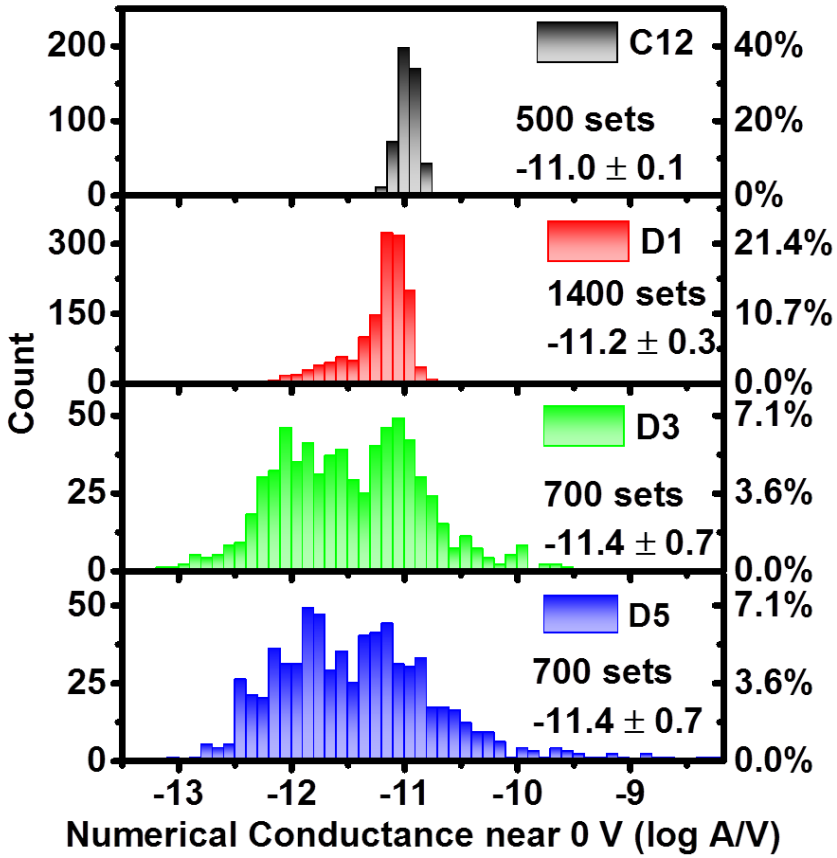

Figure 43. Histograms of the equilibrium conductance (G_{Eq}) for all measured data. The equilibrium conductance is derived by averaging the 4 data points between ± 20 mV of the numerically extracted conductance. The G_{Eq} values shown here are the reference values used to compute the low-conductance gap (V_{tunn}) of Figure 15.

B.1.3 Lack of Time Dependence in Stochastic Switching

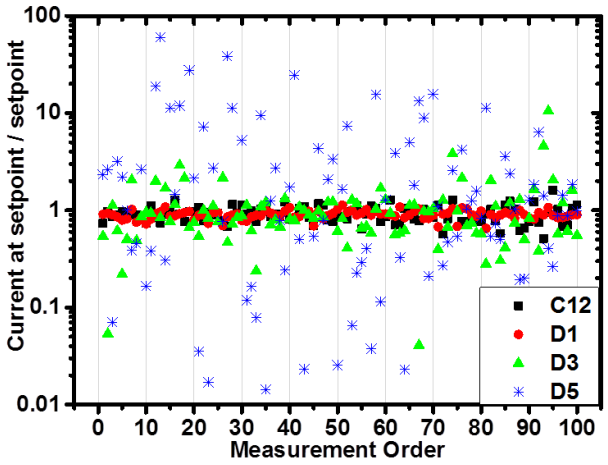

Figure 44. Stability of set-point current with successive scans, showing the set-point current ratio, P_{sp} (see Equation 11) for 100 successive scans at a constant tip location verses their recoding order. Each symbol refers to different immersion times. The data set is identical to the one used in Figure 12.

B.2 I-V Spectroscopy of Pre-Formed ZnTPPF4-SC5SH Clusters

Immersing the C12 matrix in high concentration (0.5 mM cf. 0.05 mM reported in Chapter III) of $ZnTPPF_4$-SC_5SH solution for only one day yielded a highly-crowded mixed monolayer. These samples were difficult to characterize by STM because substance appeared to be deposited on the tip. Still, it is assumed that the high concentration and high deposition rate enhance the aggregation within the clusters and therefore serves as important evidence for the effect of local organization on transport. AFM characterization of the high-concentration clusters yielded practically identical physical height to that of clusters made by immersion in low-concentration. STM, in contrast, indicated distinctly different behavior of $ZnTPPF_4$-SC_5SH clusters made after

immersion for one day in high- compared to low-concentration solutions. While immersion in low-concentration yielded fairly reproducible clusters and STS curves after one day, immersion in a high-concentration solution for the same duration yielded a large height distribution and marked differences in the I-V behavior varying from continuous tunneling to a pronounced gap-opening, as observed for longer immersion times in a low-concentration solution. A total of 14 clusters were characterized by STS, with 100 repeating scans on each cluster. Six of the clusters had a STM apparent height of 2.5 to 4 nm cf. apparent height $\leq$ 1.5 nm for low-concentration D1 samples. The rest of the tested clusters were divided to two sub-groups of four in each, showing I-V behavior similar to either short immersion (D1) in low-concentration or long-immersion time (D3) in low concentration. I-V parameters for these two sub-populations are shown as bar histograms in Figure 45. For comparison, the distribution of I-V parameters measured over low-concentration clusters are over-plotted as lines for one day (‘D1’, red) and three days (‘D3’, green).

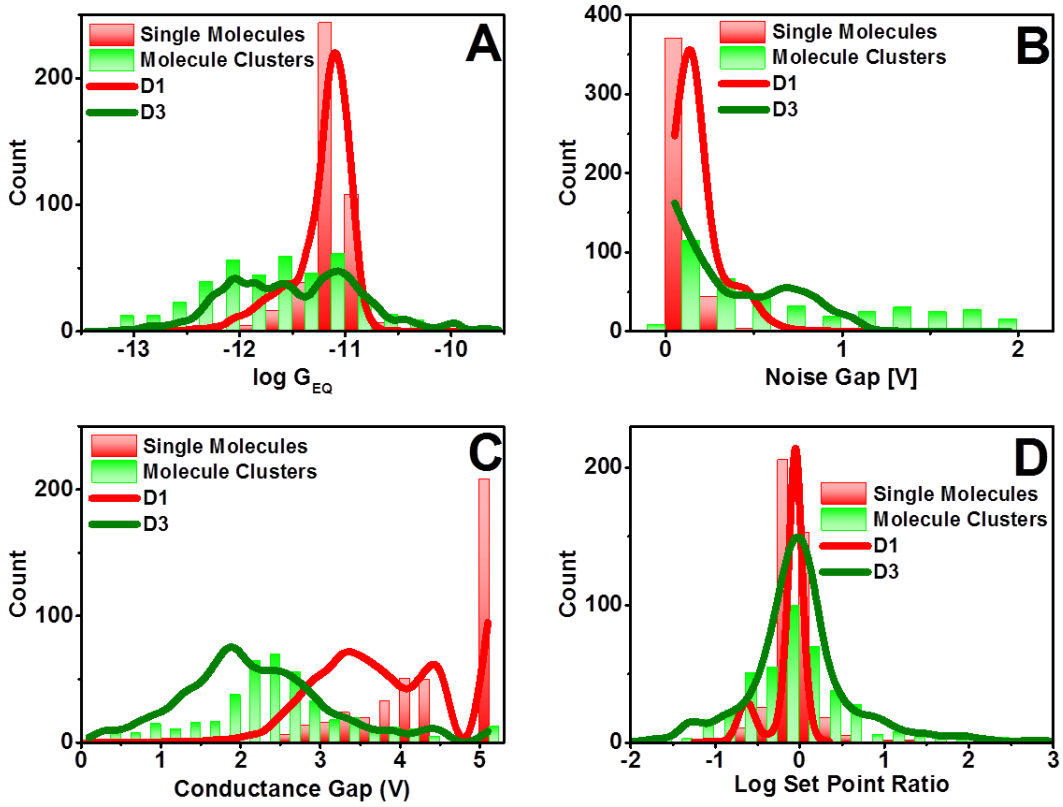

Figure 45. Histograms of I-V parameters of $ZnTPPF_4$-SC_5SH clusters formed after one day immersion in 0.5 mM solution (10 times the normal concentration). Bars are histogram of single molecules and molecular cluster; Curves are references showing histogram values for clusters made by immersion time in low-concentration solution for one day (red) and three days (green). Each panel shows a different parameter: A) Conductance near 0 V (see Figure 44), B) the noise bias gap (see Figure 14 and Equation 8), C) the low-conductance bias gap (Figure 15, Equation 9, and Equation 10), and D) the set-point log-ratio (Figure 16 and Equation 11).

B.3 Microscopy Images of $ZnTPPF_4$-SC_5SH in C12 Monolayer

$ZnTPPF_4$-SC_5SH clusters were characterized by Atomic Force Microscopy (AFM) and Scanning Tunneling Microscopy (STM). Typical AFM and STM topography images (on different locations) are shown in Figure 46 and Figure 47. The height of the clusters measured from either AFM or STM is the difference with respect to the C12

monolayer. The height measured from AFM is the physical height, δ_{AFM}, and from STM is the apparent height, δ_{STM}. Additionally, the lateral dimensions of the clusters are extracted from STM images due to finer lateral resolution than AFM. As an example of this height and lateral dimension measurement, cross sections of $ZnTPPF_4$-SC_5SH clusters are shown in Figure 46(C) and Figure 47(C).

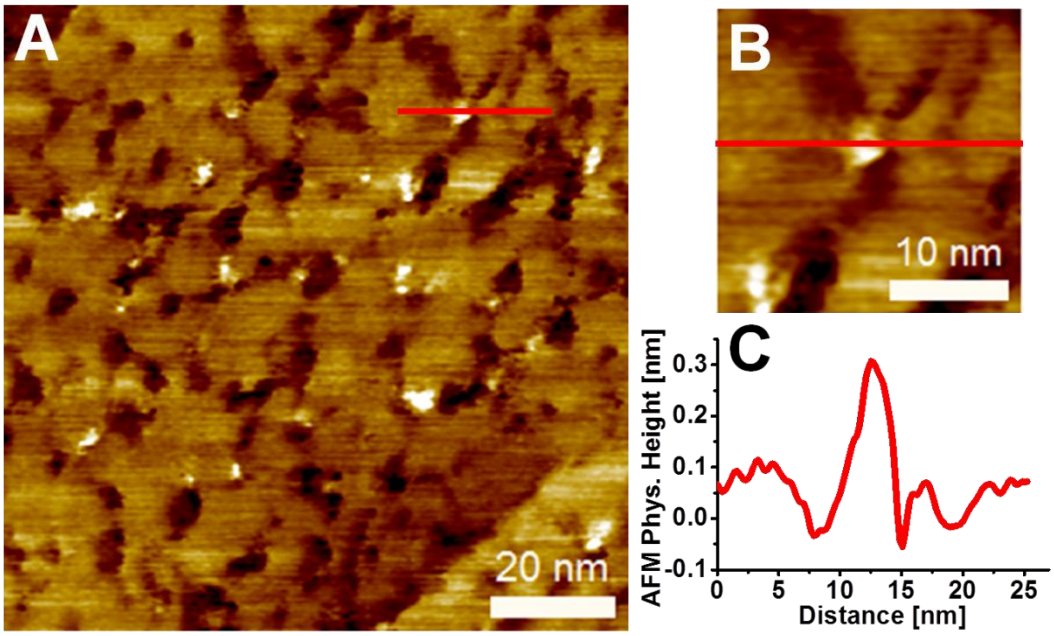

Figure 46. Typical AFM topography of $ZnTPPF_4$-SC_5SH clusters in the C12 matrix. A) AFM topography image where the white features are $ZnTPPF_4$-SC_5SH clusters. B) A closer look at a certain $ZnTPPF_4$-SC_5SH clusters from the image shown in A). A cross section is taken from this $ZnTPPF_4$-SC_5SH cluster and the profile is shown in C). The difference between the background C12 and the maximum height of the $ZnTPPF_4$-SC_5SH cluster is the physical height.

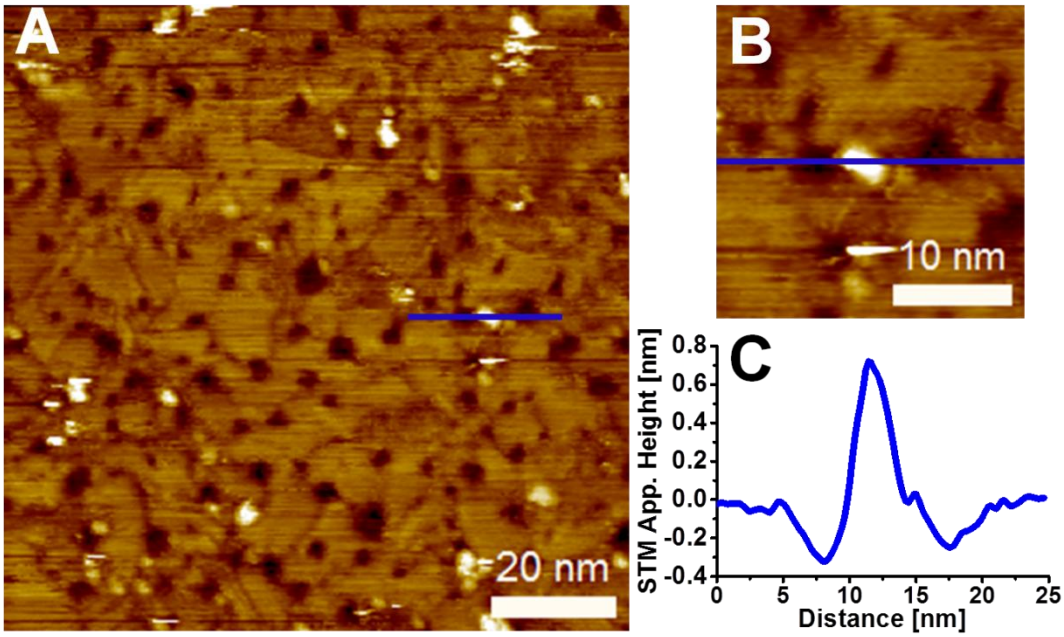

Figure 47. Typical STM topography of $ZnTPPF_4$-SC_5SH clusters in the C12 SAM. A) STM topography image where the white features are the $ZnTPPF_4$-SC_5SH clusters. B) A closer look at a certain $ZnTPPF_4$-SC_5SH cluster from the image shown in A). A cross section is taken from this $ZnTPPF_4$-SC_5SH cluster and the profile is shown in C). The difference between the background C12 and the maximum height of the cluster is the apparent height. Although this is not the identical cluster shown in Figure 46, in general the apparent height is larger than that of the physical height. The larger apparent height is due to the increased conductivity of the $ZnTPPF_4$-SC_5SH clusters with respect to the C12 SAM.

B.4 Stochastic Switching as a Function of STM Imaging Time and Set-Point

The conductive state of $ZnTPPF_4$-SC_5SH clusters formed after five days were examined by repeated and continuous STM imaging with constant imaging set-points at 1.4 V and 20 pA. Figure 48 displays the STM images recorded during 15 cycles. Initially there are 14 ZnTPPF4-SC5SH features visible as bright protrusions in the defined scan area. The apparent height and lateral dimensions of the visible ZnTPPF4-SC5SH features were monitored throughout the 15 cycles. Three of these features are shown

below where one ZnTPPF4-SC5SH feature is displayed in Figure 48(D) and the data presented in Table 6 and two ZnTPPF4-SC5SH features are displayed in Figure 48(C) and the data presented in Table 7. The apparent height of these three features stochastically fluctuates from a large apparent height, as large as 2.8 nm, to a small apparent height, as small as 0.3 nm. Additionally, in some cases, the ZnTPPF4-SC5SH feature disappears and is no longer apparent in the STM image, then reappears in a later image cycle (Figure 48(C) and Table 7). Fluctuations in the apparent height indicate that the conductive state of these ZnTPPF4-SC5SH clusters is dynamic under these imaging conditions. ZnTPPF4-SC5SH clusters stochastically fluctuate from a highly conductive "on" state (large apparent height) to a low conductive state (small apparent height) and to an even lower "off" conductive state (non-existent apparent height). In the final image only one of the ZnTPPF4-SC5SH clusters was still visible in the "on" state while the others switched to the "off" state (Figure 48(B)). When the image range was expanded to include the previously un-imaged surrounding area, it was clear that only the continuously imaged area was devoid of apparent ZnTPPF4-SC5SH features as evidenced in Figure 48(A-C). For prolonged imaging beyond the 15 cycles described here, the ZnTPPF4-SC5SH features seldom re-appeared. This suggests that prolonged STM imaging under 1.4 V and 20 pA eventually turns "off" the ZnTPPF4-SC5SH clusters in which the conductance state settles into a possible local potential minimum. Therefore, stochastic conductance switching was observed by repeated and continuous STM imaging at 1.4 V and 20 pA but eventually stochastic switching is overruled by switching "off" due to prolonged imaging.

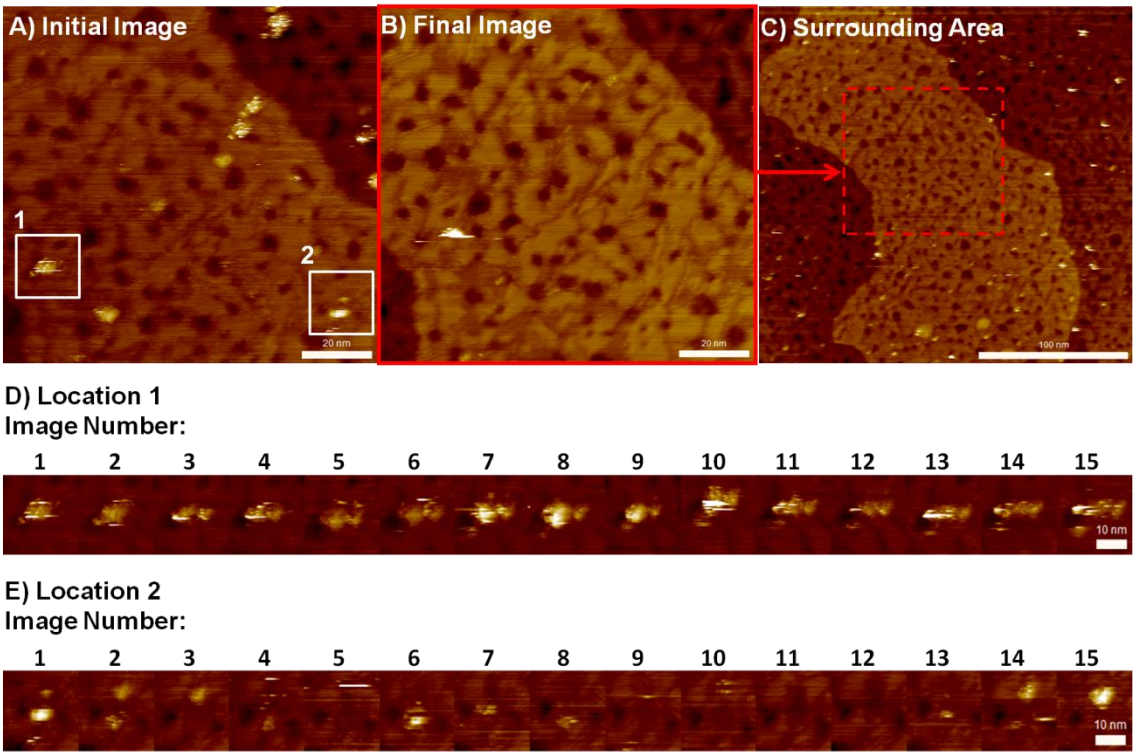

Figure 48. Investigation of stochastic switching in $ZnTPPF_4$-SC_5SH clusters formed after five days by repeated and continuous STM imaging keeping constant imaging set-points; 1.4 V and 20 pA. A) The initial STM image recorded in the series in which 14 $ZnTPPF_4$-SC_5SH features are visible. The scale bar is 20 nm. B) The final STM image after 15 continuous images in which only 1 $ZnTPPF_4$-SC_5SH features is visible. The scale bar is 20 nm. C) After the final image was recorded, the scan range was expanded to include the surrounding area. It appears that there only $ZnTPPF_4$-SC_5SH features in the surrounding, previously un-scanned area. The scale bar is 100 nm. Repeated and continuous STM images of a particular $ZnTPPF_4$-SC_5SH feature at D) location 1 and E) location 2 as indicated in A). The scale bar is 10 nm.

Location 1															
Image Number	1	2	3	4	5	6	7	8	9	10	11	12	13	14	15
Apparent Height (nm)	1.6	0.7	2.1	2.2	0.9	0.9	1.8	1.5	1.4	2.8	1.7	1.5	2.8	1.3	2.2
Lateral Dimension (nm)	11.8	11.3	8.3	12.5	12.2	8.9	18.1	10.6	11.5	12.7	15.1	13.9	16.2	16.5	18.1

Table 6. The apparent height and lateral dimension of the $ZnTPPF_4$-SC_5SH clusters shown at location 1 in Figure 48**(**D) during continuous STM imaging at constant imaging set-points, 1.4 V and 20 pA. The image numbers here are associated with the image numbers in Figure 48**(**D). The apparent height stochastically fluctuates from a large apparent height or a highly conductive state to a reduced apparent height or a less conductive state. With the apparent height fluctuations, the lateral dimension fluctuates as well.

Location 2															
Image Number	1	2	3	4	5	6	7	8	9	10	11	12	13	14	15
Apparent Height (nm)	0.4	0.5	0.5	0.5	N/A	N/A	N/A	0.5	0.5	N/A	N/A	N/A	N/A	0.7	0.9
	0.8	0.5	N/A	0.4	0.8	0.5	0.7	N/A	N/A	N/A	N/A	N/A	0.6	0.3	N/A
Lateral Dimension (nm)	3.5	6.4	7.0	1.9	N/A	N/A	N/A	5.4	3.9	N/A	N/A	N/A	N/A	8.3	9.8
	7.9	5.1	N/A	2.7	8.2	6.3	7.1	N/A	N/A	N/A	N/A	N/A	4.1	2.4	N/A

Table 7. The apparent height and lateral dimension of the $ZnTPPF_4$-SC_5SH clusters shown at location 2 in Figure 48**(**E) during continuous STM imaging at constant imaging set-points, 1.4 V and 20 pA. There are two $ZnTPPF_4$-SC_5SH features that appear in Figure 48**(**E) and both of these are tracked here in which the uppermost feature is recorded in the upper rows and the bottommost feature is recorded in the gray-highlighted, lower rows. The image numbers here are associated with the image numbers in Figure 48**(**E). The apparent height stochastically fluctuates from a large apparent height to a reduced or even a non-existent apparent height (denoted N/A). With the apparent height fluctuations, the lateral dimension fluctuates as well and sometimes is even not apparent (denoted N/A).

APPENDIX C

SUPPLEMENTAL DATA FOR CHAPTER IV

C.1 Relocating Nanometer-Sized Features in AFM and STM

Studying the same nanometer-sized features in AFM and STM is a technical challenge because it requires removing a macroscopic sample from one microscope, re-mounting and locating the same nanometer-sized area within a centimeter-sized wafer. In this work, we fabricated nanometer-sized domains of C5DT and TTPF5 facilitated by AFM and to study the structure with molecular resolution and the electronic properties of the fabricated domains, we employed STM. To provide this means for this fabrication/characterization approach we developed a relocation scheme that consists of a series of nested patterns in which the large patterns (100s of micrometers) visible optically, "point" to intermediate patterns (10s micrometers) that sequentially "point" to the small (nanometer) patterns of interest (Figure 49). The large patterns were fabricated using contact mode AFM with a stiff (spring constants of approximately 50 N/m) cantilever and large load. In contact, the tip is rastered across the Au(111) surface to remove a portion of the Au, essentially, carving away the Au to form the desired pattern. The load was controlled empirically where the minimum load was applied sufficient to carve away the Au. Carving the Au(111) surface was done in this way to pattern the large squares in Figure 49(A-B), Figure 50(A) Figure 51(A), and the intermediate matrix of squares in Figure 50(B-C).

Three variations of the nested pattern scheme are presented with countering advantages and disadvantages. First in Figure 49, the large square was carved as described above and the intermediate matrix of squares was fabricated via Focused Ion Beam (FIB). FIB is advantageous because of the ability to fabricate controlled, uniform lines (~20 nm in depth) with essentially no material build-up near the lines. However, the ion beam can alter the Au on the surface, thereby altering any absorbed monolayer that organizes with respect to the underlying Au(111) such as alkanethiols. Second, the variation shown in Figure 49 alleviates the issues of the ions beam because the intermediate matrix of squares is carved into the Au like the large square. But the carved lines can be nonuniform (depths varying from 200-20 nm) with large amounts of material build-up (visible in the contrast change near the lines in Figure 50(C) that make subsequent imaging in STM near impossible. Thirdly, to alleviate the issue of imaging carved lines with STM, large nested squares (larger than scan range of the STM) are carved in which the STM tip can be manually place (Figure 51(A)). The intermediate pattern is a star-like square that is nanografted as is the nanometer sized patterns of interest localized at the center of the star-like square (Figure 50(B)). Nanografting the intermediate pattern has the advantage of controlled, neat line with less timely, in-suit fabrication, where the intermediate pattern can serves as additional fabricated structures of interest to study in STM. In Figure 51(B), 16-mercaptohexadecanoic acid (16MUA) is nanografted into C12 and since 16MUA is taller than C12, there is sufficient contrast in the AFM image is discern the star-like square patter. However, when the combination

materials do not have sufficient contrast in AFM and/or STM (as is the case with C5DT nanografted into C12) this scheme is un-useable.

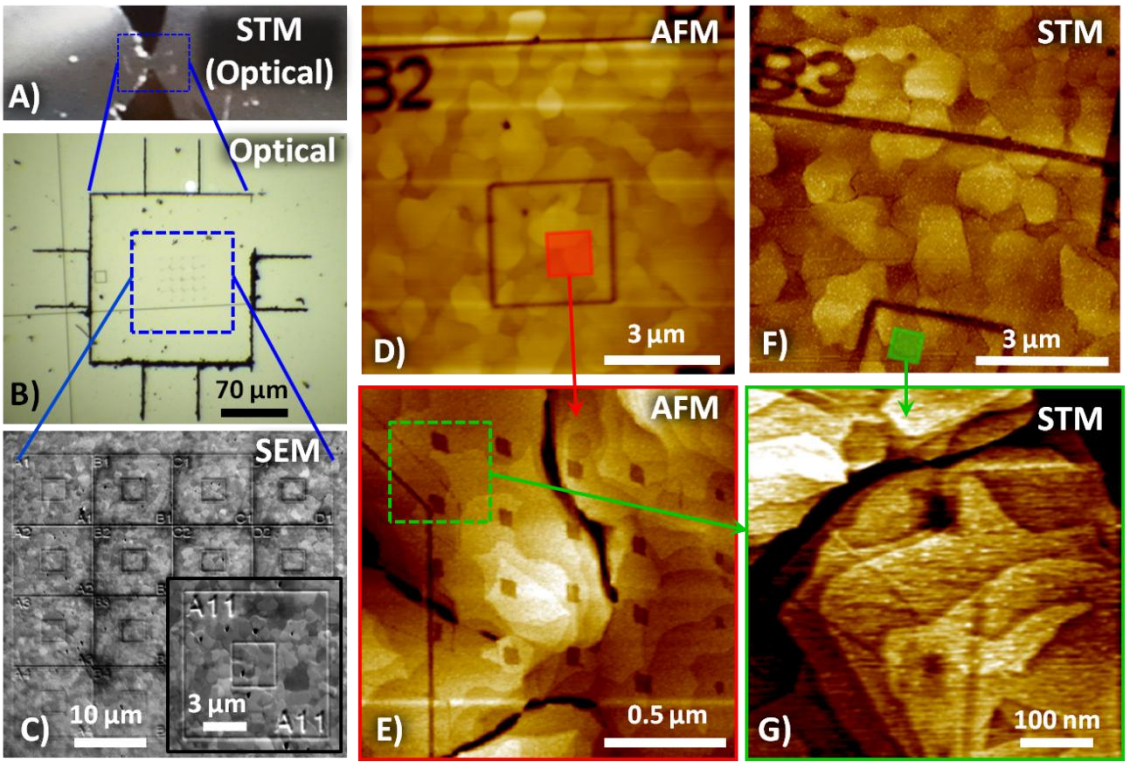

Figure 49. Nested patterning scheme used to relocate the same nanometer-sized features in the AFM and STM. A) Optical image showing a 250 μm^2 square carved in the Au(111) surface in which the STM tip is manually positioned. B) Optical image of the square carved into the Au(111). The interior of the carved square contains a matrix of smaller squares (10 μm^2) fabricated by FIB and is clearer in C). The inset in C) displays a particular pattern in the matrix that consists of an outer (10 μm^2) and inner square (3 μm^2) along with an index used to relocate a specific 3x3 µm area. D) AFM image of a square in the matrix where the nanometer sized patterns are localized to the inner square. E) Nanometer sized patterns of C5DT nanografted into C12 using AFM. F) STM image of the same square as in D). G) STM image of the same nanografts as in E).

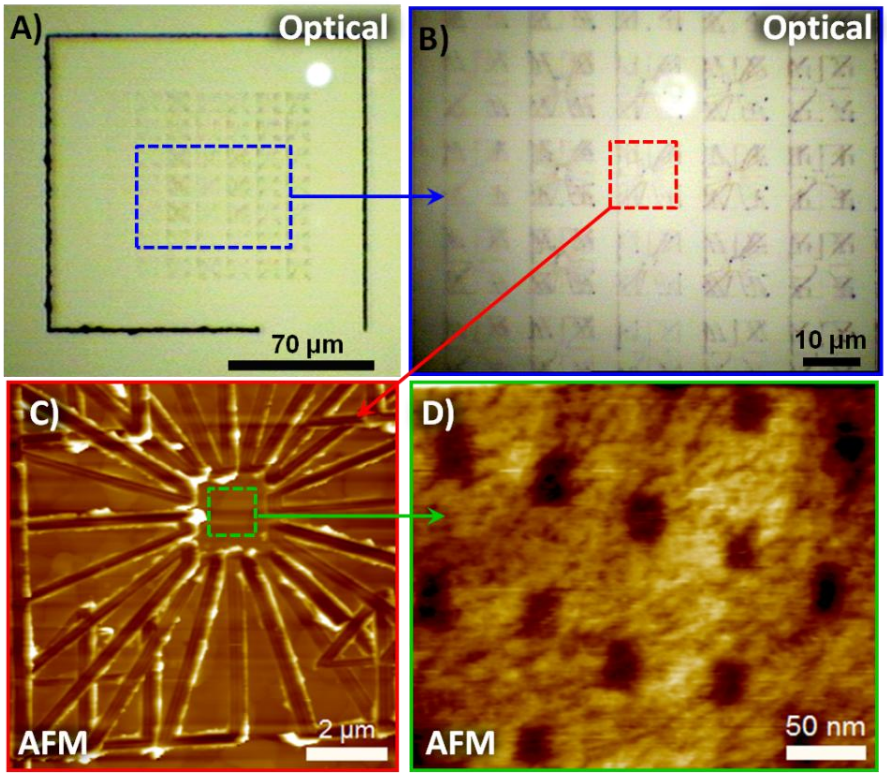

Figure 50. Alternative method for localizing nanometer sized features where the matrix of smaller patterns inside the large square A) is like-wise fabricated by carving and not by FIB as in Figure 49. C) AFM image of one star-like patterned square in the matrix with a 44 index to identify a particular pattern. D) At the center of the star-like pattern, nanometer sized features (C5DT nanografted into C12) are localized within a 2x2 µm area.

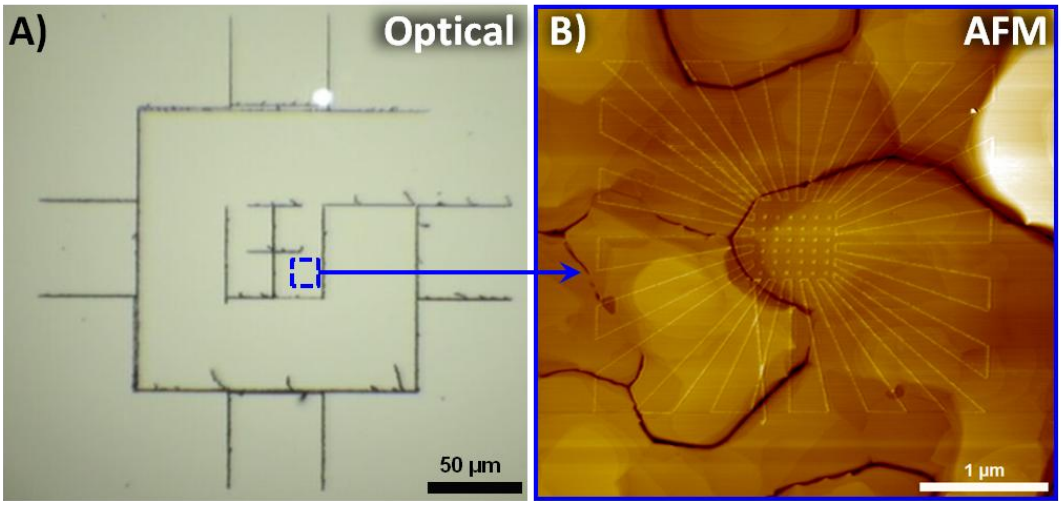

Figure 51. Alternative method for localizing nanometer sized features where a series of nested squares (150 μm^2 to 25 μm^2) are carved into the Au(111) surface A) and the smaller (2.5 μm^2) star-like pattern is nanografted inside the 25 μm^2 square B). Within the nanografted star-like pattern, nanometer sized features are localized; where here 16MUA is shown nanografted into C12.

C.2 IMAGE SEQUENCES OF THE ORDER TO DISORDER TRANSITIONS IN THE GRAFTED C5DT STRUCTURES*

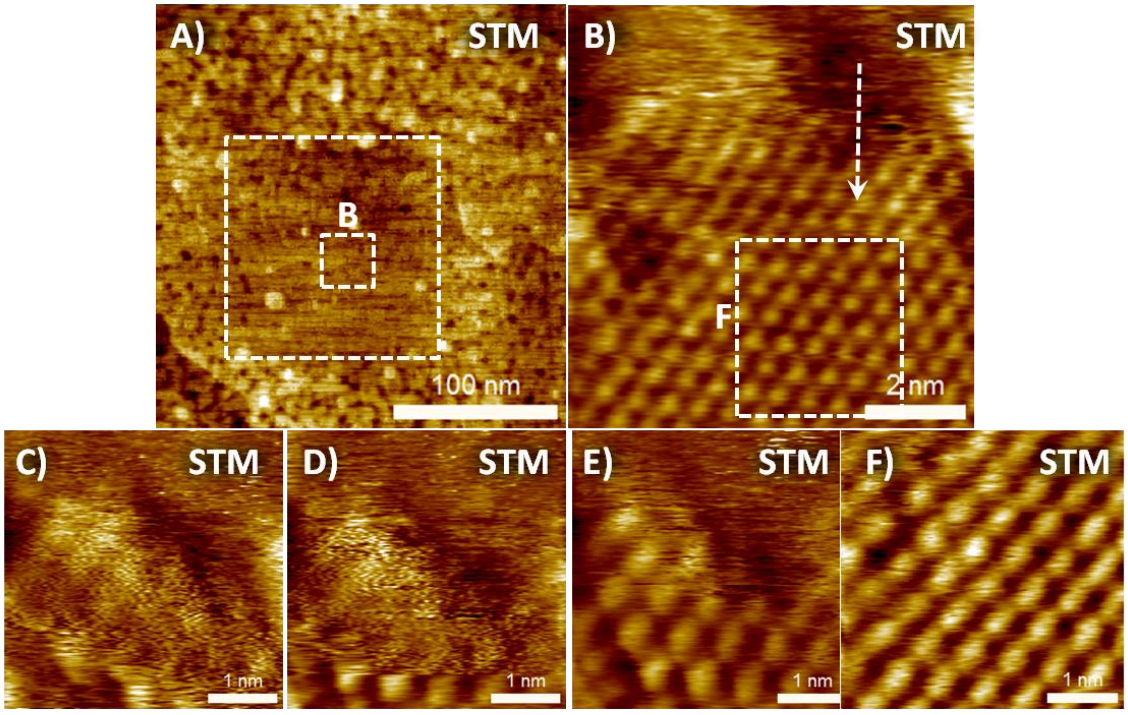

Figure 52. Imaging sequence of the 100 nm graft depicted in Figure 24 (G-I). During the imaging sequence, some tip-induced ordering is observed however the transition from order to disorder remains visible during repeated imaging.

*Reprinted from Pawlicki, A.; Avery, E.; Jurow, M.; Ewers, B.; Vilan, A.; Drain, C. M.; Batteas, J., Studies of the Structure and Phase Transitions of Nano-Confined Pentanedithiol and Its Application in Directing Hierarchical Molecular Assemblies on Au(111). J. Phys.-Cond. Matt. **2016**, *28* (9), 094013 with permission from IOPscience.

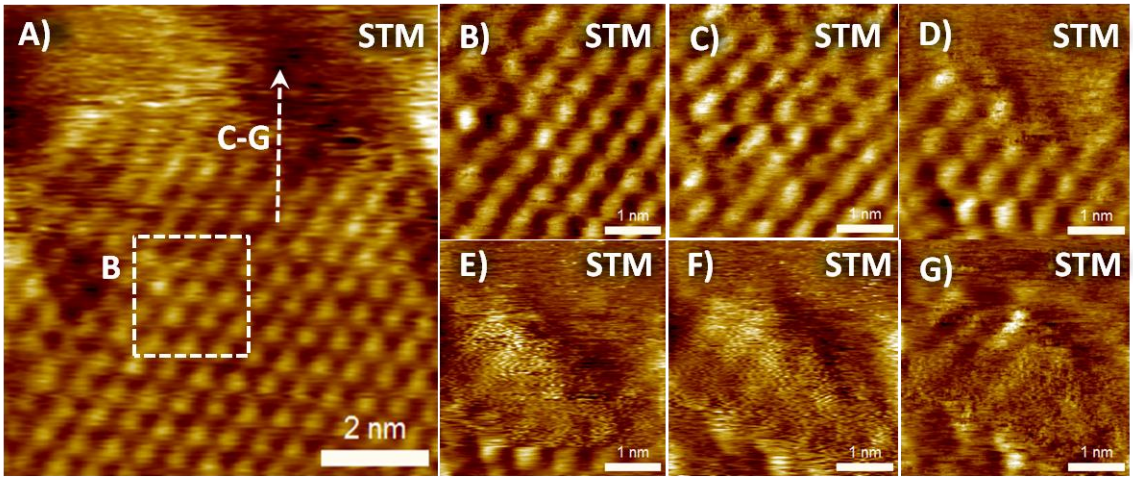

Figure 53. The imaging sequence of the 100 nm graft, depicted in Figure 24(G-I), was also conducted in reverse.

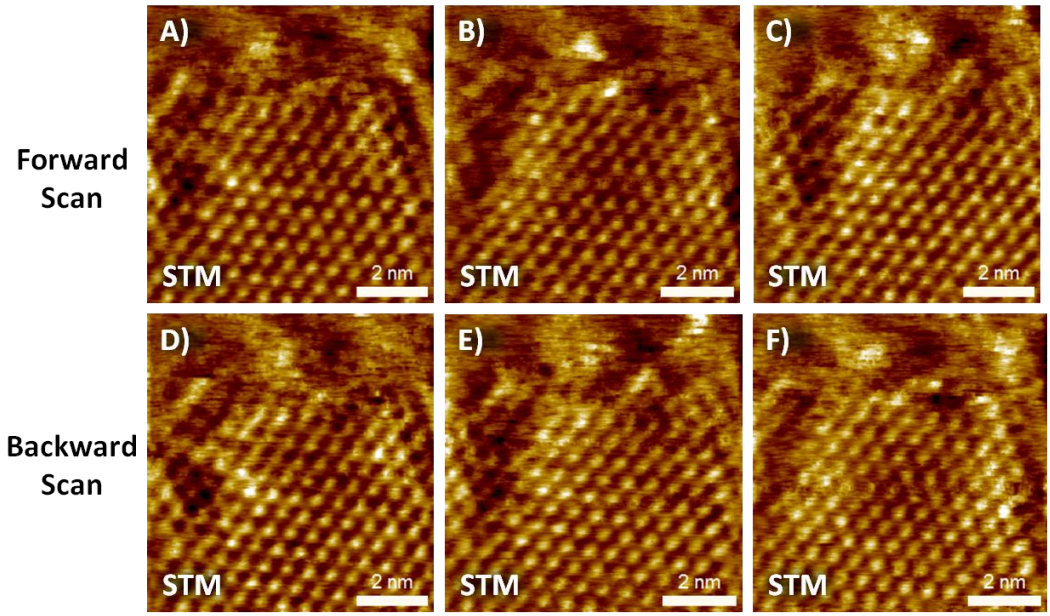

Figure 54. The ordered and disordered regions in the 100 nm graft depicted in Figure 24(G-I) was imaged repeatedly at a larger length scale. The forward scans are shown in A-C and the corresponding backward scans are shown in D-F. Upon repeated imaging, the scan region drifted slightly to the right.

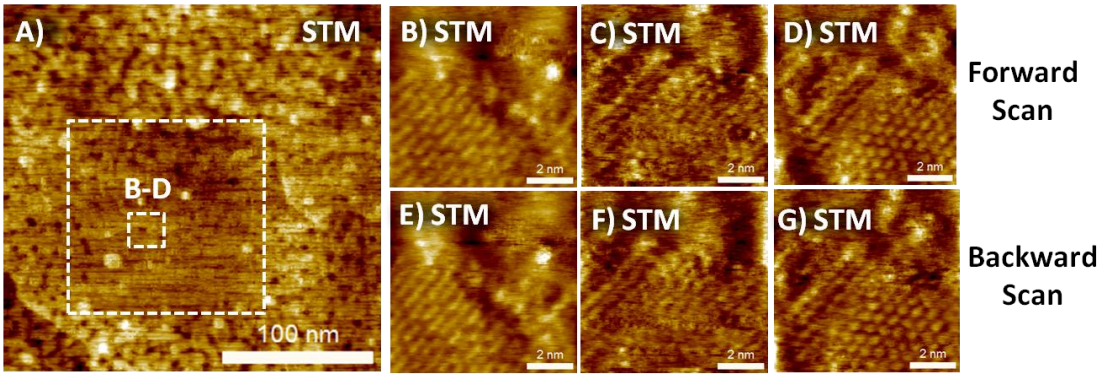

Figure 55. The order to disorder transition was imaged repeatedly in the 100 nm graft at different location; adjacent the region depicted in Figure 24**(**H). The forward scans are shown in B-D and the corresponding backward scans are shown in E-G. Again, upon repeated imaging, the scan region drifted slightly to the right.

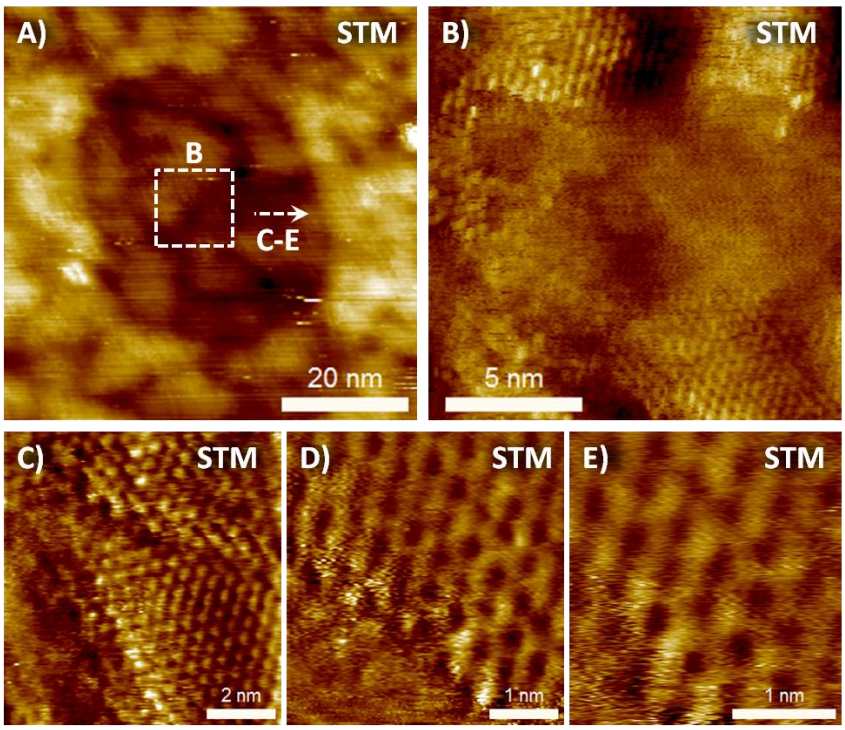

Figure 56. Imaging sequence of the 40 nm graft depicted in Figure 24**(**A-C).

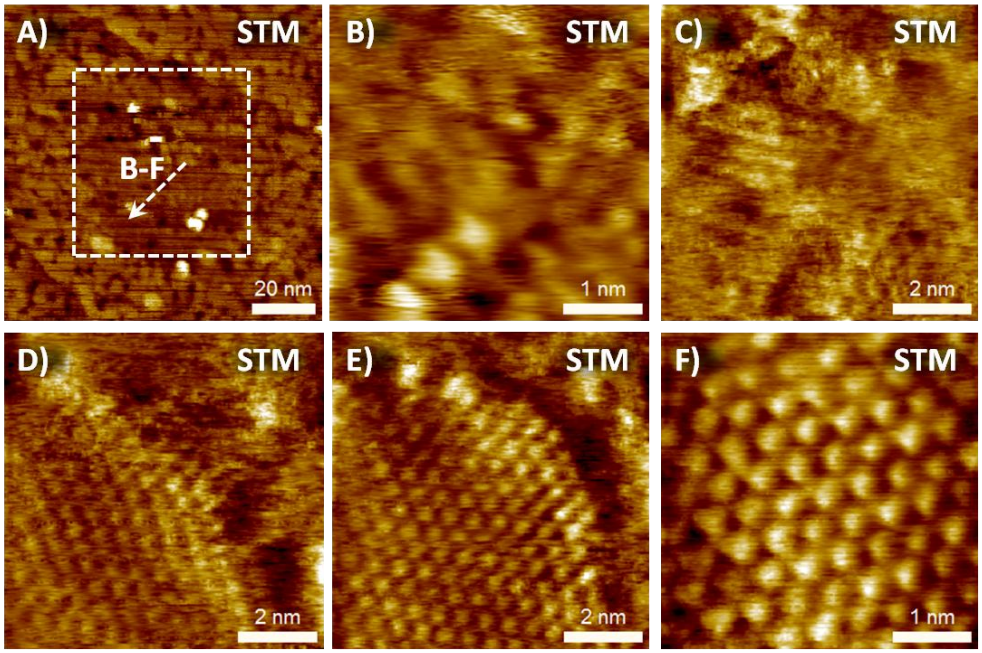

Figure 57. Imaging sequence of the 50 nm graft depicted in Figure 24**(**D-F).

APPENDIX D

METHOD FOR SCANNING TUNNELING SPECTROSCOPY (STS) MEASRUEMENTS

A method was developed to measure reliable and repeatable I-V spectroscopy of porphyrins within a C12 monolayer. This involves optimization of the STS measurement cycle including the bias intervals. Doing so is paramount because the observation of stochastic switching as discussed in Chapter III depends on the sampling rate and conditioning. Additionally, the STM tip can influence I-V spectroscopy. To minimize this influence thereby obtaining I-V curves characteristic of the porphyrin and not of the STM tip, we use a comparison method aided by the analysis of a balance factor which is defined below (Equation 13).

D.1 Scanning Tunneling Spectroscopy (STS) Measurement Cycle

The details of the STS bias intervals are provided in Figure 58. Each I-V measurement cycle starts with the feedback loop on and a 0.1 ms stabilization of the tip above the $ZnTPPF_4$-SC_5SH or C12 according to the 20 pA and 1.4 V set-points. Next, the feedback loop is turned off, the voltage is set to the starting point of the measurement (-2 V) and there is an additional 9 ms stabilization before the measurement begins. Then, the bias is scanned from -2 to 2 V for the I-V measurement. After 0.1 ms the feedback loop is tuned on again and allowed another 0.1 ms of stabilization before repeating the cycle. The cycle is repeated 10 times after which the tip is manually repositioned and the spectroscopy is carried out again to obtain a total of 100 curves. Therefore, with the

exception of the first spectra in the cycle, there is a 0.2 ms stabilization of the tip using the feedback loop before each measurement. During the measurement, 40.16 ms elapse before the feedback loop is tuned on again and the tip height is reestablished above the $ZnTPPF_4$-SC_5SH or C12 according to the 20 pA and 1.4 V set-points.

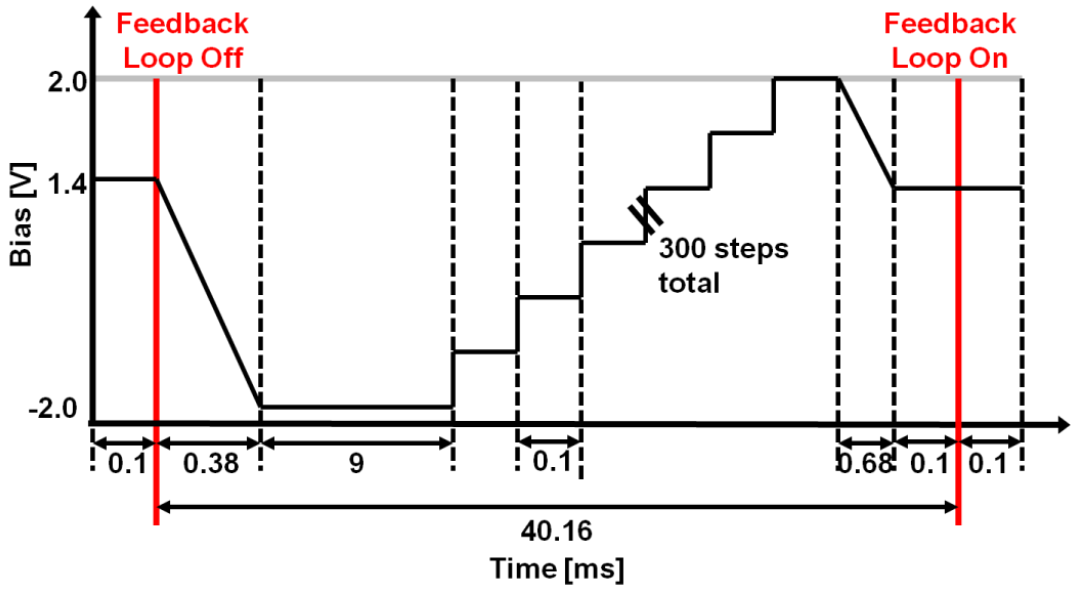

Figure 58. Schematic diagram displaying one I-V spectroscopy cycle, including delay and acquisition times.

D.2 Examining C12 I-V Curves Using a Balance Factor

To minimize spurious tip effects, like tip contamination or degradation, during I-V spectroscopy on the porphyrins, 100 current-voltage curves were collected on a near-by C12 matrix area immediately before and after the $ZnTPPF_4$-SC_5SH spectroscopy. If these reference spectra were of wide distribution or not well behaved, the results were

discarded. To examine the distribution and behavior of the C12 I-V curves, a balance factor was used. The balance factor is defined as

$$Balance = \frac{\int_0^2 \mathrm{I(V)^2V^2}dV - \int_{-2}^0 \mathrm{I(V)^2V^2}dV}{\int_{-2}^2 \mathrm{I(V)^2V^2}dV} \qquad \text{Equation 13}$$

where I is the current and V is the voltage. The balance factor was applied to each of the 100 C12 I-V curves and the results were examined in a histogram (Figure 59). A set of narrowly distributed and well behaved I-V curves is characterized by a balance factor histogram with a sharp peak in the range of -0.8 to 0.5 (Figure 59(A)). If the balance factor histogram does not have a well-defined peak and / or is outside of this range, then the data set is discarded (Figure 59(B)).

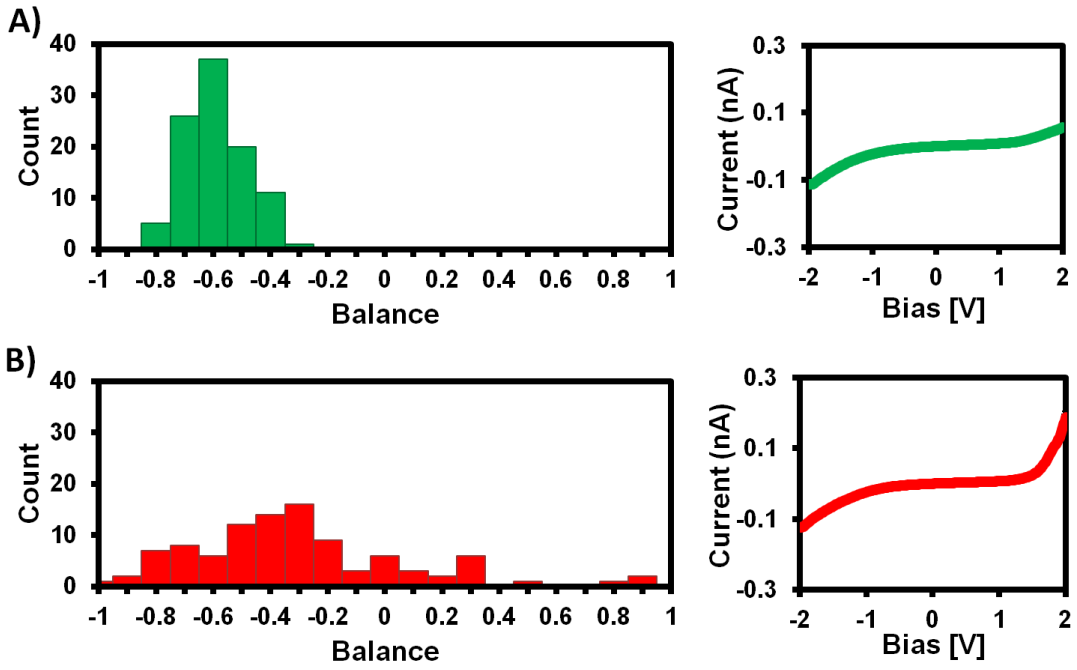

Figure 59. Representative balance factor histograms obtained from 100 I-V curves of C12 shown adjacent. In A) the data set is accepted because the histogram has a peak at between -0.8 and -0.5 and is narrowly distributed. However, in B) the data set is discarded because these criteria are not met.